

Almacenamiento de calor sensible en materiales de base cemento para infraestructuras de centrales termosolares

Sensible heat storage in cement-based materials for Solar Thermal Power Plants infrastructures

by

Tamara Lucio Martín

A dissertation submitted by in partial fulfillment of the requirements for
the degree of *Doctor of Philosophy* in Mechanical Engineering and
Industrial Organization

Universidad Carlos III de Madrid

Advisors:

Dr. María Cruz Alonso Alonso
Dr. Marcelo Izquierdo Millán

Tutor:

Dr. María del Carmen Venegas Bernal

Leganés, June 2021

This thesis is distributed under license “Creative Commons **Attribution – Non Commercial – Non Derivatives**”.

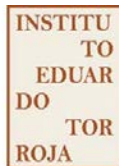
You must give appropriate credit, provide a link to the license and indicate if changes were made. You may do so in any reasonable manner, but not in any way that suggests the licensor endorses you or your use. You may not use the material for commercial purposes. If you remix, transform, or build upon the material, you may not distribute the modified material. You may not apply legal terms or technological measures that legally restrict others from doing anything the license permits.

<https://creativecommons.org/licenses/by-nc-nd/4.0/>





This PhD dissertation has been supported by the Spanish National Research Council, *Consejo Superior de Investigaciones Científicas* (CSIC) under a predoctoral contract.



The work was undertaken at Eduardo Torroja Institute for Construction Sciences, *Instituto de Ciencias de la Construcción Eduardo Torroja* (IETcc)



This project has received funding from the European Union's Horizon 2020 research and innovation programme under grant agreement No 720985.

This research has been developed in an H2020 project named NewSOL “New StOrage Latent and sensible concept for high efficient CSP Plants”

This page has been intentionally left blank.

A mis padres, M^a Victoria y Martín

This page has been intentionally left blank.

Acknowledgements

I would like to apologize to those non-Spanish speakers for writing this section in my mother tongue. As most of the people to whom I want to show my gratitude are Spanish speakers, I am going to use this langue for giving thanks for the support provided during these years.

Era un domingo de abril, pero no un domingo cualquiera. A pesar de ser el Domingo de Pascua, ya nada era como lo conocíamos años atrás. Ni siquiera nosotros. La sociedad estaba haciendo frente a una pandemia y yo me encontraba terminando una tesis. ‘*Nada volverá a ser igual*’ y ‘*Saldremos más fuertes de esta*’ eran frases que habíamos escuchado continuamente a lo largo del último año. Ambas reflexiones se podían aplicar a la tesis y a la situación sanitaria. En cuanto al desarrollo de la tesis, si algo había aprendido durante ese tiempo era que la investigación avanzaba gracias a la aportación de todos en su conjunto, y que esta debía ayudar al progreso y desarrollo de una sociedad más justa y favorable para todos. Con respecto a la pandemia, me encantaría reflexionar sobre ella en pasado. Sin embargo, quiero pensar que cuando acabe la sociedad habrá salido reforzada y haya aprendido, al menos, a ser mejor personas y a cuidarnos los unos de los otros. No pierdo la esperanza.

Comenzaré explicando que el desarrollo de esta tesis ha seguido el Principio de Superposición. Para aquel que no lo conozca, este teorema es una herramienta que trata de descomponer un problema en la suma de problemas más pequeños y sencillos. Tranquilo querido lector, este concepto técnico es el único que voy a mencionar en este apartado. Lo prometo. Quiero resaltarlo porque, aunque en la tesis aparezca solo mi nombre, en realidad soy la suma de las pequeñas contribuciones que me han aportado todas las personas con las que me he encontrado en el camino. Por ello, ha llegado la hora de mostrarles mi gratitud.

En primer lugar, quisiera agradecer a los directores de tesis Dra. M^a Cruz Alonso Alonso y Dr. Marcelo Izquierdo Millán la oportunidad que me brindaron. Es muy difícil conseguir un trabajo tan top recién titulada porque no se dan muchas oportunidades. Gracias por el reto técnico que ha supuesto y por todo lo que he aprendido bajo la tutela de dos expertos en los campos de la Ciencia del Hormigón y de la Ingeniería Térmica. Quiero agradecer también a Dra. María Venegas Bernal, tutora en la Universidad Carlos III de Madrid, por su continua disposición a ayudar durante los años de doctorado que, sin duda, han facilitado todas las gestiones y dudas generadas en este periodo.

Por otro lado, trabajar en el proyecto de investigación NewSOL me ha permitido conectar con investigadores de la Industria, centros de investigación y Universidades europeas. Quiero agradecer a todos los miembros del proyecto las discusiones técnicas de las que tanto he aprendido y la perseverancia que han demostrado por sacar el proyecto adelante.

A Marta, por enseñarme gran parte de lo que sé de hormigones y morteros, de artículos de investigación, congresos... Por compartir inquietudes, viajes, cafés, cenas y más cafés. Por su apoyo a lo largo de toda la tesis. Siempre dispuesta a ayudar y a escuchar. Hacer esta tesis ha sido muy fácil teniéndote como mentora.

A mis compañeros del *Instituto Eduardo Torroja*: Mercedes, María, Javier y Kristina, por los buenos momentos que pasamos y por todo lo que me habéis enseñado. A Virtudes, Jaime y Carlos

sin cuya ayuda no hubiera podido realizar la mayoría del trabajo experimental de esta tesis. Os debo mucho. A Jesús, por hacer el TFG en parte de la temática de esta tesis. No puedo olvidarme de Ana, Laura y Viviana, las doctorandas. Por compartir inquietudes y caminar juntas. Ni de Loli, Joan, Patri, Luis, Álvaro, Jimena y Pardis. Quiero destacar también la labor del equipo de limpieza, en especial a Ángeles y Alicia. Por cuidarnos tan bien. Asimismo, quiero extender los agradecimientos al equipo de Dirección, Gerencia, Servicios Generales y Administrativos y al Laboratorio de Hormigones por la calidad humana del trato que he recibido durante este tiempo.

A mis amigos. Laura, César, Rocío, Marcos y Edu por el apoyo, las comidas, escapadas, planes y las discusiones. A Carmen, por las '*chapas*' que ha tenido que aguantar estos años y por tratar siempre de arrojar luz en los peores momentos. A Bea, por los planes, rutas, recomendaciones deportivas (sí, las agradezco aunque no las lleve a cabo) y las conversaciones tan trascendentales que tenemos. No puedo agradecerte los audios de más de 3 minutos, pero sí la amistad que hemos forjado. Tampoco puedo terminar este párrafo sin mencionar a mis ratillas, que se han convertido en amigas y me las llevo para siempre. El concepto '*ratilla*' ha adquirido otra dimensión con vosotras y he de reconocer que me encanta. Ya sabéis que quien se hace ratilla rateará siempre. Unas más que otras, eso sí. Gracias por vuestros consejos, siempre tan acertados, por el humor y los momentos que hemos pasado juntas.

A ti, querido lector, por llegar hasta aquí y dedicarle algo de tiempo a leer parte de esta tesis.

A mi prima Laura, por demostrar que, aunque la vida pase, siempre vamos a seguir igual: planificando un viaje a Granada, paseando por Madrid y saliendo en la feria con Fran, Loli, Carballo y Juan.

A mi familia por su apoyo incondicional todos estos años. A mis abuelos por demostrarme que los valores son el título más importante que una persona puede tener. A los que nos dejaron en mitad del camino: Rodolfo y Martín. Por enseñarme que, pese a las adversidades de la vida, siempre hay ocasión para sacar una sonrisa y motivos por los que seguir luchando.

A Jaime, por el ingenio que le define y por estar siempre ahí. A Iván y su carácter inconformista, por perseguir sus sueños y, en especial, por ayudarme con los códigos de MATLAB de esta tesis. A mis padres, M^a Victoria y Martín, por inculcarme valores y por demostrar que con esfuerzo y constancia se puede llegar adonde quieras. Porque solo puedes ir más rápido, pero acompañado llegarás más lejos. Porque para poder crecer, debes tener buenos apoyos y el vuestro lo tengo siempre. Aunque no lo diga, os quiero mucho.

Gracias a todos de corazón.

The show must go on.

Published and submitted content

- **T. Lucio-Martin**, M. Roig-Flores, M. Izquierdo and M.C. Alonso, “Thermal conductivity of concrete at high temperatures for thermal energy storage applications: Experimental analysis”, *Solar Energy*, vol. 214, pp. 430-442, 2021. DOI: 10.1016/j.solener.2020.12.005.
 - Role: Author
 - This item is wholly included in the thesis in **chapters 2 and 4**.
 - The material from this source included in this thesis is not singled out with typographic means and references.
 - Contribution: T. Lucio-Martin developed the experimental test protocol and carried out the tests and the data analysis. Furthermore, she was in charge of writing the paper.
- **T. Lucio-Martin**, M. Roig-Flores, M. Izquierdo and M.C. Alonso, “Corrigendum to “Thermal conductivity of concrete at high temperatures for thermal energy storage applications: Experimental analysis” [Sol. Energy 214 (2021) 430-442]”, *Solar Energy*, 2021. DOI: 10.1016/j.solener.2021.02.044.
 - Role: Author
 - This item is partially included in the thesis in **chapter 4**.
 - The material from this source included in this thesis is not singled out with typographic means and references.
 - Contribution: T. Lucio-Martin developed the experimental test protocol and carried out the tests and the data analysis. Furthermore, she was in charge of writing the corrigendum.
- M. Roig-Flores, **T. Lucio-Martin**, M.C. Alonso and L. Guerreiro, “Evolution of thermo-mechanical properties of concrete with calcium aluminate cement and special aggregates for energy storage”, *Cement and Concrete Research*, vol 141, 2021. DOI:10.1016/j.cemconres.2020.106323.
 - Role: Co-author
 - This item is partially included in the thesis in **chapters 2, 3 and 4**.
 - The material from this source included in this thesis is not singled out with typographic means and references.
 - Contribution: T. Lucio-Martin developed the experimental tests for both the thermal cycles and the measurements of the thermal parameters. Furthermore, she was in charge of partial data analysis and wrote part of the paper.
- **T. Lucio-Martin**, M. Roig-Flores, M.C. Alonso and L. Guerreiro, “Evolution of thermal conductivity on CAC concrete at high temperatures and during thermal fatigue tests”, *Proceedings of the 6th International Workshop on Concrete Spalling due to Fire Exposure*, Sheffield (United Kingdom), September 2019.
 - Role: Author and speaker.
 - This item is partially included in the thesis in **chapters 2 and 4**.
 - The material from this source included in this thesis is not singled out with typographic means and references.
 - Contribution: T. Lucio-Martin developed the experimental test protocol and carried out the tests and the data analysis. Furthermore, she was in charge of writing the conference paper and presented the investigation at the event.

- **T. Lucio-Martin**, J. Puentes and M.C. Alonso, “Effect of geometry in concrete spalling risk subjected to high temperatures for thermal inertia studies”, *Proceedings of the 6th International Workshop on Concrete Spalling due to Fire Exposure*, Sheffield (United Kingdom), September 2019.
 - Role: Author.
 - This item is partially included in the thesis in **chapters 2 and 3**.
 - The material from this source included in this thesis is not singled out with typographic means and references.
 - Contribution: T. Lucio-Martin developed the experimental test protocol and carried out the tests and the data analysis. Furthermore, she was in charge of writing the conference paper.
- **T. Lucio-Martin**, M. Roig-Flores, J. Carretero, M.C. Alonso and M. Izquierdo, “Análisis de fisuración en hormigones de almacenamiento de energía sometidos a ciclos de fatiga térmica”, *II Jornadas de Jóvenes Científicos en Materiales de Construcción*, Instituto de Ciencias de la Construcción Eduardo Torroja (IETcc-CSIC), May 2019.
 - Role: Author and speaker.
 - This item is partially included in the thesis in **chapter 3**.
 - The material from this source included in this thesis is not singled out with typographic means and references.
 - Contribution: T. Lucio-Martin developed the experimental test protocol and carried out the image analysis. Furthermore, she was in charge of writing the conference abstract and presented the investigation at the event.
- **T. Lucio-Martin**, M.C. Alonso and M. Izquierdo, “Evolución de las propiedades termofísicas de los componentes del hormigón a alta temperatura”, *I Jornada de Jóvenes Científicos en Materiales de Construcción*, Escuela de Ingeniería de Caminos, Canales y Puertos, Universidad Politécnica de Madrid, June 2018.
 - Role: Author and speaker.
 - This item is partially included in the thesis in **chapter 2**.
 - The material from this source included in this thesis is not singled out with typographic means and references.
 - Contribution: T. Lucio-Martin developed the database of the evolution of thermophysical properties of different components from the analysis of the data available in the literature. Furthermore, she was in charge of writing the conference abstract and presented the investigation at the event.

- Patent of invention: “Procedimiento y equipo de medida para detectar, de forma continua y no destructiva, el secado de una estructura de hormigón”. Inventors: M.C. Alonso and **T. Lucio-Martin**. Application number P202031076, submitted and registered at Oficina Española de Patentes y Marcas on 28th October 2020.
 - Role: Inventor.
 - This item is partially included in the thesis in **chapters 5, 6 and 9**.
 - The material from this source included in this thesis is not singled out with typographic means and references.
 - Contribution: T. Lucio-Martin carried out the experimental protocol developed during the thesis, wrote the initial version of the patent and studied the closest prior art of the invention.

Other research merits

- **T. Lucio-Martin**, “Almacenamiento de calor sensible en materiales de base cemento para infraestructuras de centrales termosolares”. Thesis Talk 2019. Present your research in 3 minutes, Universidad Carlos III de Madrid, June-July 2019.
 - Role: Speaker.
 - Contribution: T. Lucio-Martin presented the research developed in the thesis before a non-specialist audience in 3 minutes. T. Lucio-Martin was classified in the second semifinal (28th June 2019) for participating in the final session that took place on 12th July 2019.
 - URL semifinal: <https://media.uc3m.es/video/5d25adc48f4208ecb18b456e>
 - URL final session: <https://media.uc3m.es/video/5d2ed2a08f420881a08b4568>

This page has been intentionally left blank.

Abstract

The continuous increase in global energy demand has intensified the negative effects of Climate Change, owing to the fact that the current models for producing energy are mainly based on fossil fuels. That is the reason why society needs for accelerating the transition into renewable energy sources and world leaders are struggling to cope with the future of energy to attain a better sustainable world.

Research in solar energy with the aim of finding a clean alternative to fossil fuels began to become popular almost 4 decades ago. However, energy storage and particularly thermal energy storage became popular at the beginning of the 21st century. The importance of doing a transition to a society based on renewable energies has expanded the interest and funding of these kinds of technologies and, as a consequence, the research has grown exponentially over the last 10 years.

Because of the increasing construction of Concentrated Solar Power (CSP) Plants around the World, the interest in thermal energy storage systems able to store energy at high temperatures has been also increased. The use of concrete as solid material for Thermal Energy Storage (TES) has been proved in some trials at laboratory and demonstration sites up to 450°C. However, as the knowledge on the topic goes on, the limits of operation are changing to upper temperatures and the mediums of TES needs to be adapted and improved without compromising its performance for the operation of the facility.

Nevertheless, the new limits of operation up to 600°C due to the advances in the molten salts force the designed concrete for TES to operate at higher limits of temperatures and under thermal cycling. Unfortunately, the knowledge on the performance of concrete at high temperatures is most limited to structures under a fire scenario. However, the boundary conditions of concrete exposed to a fire differs from the application of energy storage, in the first case the concrete is designed for resisting under Ultimate Limit State (ULS) and the second for Serviceability Limit State (SLS).

New limits also influence the thermophysical properties of concrete, whose evolution with temperature is limited in the literature. This fact also affects the results of the heat transfer models because those parameters are usually assumed constant and temperature-independent.

This doctoral thesis focuses on demonstrating the suitability of using concrete for TES infrastructures at temperatures up to 550°C and validating the performance in both the commissioning and operation processes.

To do so firstly has been proposed the design and testing of concrete for being operated under cyclic regimes of the temperature of a CSP Plant so as to validate the performance and its appropriateness for being used in the TES infrastructures. A wide set of experiments were carried out in order to characterize the mechanical and physicochemical properties of the materials. Furthermore, the evolution of the thermal parameters was analysed in depth owing to the importance of the application of TES. A test protocol for measuring the thermal conductivity of concrete at high temperatures was developed and the parameter was measured during two heating and cooling processes. This is the most complete work up to date in the evolution of thermal conductivity with temperatures up to 600°C and for repetitive heating and cooling cycles. This outcome has revealed that the variations in the thermal conductivity of concretes exposed to the

cycles experienced a significant variation in the first heating and, hence, the temperature-dependence expressions are valuable for models of heat transfer.

Later, the commissioning of concrete before its operation at high temperatures was validated in different compositions. The proposed protocol allows following the level of drying of concrete exposed to heat in real time by monitoring the concrete. The level of drying detectable with this methodology was above 90% and it was verified at the lab-scale. The lack of knowledge in the closest prior art of this discovery made it feasible to protect the knowledge and apply for a National Patent, which was registered at OEPM.

After that, a mock-up section of a thermocline tank made of concrete was built in collaboration with some industrial partners to evaluate the commissioning and operation at an up-scale. The challenge consisted of using concrete as an element in thermocline tanks where both cold and heated molten salts are placing in the same tank. The mock-up of a section of a thermocline tank simulates the following components: a steel container, an air chamber, a concrete layer and finally, the insulating layer. The outcomes of this development allowed learning some lessons related to the construction, commissioning and operation of thermocline tanks made of concrete for the TES of molten salts in CSP Plants.

Then, the thermal performance of the mock-up section of a thermocline tank was simulated through two MATLAB® codes. The first one represented the profiles of temperature in the prototype for analyzing the depth of the heat along with the prototype during the test. The second code simulates a thermal model of the whole mock-up in order to analyze in more detail the type of convection in the air chamber during the thermal cyclic performance. The results of both codes highlighted the role of the concrete as an insulating material and its adequacy for being used in the TES infrastructure. Furthermore, the effect of the air gap between the steel and the concrete is significant due to the forced convection during the operation.

The evolution of the research developed in this PhD has produced an improvement in the Technology Readiness Level (TRL) starting from the idea or concept (TRL 2-3), which was probed and validated at lab-scale (TRL 4) and in a relevant simulated environment (TRL 5).

As the research of the thesis has been undertaken under a European Innovation Project within Horizon 2020 Framework Programme (“NewSOL”, grant agreement No 720985), the present thesis has applied for the Industrial PhD distinction.

Keywords: concrete, high-temperature, thermal energy storage, thermal conductivity, infrastructures, commissioning, operation, thermocline tank.

Resumen

El continuo aumento de la demanda de energía mundial ha intensificado los efectos negativos del cambio climático debido al hecho de que los modelos actuales de producción de energía están basados principalmente en combustibles fósiles. Esa es la razón por la cual la sociedad necesita acelerar la transición hacia fuentes de energía renovables y los líderes mundiales se esfuerzan por afrontar el futuro de la energía para conseguir un mundo mejor y más sostenible.

La investigación en energía solar con el objetivo de encontrar una alternativa limpia a los combustibles fósiles comenzó a popularizarse hace casi cuatro décadas. Sin embargo, el almacenamiento de energía, y en particular el almacenamiento de energía térmica comenzó a popularizarse a principios del siglo XXI. La importancia de hacer una transición hacia una sociedad basada en energías renovables ha incrementado el interés y la financiación de este tipo de tecnologías y, como consecuencia, la investigación ha crecido exponencialmente en los últimos 10 años.

Debido a la creciente construcción de plantas termosolares de concentración en todo el mundo, también ha aumentado el interés por los sistemas de almacenamiento de energía térmica capaces de almacenar energía a altas temperaturas. El uso del hormigón como material sólido para el Almacenamiento de Energía Térmica (AET) ha sido probado en algunos ensayos en laboratorio y en demostradores hasta 450°C. Sin embargo, a medida que avanzan los conocimientos sobre el tema, los límites de funcionamiento están cambiando a temperaturas superiores y es necesario adaptar y mejorar los medios de AET sin comprometer su rendimiento para el funcionamiento de la instalación.

Los nuevos límites de funcionamiento hasta 600°C debido a los avances en las sales fundidas obligan a que el hormigón diseñado para el AET funcione con límites de temperaturas más elevados y bajo ciclos térmicos. Lamentablemente, el conocimiento sobre el comportamiento del hormigón a altas temperaturas se limita sobre todo a las estructuras sometidas a fuego. Sin embargo, las condiciones de contorno del hormigón expuesto a un incendio difieren de la aplicación del almacenamiento de energía, en el primer caso el hormigón se diseña para resistir bajo el Estado Límite Último (ELU) y en el segundo para el Estado Límite de Servicio (ELS).

Los nuevos límites también influyen en las propiedades termofísicas del hormigón, cuya evolución con la temperatura es muy limitada en la literatura. Este hecho también afecta a los resultados de los modelos de transferencia de calor, ya que estos parámetros se suelen suponer constantes e independientes de la temperatura.

Esta tesis doctoral se centra en demostrar la capacidad del uso del hormigón para infraestructuras de AET a temperaturas de hasta 550°C y en validar el funcionamiento tanto en el proceso de puesta en marcha como en el de operación de la instalación.

Para ello se ha propuesto, en primer lugar, el diseño y ensayo de hormigones operados bajo regímenes cíclicos de temperatura propios de una central termosolar con el fin de validar las prestaciones y su idoneidad para ser utilizados en las infraestructuras AET. Se realizó un amplio conjunto de experimentos para caracterizar las propiedades mecánicas y fisicoquímicas de los materiales. Además, se analizó la evolución de los parámetros térmicos en profundidad debido a su importancia en aplicaciones de AET. Se desarrolló un protocolo de ensayo para medir la

conductividad térmica del hormigón a altas temperaturas y se midió el parámetro durante dos procesos de calentamiento y enfriamiento. Este es el trabajo más completo hasta la fecha en la evolución de la conductividad térmica con temperaturas de hasta 600°C y para ciclos repetitivos de calentamiento y enfriamiento. Los resultados han revelado que las variaciones de la conductividad térmica de los hormigones expuestos a ciclos experimentaron un cambio significativo en el primer calentamiento y, por tanto, las expresiones que demuestran su dependencia con la temperatura son valiosas para los modelos de transferencia de calor.

Posteriormente, se validó la puesta en servicio del hormigón antes de su funcionamiento a altas temperaturas en diferentes composiciones. La metodología propuesta permite seguir el nivel de secado del hormigón expuesto al calor en tiempo real mediante su monitorización. El nivel de secado detectable con este protocolo fue superior al 90% y se verificó a escala de laboratorio. La falta de conocimiento en el estado de la técnica más cercano de este descubrimiento hizo que se protegiera el conocimiento y se solicitara una Patente Nacional, que fue registrada en la OEPM.

Posteriormente, se construyó una maqueta de un tanque termocílico de hormigón en colaboración con algunos socios industriales para evaluar la puesta en marcha y el funcionamiento a escala superior. El reto consistía en utilizar el hormigón como elemento en tanques termocílicos en los cuales se alojan sales fundidas tanto frías como calientes en el mismo tanque. La maqueta de la sección de tanque termocílico simuló los siguientes componentes: un depósito de acero, una cámara de aire, una capa de hormigón y finalmente, una capa de aislante. Los resultados de este desarrollo permitieron aprender algunas lecciones relacionadas con la construcción, la puesta en marcha y operación de los tanques termocílicos hechos de hormigón para el AET de sales fundidas en las plantas termosolares de concentración.

A continuación, se simuló el funcionamiento térmico de la maqueta de la sección de un tanque termocílico mediante dos códigos MATLAB®. El primero representó los perfiles de temperatura en el prototipo para analizar la profundidad del calor a través del prototipo durante el ensayo. El segundo código simuló un modelo térmico de todo el prototipo para analizar con más detalle el tipo de convección en la cámara de aire durante el funcionamiento de los ciclos térmicos. Los resultados de ambos códigos pusieron de manifiesto el papel del hormigón como material aislante y su idoneidad para ser utilizado en la infraestructura de AET. Además, el efecto del aire entre el acero y el hormigón es significativo debido a la convección forzada durante la operación.

El desarrollo de la investigación llevada a cabo en este doctorado ha producido una mejora en el Nivel de Madurez de la Tecnología (NMT) partiendo de la idea o concepto (NMT 2-3), que fueron probados y validados a escala de laboratorio (NMT 4) y en un entorno simulado relevante (NMT 5).

Dado que la investigación de la tesis se ha llevado a cabo en el marco de un Proyecto Europeo de Innovación dentro del Programa Marco Horizonte 2020 ("NewSOL", acuerdo nº 720985), se ha solicitado la Mención de Doctorado Industrial para la presente tesis.

Palabras clave: hormigón, alta temperatura, almacenamiento de energía térmica, conductividad térmica, infraestructuras, puesta en marcha, operación, tanque termocílico.

Acronyms

| | |
|--------|--|
| AG | Air Gap |
| ATD | Thermogravimetric Analysis |
| BFS | Blast Furnace Slag |
| BSEM | Electronic Microscope in Backscattered Mode |
| CAC | Calcium Aluminate Cement |
| CFC | Chlorofluorocarbons |
| CS | Case Study |
| CSH | Calcium Silicate Hydrates |
| CSP | Concentrating Solar Power |
| CSIC | Consejo Superior de Investigaciones Científicas (Spanish National Research Council) |
| CTE | Coefficient of Thermal Expansion |
| CTES | Concrete as a Thermal Energy Storage |
| DRX | X-ray diffraction |
| dTG | Differential Thermogravimetric Analysis |
| EMSP | Evora Molten Salts Platform |
| EPS | Expanded Polystyrene |
| EU | European Union |
| FEM | Finite Element Models |
| GHG | Greenhouse gas |
| H2020 | Horizon 2020 |
| HCFC | Hydrochlorofluorocarbons |
| HFC | Hydrofluorocarbons |
| HHM | Higher Heating Mat |
| H/L | Height/Lenght Ratio |
| HT | High Temperature |
| HTF | Heat Transfer Fluid |
| I | Insulation |
| IETcc | Instituto de Ciencias de la Construcción Eduardo Torroja (Eduardo Torroja Institute for Construction Sciences) |
| IL | Interface Layer |
| INECP | Integrated National Energy and Climate Plan |
| k | Thermal Conductivity |
| LCOE | Levelized Cost of Energy |
| LHM | Lower Heating Mat |
| MIP | Mercury Intrusion Porosimetry |
| NewSOL | New StOrage Latent and sensible concept for high efficient CSP Plants |
| NREL | National Renewable Energy Laboratory |
| NSC | Normal Strength Concrete |
| OEPM | Oficina Española de Patentes y Marcas (Spanish Patents and Trademarks Office) |
| OPC | Ordinary Portland Cement |
| PFC | Perfluorocarbons |

| | |
|--------|---|
| PPE | Personal Protective Equipments |
| PPF | Polypropylene Fibres |
| PT | Parabolic Trough |
| PCT | Patent Cooperation Treaty |
| RH | Relative Humidity |
| RT | Room Temperature |
| SCC | Self-Compacting Concrete |
| SDG | Sustainable Development Goals |
| SEM | Electronic microscope |
| SET | Strategic Energy Technology |
| SI | International System Units |
| SL | Steel Liner |
| SLS | Serviceability Limit State |
| SME | Small and medium-sized enterprises |
| ST | Solar Tower |
| STPP | Solar Thermal Power Plants |
| S/V | Surface/Volume Ratio |
| TES | Thermal Energy Storage |
| TP | Thermal Power |
| TRL | Technology Readiness Level |
| U | Uncertainties |
| UHPFRC | Ultra-High-Performance Fibre Reinforcement Concrete |
| ULS | Ultimate Limit State |
| UPV | Ultrasonic Pulse Velocity |
| WHRS | Waste Heat Recovery Systems |
| WOS | Web of Science |
| w/c | Water/Cement Ratio |

Greek symbols

| | |
|----------|---------------------|
| α | Thermal Diffusivity |
| ν | Kinematic Viscosity |
| σ | Standard Deviation |

Compounds

| | |
|--------------------------------|--|
| AH ₃ | Aluminum Hydroxide |
| Al ₂ O ₃ | Aluminium Oxide |
| C ₁₂ A ₇ | Dodecalcium Hepta-aluminate (Unhydrated Calcium Aluminate) |
| C ₂ AH ₈ | Calcium Aluminate Hydrate |
| CA | Unhydrated Calcium Aluminate |
| CAH ₁₀ | Calcium Aluminate Hydrate |
| CaO | Calcium Oxide |
| CH | Calcium Hydroxide |
| CH ₄ | Methane |

| | |
|--------------------------------|------------------|
| CO ₂ | Carbon Dioxide |
| Fe ₂ O ₃ | Iron (III) Oxide |
| K ₂ O | Potassium Oxide |
| MgO | Magnesium Oxide |
| Na ₂ O | Sodium Oxide |
| NO _x | Nitrous Oxides |
| SiO ₂ | Silicone Dioxide |
| SO ₃ | Sulfur Trioxide |

Content

| | |
|---|-------|
| Abstract | XIII |
| Resumen..... | XV |
| Acronyms | XVII |
| List of figures..... | XXIII |
| List of tables..... | XXVII |
| 1. Chapter 1 | 1 |
| 1.1. Context | 1 |
| 1.2. Motivation | 4 |
| 1.3. The Industrial project “NewSOL” | 5 |
| 1.4. Working Hypotheses | 7 |
| 1.5. Objectives..... | 7 |
| 1.6. Methodology..... | 8 |
| 1.7. Structure of the document..... | 9 |
| 1.8. References | 11 |
| 2. Chapter 2..... | 15 |
| 2.1. Field of research..... | 15 |
| 2.2. CSP and thermal energy storage | 17 |
| 2.3. Types of tanks of Molten salts | 18 |
| 2.3.1. 2-tanks | 18 |
| 2.3.2. Thermocline tank | 20 |
| 2.4. Role of concrete in CSP Plants | 21 |
| 2.5. Concrete at high temperature..... | 22 |
| 2.5.1. Thermal properties..... | 22 |
| 2.5.2. Spalling phenomenon | 26 |
| 2.5.3. Mechanical properties..... | 27 |
| 2.5.4. Electrical properties | 28 |
| 2.6. Challenges and gaps in the literature | 28 |
| 2.7. References | 30 |
| 3. Chapter 3..... | 39 |
| 3.1. Introduction | 40 |
| 3.2. Influence of concrete design and sample geometry in the risk of spalling of concrete at high temperature | 41 |
| 3.2.1. Methodology | 41 |
| 3.2.2. Results and discussion | 43 |
| 3.2.3. Partial conclusions on the spalling risk analysis | 47 |
| 3.3. Durability of High Thermal Performance Concrete under thermal cyclic operation and suitability for CSP infrastructures..... | 47 |
| 3.3.1. Methodology of the durability of High Thermal Performance Concrete under thermal cyclic operation and suitability for CSP infrastructures..... | 47 |
| 3.3.2. Results of the durability of High Thermal Performance Concrete under thermal cyclic operation and suitability for CSP infrastructures | 57 |
| 3.3.3. Partial conclusions on the design and performance of High Thermal Performance Concrete | 74 |
| 3.4. References | 76 |
| 4. Chapter 4..... | 79 |
| 4.1. Introduction | 79 |
| 4.2. Thermal properties of concrete after exposure at high temperature cycling | 80 |
| 4.2.1. Experimental procedure | 81 |

| | |
|---|-----|
| 4.2.2. Results and discussion | 83 |
| 4.2.3. Partial conclusions on the evolution of thermal parameters measured at room temperature..... | 87 |
| 4.3. Thermal properties of concrete at high temperature and during cycling | 88 |
| 4.3.1. Methodology | 88 |
| 4.3.2. Results and discussion | 93 |
| 4.3.3. Partial conclusions on the evolution of thermal conductivity at high temperature | 105 |
| 4.4. References | 107 |
| 5. Chapter 5..... | 111 |
| 5.1. Introduction: Moisture content preconditioning | 111 |
| 5.2. The methodology of the drying process..... | 112 |
| 5.2.1. Materials..... | 112 |
| 5.2.2. Methodology | 113 |
| 5.3. Results and discussion | 117 |
| 5.3.1. Test 1: Evolution of parameters for the drying + thermal cycling process up to 600°C | 117 |
| 5.3.2. Test 2: Evolution of parameters during the complete drying process at 105°C | 122 |
| 5.4. Conclusions..... | 130 |
| 5.5. References | 132 |
| 6. Chapter 6..... | 133 |
| 6.1. Up-scaling from lab-scale to a mock-up section of a thermocline tank | 133 |
| 6.2. Methodology | 135 |
| 6.2.1. Instrumentation of the mock-up..... | 137 |
| 6.2.2. Thermal regime..... | 139 |
| 6.3. Results..... | 140 |
| 6.3.1. Construction of the concrete layer | 140 |
| 6.3.2. Final arrangement of the mock-up | 143 |
| 6.3.3. Thermal performance | 145 |
| 6.4. Lessons learned | 150 |
| 6.5. Conclusions..... | 151 |
| 6.6. References | 153 |
| 7. Chapter 7..... | 155 |
| 7.1. Monitoring of the thermal performance of the up-scaled mock-up | 155 |
| 7.2. Methodology | 156 |
| 7.2.1. Thermal cycle | 156 |
| 7.2.2. Characterisation of the concrete layer after the thermal exposure | 158 |
| 7.3. Results and discussion | 160 |
| 7.3.1. Thermal cyclic operation of the mock-up | 160 |
| 7.3.2. Characterisation of the concrete layer after the thermal test | 164 |
| 7.4. Lessons learned and thermocline discussion | 175 |
| 7.5. Conclusions..... | 176 |
| 7.6. References | 178 |
| 8. Chapter 8..... | 181 |
| 8.1. Thermal model of the prototype | 181 |
| 8.1.1. Definition of variables and thermal powers | 181 |
| 8.1.2. Energy balances | 187 |
| 8.1.3. Convection heat transfer in the Air Gap | 193 |
| 8.1.4. Case studies | 195 |
| 8.1.5. Results of the theoretical thermal model | 195 |

| | |
|---|-----|
| 8.2. Simulations of the temperature of the prototype..... | 201 |
| 8.2.1. Definition of the MATLAB code..... | 201 |
| 8.2.2. Results of the simulation of the temperature of the prototype | 202 |
| 8.3. Lessons learned and limitations of the model | 205 |
| 8.4. Conclusions..... | 206 |
| 8.5. References | 207 |
| 9. Chapter 9..... | 209 |
| 9.1. Background of the invention..... | 209 |
| 9.2. Patent analysis..... | 211 |
| 9.3. Evaluation of patentability..... | 214 |
| 9.4. Application for a National Patent..... | 214 |
| 9.5. Conclusions..... | 215 |
| 9.6. References | 216 |
| 10. Chapter 10 | 217 |
| 10.1. Validation of Objectives | 217 |
| 10.2. Validation of Working Hypotheses..... | 222 |
| 10.3. Future Work | 224 |
| Conclusions..... | 227 |
| Appendix A..... | 229 |
| Appendix B | 231 |
| Appendix C..... | 233 |
| C.1) Temperature profiles at different depths (X-Planes)..... | 233 |
| C.2) Temperature profiles at different depths from the heat source (Y-Planes) | 238 |
| C.3) Temperature profiles at different heights (Z-Planes) | 244 |
| Appendix D | 251 |
| Appendix E..... | 257 |
| E.1) Publications in Journals Indexed in the Journal Citation Report | 258 |
| E.2) International Conference Papers | 260 |
| E.3) National Conference Papers | 261 |

List of figures

| | |
|---|----|
| Figure 1.1: Annual CO ₂ emissions from fossil fuels and cement production from 1750-2018. Source: [2]..... | 2 |
| Figure 1.2: Publications per year containing “solar energy”, “energy storage” and “thermal energy storage”. Source: data extracted from Web of Science (WOS) on 1 st of January of 2021..... | 4 |
| Figure 2.1: Materials Science & Engineering double tetrahedron. Source: adapted from [1]. | 16 |
| Figure 2.2: CSP technologies. Adapted from [3]..... | 17 |
| Figure 2.3: PT CSP Plant with a 2-tank indirect thermal energy storage and the power block. Source: NREL [11]..... | 19 |
| Figure 2.4: Types of molten salts storage. Source: Adapted from [15]..... | 19 |
| Figure 2.5: Charging and discharging processes of a thermocline tank..... | 21 |
| Figure 2.6: Evolution of thermal conductivity of different aggregates with temperature. Graph representing data published in [59-65]. | 24 |
| Figure 2.7: Evolution of specific heat of different aggregates with temperature. Graph representing data published in [66-68]..... | 25 |
| Figure 3.1: Geometries and thermocouples located inside the concrete samples..... | 42 |
| Figure 3.2: First dehydration stage: CYLINDRICAL and CUBIC samples..... | 43 |
| Figure 3.3: First dehydration stage: PRISMATIC sample..... | 44 |
| Figure 3.4: Prismatic sample after the spalling phenomenon..... | 45 |
| Figure 3.5: First dehydration stage for all geometries..... | 46 |
| Figure 3.6: Thermal cycle and stages..... | 48 |
| Figure 3.7: Detailed heating rates and repetitive cycles..... | 49 |
| Figure 3.8. Position of the concrete cylinders and disks inside the oven (left) and detail (right). | 54 |
| Figure 3.9: Experimental set-up in the SATER oven..... | 54 |
| Figure 3.10. Cylindrical samples and disks drying in the oven at 105°C. | 55 |
| Figure 3.11: Mean value of mass variation after thermal cycles..... | 57 |
| Figure 3.12: Mean value of mass variation at long-term for B-C-S15%..... | 57 |
| Figure 3.13: Compressive strength mean values at 7 and 28 days. | 58 |
| Figure 3.14: Compressive strength after 1, 5 and 10 thermal cycles. | 59 |
| Figure 3.15: Evolution of the compressive strength estimated through the experimental results of this work, considering daily thermal cycles..... | 60 |
| Figure 3.16: Evolution of UPV (left) and Elastic Modulus of concrete samples after thermal cycles. | 61 |
| Figure 3.17: Evolution of Elastic Modulus for the B-C-S15% composition at long-term performance..... | 61 |
| Figure 3.18: Procurement process of the crack mapping with software GIMP® (left) and real picture with coloured pattern (right) of composition B-C-S15% after being exposed to 1 thermal cycle..... | 62 |
| Figure 3.19: Comparison of micro-cracks mapping for B-C-S15% (left) and C (right)..... | 67 |
| Figure 3.20: Comparison of micro-cracks mapping for B-C-S15% after 1 to 10 thermal cycles (left) and after 25-75 thermal cycles (right)..... | 68 |
| Figure 3.21: Crack area variation of the four concrete mixes after 1, 6, and 10 cycles, measured in % of an area of 162.42 mm ² | 69 |
| Figure 3.22: Pictures taken at different locations of the cylindrical specimen..... | 69 |
| Figure 3.23: Maximum width cracks for B-C-S15%, B-S, C, B-C-S30% and S after thermal cycles..... | 70 |

| | |
|--|-----|
| Figure 3.24: Cracks produced in the interfaces between the cement paste and the three aggregates after thermal cycles..... | 71 |
| Figure 3.25: Pore size distribution for the four concrete mixes before and after thermal cycling..... | 72 |
| Figure 3.26: X-ray diffraction results of B-C-S15% mix before and after the thermal cycles..... | 73 |
| Figure 3.27: ATD/dTG results for mixes before and after the thermal cycles..... | 74 |
| Figure 4.1: Equipment QTM-700 and probe for measuring at room temperature. | 83 |
| Figure 4.2: Equipment ISOMET (model 2104) and probe for measuring at room temperature..... | 83 |
| Figure 4.3: Thermal conductivity in wet and dried states. | 84 |
| Figure 4.4: Residual heat capacity (left) and diffusivity (right) | 84 |
| Figure 4.5: Evolution of thermal conductivity of all compositions after 0, 1, 5 and 10 thermal cycles. | 85 |
| Figure 4.6: Evolution of thermal conductivity after a long-term performance of B-C-S15% composition. | 85 |
| Figure 4.7: Residual values of heat capacity and diffusivity after 5 thermal cycles. | 87 |
| Figure 4.8: Graphical layout of the test facility and equipment. | 90 |
| Figure 4.9: Experimental set-up of the real test facility..... | 90 |
| Figure 4.10: Thermal cycle with the stages in different colours..... | 92 |
| Figure 4.11: Thermal conductivity at room temperature measured with the two probes.... | 94 |
| Figure 4.12: Evolution of thermal conductivity up to 600°C for the CAC concrete mixes.95 | |
| Figure 4.13: Measured thermal conductivity of CAC concretes and comparison to concretes from the literature [15-19]..... | 97 |
| Figure 4.14: Evolution of thermal conductivity up to 600°C for the 3-B-C-S with different heating rates. | 99 |
| Figure 4.15: Evolution of thermal conductivity when heating from 300°C to 600°C during the 1H and 2H for the CAC concrete mixes. | 100 |
| Figure 4.16: Percentage of variation between the two heating processes..... | 100 |
| Figure 4.17: Evolution of thermal conductivity when cooling from 600°C to 300°C (1C) and from 600 to 25°C (2C) for the CAC concrete mixes. | 101 |
| Figure 4.18: Percentage of variation between the two cooling processes. | 102 |
| Figure 4.19: Example of microscopic analysis after the thermal exposure for the 5-S composition (each value of “length” indicates the crack width measured at the point indicated). | 103 |
| Figure 4.20: Crack width for the concrete mixes after the thermal cycle. | 103 |
| Figure 4.21: Evolution of thermal conductivity of 3-B-C-S with temperature for successive heating and cooling processes obtained from fitted equations. | 104 |
| Figure 4.22: Estimation of thermal conductivity at 600°C during the thermal cycles of 3-B-C-S concrete mix. | 105 |
| Figure 5.1: Picture of the furnace with instrumented samples..... | 115 |
| Figure 5.2: left) detail of metallic mesh containing UHPFRC samples and right) picture of empty samples..... | 115 |
| Figure 5.3: Thermal cycle and stages..... | 116 |
| Figure 5.4: Mass loss at different hours of the drying stage for the five materials tested. . | 118 |
| Figure 5.5: left) Evolution of mass during drying and right) level of drying during the testing time..... | 118 |
| Figure 5.6: Evolution of the electrical resistance: left) with the temperature and right) with the testing time..... | 119 |
| Figure 5.7: Electrical resistance and percentage of free water loss during drying. | 120 |
| Figure 5.8: Mass loss during the first heating at different temperatures up to 600°C. | 121 |

| | |
|--|-----|
| Figure 5.9: Cumulative mass loss during the first and successive heating and cooling cycles. | 121 |
| Figure 5.10: Images of the OPC-UHPFRC after suffering from a spalling phenomenon. | 122 |
| Figure 5.11: Percentage of drying at different times of testing. | 123 |
| Figure 5.12: left) Evolution of mass loss during drying and right) level of drying during the testing time. | 124 |
| Figure 5.13: Evolution of electrical resistance during the test. | 124 |
| Figure 5.14: Evolution of electrical resistance and the percentage of drying of conventional concretes. | 125 |
| Figure 5.15: Evolution of electrical resistance and the percentage of drying of OPC-UHPFRC. | 125 |
| Figure 5.16: Thermal conductivity before and after dried, at high and room temperature. | 126 |
| Figure 5.17: Cross-section of OPC-Insulating left) before and right) after the drying process. | 128 |
| Figure 5.18: Cumulative pore volume for the four concrete compositions before and after the drying process. | 129 |
| Figure 5.19: Total porosity before and after the drying process at 105°C. | 130 |
| Figure 6.1: Layers of the mock-up section of a thermocline tank. | 136 |
| Figure 6.2: Location of thermocouples in the mock-up. | 137 |
| Figure 6.3: Schematic representation of the electrical connections at the top of the concrete layer. | 139 |
| Figure 6.4: Drying and dehydration curve. | 140 |
| Figure 6.5: Pictures of the mould and appearance of fresh concrete. | 141 |
| Figure 6.6: Evolution of temperature within concrete during the hydration and hardening. | 142 |
| Figure 6.7: Final aspect of the concrete layer with the embedded sensors. | 142 |
| Figure 6.8: Assembly of the mock-up section of a thermocline tank. | 145 |
| Figure 6.9: Evolution of temperature in the layers of the mock-up of a thermocline section. Drying and dehydration stage. | 146 |
| Figure 6.10: Evolution of temperature in the layers of the mock-up of a thermocline section. Drying and dehydration stage. | 147 |
| Figure 6.11: Temperature differences in the layers of the mock-up of a thermocline section. Drying and dehydration stage. | 147 |
| Figure 6.12: Evolution of temperature along with the heat source at the end of the drying and dehydration stage. | 149 |
| Figure 6.13: Evolution of the electrical resistance of the 5 connections during the drying and dehydration stage. | 150 |
| Figure 6.14: Evolution of electrical resistance and temperature inside the concrete for the 2 levels of depth. | 150 |
| Figure 7.1: Simulated thermal cycling process operation of the mock-up in the heating mats. | 157 |
| Figure 7.2: Thermal cycling curve. | 158 |
| Figure 7.3: Position of the drilled core samples of the concrete. | 159 |
| Figure 7.4: Evolution of temperature in the layers of the mock-up of a thermocline section. Thermal cycling stage. | 161 |
| Figure 7.5: Evolution of temperatures in the concrete layer. Thermal cycling stage. | 162 |
| Figure 7.6: Temperature differences in the layers of the mock-up. Thermal cycling stage. | 162 |
| Figure 7.7: Evolution of temperature along with the heat source when the mock-up was operating at 500°C. | 164 |

| | |
|--|-----|
| Figure 7.8: Evolution of temperature along with the heat source when the mock-up was operating at 200°C..... | 164 |
| Figure 7.9: Pictures taken on the concrete element after thermal exposure..... | 165 |
| Figure 7.10: Position of the drilled core samples (left), extracted from the element (centre) and core sample 1 (right). | 165 |
| Figure 7.11: Identification of sensors of core sample 1..... | 166 |
| Figure 7.12: Colour profile of the core sample 2 in 62.23 mm..... | 167 |
| Figure 7.13: Depth of colour change of all core samples. | 167 |
| Figure 7.14: Crack width with depth from the heat source..... | 168 |
| Figure 7.15: top-left) Compressive strength, top-right) UPV and bottom) Elastic modulus in core samples 3, 6 and 9..... | 169 |
| Figure 7.16: top) UPV and bottom) Elastic modulus in core samples 2, 5 and 8 along with the depth of the concrete to the heat source..... | 170 |
| Figure 7.17: left) Thermal conductivity and right) electrical resistivity of samples 3, 6 and 9. | 171 |
| Figure 7.18: Evolution in the depth of thermal conductivity of samples 2, 5 and 8..... | 171 |
| Figure 7.19: Evolution in the depth of accessible porosity of samples 2, 5 and 8. | 172 |
| Figure 7.20: DRX results of CAC concrete samples at 10, 60, 150, 200 and 290 mm from the heated surface. | 173 |
| Figure 7.21: TG/DTG analyses for CAC concrete powder located at different depths: top) 10 and 60 mm, middle) 150 and 200 mm and bottom) 290 mm..... | 174 |
| Figure 8.1: Schema of the thermal powers across the prototype..... | 182 |
| Figure 8.2: Circuit of equivalent thermal resistances of the prototype. | 183 |
| Figure 8.3: Thermal resistances in the upper part of the insulating layer. | 191 |
| Figure 8.4: Thermal powers in the Air gap. Power supply (Q_1, Q_2), heat transfer powers to concrete (Q_3, Q_4), heat transfer losses (Q_{loss1}, Q_{loss2}) and heat power from bottom to top (Q_5). | 196 |
| Figure 8.5: Thermal powers across all the layers and heat transfer losses. | 197 |
| Figure 8.6: Evolution of the Rayleigh number during the testing time. | 198 |
| Figure 8.7: Evolution of the convection heat transfer coefficient in the air gap..... | 198 |
| Figure 8.8: Evolution of the theoretical Nusselt number for free convection inside a rectangular cavity during the testing time..... | 200 |
| Figure 8.9: Evolution of the experimental Nusselt number during the testing time. | 201 |
| Figure 8.10: Layers of the prototype in isometric perspective. | 202 |

List of tables

| | |
|---|-----|
| Table 2.1: PT CSP Plants around the World: characteristics, dimensions of tanks and costs. Source: [20-33]..... | 20 |
| Table 2.2: Thermal conductivity and thermal expansion coefficient of rocks and concretes with different aggregates at room temperature. Source: [57, 58] | 23 |
| Table 3.1: Concrete composition..... | 41 |
| Table 3.2: Location of thermocouples..... | 42 |
| Table 3.3: Specimen characteristics and the relationship between shape, size and volume. | 42 |
| Table 3.4: Temperature differences between the furnace and the core of the specimens..... | 46 |
| Table 3.5: Sand and gravel aggregates used in the compositions..... | 50 |
| Table 3.6: TG/DTG analysed for basal sand and gravel, CAT sand and gravel, slag sand and gravel, siliceous sand and CAC cement..... | 51 |
| Table 3.7: Composition of CAC cement (wt.%) | 51 |
| Table 3.8: Concrete compositions | 52 |
| Table 3.9: Furnaces and technical characteristics used in this study. | 53 |
| Table 3.10: Experimental campaign and specimens analysed in this study..... | 55 |
| Table 3.11: Crack mappings of B-C-S15% in the centre of the samples after 1, 5, 10, 25 and 75 thermal cycles. | 63 |
| Table 3.12: Crack mappings of B-C in the centre of the samples after 1, 5, 10, 25 and 75 thermal cycles. | 64 |
| Table 3.13: Crack mappings of C in the centre of the samples after 1, 5 and 10 thermal cycles..... | 65 |
| Table 3.14: Crack mappings of B-C-S30% in the centre of the samples after 1, 5 and 10 thermal cycles. | 65 |
| Table 3.15: Crack mappings of S in the centre of the samples after 1, 5 and 10 thermal cycles..... | 66 |
| Table 4.1: Concrete compositions | 81 |
| Table 4.2: Mix compositions used in this work..... | 89 |
| Table 4.3: Mean values and uncertainties of thermal conductivity for the first heating up to 600°C. | 98 |
| Table 5.1: Instrumentation of samples for carrying out the tests. | 113 |
| Table 5.2: Summary of the tests carried out in this chapter. | 117 |
| Table 6.1: Dimensions and up-scale volume factor between the samples tested in this thesis. | 135 |
| Table 6.2: Composition and properties of the concrete layer. | 137 |
| Table 6.3: Coordinates of the thermocouples placed in the mock-up..... | 138 |
| Table 7.1: Tests of visual analysis of core samples. | 159 |
| Table 7.2: Tests of physicochemical characterisation of core samples. | 159 |
| Table 7.3: Coordinates of sensors localized in core sample 1 | 166 |
| Table 8.1: Dimensions and properties of layers of the prototype. | 184 |
| Table 8.2: Thermal properties of layers of the prototype. | 184 |
| Table 8.3: Parameters of the heat transfer analysis | 186 |
| Table 8.4: Type of convection and typical values. Source: [1]..... | 194 |
| Table 8.5: Case studies for the simulations and the thermal model. | 195 |
| Table 8.6: Type of convection for the cases studied. | 199 |
| Table 8.7: Temperature profile of the prototype at different times of testing..... | 203 |
| Table 8.8: Temperature across layers in X, Y and Z-planes for the case studies analysed. | 205 |
| Table 9.1: Patents closer to the prior art of the methodology and device for monitoring the drying process from Google Patents, Patentscope, Espacenet and INVENES. | 213 |

This page has been intentionally left blank.

Chapter 1

Introduction

In this chapter, it is introduced the work that has been performed during this Industrial PhD thesis. To begin, *section 1.1* describes the context in which the work is involved and the disciplines surrounding the field of study. Secondly, *section 1.2* describes the motivation and the increasing interest in the field of energy storage by researchers over the last decades.

Section 1.3 clarifies the motivation for this thesis by explaining the Industrial European project “NewSOL” where the present Industrial thesis is developed and the problem to solve. Given that, the study starts with a working hypothesis counted in *section 1.4* in order to accomplish the research, whose aim and objectives are described in *section 1.5*.

As the research involves both experimental and theoretical tasks, *section 1.6* gives a brief summary of the methodological approach so as to achieve the goals of the present study.

Finally, *section 1.7* gives a brief overview of the structure of the document.

1.1. Context

The continuous increase in global energy demand has intensified the negative effects of Climate Change. World energy production, mainly based on fossil fuels, is the principal source of CO₂ emissions. Fossil fuel depletion has been considered as a future challenge and some researchers highlight the need for a holistic solution [1].

Climate Change is mainly affected by Greenhouse Gas (GHG) emissions, which include Carbon Dioxide (CO₂), Methane (CH₄), Nitrous Oxides (NO_x) and Fluorinated gases that are emitted in a wide variety of industrial processes, such as Hydrofluorocarbons (HFC), Chlorofluorocarbons (CFC), Hydrochlorofluorocarbons (HCFC), Perfluorocarbons (PFC), Sulphur Hexafluoride, etc. Figure 1.1 shows the annual CO₂ emissions from fossil fuels and cement production in the World since 1751. In 2018 more than 35 GT of CO₂ emissions were mainly produced in Asia and United States. Europe is the exclusive region that is reducing its emissions.

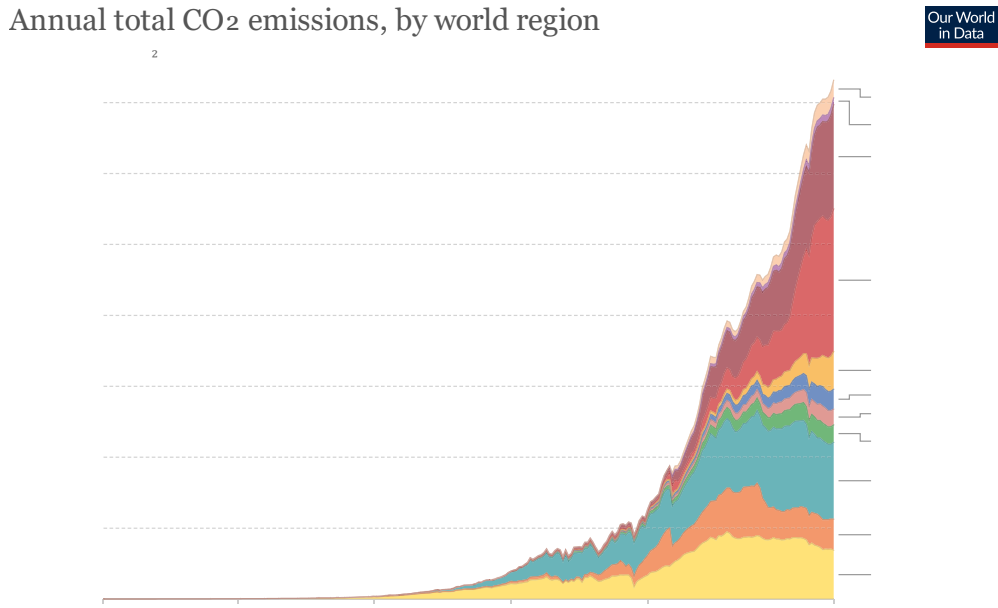


Figure 1.1: Annual CO₂ emissions from fossil fuels and cement production from 1750-2018. Source: [2].

Cold snaps and heat waves, droughts, floods, desertification and pollution are among the principal consequences of human action, but the list is still rather big. Some researchers point out that Climate Change is the biggest issue to deal with in the World in the XXI century [3, 4]. The reason is the increase in the energy demand and the current models for producing energy based on fossil fuels. For that reason, society needs for accelerating the transition into renewable energy sources and regions such as European Union (EU) are struggling to cope and shape its future and to attain a net-zero emissions continent for 2050.

European legislation

EU leaders agreed to reduce the GHG progressively up to 2050 to achieve a low-carbon economy. For that aim, they planned some energy targets by 2020, 2030 and finally 2050. The goal for 2020 was to achieve a decrease of 20% of the GHG emissions from 1990, to have a 20% of the EU energy renewable and to improve in 20% the energy efficiency. For the year 2030, the targets are more ambitious: reduction of at least 40% of GHG emissions from 1990, to have at least 32% of energy renewable and an improvement in the energy efficiency of at least 32.5%. Finally, the EU wishes to be climate-neutral by 2050 with a reduction in the GHG to zero [5].

On the other hand, the United Nations collects 17 goals to transform the World called the Sustainable Development Goals (SDG) to promote prosperity at the same time that the protection of the planet. Some goals are related to the energy and climate sector. Goals 7 and 13 named ‘Affordable and Clean Energy’ and ‘Climate Action’, respectively are the ones facing the issues explained above to reshape and change the future in a sustainable way [6]. The targets of goal 7 for 2030 are as follows [7]:

“1) ensure universal access to affordable, reliable and modern energy services, 2) increase substantially the share of renewable energy in the global energy mix, 3) double the global rate of improvement in energy efficiency, 4) enhance international cooperation to facilitate access to clean

energy research and technology, including renewable energy, energy efficiency and advanced and cleaner fossil-fuel technology, and promote investment in energy infrastructure and clean energy technology and 5) expand infrastructure and upgrade technology for supplying modern and sustainable energy services for all in developing countries, in particular least developed countries, small island developing States, and land-locked developing countries, in accordance with their respective programmes of support”.

The targets for goal 13 related to ‘Climate Action’ are the following [8]:

“1) Strengthen resilience and adaptive capacity to climate-related hazards and natural disasters in all countries, 2) Integrate climate change measures into national policies, strategies and planning, 3) Improve education, awareness-raising and human and institutional capacity on climate change mitigation, adaptation, impact reduction and early warning, 4) Implement the commitment undertaken by developed-country parties to the United Nations Framework Convention on Climate Change to a goal of mobilizing jointly \$100 billion annually by 2020 from all sources to address the needs of developing countries in the context of meaningful mitigation actions and transparency on implementation and fully operationalize the Green Climate Fund through its capitalization as soon as possible and 5) Promote mechanisms for raising capacity for effective climate change-related planning and management in least developed countries and small island developing States, including focusing on women, youth and local and marginalized communities”.

EU has achieved the target for the reduction of emissions for 2020 and recently has provided an action plan called European Green Deal [9]. It belongs to the Commission’s strategy to implement both the SDGs and the European Agenda 2030-2050 for achieving a continent climate neutral in 2050. The action plan aims at removing GHG emission by 2050 and promoting the circular economy with efficient use of resources, reducing pollution and restoring biodiversity. The Green Deal also promotes funding for research and development in the topics mentioned above for the period 2019-2024.

Spanish legislation

The Spanish Ministry of Industry has made an Integrated National Energy and Climate Plan (INECP) in order to accomplish the transition into renewable energies by 2030. The main objective is to reduce 21% of GHG emissions from 1990 up to 2030, followed by an improvement of 39.5% of the energy efficiency [10]. Furthermore, the expected renewable energies share is 42% for the final energy use and with 74% of renewable energy in electric power generation [10]. The forecast of the installed power is 161 GW from the following energy sources: 50 GW of wind energy, 36 GW of solar photovoltaic energy, 27 GW of gas combined-cycle, 16 GW of hydraulic, 9.5 GW of pumping, 7 GW of solar thermoelectric and 3 GW of nuclear energy. Technologies of energy storage of around 6 GW of storage capacity from hydraulic pumping and batteries will be created by 2030. Other types of storage and the use of hydrogen will have an important role in this decade.

The INECP considers research in topics facing Climate Change and the energy transition through the working lines: 1) energy efficiency, 2) renewable energy technologies, 3) energy storage (electric, thermal, hydroelectric and chemical) and 4) electric vehicle, batteries installation and optimization of charging points.

Having this context in mind, the seek for an economy based on a neutral climate needs being met from renewable energies and optimized technologies of energy harvesting, storage and transport to the final consumer at a low price. The present thesis is developed within this context and aims at storing thermal energy from the solar source.

1.2. Motivation

Solar energy is an alternative energy source whose main advantages are sustainability and the no-generation of GHG emissions. The limitation of the Solar Thermal Power Plants (STPP) is the intermittence of the source because of the lack of solar radiation at nights or in daily periods with clouds. Thermal Energy Storage (TES) systems are the solution to the problem since they ensure the viability of the STPP by satisfying the energy demand when the solar input is insufficient. Moreover, the development of thermal energy storage technology achieves a higher level of sustainability of the STPP [11-13].

Even though the interest in solar energy and energy storage date from the 1980s, the research on thermal energy storage became popular in the 2000s. From that moment until now, the number of publications in the topics related to '*Solar energy*', '*Energy storage*' and '*Thermal energy storage*' has grown exponentially, where the majority of the research has been carried out within the last 10 years (Figure 1.2). The importance of doing a transition into an Industry and society based on renewable energies has expanded the interest and funding in these kinds of technologies.

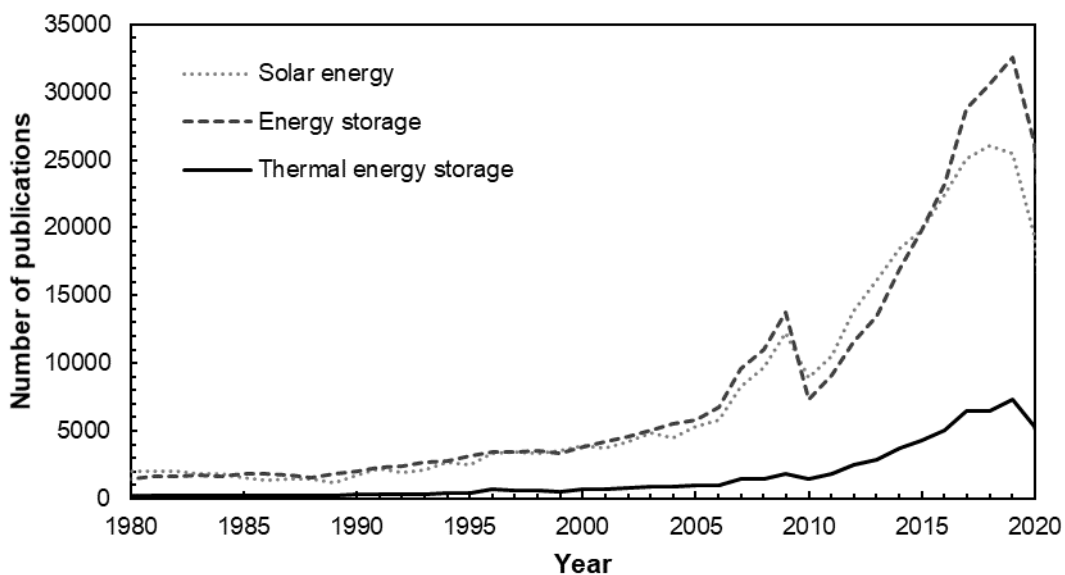


Figure 1.2: Publications per year containing “solar energy”, “energy storage” and “thermal energy storage”.
Source: data extracted from Web of Science (WOS) on 1st of January of 2021.

In recent years, many experimental studies have demonstrated the usefulness of concrete as solid material for thermal energy storage (CTES) [14-16]. Besides, some studies have probed its appropriateness as CTES in Concentrated Solar Power (CSP) Plants [17-22]. Concrete presents several advantages such as its worldwide availability at a relatively low price, it is easy to handle, and it can be worked onsite [17].

However, as the research goes on, the limits of operation at high temperatures are changing and the medium of thermal storage needs other properties. For example, brand-new studies on molten salts from CSP Plants have demonstrated the suitability for working even at higher temperatures up to 600°C. Therefore, the thermal energy storage material has to be able to store energy at a higher temperature without compromise its performance when it is being operated.

The use of concrete under high temperature regimes has been probed in real prototypes up to 450°C [19, 23]. On the other hand, numerical simulations have also reported the feasibility and cost-effectiveness of this type of thermal energy storage material. However, most simulations are made assuming thermal properties with constant values, that is, considering them as temperature-independent properties.

Determining properties at high temperatures gets even more complicated if the working temperature arrives at 600°C. The lack of devices and test protocols for measuring thermal and electrical properties makes this issue a challenging task. Also, as the experimental tests are too complex, the lack of data makes that the results of computational models do not fit with the real operation, affecting the expectations. The real operation of the facility will be far from the designed and optimal solution simulated before the construction of the installation.

Research on concrete at high temperature has mainly been carried out in the field of fire. When a concrete structure is exposed to fire, it has to resist high temperatures (1000°C). Nevertheless, the boundary conditions differ to the application of energy storage owing to the fact that in a fire the material is designed for resisting under Ultimate Limit State (ULS) and the second for Serviceability Limit State (SLS).

Finally, some works have demonstrated the evolution of the thermo-physical properties of concrete at high temperatures, such as thermal conductivity and electrical resistance, but this area still remains unexplored.

1.3. The Industrial project “NewSOL”

The present Industrial PhD thesis has been developed within an Industrial Innovation project. The requirements for the Industrial PhD distinction according to art. 15 bis of RD 99/2011 are as follows: “*a) an employment or commercial contract of the PhD candidate by a private or public sector company or by a Public Administration other than the university, and b) participation of the PhD candidate in an industrial research or experimental development project hosted by the employing company or Public Administration (other than a university). The project must be directly related to the PhD thesis of the candidate, who is required to provide a progress report as proof of this attachment. The report will be subsequently validated by the university*” [24].

The research carried out in this thesis has been undertaken at the *Instituto de Ciencias de la Construcción Eduardo Torroja*, from the Spanish National Research Council (IETcc-CSIC) and the PhD candidate was contracted for working in a European Innovation Project within Horizon 2020 Framework Programme.

The European Strategic Energy Technology Plan (SET Plan) has coordinated research in low-carbon technologies and funding projects since 2007. Horizon 2020 was the

biggest EU Research and Innovation Programme with funding of €80 billion for research projects within the period 2014-2020. It promoted research and innovation between the public and private sectors. The main pillars of H2020 were: Excellence Science, Industrial Leadership and Societal Challenges [25].

NewSOL “*New StOrage Latent and sensible concept for high efficient CSP Plants*” was approved by the European Commission within the Horizon 2020 Framework in the category “Advanced materials solutions and architectures for high efficiency solar energy harvesting” and NMBP-17-2016. This category belongs to the “Industrial Leadership” pillar, whose main objective is to “*speed up the development of the technologies and innovations that will underpin tomorrow's businesses and help innovative European Small and medium-sized enterprises (SME) to grow into world-leading companies*” [26].

NewSOL addresses “*the specific challenge towards high efficiency solar energy harvesting by advance materials solutions and architectures that are in line with those specified in the European Strategic Energy Technology Plan (SET-Plan)*” [27]. The project aimed at developing new materials for technologies of energy storage in CSP Plants. Moreover, those developments would be validated and monitored in real time in the Évora Molten Salts Platform (EMSP) from the University of Évora (Portugal). The innovations of the TES mediums were related to both latent and sensible energy storage of the heat transfer fluids (molten salts) and the infrastructures based on concrete with the development of insulating materials and a High Thermal Performance Concrete. The materials developed would be commissioned and tested in an innovative TES infrastructure of a thermocline tank made of concrete [27, 28].

The partners involved in the project have multidisciplinary profiles of expertise including Industry, SME, Research Centres and Universities. The Universities involved were Univ. of Évora (Portugal), which was the project coordinator, and ETH Zürich (Switzerland). Regarding the Research Centres, partners were from CSIC (Spain), AIMEN (Spain), DLR (Germany), LNEG (Portugal) and SINTEF (Norway). In respect of industries, there were Large Enterprises such as ACCIONA Ingeniería (Spain), ACCIONA Industrial (Spain), ACCIONA Construcción (Spain), Yara International ASA (Norway) and SECIL (Portugal). Finally, the SMEs involved were Sestosensor SRL (Italy) and Institute of Applied Economics APS (Denmark).

On the other hand, the innovation EU policy implemented the Technology Readiness Level (TRL) scale in the EU framework program H2020 for all the public funded projects of innovation [29]. TRL is an indicator that shows the level of maturity of a technology to be used in an operational environment. The evaluation of the TRL is given by the following levels [29, 30]:

- TRL 1: Basic principles observed and reported.
- TRL 2: Technology concept formulated.
- TRL 3: Analytical and experimental proof of concept.
- TRL 4: Technology validated in the laboratory.
- TRL 5: Technology validated in a relevant simulated environment.
- TRL 6: Technology demonstrated in a relevant environment.
- TRL 7: System prototype demonstration in an operational environment.
- TRL 8: System complete and qualified through test and demonstration.

- TRL 9: Actual system proven in an operational environment.

'NewSOL' project is classified as a highly-technological level TRL 7 whose final aim is to build a prototype of a thermocline tank and to validate the improvements related to the materials developed in the project under a real scenario of CSP Plants. As the present Industrial PhD is developed within this project, the current document follows the indicator TRL and the technology developed is classified with the level of maturity.

1.4. Working Hypotheses

Section 1.2 described some facts that were the motivation for starting this research. Additionally, the investigation carried out in the present thesis began with the following working hypotheses:

- Some concrete structures are designed to withstand high temperatures in case of fire risk, but those concrete compositions might not be optimal for working under thermal fatigue cycles between 300-600°C.
- The concrete composition for an application of a solid medium of thermal energy storage is not optimized. The type of aggregates influences the thermal response and more thermal conductive aggregates might produce more cracking during the performance despite theoretically performing better the conduction of heat than the more thermal stable aggregates.
- The risk of spalling of concrete exposed to high temperature increases for temperatures above 100°C.
- Thermo-physical properties such as thermal conductivity present a temperature dependence and its evolution with temperature is not available in the literature.
- The effect of thermal fatigue cycles on thermal conductivity is unknown to the knowledge of the researchers.
- Numerical simulations of heat transfer usually employ constant values of thermal conductivity with temperature, which are far from optimal.
- The commissioning of infrastructures based on concrete operating at high temperatures is not clear.
- Although the suitability of concrete for applications at high temperatures has been demonstrated at lab-scale, the up-scaled infrastructures of concrete for TES at temperatures up to 500°C are not common in Industry.

1.5. Objectives

Considering the above motivations and working hypotheses, the main aim of this thesis is the following:

To demonstrate the capacity of thermal energy storage of concrete at temperatures up to 550°C and to validate the performance in the commissioning and operating conditions of concrete infrastructures at high temperatures.

Some partial objectives are proposed in order to achieve the global aim:

- 1) Analyses of the current knowledge on concrete exposed at high temperatures, including the evolution of thermal parameters at high temperatures and possible risks due to the operation at high temperatures. Identification of gaps. This study

will also include the literature review of materials and configurations of thermal energy storage in CSP Plants.

- 2) Design of High Thermal Performance Concrete and experimental characterisation. Identify different concrete dosages and evaluation of the performance at high temperatures and to thermal cycles, following temperature regimes of molten salts (limits of stability between 290-550°C). This study will allow evaluating whether the concrete as thermal energy storage is a suitable material to withstand long-term high temperature regimes. The effect of the heat is evaluated through changes in mechanical and physicochemical properties as well as the risk of spalling.
- 3) Characterisation of thermal properties of different concrete compositions exposed to high temperatures and thermal cycles. Evaluation of the effect of the heat in concrete at high temperatures.
- 4) Design and propose the commissioning of concrete infrastructures exposed to high temperatures through the evolution of the moisture content and dehydration of concrete by monitoring the evolution of the electrical resistance during the heating process. The demonstration of the viability of this challenging idea implies proposing methodologies for the commissioning, which will be validated in different concrete compositions, to evaluate the drying process by monitoring the structure in real time.
- 5) Up-scaling and thermal operation of concrete specimens at high temperatures simulating the operating conditions of a CSP Plant. Commissioning of the test protocols at a higher scale and monitoring of thermal and electrical properties within the up-scaled concrete, simulating the operation of a thermocline tank. Lessons learned for the suitability of this application.
- 6) Simulations of the up-scaled concrete exposed to high temperatures assuming the evolution of thermal conductivity with the temperature obtained experimentally.
- 7) Analysis of the results and validation of the working hypothesis.

1.6. Methodology

To achieve the objectives mentioned above, the study has been developed in the following steps:

- 1) Review of the state of the art in thermal energy storage materials and operating conditions of CSP Plants as well as literature related to concrete exposed to high temperatures. This study will be analysed in order to find the requirements of the materials for the operation in CSP Plants and the risks and transformations within the concrete when it is exposed to temperatures up to 600°C.
- 2) Proposal of thermal tests for both the commissioning and testing of concrete structures for being used in CSP infrastructures. These experimental studies will start from a TRL 3 (experimental proof of concept) to reach TRL 4 (technology validated in the laboratory).

- 3) Evaluation of physicochemical, mechanical and thermal properties before, during and after the thermal performance. These properties will be evaluated within TRL 3 to TRL 4.
- 4) Developing a non-destructive monitoring system to assess the preconditioning of the concrete through a drying process before operation. This study starts in TRL 2 (technology concept formulated) and the performance will be demonstrated in a relevant environment, achieving a TRL 5 and allowing to apply for a patent of invention.
- 5) Validation of the above-developed experimental methodologies in up-scaled concrete elements for a relevant environment and improving the technology level from TRL 4 to TRL 5.
- 6) Simulations of heat transfer in concrete infrastructures for CSP Plants. Analysis of different case studies using input data obtained in the experimental tests.
- 7) Continuous analysis of the results of the work and proposal of future lines of work related to the research.

1.7. Structure of the document

The content of this document is structured as follows:

Chapter 2 provides a literature review of thermal energy storage in CSP Plants and describes the common tanks of molten salts used in the current CSP Plants. Furthermore, a review of the components of concrete and the evolution of the thermo-physical and electrical properties with temperature is mentioned. The spalling phenomenon of concrete subjected to high temperatures is also explained.

Chapter 3 describes the research methodology for experimental tests and materials. It describes the thermal performance carried out at lab scale. It includes an initial study on spalling risk to evaluate the effect of geometry and materials. Furthermore, the evolution of mechanical properties of different concrete mixes at long-term as well as the stability under thermal cycles are analysed. It includes the loss of compressive strength, the evolution of microcracking and physico-chemical performance at residual state after being exposed to a different number of thermal cycles.

Chapter 4 includes the evolution of thermal parameters such as thermal conductivity, heat capacity and thermal diffusivity measured at room temperature before and after thermal tests. Furthermore, the evolution of thermal conductivity was obtained at high temperatures up to 600°C and during thermal cycles between 300-600°C for different compositions of concrete.

Chapter 5 provides the commissioning of a test protocol for measuring the electrical resistance at high temperature during the drying stage for different types of concrete. The suitability of this test protocol for the commissioning of the drying process of concrete infrastructures is analysed.

Chapter 6 describes the construction of a mock-up of a section of a TES thermocline tank made of concrete and the commissioning and preconditioning of the up-

scaled system before the thermal exposure. It gives some lessons learned for further construction and preconditioning of a prototype tank for CSP Plants. Additionally, the protocol developed in Chapter 5 is validated and the maturity of the technology is improved up to TRL 5.

Chapter 7 deals with the experimental tests at mid-scale carried out on the mock-up up-scaled section of a thermocline tank. It includes the evolution of thermal parameters during the operation under thermal cyclic regimes and the suitability of concrete for TES infrastructures. The validation of concrete is demonstrated through a characterisation of the material after the thermal operation.

Chapter 8 describes the simulations of heat transfer and the case studies analysed by using the temperature dependence of the thermal conductivity as well as the thermal model of the up-scaled prototype of concrete for a thermocline tank.

Chapter 9 provides a feasibility study on the establishment of a National Patent to follow the drying process by monitoring the structure in real time during heating. It includes an analysis of patents close to the prior art and an evaluation of patentability of the invention developed and demonstrated in the thesis.

Chapter 10 validates the objectives and working hypotheses and includes also potential future works in the research area. Finally, summarises the conclusive remarks for the work developed in the thesis.

And eventually, some appendices have been included to provide relevant information about the present thesis:

Appendix A includes the equations of the evolution of thermal conductivity with temperature up to 600°C for two heating and cooling processes for a wide variety of materials tested.

Appendix B presents the location of thermocouples in the core samples extracted from the mock-up section of the thermocline tank.

Appendix C includes the simulations of the thermal operation of the mock-up section of a thermocline tank. The simulations show the temperature profiles of all the layers of the mock-up and across the X, Y and Z-planes for different case studies of the thermal cycling stage.

Appendix D provides the registered application for a National Patent at Oficina Española de Patentes y Marcas (OEPM) related to partial content developed in the present thesis.

Appendix E summarises the accountability of the tasks developed during the PhD, including the list of publications in journals and conferences papers and explaining the assessment process followed during this period by the University.

1.8. References

- [1] M. Höök and X. Tang, "Depletion of fossil fuels and anthropogenic climate change—A review," *Energy Policy*, vol. 52, pp. 797-809, 2013. Available: <http://www.sciencedirect.com/science/article/pii/S0301421512009275>. DOI: <https://doi.org/10.1016/j.enpol.2012.10.046>.
- [2] H. Ritchie and M. Roser, "CO₂ and greenhouse gas emissions," *Published Online at OurWorldInData.Org*, 2017. Available: <https://ourworldindata.org/co2-and-other-greenhouse-gas-emissions>.
- [3] J. P. Holdren, "The energy innovation imperative: Addressing oil dependence, climate change, and other 21st century energy challenges," *Innovations: Technology, Governance, Globalization*, vol. 1, (2), pp. 3-23, 2006.
- [4] B. A. Iqbal and F. N. Ghauri, "Climate Change: The Biggest Challenge in 21st Century," *Mediterranean Center of Social and Educational Research*, vol. 2, pp. 41, 2011.
- [5] European Commission. *Climate strategies and targets. 2050 long-term strategy*. Available: https://ec.europa.eu/clima/policies/strategies/2050_en.
- [6] (Last visited on 20-12-22). United Nations. *Sustainable Development Goals*. Available: <https://www.un.org/sustainabledevelopment/sustainable-development-goals/>.
- [7] United Nations. *Affordable and clean energy. Ensure access to affordable, reliable, sustainable and modern energy*. Available: <https://www.un.org/sustainabledevelopment/energy/>.
- [8] United Nations. *Climate Action. Goal 13: Take urgent action to combat climate change and its impacts*. Available: <https://www.un.org/sustainabledevelopment/climate-change/>.
- [9] (Last visited on 20-12-22). European Commission. *The European Green Deal*. Available: https://ec.europa.eu/info/strategy/priorities-2019-2024/european-green-deal_en.
- [10] Gobierno de España, "Plan Nacional Integrado de Energía y Clima," *Published Online at Miteco.Gob.Es*, 2020. Available: https://www.miteco.gob.es/images/es/pnieccompleto_tcm30-508410.pdf.
- [11] R. Adinberg, "Simulation analysis of thermal storage for concentrating solar power," *Appl. Therm. Eng.*, vol. 31, (16), pp. 3588-3594, 2011. DOI: [10.1016/j.applthermaleng.2011.07.025](https://doi.org/10.1016/j.applthermaleng.2011.07.025).
- [12] M. Monjurul Ehsan, Z. Guan, H. Gurgenci and A. Klimenko, "Novel design measures for optimizing the yearlong performance of a concentrating solar thermal power plant using thermal storage and a dry-cooled supercritical CO₂ power block," *Energy Conversion and Management*, vol. 216, 2020. DOI: [10.1016/j.enconman.2020.112980](https://doi.org/10.1016/j.enconman.2020.112980).
- [13] M. Mehrpooya, B. Ghorbani, A. Shahsavari and A. Zaitsev, "Conversion and storage of solar energy in the forms of liquid fuel and electricity in a hybrid energy storage system using methanol and phase change materials," *Energy Conversion and Management*, vol. 209, 2020. DOI: [10.1016/j.enconman.2020.112669](https://doi.org/10.1016/j.enconman.2020.112669).

- [14] V. D. Cao, S. Pilehvar, C. Salas-Bringas, A. M. Szczotok, J. F. Rodriguez, M. Carmona, N. Al-Manasir and A. Kjønksen, "Microencapsulated phase change materials for enhancing the thermal performance of Portland cement concrete and geopolymer concrete for passive building applications," *Energy Conversion and Management*, vol. 133, pp. 56-66, 2017. . DOI: 10.1016/j.enconman.2016.11.061.
- [15] L. F. Cabeza, L. Navarro, A. L. Pisello, L. Olivieri, C. Bartolomé, J. Sánchez, S. Álvarez and J. A. Tenorio, "Behaviour of a concrete wall containing micro-encapsulated PCM after a decade of its construction," *Solar Energy*, vol. 200, pp. 108-113, 2020. . DOI: 10.1016/j.solener.2019.12.003.
- [16] Y. Liu, M. Xie, E. Xu, X. Gao, Y. Yang and H. Deng, "Development of calcium silicate-coated expanded clay based form-stable phase change materials for enhancing thermal and mechanical properties of cement-based composite," *Solar Energy*, vol. 174, pp. 24-34, 2018. . DOI: 10.1016/j.solener.2018.08.085.
- [17] M. C. Alonso, J. Vera-Agullo, L. Guerreiro, V. Flor-Laguna, M. Sanchez and M. Collares-Pereira, "Calcium aluminate based cement for concrete to be used as thermal energy storage in solar thermal electricity plants," *Cement and Concrete Research*, vol. 82, pp. 74-86, 2016. Available: <http://www.sciencedirect.com/science/article/pii/S0008884615003075>. DOI: <https://doi.org/10.1016/j.cemconres.2015.12.013>.
- [18] E. John, M. Hale and P. Selvam, "Concrete as a thermal energy storage medium for thermocline solar energy storage systems," *Solar Energy*, vol. 96, pp. 194-204, 2013. Available: <http://www.sciencedirect.com/science/article/pii/S0038092X13002636>. DOI: <https://doi.org/10.1016/j.solener.2013.06.033>.
- [19] D. Laing, C. Bahl, T. Bauer, M. Fiss, N. Breidenbach and M. Hempel, "High-Temperature Solid-Media Thermal Energy Storage for Solar Thermal Power Plants," *Proc IEEE*, vol. 100, (2), pp. 516-524, 2012. . DOI: 10.1109/JPROC.2011.2154290.
- [20] A. Buscemi, D. Panno, G. Ciulla, M. Beccali and V. Lo Brano, "Concrete thermal energy storage for linear Fresnel collectors: Exploiting the South Mediterranean's solar potential for agri-food processes," *Energy Conversion and Management*, vol. 166, pp. 719-734, 2018. . DOI: 10.1016/j.enconman.2018.04.075.
- [21] K. Bataineh and A. Gharaibeh, "Optimal design for sensible thermal energy storage tank using natural solid materials for a parabolic trough power plant," *Solar Energy*, vol. 171, pp. 519-525, 2018. . DOI: 10.1016/j.solener.2018.06.108.
- [22] V. A. Salomoni, C. E. Majorana, G. M. Giannuzzi, A. Miliozzi, R. Di Maggio, F. Girardi, D. Mele and M. Lucentini, "Thermal storage of sensible heat using concrete modules in solar power plants," *Solar Energy*, vol. 103, pp. 303-315, 2014. . DOI: 10.1016/j.solener.2014.02.022.
- [23] N. Hoivik, C. Greiner, J. Barragan, A. C. Iniesta, G. Skeie, P. Bergan, P. Blanco-Rodriguez and N. Calvet, "Long-term performance results of concrete-based modular thermal energy storage system," *Journal of Energy Storage*, vol. 24, pp. 100735, 2019. . DOI: 10.1016/j.est.2019.04.009.

- [24] *Universidad Carlos III de Madrid. Industrial PhD.*. Available: https://www.uc3m.es/ss/Satellite/Doctorado/en/TextoDosColumnas/1371242118169/I_nustrial_Ph.D.
- [25] European Commission, "Horizon 2020," *Published Online at Ec.Europa.Eu*, Available: <https://ec.europa.eu/programmes/horizon2020/en/h2020-sections>.
- [26] European Commission, "Industrial Leadership. Horizon 2020," *Published Online at Ec.Europa.Eu*, Oct 20, 2020. Available: <https://ec.europa.eu/programmes/horizon2020/en/h2020-section/industrial-leadership>.
- [27] CORDIS European Commission. *New StOrage Latent and sensible concept for high efficient CSP Plants*. Available: <https://cordis.europa.eu/project/id/720985>.
- [28] *NewSOL project Webpage*. Available: <http://www.newsol.uevora.pt/>.
- [29] M. Héder, "From NASA to EU: the evolution of the TRL scale in Public Sector Innovation," *The Innovation Journal*, vol. 22, (2), pp. 1-23, 2017.
- [30] B. Sauser, D. Verma, J. Ramirez-Marquez and R. Gove, "From TRL to SRL: The concept of systems readiness levels," in *Conference on Systems Engineering Research, Los Angeles, CA*, 2006, pp. 1-10.

This page has been intentionally left blank.

Chapter 2

State of the art

The aim of this chapter is to introduce the state of the art of technologies of thermal energy storage in CSP Plants to understand the scope of this thesis. For that purpose, in *section 2.1* the field of study and the context related to the research in Materials Science and Engineering are provided. The application of study has been located in the area as well as the interdependencies between the disciplines close to the field of study.

Later, *sections 2.2 and 2.3* deal with the CSP and different configurations of thermal energy storage, where the commonly-used two tanks for storing molten salts in CSP Plants around the world are given. Special consideration was given to thermocline tanks whose configuration is being increasingly considered due to reductions in costs.

After that, the role of the concrete in CSP infrastructures is covered in *section 2.4* as both a material for thermal energy storage and as a structural element in the technologies for energy storage. Later, *section 2.5* describes the alterations on concrete materials when are exposed to high temperatures. Changes in the mechanical, thermal and electrical properties are described. This is of relevant importance because it is the base of this thesis and thus the concepts are explained in detail along with the chapter.

Finally, the challenges and gaps found in the literature are presented in *section 2.6* as well as the interest of the work carried out in the present thesis.

2.1. Field of research

The present thesis comprises research in the field of Materials Science and Engineering. It is a broad field including studies related to the design of the material, analysis of the physicochemical properties and characterisations, civil and mechanical engineering, durability, simulations, etc. The commonly known paradigm of Materials Science and Engineering comprises a structure, properties, processes and performance, as it is shown in the upper tetrahedron of Figure 2.1. It reflects the interdependency between them and answers the following questions:

- How can the process achieve the structure?

- How does the process impact on the performance (durability, service life...)?
- How does the performance transform the specific material properties?
- What structure is needed for achieving the desired properties?

The previous interdependences can only be achieved with the core disciplinary of the field “Characterisation and modeling” where highly integrated experimental and computational approaches are key for reaching the best material for each application.

However, another item is added to the paradigm and converts the conventional tetrahedron into a double tetrahedron, as was explained in [1] and shown in Figure 2.1. The materials’ mechanical, electrical and chemical states have an influence on the properties, structure and processing. The thermo-physical and electrical properties are studied in deep in this thesis and the discoveries highlight the focus of this issue.

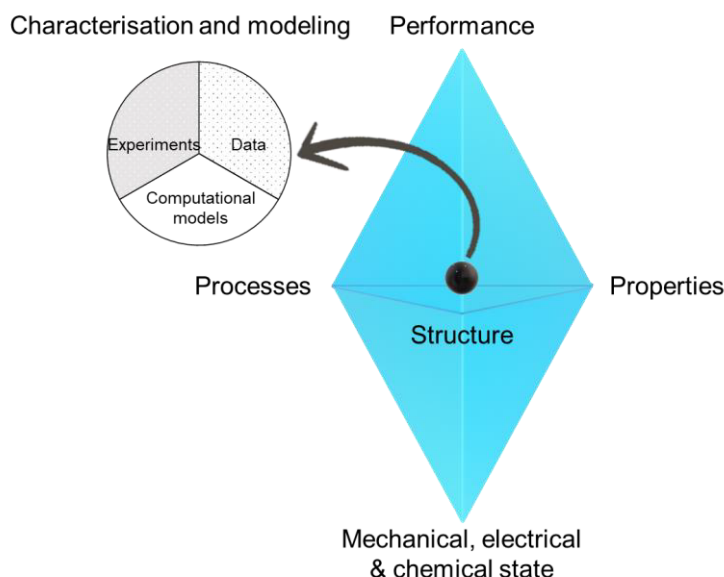


Figure 2.1: Materials Science & Engineering double tetrahedron. Source: adapted from [1].

To be more specific, the research in this thesis is focused on cement-based materials, namely: mortars and concrete. Nevertheless, the most used materials in the World are first water and secondly, concrete [2]. This Industrial PhD is mainly based around the specific field of application of infrastructures of energy made of cement-based materials.

In spite of enclosing the field of application, it is still rather big. The infrastructures of energy used to put concrete to work as a structural material for its compressive strength. Examples of these concrete structures are the wind farms where concrete supports the wind turbine located at the top and are placed onshore and offshore. Other applications are hydroelectric dams and hydraulic fracturing or “fracking”. They are large structures build to store high amounts of water or oil and gas wells that inject fluids under high pressure into a bedrock formation, respectively. Nonetheless, the spotlight in this work is put on the commissioning and operation of the infrastructures at high temperatures, namely: Geothermal, Nuclear and Solar Power Plants. Whereas the first ones work up to 300°C, the CSP Plants achieve a working temperature of nearly 600°C. The goal is to make the best commissioning of the infrastructure with the lesser damage of the material and to adequate the material to the operation required with the properties needed. For this purpose, the

present thesis will go into more detail in two subfields, namely: heat transfer and electrical properties at high temperatures.

2.2. CSP and thermal energy storage

Solar energy is an alternative energy source whose main advantages are sustainability and the no-generation of greenhouse emissions. There exist two types of technologies: solar thermal energy and solar photovoltaics. While the first one uses solar energy to produce heat, the second one generates electrical energy from the solar source. This thesis is focused on solar thermal energy technology, and more specifically in Concentrating Solar Power (CSP).

CSP Plants usually produce electricity from solar energy by using a power block based on a Rankine cycle. Rankine is a thermodynamic cycle that produces electrical power with the input of heat. The operation is based on a fluid that is evaporated and, then, it is condensed. In the case of Thermal Power (TP) Plants, water is the fluid generally used. An external heat supply from the solar field is required to produce steam. Once the water changes the phase, the steam passes through the turbine and generates electrical power.

CSP Plants are characterised by concentrating the solar radiation on a specific surface in order to increase the temperature of the Heat Transfer Fluid (HTF). There exist different types of CSP Plants, as follows: parabolic trough, linear Fresnel reflector, central receiver, and parabolic dish. Figure 2.2 shows a schema of the mentioned CSP technologies, adapted from [3]. Parabolic Trough (PT) are collectors that reflects the direct normal radiation to the focal line where the absorber tube is located. HTF circulates inside the absorber and the temperature is increased as it passes through the collectors. Linear Fresnel are curved mirrors that reflect the solar radiation to an absorber tube located at the centre. HTF circulates inside the tube and increases its temperature due to the sun-rays. Central receiver are plants mainly formed by a heliostat field that concentrates the solar radiation to the top of a solar tower. HTF is pumped through the solar tower and it increases its temperature when arrives at the central receiver. On the other hand, a parabolic dish concentrates the radiation into a single point located at the centre and it can achieve even higher temperatures because the ratio of concentration is higher.

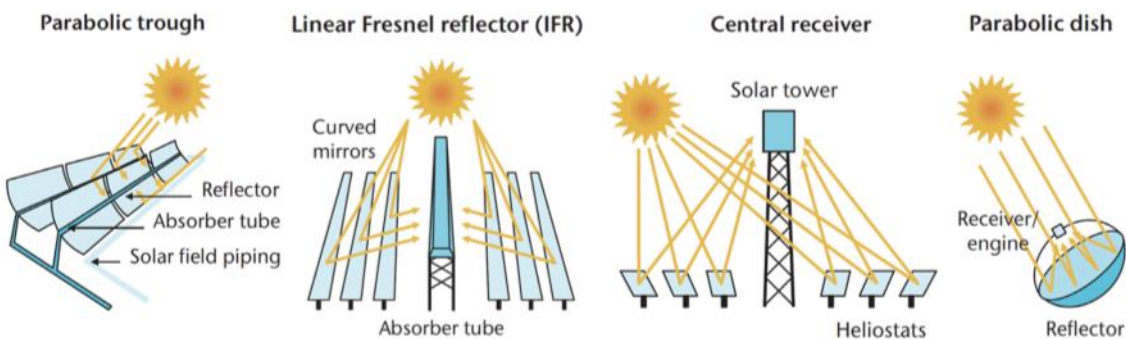


Figure 2.2: CSP technologies. Adapted from [3].

The limitation of the Solar Thermal Power Plants (STPP) is the intermittence of the source because of the lack of solar radiation at nights or in daily periods with clouds. Thermal Energy Storage (TES) systems are the solution to the problem since they ensure the viability of the STPP by satisfying the energy demand when the solar input is insufficient. Moreover,

the development of thermal energy storage technology achieves a higher level of sustainability of the STPP [4-6].

TES can be divided into 3 categories: sensible, latent and thermochemical heat storage [7]. Sensible heat storage is produced by differences in temperature in the material. Latent heat is produced when the material experiences a phase change at an almost constant temperature. Thermochemical heat storage and discharge are produced when the molecular bonds are broken or reformed. The amount of energy stored for a specified system is defined by the energy density and depends on its heat capacity [8]. Latent heat storage materials are characterised by having higher energy density, but their lower thermal conductivity makes them materials with a slower storage rate [7]. Regarding the thermochemical heat storage materials, they are more complex and expensive at the current level of development.

Sensible heat storage materials are characterised by low-medium energy density, but their moderate cost and broad knowledge make them a valuable solution for thermal storage [9]. In addition, sensible heat can be stored in liquid and solid materials. The problem when using liquid storage materials is that the technology employed needs high dimensions for the tanks and heat exchangers, which increase the cost of the storage application [10].

2.3. Types of tanks of Molten salts

2.3.1. 2-tanks

In CSP Plants, once the energy is captured by one of the previous technologies explained, it is usually stored and then produces electric energy on demand. Figure 2.3 shows a diagram of a solar field of PT collectors that also has thermal energy storage with salts, obtained from the National Renewable Energy Laboratory (NREL) of the USA [11]. Three different blocks can be seen: capture, storage and power block. In the capture block, the HTF, which in this case is thermal oil, circulates inside the tubes across the solar field, increasing its temperature to a limit of approximately 400°C; above this temperature the oil decomposes. The hot oil then transfers heat to the molten salts via a heat exchanger. In the storage block, the molten salts leave the cold tank, capture the heat yielded by the thermal oil and are stored in the hot tank for future use in demanding periods. The salts are characterised by their greater heat transfer and storage capacity than oil, as they can reach higher temperatures generally up to 565°C [12, 13]. However, recent studies have demonstrated the suitability of using the Solar Salt to a new limit up to 600°C [14]. The problem they present is corrosion. In addition, they have high melting points of around 230°C so they cannot be cooled down to the freezing point. That is the reason why the cold temperature of molten salts are around 290°C [12, 13]. Finally, heat is added to the power block. The fluid usually used is water that circulates through the Rankine cycle. When it passes through the turbine it rotates a shaft connected to an alternator, which generates electrical power.

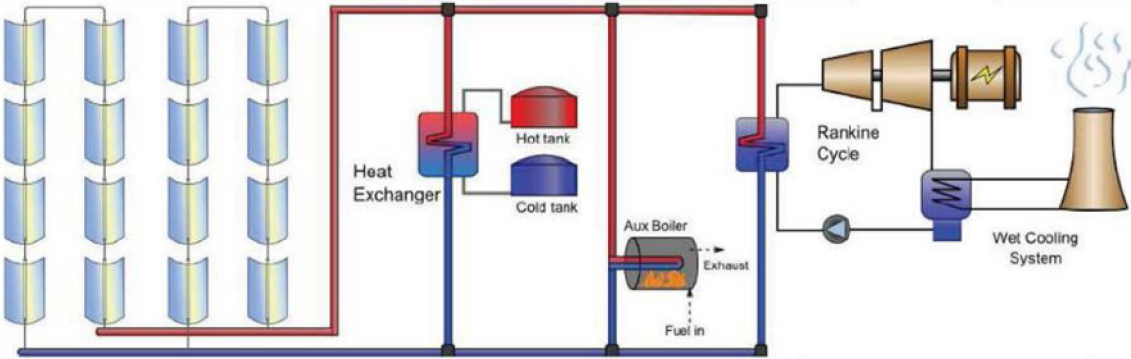


Figure 2.3: PT CSP Plant with a 2-tank indirect thermal energy storage and the power block. Source: NREL [11].

There are two types of Molten Salts TES, depending on if it is direct or indirect [15]. If the energy is stored in the same HTF that is heated in the solar field the storage is direct. On the contrary, if there are 2 types of fluids, one for the capture block and another for the storage block, the storage is indirect. Figure 2.4 shows the two type of molten salts storage and the loops of oil and salts are specified, as well as the heat exchanger.

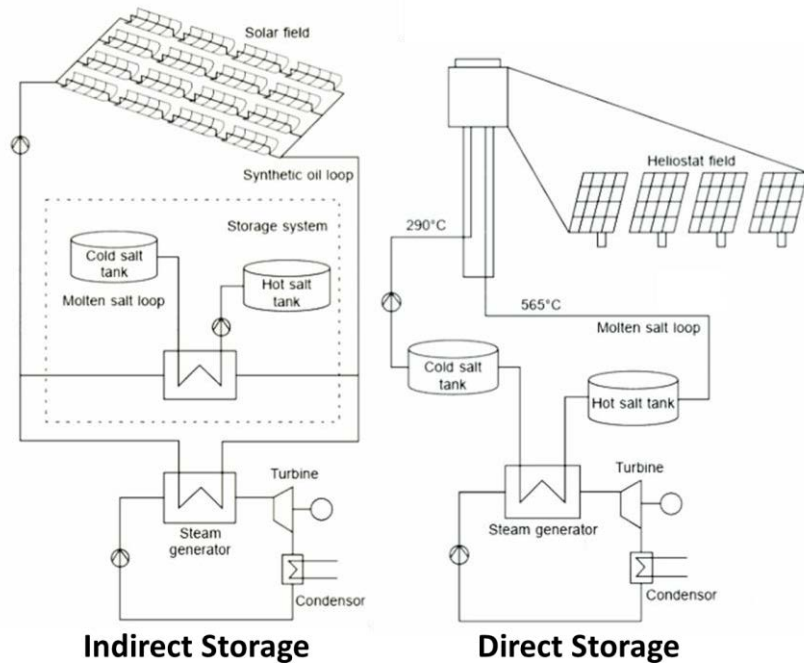


Figure 2.4: Types of molten salts storage. Source: Adapted from [15].

The commonly-used HTF circulating for the solar field is synthetic oil, whose maximum temperature is around 400°C due to the decomposition at higher temperatures [16]. However, recent studies have proved the use of molten salts to capture the energy as well [17, 18]. This technology is being proved and tested in a pilot plant that ENEA has recently built in Italy. The main advantage of circulating molten salts for the absorber tube in a PT CSP Plant is that a higher temperature can be achieved in the solar field. This fact undoubtedly increases the storage capacity and, hence, the overall efficiency. Not only the efficiency is improved but also the reduction of the Levelized Cost of Energy (LCOE), which

makes this technology more competitive in both economical and energetic aspects. A probe of that is a simulation carried out comparing oil and Solar Salt circulating for the absorber tube in CSP Plants of 100 MW, where the efficiencies of the power block when using oil and Solar Salt were 38.5 and 43.3%, respectively. Regarding the LCOE, this parameter decreases from 13.9 cents €/kWh in 100 MW with oil as HTF to 11.2 cents €/kWh for 100 MW when using Solar Salt [19].

The 2-tanks for storing molten salts are large infrastructures. Table 2.1 shows a review of 4 PT CSP Plants around the World, as follows: Noor (Morocco), Solana Generating Station (USA), Andasol (Spain) and Extresol (Spain) [20-33]. The geometries of the molten salts TES tanks are $36 < \Phi < 46.5 \text{ m}$ and $13 - 14 \text{ m}$ of height. In spite of increasing the construction cost, the electricity costs are below 22.7 cents €/kWh, achieving 11.7 cents €/kWh in Noor for a combining technology of PT and Solar Tower (ST). The equivalence between UDS and EURO were done according to the conversion (1 USD = 0.84 €) on 22nd March of 2021.

| Name | Country | Technology | Electrical capacity (MW) | Dimensions 2-Tanks | Construction Cost | Cents € /kWh |
|---------------------------|-----------------|------------|--------------------------|--|--|--------------------------|
| Noor | Morocco | PT+ST | 510 [20-22] | $\Phi=46.5\text{m}$, $h=14\text{m}$ | 2.5 bill USD 2095 mill € [20-22] | 11.7- 15.9 [20-22] |
| Solana Generating Station | Arizona, USA | PT | 280 [23] | $\Phi=42.6\text{m}$, $h=13\text{m}$ [24] | 2 bill USD 1676 mill € [25] | 11.7 [26] |
| Andasol | Spain | PT | 150 [27-29] | $\Phi=36\text{m}$, $h=14\text{m}$ | 300 mill € [30] | 22.7 [27-29] |
| Extresol | Spain | PT | 150 [31-33] | $\Phi=36\text{m}$, $h=14\text{m}$ | 300 mill € [30] | 22.7 [31-33] |

Table 2.1: PT CSP Plants around the World: characteristics, dimensions of tanks and costs.

Source: [20-33].

2.3.2. Thermocline tank

The architecture of 2-tanks is presented in mostly CSP with storage systems, but recent studies have demonstrated the use of a single-one thermocline tank gives better results in terms of cost reduction [9, 34, 35].

In a thermocline tank, both cold and hot HTF are placed inside the tank and separated due to stratification. When the tank is charging energy, the heated molten salts come into the tank from the upper part and displace the thermocline region to the bottom. At the same time, the cold HTF is being gone out of the thermocline from the bottom part. In the discharging process, hot molten salts get out of the tank from the top and the thermocline zone is moved to the top [36].

Figure 2.5 shows the processes of charging and discharging energy as well as the temperatures in the hot, cold and thermocline regions. The HTF with higher temperature (*hot fluid*) and lower density is located at the top of the tank and the one with lower temperature (*cold fluid*) and higher density is placed at the bottom. The initial state is the end of the filling process of the tank with molten salts at the cold temperature. The charging process starts from the top, and the heated molten salts come into the tank from the upper part and the cold ones go out of the tank from the bottom. If the thermocline region arrives at the bottom, the thermocline tank is fully charged. The discharge of energy is produced backwards, and the heated molten salts go out of the tank from the top and the cold salts come into the tank from the bottom. Given this process, once the minimum temperature arrives at the top, the tank is fully discharged. Nevertheless, the charging process might not be fully completed because it depends on the solar source. At the same time, the discharge of energy is subjected to the demand for energy and might not be necessarily the discharge of the full tank.

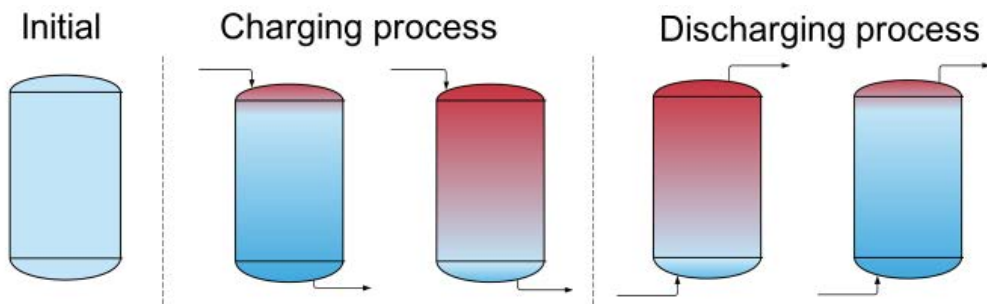


Figure 2.5: Charging and discharging processes of a thermocline tank.

The main advantages of the thermocline tank is the reduction of costs, estimated at a decrease of 34% compared to the cost of the two tanks [37]. The authors also highlight the ability to transfer thermal energy at a constant temperature during the cycle of discharge. Additionally, the tank can be filled with a material in order to reduce the amount of molten salts and, hence, the total cost of the TES. The filler material might be rocks, concrete, sand or even waste slags from other industries. Another advantage of the filler is to reduce the contact surface between the cold and hot molten salts and enhance the stratification by avoiding the convection of the fluids. The material helps to maintain the thermal gradient in the tank improving the overall efficiency [38].

2.4. Role of concrete in CSP Plants

In recent years, many experimental studies have demonstrated the usefulness of concrete as solid material for thermal energy storage (CTES) [39-41]. In addition, there are studies that have probed its appropriateness as CTES in Concentrated Solar Power (CSP) Plants [42-47]. Concrete presents several advantages such as its worldwide availability at a relatively low price, it is easy to handle, and it can be worked onsite [42].

The use of concrete under high-temperature regimes has been probed in real prototypes [44, 48]. Those prototypes have been useful for measuring some thermal and mechanical parameters of concrete during the operation at high temperatures up to 450°C. Numerical simulations of CTES have also reported the feasibility and cost-effectiveness of

this type of thermal energy storage material [49]. However, most simulations are made assuming thermal properties with constant values, that is, considering them as temperature-independent properties [45-47, 49-54]. Additionally, due to the high difficulty of evaluating these properties at high temperatures, in many studies, the thermal conductivity obtained at room temperature is used for the simulations [55].

Concrete is usually considered as a structural element in infrastructures of energy. However, the material can also have different roles. It is the case of the two tanks of molten salts, where concrete usually is located in the foundations as a structural element. Additionally, as the temperatures in the tanks are elevated, the tanks are placed above a refractory concrete ring whose aim is to avoid loss of energy from the tank to the soil. On the other hand, concrete can be considered as a thermal energy storage material with the purpose of store energy from the HTF.

The desired thermo-physical properties of concrete depend on the application. Hence, concrete used as an insulating material would require lower values of thermal conductivity to reduce the increase of the temperature within the material. On the contrary, concrete as a thermal energy storage material would require a balance between high thermal conductivity and low thermal losses. It is explained as follows: the higher thermal conductivity the faster the thermal energy is stored because the heat is exchanged more efficiently. Nonetheless, it implies lower heat capacity values because the heat might be lost to the surroundings faster. That is the reason why a balance between those two parameters is needed for thermal energy storage applications.

2.5. Concrete at high temperature

2.5.1. Thermal properties

The analysis of the heat transfer at high temperatures for applications of thermal energy storage is of interest to predict the appropriateness of the application analysed in working conditions. In particular for CTES, when concrete is heated, the conduction is the dominant heat transfer mechanism within the solid medium. The thermal conductivity is the parameter that governs the conduction and gives the proportion between the heat flux and the thermal gradients that take place between the core and the external surface of the material [56]. Some authors highlight the temperature dependence of the thermo-physical properties of the storage materials for the overall performance of the storage applications [7]. For that reason, a better knowledge of the evolution of the thermal conductivity with temperature in the heat storage system is of interest for the optimisation of concrete working under thermal fatigue cycles at high temperatures.

In concrete, around 70% of the volume is comprised of aggregates. Consequently, the overall thermal response is heavily influenced by their behaviour, playing an important role in heat transfer. In addition to the aforementioned parameter of thermal conductivity, key for heat transfer processes, another parameter of interest is the thermal expansion of aggregates, which will influence the expansion/shrinkage response of the material producing stresses and/or cracks. Table 2.2 summarises the thermal conductivity and thermal expansion coefficient (CTE) at room temperature of different conventional aggregates in rocks or concrete, obtained from the literature [57, 58]. Siliceous aggregates reach the highest

thermal conductivity and thermal expansion, whereas calcareous aggregates achieve the lowest [57].

| Type | Rock or concrete | Thermal conductivity [W/(m·K)] | CTE $\times 10^6$ [°C ⁻¹] |
|------------|------------------|-----------------------------------|--|
| Siliceous | Rock | 1.8-3.9 | 9.3 |
| | Concrete | 2.4-3.6 [OPC] | 11.4 |
| Basalt | Rock | 1.7 | 6.4 |
| | Concrete | 1-1.6 [OPC] | 9.3 |
| Calcareous | Rock | 1.2-1.4 | 5.5 |
| | Concrete | 1.9-2.8 [OPC] | 8.6 |

Table 2.2: Thermal conductivity and thermal expansion coefficient of rocks and concretes with different aggregates at room temperature. Source: [57, 58].

Nevertheless, since aggregates' behaviour at high temperatures is different from its behaviour at room temperature, their thermal parameters will have different values, which will influence the overall thermal performance and energy stored. Figure 2.6 shows the evolution of thermal conductivity of different type of rocks at temperatures up to 600°C obtained from the literature [59-65]. Siliceous aggregates obtained the highest values at room temperature but also experienced the biggest drop when they are heated up to 600°C. The loss of thermal conductivity is more pronounced in siliceous ($\approx 50\%$) than basalt and calcareous aggregates, whose decrease in the thermal conductivity is less accentuated.

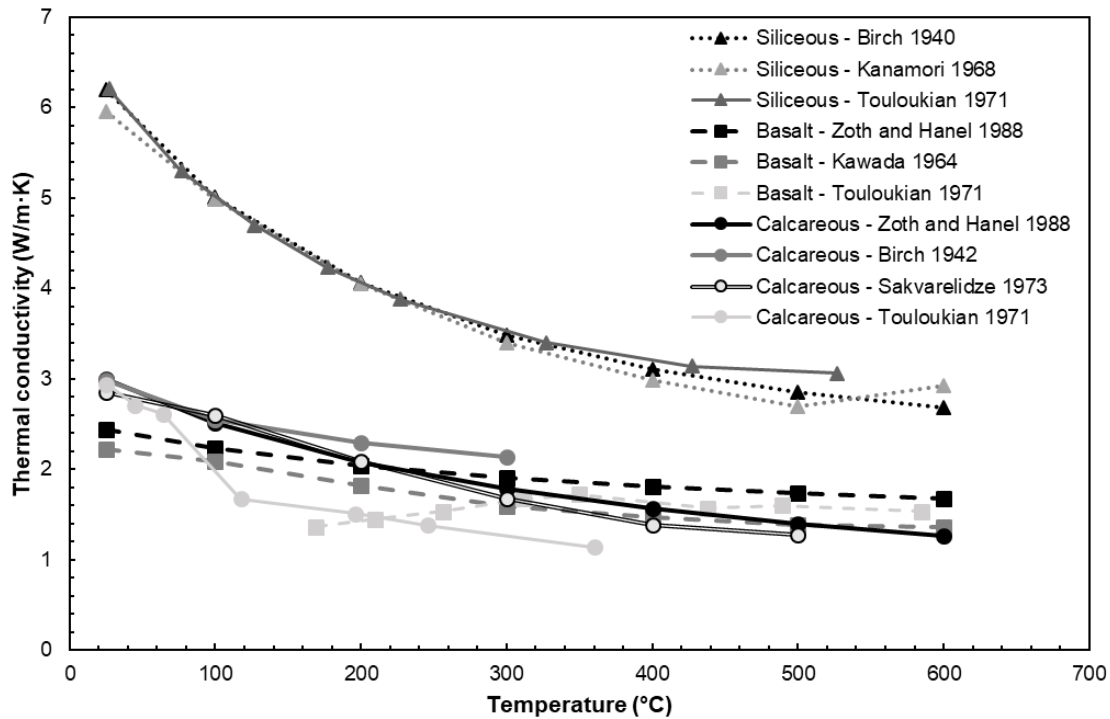


Figure 2.6: Evolution of thermal conductivity of different aggregates with temperature. Graph representing data published in [59-65].

Another parameter of interest in thermal storage applications is the specific heat. Figure 2.7 summarises the evolution of the thermal parameter at temperatures up to 600°C for different types of rocks, obtained from the literature [66-68]. The differences found among the types of rocks analysed are lower and, in all cases, the specific heat ranges between 1-1.2 kJ/(kg·K) when the temperature reaches 600°C. However, the value is increased ($\approx 50\%$) when compared with the one obtained at room temperature. The importance of having data on the evolution at high temperatures is, once again, highlighted for making better predictions and simulations of the behaviour in operating conditions.

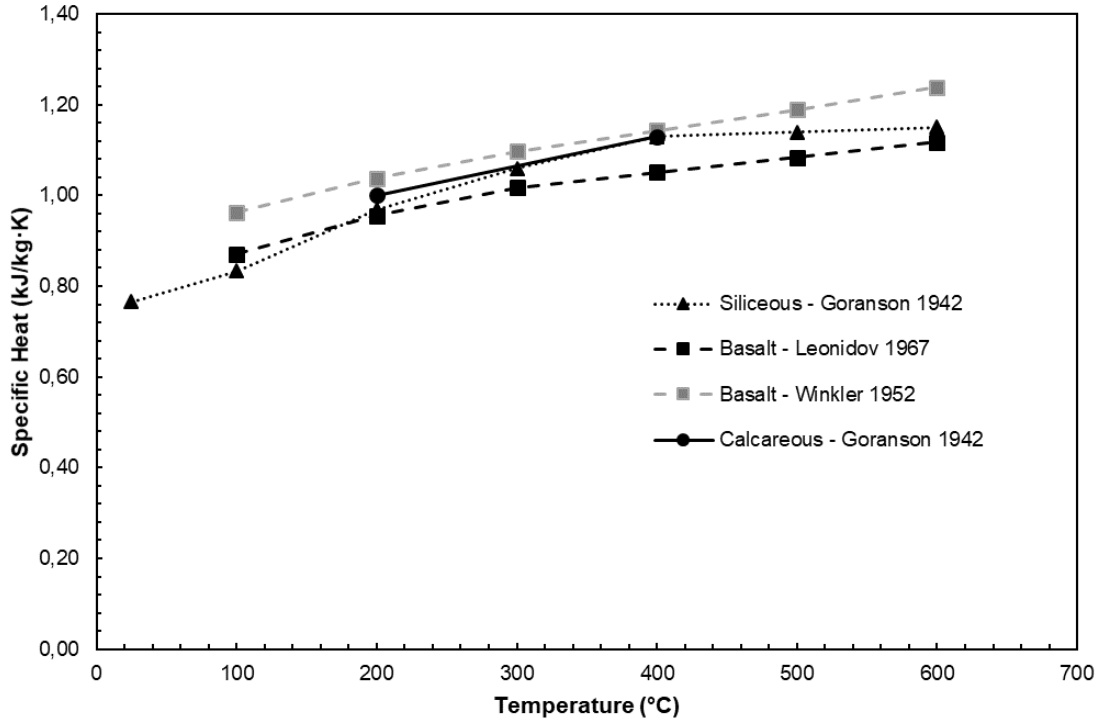


Figure 2.7: Evolution of specific heat of different aggregates with temperature. Graph representing data published in [66-68].

Nonetheless, the response of concrete at high temperatures changes due to several factors: chemical changes in the cement paste, mechanical changes due to the expansion of aggregates, and shrinkage of the cement paste [58, 69]. These physicochemical changes take place at different temperatures and all these changes affect thermal conductivity. Regarding the cement influence, Calcium Aluminate Cement (CAC) withstands severe operating conditions because its heat capacity is higher than the Ordinary Portland Cement (OPC) concretes at temperatures up to 700°C, 1.5 and 1 KJ/(kg·K), respectively [70]. The thermal conductivity of CAC pastes at high temperatures ranged between 0.96 and 1.1 W/(m·K) at 25 and 80°C, respectively [71]. At higher temperatures, one study reported [72] that the values of thermal conductivity of CAC pastes measured in residual conditions decreased from 1.187, measured at 105°C, to 0.621 and 0.542 W/(m·K), after being exposed to 350 and 900°C, respectively. The dehydration of CAC cement paste takes place up to 300°C with the decomposition of hydrated phases, mainly CAH₁₀ and AH₃ [73]. Regarding the OPC cement, CSH gels decompose from 100 to 400°C and portlandite, CH, decomposes between 400 and 500°C [74].

The publications reporting the evolution of thermal conductivity on concrete at high temperatures are limited in number. Several authors reported measurement of thermal conductivity on concrete used for TES, but the maximum temperature evaluated was 450°C [44, 48, 75]. Recently innovations in the molten salts have demonstrated its stability at temperatures of 600°C [14]. For that reason, it is important to evaluate the thermal performance of concrete reaching higher temperatures.

The studies performed at high temperatures show that the measure of thermal conductivity of concrete at high temperatures is heavily affected by many parameters such

as porosity, moisture content, type and amount of aggregates [76-79]. In fact, the reduction of thermal conductivity when heating is more remarkable in concretes with siliceous aggregates in their composition than with calcareous or lightweight aggregates [77-79].

The lack of thermal conductivity tests on concretes up to 600°C and the need to improve the input data in CTES numerical models made necessary this experimental study. In addition, the evolution of the thermal parameter under successive thermal fatigue cycles between the temperature regime 300-600°C has only been found in one study [80] for two concrete types.

2.5.2. Spalling phenomenon

The behaviour of concrete exposed to high temperatures has been studied for a long time from the point of view of the material in the presence of fire. However, in recent years, new applications in energy infrastructures have consolidated their own line of research. Concrete is exposed to high temperature environments in Nuclear and Geothermal Power Plants. Those infrastructures operate at constant temperature once they are being operated. On the contrary, the novel use of concrete as a TES in CSP Plants requires a cyclic operation where the temperature ranges during the performance. Nevertheless, the commissioning of those concrete infrastructures for working at high temperatures implies exposure at higher temperatures.

When concrete is exposed to high temperatures, the spalling risk increases owing to thermal gradients between the surface and the core and pore pressures. The high temperatures caused by a fire or the thermal conditions formed in the concrete infrastructure originate the release of water and the evaporation of this component [81]. At the same time, the specimen undergoes different temperatures on the external surface and in the core. Those thermal gradients originate stresses, and it is one mechanism that has been widely accepted to explain the spalling phenomenon in concrete under fire [82-84]. The spalling phenomenon happens when the stresses exceed the maximum allowable tensile stress of the concrete and the structure collapses.

Several authors have studied other factors that affect spalling such as pore pressures, thermal dilation of aggregates and shrinkage due to cement paste dehydration and the thermal incompatibility between the components of concrete [85, 86]. Moreover, different thermal expansion coefficients between aggregates and cement paste inducing severe cracking can even produce further spalling risk [87, 88].

The geometry of the concrete infrastructure and how the heat source is applied to the surface have been also identified to influence the concrete spalling. That is the reason why the heating rate must be slow enough to ensure that the temperature is being increased in the core and the thermal gradients between the core and the surface are low [69].

There are many different mechanical testing methods for concrete exposed to high temperatures in the literature [69]. Two groups of tests are distinguished as follows: steady-state and transient tests. The first ones are done once the temperature has been stabilised in the concrete samples. On the contrary, transient tests are those carried out when the temperature is being increased at the same time the mechanical test is being performed. Many investigators generally employ heating rates ranges between 0.1-10°C/min [69, 83, 89].

However, explosive spalling has been reported even at heating rates of 1°C/min, because the sizing and geometry should be also taken into account [69, 81].

The spalling risk can be reduced with the addition of polypropylene fibres (PPF) in the concrete mix. The fibres melt when the temperature reaches 165°C and vaporize at 350°C, creating voids that are thought to support relieving internal stresses [90, 91] produced by the internal steam movements at high temperatures.

2.5.3. Mechanical properties

Exposure to high temperatures influences the mechanical properties as well. The thermal degradation that takes place in the material damage the compressive and tensile strengths. Examples such as accidental situations in reactors of Nuclear Power Plants where the concrete structure can last several days needs the knowledge of creep and its temperature dependency [69, 76].

However, the literature review on the evolution of mechanical properties with temperature had been focused on fire testing where the temperature increases quickly up to the collapse of the infrastructure. Mechanical tests have been carried out at hot or residual testing, once the temperature has been cooled down to room temperature. Attending to the heating process, there are steady-state or transient tests made at constant or increasing temperature, respectively [69].

The compressive strength is reduced when temperature increases due to the physicochemical and thermal transformations that take place in the material. Some authors reported that the highest drop in the compressive strength was found when temperature ranges from 100-450°C, whose decay was half of its initial value at room temperature [69, 92, 93]. When comparing values of compressive strength at hot or residual state, the results are higher when the test is carried out during heating (hot state) [69, 94, 95]. Nevertheless, the brand-new concept of use concrete for cyclic regimes of high temperatures needs a better understanding of how the mechanical properties are changing during the thermal operation.

In the case of TES, the reduction in the mechanical properties can even be faster due to thermal cycling operation since the occurrence of hysteresis effects and increased residual expansion. Only a few studies have been conducted on concrete under thermal cycling conditions, as follows. Emerson, J. et al. [43] studied OPC concretes with limestone (calcium), sandstone (siliceous) and syenite aggregate (similar to granite) under 30 thermal cycles at temperatures between 300-600°C. Their results indicate that the average final compressive strength value is about 30% of its initial value, which is the opposite of the strength loss reported under constant temperature conditions. Alonso, M.C. et al. [42] used CAC mixed with blast furnace slag (BFS). The microscopic and macroscopic changes caused by concrete dehydration and continuous heating and cooling cycles between 290-550°C were studied. Their experiments show reductions in compressive strength up to 50% after the first thermal cycle. Their results showed that concrete based on blended CAC with appropriate design could be employed for TES up to 550°C in Solar Thermal Power Plants (STPP).

As the infrastructure needs to withstand the performance during the lifetime of the STPP, the evolution and remain of the compressive strength is a parameter of importance.

2.5.4. Electrical properties

The electrical resistance is the resistance that the concrete offers to transport ions when the material is subjected to an electrical field. Concrete is a compound porous material mainly formed by aggregates, cement paste, pores of water and air and it can include fibres as well. There are interconnected channels between the pores in the cement paste. All the components affect the electrical transfer through ions and it makes the electrical parameter a characteristic property of the material, which also depends on the geometry of the specimen. Therefore, the electrical resistance can be used to determine the interconnection among the pores and to detect cracks within the material.

Nevertheless, the measure of the electrical resistance shows a high dependency on the moisture content. Therefore, concrete with a high degree of saturated pores would reach low electrical resistance values and the same concrete at dried conditions would achieve a high value and less electrical conductive properties.

The moisture condition is considered one of the most important variables for the durability of a concrete infrastructure [96]. The main advantage of measure electrical resistance is that the structure can be monitored in situ. However, the electrical parameter also depends on temperature and the composition of the water in the pores, as it is mentioned by the authors in [96].

The test for measuring the electrical resistance is non-destructive. The widely-known method for carrying out the test is the four-terminal sensing. The concrete sample has four electrodes and the measuring technique introduces an electrical current for 2 terminals and measures the voltage between the others to obtain the electrical impedance of the material. There exist a simpler two-probe method that can be used for obtaining the electrical resistance. It includes only 2 electrodes and the electrical resistance can be directly collected in multimeters, data acquisition systems or using a Wheatstone bridge method [97, 98].

When the material is saturated, the transport of ions takes place mainly by the pores and the interconnected channels [99]. When the temperature increases, the changes in the volume of the specimen modify the distances within the material. Additionally, the increase in the temperature will vary the transition energy of the electrons, changing the water content as well and the moisture of the concrete [97].

The measure of the electrical parameters can be useful for commissioning and preconditioning concrete infrastructures before starting with the operation in CSP at high temperatures. As the test is non-destructive it could give reliable information of the state of the structure in real time, while it is being heated. However, the property is particular for each material and deeper knowledge of its evolution with temperature is needed.

2.6. Challenges and gaps in the literature

Properties of concrete at high temperatures have been widely studied in the field of fire exposure when the infrastructure is being exposed to a quick heating process. However, the new concept of using concrete for STPP infrastructures needs to improve the knowledge in this field. As it was commented before, some researchers have proved the suitability of concrete for TES. However, the experiences were carried out at lab scale in small concrete samples or mid-scale prototypes of concrete modules [44, 48].

Not only concrete can be used for the role of thermal energy storage. Energy infrastructures also need insulating materials able to withstand high temperatures with the aim of reducing the heat transfer losses to the environment. Those plants also need materials to support the structures and concrete is widely used in structures.

Not only the operation of the concrete under charging and discharging processes is important, but also the commissioning and preconditioning of this infrastructure for achieving better results in operation.

To prove that the previous lab-scale results could be applicable to the industry, and with the aim to search the different options of concrete in a CTES infrastructure in CSP Plants, this thesis goes deeper into both the commissioning and operating of concrete under high temperatures.

(Chapter 3 on page 39)

2.7. References

- [1] J. D. Nicholas, Y. Qi, S. R. Bishop and P. P. Mukherjee, "Introduction to mechano-electro-chemical coupling in energy related materials and devices," *J. Electrochem. Soc.*, vol. 161, (11), pp. Y11-Y12, 2014.
- [2] B. J. Mathew, M. Sudhakar and C. Natarajan, "Strength, economic and sustainability characteristics of coal ash–GGBS based geopolymers concrete," *International Journal of Computational Engineering Research*, vol. 3, (1), pp. 207-212, 2013.
- [3] IEA, *Technology Roadmap Solar Thermal Electricity*. Paris: Paris: OECD Publishing, 2015. DOI: 10.1787/9789264238824-en.
- [4] R. Adinberg, "Simulation analysis of thermal storage for concentrating solar power," *Appl. Therm. Eng.*, vol. 31, (16), pp. 3588-3594, 2011. DOI: 10.1016/j.applthermaleng.2011.07.025.
- [5] M. Monjurul Ehsan, Z. Guan, H. Gurgenci and A. Klimenko, "Novel design measures for optimizing the yearlong performance of a concentrating solar thermal power plant using thermal storage and a dry-cooled supercritical CO₂ power block," *Energy Conversion and Management*, vol. 216, 2020. DOI: 10.1016/j.enconman.2020.112980.
- [6] M. Mehrpooya, B. Ghorbani, A. Shahsavari and A. Zaitsev, "Conversion and storage of solar energy in the forms of liquid fuel and electricity in a hybrid energy storage system using methanol and phase change materials," *Energy Conversion and Management*, vol. 209, 2020. DOI: 10.1016/j.enconman.2020.112669.
- [7] C. R. C. Rao, H. Niyas and P. Muthukumar, "Performance tests on lab-scale sensible heat storage prototypes," *Applied Thermal Engineering*, vol. 129, pp. 953-967, 2018. Available: <http://www.sciencedirect.com/science/article/pii/S1359431117353991>. DOI: <https://doi.org/10.1016/j.applthermaleng.2017.10.085>.
- [8] H. Nazir, M. Batool, F. Bolivar Osorio J., M. Isaza-Ruiz, X. Xu, K. Vignarooban, P. Phelan, Inamuddin and A. M. Kannan, "Recent developments in phase change materials for energy storage applications: A review," *Int. J. Heat Mass Transfer*, vol. 129, pp. 491-523, 2019. DOI: 10.1016/j.ijheatmasstransfer.2018.09.126.
- [9] A. Gil, M. Medrano, I. Martorell, A. Lázaro, P. Dolado, B. Zalba and L. F. Cabeza, "State of the art on high temperature thermal energy storage for power generation. Part 1—Concepts, materials and modellization," *Renewable and Sustainable Energy Reviews*, vol. 14, (1), pp. 31-55, 2010.
- [10] E. Oró, A. Gil, A. de Gracia, D. Boer and L. F. Cabeza, "Comparative life cycle assessment of thermal energy storage systems for solar power plants," *Renewable Energy*, vol. 44, pp. 166-173, 2012. Available: <http://www.sciencedirect.com/science/article/pii/S0960148112000195>. DOI: <https://doi.org/10.1016/j.renene.2012.01.008>.
- [11] M. J. Wagner and P. Gilman, "Technical Manual for the SAM Physical Trough Model," 2011. DOI: 10.2172/1016437.

- [12] A. Bonk, S. Sau, N. Uranga, M. Hernaiz and T. Bauer, "Advanced heat transfer fluids for direct molten salt line-focusing CSP plants," *Progress in Energy and Combustion Science*, vol. 67, pp. 69-87, 2018. . DOI: 10.1016/j.pecs.2018.02.002.
- [13] S. Ushak, A. G. Fernández and M. Grageda, "3 - Using molten salts and other liquid sensible storage media in thermal energy storage (TES) systems," *Advances in Thermal Energy Storage Systems*, pp. 49-63, 2015. Available: <http://www.sciencedirect.com/science/article/pii/B9781782420880500031>. DOI: <https://doi.org/10.1533/9781782420965.1.49>.
- [14] A. Bonk, M. Braun, V. A. Sötz and T. Bauer, "Solar Salt – Pushing an old material for energy storage to a new limit," *Applied Energy*, vol. 262, pp. 114535, 2020. Available: <http://www.sciencedirect.com/science/article/pii/S0306261920300477>. DOI: <https://doi.org/10.1016/j.apenergy.2020.114535>.
- [15] L. Cabeza F., *Advances in Thermal Energy Storage Systems: Methods and Applications*. Cambridge: Cambridge Elsevier Science & Technology, 201466. DOI: 10.1016/C2013-0-16453-7.
- [16] M. J. Montes, A. Abánades, J. M. Martínez-Val and M. Valdés, "Solar multiple optimization for a solar-only thermal power plant, using oil as heat transfer fluid in the parabolic trough collectors," *Solar Energy*, vol. 83, (12), pp. 2165-2176, 2009. Available: <https://www.sciencedirect.com/science/article/pii/S0038092X09001947>. DOI: <https://doi.org/10.1016/j.solener.2009.08.010>.
- [17] F. Matino and A. Maccari, "Molten Salt Receivers Operated on Parabolic Trough Demo Plant and in Laboratory Conditions," *Energy Procedia*, vol. 69, pp. 481-486, 2015. . DOI: 10.1016/j.egypro.2015.03.056.
- [18] A. Maccari, D. Bissi, G. Casubolo, F. Guerrini, L. Lucatello, G. Luna, A. Rivaben, E. Savoldi, S. Tamano and M. Zuanella, "Archimede Solar Energy Molten Salt Parabolic Trough Demo Plant: A Step Ahead towards the New Frontiers of CSP," *Energy Procedia*, vol. 69, (Supplement C), pp. 1643-1651, 2015. Available: <http://www.sciencedirect.com/science/article/pii/S1876610215004282>. DOI: <https://doi.org/10.1016/j.egypro.2015.03.122>.
- [19] T. Ruegamer, H. Kamp, T. Kuckelkorn, W. Schiel, G. Weinrebe, P. Nava, K. Riffelmann and T. Richert, "Molten Salt for Parabolic Trough Applications: System Simulation and Scale Effects," *Energy Procedia*, vol. 49, pp. 1523-1532, 2014. . DOI: 10.1016/j.egypro.2014.03.161.
- [20] National Renewable Energy Laboratory, "Concentrating Solar Power Projects: Noor I," *Published Online at Solarpaces.Nrel.Gov*, 2017. Available: <https://solarpaces.nrel.gov/noor-i>.
- [21] National Renewable Energy Laboratory, "Concentrating Solar Power Projects: Noor II," *Published Online at Solarpaces.Nrel.Gov*, 2018. Available: <https://solarpaces.nrel.gov/noor-ii>.
- [22] National Renewable Energy Laboratory, "Concentrating Solar Power Projects: Noor III," *Published Online at Solarpaces.Nrel.Gov*, 2019. Available: <https://solarpaces.nrel.gov/noor-iii>.

- [23] National Renewable Energy Laboratory, "Concentrating Solar Power Projects: Solana Generating Station," Published Online at *Solarpaces.Nrel.Gov*, 2015. Available: <https://solarpaces.nrel.gov/solana-generating-station>.
- [24] (Last visited on 21-01-13). *Solana Solar Power Generating Station, Arizona, US*. Available: <https://www.power-technology.com/projects/solana-solar-power-generating-arizona-us/>.
- [25] R. Peltier, "Solana Generating Station, Maricopa County, Arizona," *Power*, vol. 158, (12), pp. 32, 2014.
- [26] M. Mendelsohn, T. Lowder and B. Canavan, "Utility-Scale Concentrating Solar Power and Photovoltaic Projects: A Technology and Market Overview," 2012. Available: <https://doi.org/10.2172/1039803>.
- [27] National Renewable Energy Laboratory, "Concentrating Solar Power Projects: Andasol I," Published Online at *Solarpaces.Nrel.Gov*, 2017. Available: <https://solarpaces.nrel.gov/andasol-1>.
- [28] National Renewable Energy Laboratory, "Concentrating Solar Power Projects: Andasol II," Published Online at *Solarpaces.Nrel.Gov*, 2017. Available: <https://solarpaces.nrel.gov/andasol-2>.
- [29] National Renewable Energy Technology, "Concentrating Solar Power Projects: Andasol III," Published Online at *Solarpaces.Nrel.Gov*, 2013. Available: <https://solarpaces.nrel.gov/andasol-3>.
- [30] A. Jäger-Waldau, H. Bloem and R. L. Arantegui, "Renewable Energy Snapshots 2011," *Publications Office of the European Union*, 2011. . DOI: 10.2788/79032.
- [31] National Renewable Energy Laboratory, "Concentrating Solar Power Projects: Extresol I," Published Online at *Solarpaces.Nrel.Gov*, 2017. Available: <https://solarpaces.nrel.gov/extresol-1>.
- [32] National Renewable Energy Laboratory, "Concentrating Solar Power Plants: Extresol II," Published Online at *Solarpaces.Nrel.Gov*, 2017. Available: <https://solarpaces.nrel.gov/extresol-2>.
- [33] National Renewable Energy Technologies, "Concentrating Solar Power Projects: Extresol III," Published Online at *Solarpaces.Nrel.Gov*, 2017. Available: <https://solarpaces.nrel.gov/extresol-3>.
- [34] J. López Sanz, F. Cabello Nuñez and F. Zaversky, "Benchmarking analysis of a novel thermocline hybrid thermal energy storage system using steelmaking slag pebbles as packed-bed filler material for central receiver applications," *Solar Energy*, vol. 188, pp. 644-654, 2019. . DOI: 10.1016/j.solener.2019.06.028.
- [35] D. Brosseau, J. W. Kelton, D. Ray, M. Edgar, K. Chisman and B. Emms, "Testing of thermocline filler materials and molten-salt heat transfer fluids for thermal energy storage systems in parabolic trough power plants," *J.Sol.Energy Eng.*, vol. 127, (1), pp. 109-116, 2005.

- [36] Z. Yang and S. V. Garimella, "Thermal analysis of solar thermal energy storage in a molten-salt thermocline," *Solar Energy*, vol. 84, (6), pp. 974-985, 2010.
- [37] J. E. Pacheco, S. K. Showalter and W. J. Kolb, "Development of a molten-salt thermocline thermal storage system for parabolic trough plants," *Transactions-American Society of Mechanical Engineers Journal of Solar Energy Engineering*, vol. 124, (2), pp. 153-159, 2002.
- [38] S. Flueckiger, Z. Yang and S. V. Garimella, "An integrated thermal and mechanical investigation of molten-salt thermocline energy storage," *Appl. Energy*, vol. 88, (6), pp. 2098-2105, 2011.
- [39] V. D. Cao, S. Pilehvar, C. Salas-Bringas, A. M. Szczotok, J. F. Rodriguez, M. Carmona, N. Al-Manasir and A. Kjønksen, "Microencapsulated phase change materials for enhancing the thermal performance of Portland cement concrete and geopolymer concrete for passive building applications," *Energy Conversion and Management*, vol. 133, pp. 56-66, 2017. . DOI: 10.1016/j.enconman.2016.11.061.
- [40] L. F. Cabeza, L. Navarro, A. L. Pisello, L. Olivieri, C. Bartolomé, J. Sánchez, S. Álvarez and J. A. Tenorio, "Behaviour of a concrete wall containing micro-encapsulated PCM after a decade of its construction," *Solar Energy*, vol. 200, pp. 108-113, 2020. . DOI: 10.1016/j.solener.2019.12.003.
- [41] Y. Liu, M. Xie, E. Xu, X. Gao, Y. Yang and H. Deng, "Development of calcium silicate-coated expanded clay based form-stable phase change materials for enhancing thermal and mechanical properties of cement-based composite," *Solar Energy*, vol. 174, pp. 24-34, 2018. . DOI: 10.1016/j.solener.2018.08.085.
- [42] M. C. Alonso, J. Vera-Agullo, L. Guerreiro, V. Flor-Laguna, M. Sanchez and M. Collares-Pereira, "Calcium aluminate based cement for concrete to be used as thermal energy storage in solar thermal electricity plants," *Cement and Concrete Research*, vol. 82, pp. 74-86, 2016. Available: <http://www.sciencedirect.com/science/article/pii/S0008884615003075>. DOI: <https://doi.org/10.1016/j.cemconres.2015.12.013>.
- [43] E. John, M. Hale and P. Selvam, "Concrete as a thermal energy storage medium for thermocline solar energy storage systems," *Solar Energy*, vol. 96, pp. 194-204, 2013. Available: <http://www.sciencedirect.com/science/article/pii/S0038092X13002636>. DOI: <https://doi.org/10.1016/j.solener.2013.06.033>.
- [44] D. Laing, C. Bahl, T. Bauer, M. Fiss, N. Breidenbach and M. Hempel, "High-Temperature Solid-Media Thermal Energy Storage for Solar Thermal Power Plants," *Proc IEEE*, vol. 100, (2), pp. 516-524, 2012. . DOI: 10.1109/JPROC.2011.2154290.
- [45] A. Buscemi, D. Panno, G. Ciulla, M. Beccali and V. Lo Brano, "Concrete thermal energy storage for linear Fresnel collectors: Exploiting the South Mediterranean's solar potential for agri-food processes," *Energy Conversion and Management*, vol. 166, pp. 719-734, 2018. . DOI: 10.1016/j.enconman.2018.04.075.
- [46] K. Bataineh and A. Gharaibeh, "Optimal design for sensible thermal energy storage tank using natural solid materials for a parabolic trough power plant," *Solar Energy*, vol. 171, pp. 519-525, 2018. . DOI: 10.1016/j.solener.2018.06.108.

- [47] V. A. Salomoni, C. E. Majorana, G. M. Giannuzzi, A. Miliozzi, R. Di Maggio, F. Girardi, D. Mele and M. Lucentini, "Thermal storage of sensible heat using concrete modules in solar power plants," *Solar Energy*, vol. 103, pp. 303-315, 2014. . DOI: 10.1016/j.solener.2014.02.022.
- [48] N. Hoivik, C. Greiner, J. Barragan, A. C. Iniesta, G. Skeie, P. Bergan, P. Blanco-Rodriguez and N. Calvet, "Long-term performance results of concrete-based modular thermal energy storage system," *Journal of Energy Storage*, vol. 24, pp. 100735, 2019. . DOI: 10.1016/j.est.2019.04.009.
- [49] K. Vigneshwaran, G. Singh Sodhi, P. Muthukumar and S. Subbiah, "Concrete based high temperature thermal energy storage system: Experimental and numerical studies," *Energy Conversion and Management*, vol. 198, 2019. . DOI: 10.1016/j.enconman.2019.111905.
- [50] B. Xu, J. Han, A. Kumar, P. Li and Y. Yang, "Thermal storage using sand saturated by thermal-conductive fluid and comparison with the use of concrete," *Journal of Energy Storage*, vol. 13, pp. 85-95, 2017. . DOI: 10.1016/j.est.2017.06.010.
- [51] F. Bai and C. Xu, "Performance analysis of a two-stage thermal energy storage system using concrete and steam accumulator," *Appl. Therm. Eng.*, vol. 31, (14-15), pp. 2764-2771, 2011. . DOI: 10.1016/j.applthermaleng.2011.04.049.
- [52] G. Chen, X. Ding, M. Cai and W. Qiao, "Analytical solution for temperature field of nonmetal cooling pipe embedded in mass concrete," *Appl. Therm. Eng.*, vol. 158, 2019. . DOI: 10.1016/j.applthermaleng.2019.113774.
- [53] Y. Jian, F. Bai, Q. Falcoz, C. Xu, Y. Wang and Z. Wang, "Thermal analysis and design of solid energy storage systems using a modified lumped capacitance method," *Appl. Therm. Eng.*, vol. 75, pp. 213-223, 2015. . DOI: 10.1016/j.applthermaleng.2014.10.010.
- [54] G. M. Giannuzzi, R. Liberatore, D. Mele, G. Mazzucco, G. Xotta, V. A. Salomoni, C. E. Majorana and R. Di Maggio, "Experimental campaign and numerical analyses of thermal storage concrete modules," *Solar Energy*, vol. 157, pp. 596-602, 2017. . DOI: 10.1016/j.solener.2017.08.041.
- [55] L. Doretti, F. Martelletto and S. Mancin, "A simplified analytical approach for concrete sensible thermal energy storages simulation," *Journal of Energy Storage*, vol. 22, pp. 68-79, 2019. Available: <http://www.sciencedirect.com/science/article/pii/S2352152X18306741>. DOI: <https://doi.org/10.1016/j.est.2019.01.029>.
- [56] F. P. Incropera, *Introduction to Heat Transfer*. (5th ed. ed.) Hoboken, NJ: Hoboken, NJ : John Wiley & Sons, 2006.
- [57] D. G. R. Bonnell and F. C. Harper, "The thermal expansion of concrete. Engineering Research.(Summary of a report to be published by The Building Research Station)." *Journal of the Institution of Civil Engineers*, vol. 33, (4), pp. 320-330, 1950.
- [58] Z. P. Bažant, M. F. Kaplan and Z. P. Bazant, "Concrete at high temperatures: material properties and mathematical models," 1996.

- [59] F. Birch and H. Clark, "The Thermal Conductivity of Rocks and Its Dependence Upon Temperature and Composition.," *American Journal of Science*, vol. 238, (8), pp. 529-558, 1940.
- [60] H. Kanamori, N. Fujii and H. Mizutani, "Thermal diffusivity measurement of rock-forming minerals from 300° to 1100° K," *Journal of Geophysical Research*, vol. 73, (2), pp. 595-605, 1968.
- [61] G. Zoth and R. Hänel, "Handbook of Terrestrial Heat Flow Density Determination," 1988.
- [62] K. Kawada, "Studies of the thermal state of the earth," in *The 17th Paper: Variation of Thermal Conductivity of Rocks* Anonymous 1964, pp. 631-647.
- [63] F. Birch, J. F. Schairer and H. C. Spicer, "Handbook of physical constants: Geol." Soc.America Special Paper, vol. 36, pp. 325, 1942.
- [64] E. A. Sakvarelidze, "Verkhnaya mantiya, No. 12," 1973.
- [65] Y. S. Touloukian, R. W. Powell, C. Y. Ho and P. G. Klemens, "Thermophysical Properties of Matter - The TPRC Data Series. Volume 2. Thermal Conductivity - Nonmetallic Solids," 1971.
- [66] R. W. Goranson, "Heat conductivity of minerals Hb," *Phy. Const., Geol.Soc.Am.Sp.Pap*, (36), 1942.
- [67] V. Y. Leonidov, "Heat capacities of rocks at high temperatures," *Geochemistry International Ussr*, vol. 4, (2), pp. 400-&, 1967.
- [68] W. Winkler, "HGF: Heidelberger Beitr," *Mineral.Petrog*, vol. 3, pp. 297, 1952.
- [69] P. Pimienta, R. J. McNamee and J. Mindegua, *Physical Properties and Behaviour of High-Performance Concrete at High Temperature*. Springer, 2018.
- [70] J. S. Dolado, "Thermal properties of cement-based materials. Proceeding of the Workshop on Concrete Modelling and Materials Behaviour." 2018.
- [71] N. Ukrainczyk and T. Matusinović, "Thermal properties of hydrating calcium aluminate cement pastes," *Cem. Concr. Res.*, vol. 40, (1), pp. 128-136, 2010. . DOI: 10.1016/j.cemconres.2009.09.005.
- [72] H. Yuan, Y. Shi, Z. Xu, C. Lu, Y. Ni and X. Lan, "Effect of nano-MgO on thermal and mechanical properties of aluminate cement composite thermal energy storage materials," *Ceram. Int.*, vol. 40, (3), pp. 4811-4817, 2014. . DOI: 10.1016/j.ceramint.2013.09.030.
- [73] F. A. Cardoso, M. D. M. Innocentini, M. M. Akiyoshi and V. C. Pandolfelli, "Effect of curing time on the properties of CAC bonded refractory castables," *Journal of the European Ceramic Society*, vol. 24, (7), pp. 2073-2078, 2004. Available: <https://www.sciencedirect.com/science/article/pii/S0955221903003716>. DOI: [https://doi.org/10.1016/S0955-2219\(03\)00371-6](https://doi.org/10.1016/S0955-2219(03)00371-6).

- [74] C. Alonso and L. Fernandez, "Dehydration and rehydration processes of cement paste exposed to high temperature environments," *J. Mater. Sci.*, vol. 39, (9), pp. 3015-3024, 2004. . DOI: 10.1023/B:JMSC.0000025827.65956.18.
- [75] Y. Grosu, I. Ortega-Fernández, L. González-Fernández, U. Nithiyantham, Y. F. Baba, A. Al Mers and A. Faik, "Natural and by-product materials for thermocline-based thermal energy storage system at CSP plant: Structural and thermophysical properties," *Appl. Therm. Eng.*, vol. 136, pp. 185-193, 2018. . DOI: 10.1016/j.applthermaleng.2018.02.087.
- [76] A. Millard and P. Pimienta, *Modelling of Concrete Behaviour at High Temperature. State-of-the-Art Report of the RILEM Technical Committee 227-HPB*. Springer, 2019.
- [77] J. Mindegua, "Contribution expérimentale à la compréhension des risques d'instabilité thermique des bétons , " 2009.
- [78] R. Jansson, "Measurement of concrete thermal properties at high temperature," *Proceedings from the Fib Task Group*, vol. 4, pp. 2-3, 2004.
- [79] Z. Xing, A. Beaucour, R. Hebert, A. Noumowe and B. Ledesert, "Aggregate's influence on thermophysical concrete properties at elevated temperature," *Construction and Building Materials*, vol. 95, pp. 18-28, 2015. Available: <http://www.sciencedirect.com/science/article/pii/S095006181530057X>. DOI: <https://doi.org/10.1016/j.conbuildmat.2015.07.060>.
- [80] T. Lucio-Martin, M. Roig-Flores, M. C. Alonso and L. Guerreiro, "Evolution of thermal conductivity on CAC concrete at high temperatures and during thermal fatigue tests." vol. Proceedings of the 6th International Workshop on Concrete Spalling due to Fire Exposure, 2019.
- [81] Y. Fu, Y. Fu, L. Li and L. Li, "Study on mechanism of thermal spalling in concrete exposed to elevated temperatures," *Mater. Struct.*, vol. 44, (1), pp. 361-376, 2011. . DOI: 10.1617/s11527-010-9632-6.
- [82] Z. P. Bazant, "Analysis of pore pressure, thermal stresses and fracture in rapidly heated concrete," *International Workshop on Fire Performance of High-Strength Concrete*, 1997.
- [83] G. A. Khouri, C. E. Majorana, F. Pesavento and B. A. Schrefler, "Modelling of heated concrete," *Magazine of Concrete Research*, vol. 54, (2), pp. 77-101, 2002.
- [84] W. Nechnech, F. Meftah and J. M. Reynouard, "An elasto-plastic damage model for plain concrete subjected to high temperatures," *Eng. Struct.*, vol. 24, (5), pp. 597-611, 2002. . DOI: 10.1016/S0141-0296(01)00125-0.
- [85] P. Kalifa, F. Menneteau and D. Quenard, "Spalling and pore pressure in HPC at high temperatures," *Cem. Concr. Res.*, vol. 30, (12), pp. 1915-1927, 2000. . DOI: 10.1016/S0008-8846(00)00384-7.
- [86] Z. Pan, J. G. Sanjayan and D. L. Y. Kong, "Effect of aggregate size on spalling of geopolymer and Portland cement concretes subjected to elevated temperatures," *Construction & Building Materials*, vol. 36, pp. 365-372, 2012. . DOI: 10.1016/j.conbuildmat.2012.04.120.

- [87] Z. P. Bazant and M. T. Kazemi, "Determination of fracture energy, process zone length and brittleness number from size effect, with application to rock and concrete," *Int. J. Fract.*, vol. 44, (2), pp. 111-131, 1990.
- [88] M. Kanéma, P. Pliya, A. Noumowé and J. Gallias, "Spalling, Thermal, and Hydrous Behavior of Ordinary and High-Strength Concrete Subjected to Elevated Temperature," *J. Mater. Civ. Eng.*, vol. 23, (7), pp. 921-930, 2011. . DOI: 10.1061/(ASCE)MT.1943-5533.0000272.
- [89] I. Gaweska, "Thermal behavior of high performance concretes at high temperature-evolution of mechanical properties," 2004.
- [90] P. Kalifa, G. Chéné and C. Gallé, "High-temperature behaviour of HPC with polypropylene fibres: From spalling to microstructure," *Cem. Concr. Res.*, vol. 31, (10), pp. 1487-1499, 2001. Available: <http://www.sciencedirect.com/science/article/pii/S0008884601005968>. DOI: [https://doi.org/10.1016/S0008-8846\(01\)00596-8](https://doi.org/10.1016/S0008-8846(01)00596-8).
- [91] X. Liu, G. Ye, G. De Schutter, Y. Yuan and L. Taerwe, "On the mechanism of polypropylene fibres in preventing fire spalling in self-compacting and high-performance cement paste," *Cem. Concr. Res.*, vol. 38, (4), pp. 487-499, 2008. Available: <http://www.sciencedirect.com/science/article/pii/S0008884607002931>. DOI: <https://doi.org/10.1016/j.cemconres.2007.11.010>.
- [92] U. Diederichs, U. M. Jumppanen and V. Pentalla, "Behaviour of high strength concrete at high temperature," *Report 92*, pp. 1-76, 1989.
- [93] P. Pimienta and I. Hager, "Mechanical behaviour of HPC at high temperature," in *6th International Symposium on Utilisation of High Strength/High Performance Concrete*, 2002.
- [94] G. A. Khoury, "Mechanical behaviour at high temperature in compression," *HITECO Report, Imperial College*, 1999.
- [95] J. Horvath, U. Schneider and U. Diederichs, *Brandverhalten Von Hochleistungsbetonen*. Inst. für Baustofflehre, Bauphysik u. Brandschutz, TU Wien, 2004.
- [96] W. Elkey and E. J. Sellevold, "Electrical resistivity of concrete," *Directorate of Public Roads. Norwegian Road Research Laboratory*, 1995.
- [97] B. Han, S. Ding and X. Yu, "Intrinsic self-sensing concrete and structures: A review," *Measurement: Journal of the International Measurement Confederation*, vol. 59, pp. 110-128, 2015. . DOI: 10.1016/j.measurement.2014.09.048.
- [98] F. Reza, G. B. Batson, J. A. Yamamuro and J. S. Lee, "Resistance changes during compression of carbon fiber cement composites," *J. Mater. Civ. Eng.*, vol. 15, (5), pp. 476-483, 2003.
- [99] I. Hansson and C. M. Hansson, "Electrical resistivity measurements of Portland cement based materials," *Cem. Concr. Res.*, vol. 13, (5), pp. 675-683, 1983.

This page has been intentionally left blank.

Chapter 3

Concrete risk under the high temperature scenario in CSP Plants

This chapter deals with the analysis of the feasibility of using concrete in infrastructures of TES in CSP Plants. The structure of the chapter has been distributed in different sections.

Firstly, *section 3.1* includes a brief introduction about the risks of concrete when the material is subjected to high temperatures. Two main requirements are presented: 1) the spalling risk and 2) the performance under the thermal cyclic operation.

Later, *section 3.2* includes a study related to the influence of geometry and the concrete characteristics in the risk of the spalling phenomenon. This section deals with a fundamental analysis of concrete exposed to high temperatures but under the scope of having a material designed for resisting under Serviceability Limit State (SLS). Contingencies and conclusions on the designing for the optimal concrete composition for the suitability under CSP Plants regimes are analysed to understand the contribution of concrete components in the thermal response.

Section 3.3 includes a deeper characterisation of the mechanical and physicochemical properties of different concrete components exposed to thermal cyclic regimes simulating conditions of a TES infrastructure for a CSP Plant. It includes the evolution of the thermo-mechanical stability under repetitive heating and cooling cycles by evaluating the compressive strength and Elastic Modulus. A novelty in this work is the determination of the evolution of the cracking for different concrete compositions exposed to cycling and the measure of the crack width. The study finalises with the microstructural characterisation (X-ray diffraction and thermogravimetric) to evaluate the critical changes in the concrete when is exposed to high temperatures.

Finally, the suitability of using concrete in a TES infrastructure is evaluated and some preliminary conclusions on the performance of concrete under high temperature scenario as the ones performed in a CSP Plant are highlighted.

3.1. Introduction

This chapter deals with the analysis of the feasibility of using concrete in CSP energy storage infrastructures. As the HTF can operate up to 600°C, the concrete needs to reach the following requirements for being a material suitable for being used in infrastructures operated at high temperatures:

1. Avoid spalling risk when it is subjected to high temperatures. Influence of concrete design and sample geometry in the risk of spalling of concrete at high temperature.

The behaviour of concrete exposed to high temperatures has been studied for a long time from the point of view of the material in the presence of fire. However, in recent years, new applications in energy infrastructures have consolidated their own line of research. The use of concrete as thermal energy storage in CSP Plants has been verified recently [1-3]. The highest concern about this type of use of concrete is the thermal stability of the concrete when is exposed to heat charge and discharge.

From the point of view of the development of high temperature concrete design, several alternatives have allowed a better performance. The use of polypropylene fibres (PPF) [2, 4], thermally stable and low expansion aggregates and its size distribution in the mix [2] has been proved useful to have a better performance. Concrete spalling risk is one of the major cause of failure of concrete when exposed to high temperature and fire. Different authors have related the concrete spalling with the specimen dimensions [5, 6] but the geometry effect is not clear yet and needs to go for deeper study.

The spalling phenomenon is one of the riskiest factors when concrete is exposed to high temperatures. The first heating, when the concrete undergoes dehydration, is fundamental in the operation of the elements used for energy storage in CSP. The maximum temperature of use is limited to up to 600°C [2] and it is considered the most critical stage. During the first heating, the dehydration of cement paste takes place liberating vapour. During this stage, the risk of spalling is higher mainly because of two aspects: i) The thermal gradients generated between the heated surfaces and the core of the samples, which induce high thermal stresses, and ii) the accumulation of vapour in the bulk of the concrete limiting the vapour to be released and generating high pressures in the bulk [5, 7-9].

In order to go deeper, the first part of this chapter investigates the first heating for a concrete designed to withstand high temperature, to be suitable for thermal storage up to 550°C. For that purpose, the effect of geometry on the risk of spalling was analysed for the dehydration of concrete owing to the heating process.

2. Design and durability of High Thermal Performance Concrete under thermal fatigue operation and suitability for CSP infrastructures.

Several requirements have to be reached for concrete for being used as a part of the thermal energy storage infrastructure. The suitability for being used in a CSP Plant involves a long-term performance of up to 25 years, which is considered to be the lifetime of CSP Plants [10]. For that aim, concrete needs to maintain stability in the long term.

During the second part of this chapter, different concrete compositions were subjected to the cyclic operating conditions of a CSP Plant simulating the working temperature regime of the molten salts as HTF. The durability and appropriateness of concrete for the thermal energy storage infrastructure were analysed through different mechanical, thermal and physicochemical parameters.

3.2. Influence of concrete design and sample geometry in the risk of spalling of concrete at high temperature

When the PhD candidate started working at IETcc-CSIC, the first study was to analyse the risk of spalling and the effect of the geometry and up-scaling of a concrete composition. This study was carried out in another H2020 project named LORCENIS “*Long Lasting Reinforced Concrete for Energy Infrastructure under Severe Operating Conditions*” [11, 12]. The PhD candidate participated exclusively in the analysis that is shown in this section.

3.2.1. Methodology

3.2.1.1. Material and production of samples

The concrete used for LORCENIS study [11, 12] was fabricated using CEM II containing 30% of micro blast furnace slag. This binder was blended with fly ash class F up to 20%. Calcareous and basalt aggregates (0-6 and 6-12 mm) were selected as considered to have good thermal stability up to the maximum temperature (550°C). Also, clinker as aggregate (0-5.6 mm size) was added. Finally, limestone filler was included to achieve the self-compacting ability to produce the concrete. Table 3.1 shows the concrete composition and mechanical properties at hardened conditions.

| Component | C-1 mix |
|--|---------|
| CEM II/B-S 52.5 R (kg/m ³) | 319 |
| Fly Ash (kg/m ³) | 130 |
| Limestone Filler (kg/m ³) | 157 |
| Calcareous 0-6 mm (kg/m ³) | 465 |
| Basalt 0-6 mm (kg/m ³) | 212 |
| Clinker 0-5.6 mm (kg/m ³) | 191 |
| Calcareous 6-12 mm (kg/m ³) | 531 |
| Basalt 6-12 mm (kg/m ³) | 315 |
| Superplasticizer additive 1 | 1 |
| Superplasticizer additive 2 | 1.2 |
| Viscosity modifier additive | 0.9 |
| w/b | 0.39 |
| Density (kg/m ³) | 2400 |
| Open porosity (%) | 4.51 |
| f _{ck} ^a 7 days (MPa) | 66.1 |
| f _{ck} ^a 28 days (MPa) | 84.5 |
| MIP porosity (%) | 6.61 |

^aThe compressive strength was measured on cubic specimens (150×150×150 mm³).

Table 3.1: Concrete composition

The influence of heat on spalling has been analysed in one concrete mix varying the type of geometry and size of the element: cylindrical (75 mm of diameter and 150 mm of height), cubic ($150 \times 150 \times 150$ mm 3), and prismatic ($150 \times 150 \times 400$ mm 3). The samples had K-type thermocouples embedded. Figure 3.1 shows the samples and thermocouples embedded in each specimen, and Table 3.2 specifies the location of thermocouples with respect to the reference system shown in Figure 3.1.

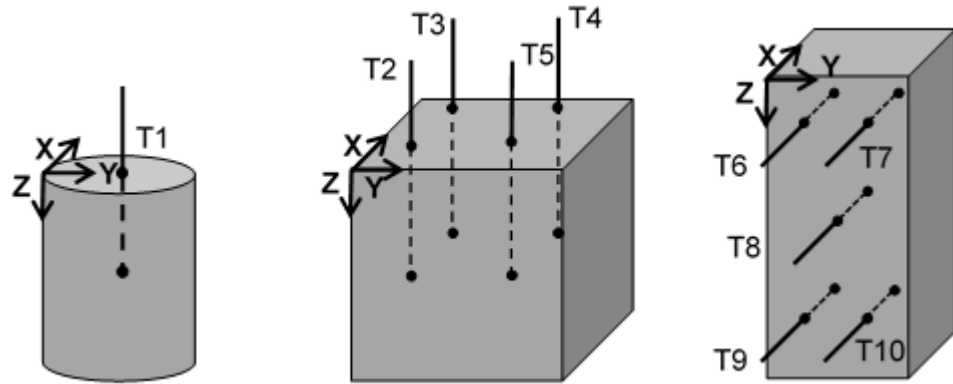


Figure 3.1: Geometries and thermocouples located inside the concrete samples.

| Geometry | ID | Coordinates (mm) | | | Geometry | ID | Coordinates (mm) | | |
|-------------|----|------------------|------|----|-----------|-----|------------------|-----|-----|
| | | X | Y | Z | | | X | Y | Z |
| Cylindrical | T1 | 0 | 37.5 | 75 | Prismatic | T6 | 75 | 50 | 50 |
| Cubic | T2 | 30 | 30 | 75 | | T7 | 75 | 115 | 50 |
| | T3 | 120 | 30 | 75 | | T8 | 75 | 75 | 200 |
| | T4 | 120 | 120 | 75 | | T9 | 75 | 50 | 350 |
| | T5 | 30 | 120 | 75 | | T10 | 75 | 115 | 350 |

Table 3.2: Location of thermocouples.

Before starting the thermal test, samples were stored in a humidity chamber at 20°C and 98% of relative humidity (RH). At the time of testing, the samples had an age varying between 28 and 90 days, as is shown in Table 3.3. The variables under study were: the effect of geometry in spalling risk and the differences in temperature between the core and the surface. The sample geometry, dimensions, and surface (S), volume (V) and the S/V ratio are included in Table 3.3.

| Test | Curing Conditions | Ageing (days) | Shape | Dimensions (mm) | S/V (m $^{-1}$) |
|-------------------------------------|-------------------|---------------|-------------|-----------------|------------------|
| Effect of geometry in spalling risk | 20°C/98%RH | ≥ 28 | Cylindrical | Φ75, H 150 | 66.67 |
| | | ≥ 90 | Cubic | 150×150×150 | 40 |
| | | ≥ 28 | Prismatic | 150×150×400 | 31.67 |

Table 3.3: Specimen characteristics and the relationship between shape, size and volume.

3.2.1.2. Thermal test

Before starting the thermal tests, samples were dried inside the furnace at 105°C for 3 days to reduce the free water from the pores. After that, the thermal test was launched up to 550°C, following a slow first heating rate of 1°C/min in order to induce low thermal gradients in the specimen and decrease the risk of spalling.

3.2.2. Results and discussion

3.2.2.1. Evolution of temperatures

Figure 3.2 shows the evolution of temperature recorded by thermocouples located inside the specimens and in the furnace during the first heating from room temperature up to 550°C. According to geometry, cylindrical and cubic specimens adapted fast to temperature changes following almost the same heating rate of the furnace. This is mainly due to the smaller specimen size, which means that heat reaches the geometrical centre of the specimen earlier and vapour evacuate also easily. Moreover, smaller specimen sizes mean a higher amount of air inside the furnace, which improves the convection heat transfer mechanism between the furnace and the samples.

Regarding the difference in temperature inside the concrete sample, it was higher in the cubic and lower in the cylindrical. Thermocouples T2, T3, T4 and T5 distanced 30 mm from the heated surface recorded almost the same temperature as T1 located 37.5 mm from the heated surface. This is explained because of the “corner effect” that makes the heat cross more slowly through the sample before arriving at the geometrical centre of the specimen. Taking into account that the temperature in the centre of the cubic sample was not recorded, this critical point would have experienced higher thermal gradients because of the distance from the heat source and the corner effect. The furnace heating rate was fixed at 1°C/min but the real heating rate inside the samples was 0.9°C/min for both specimens.

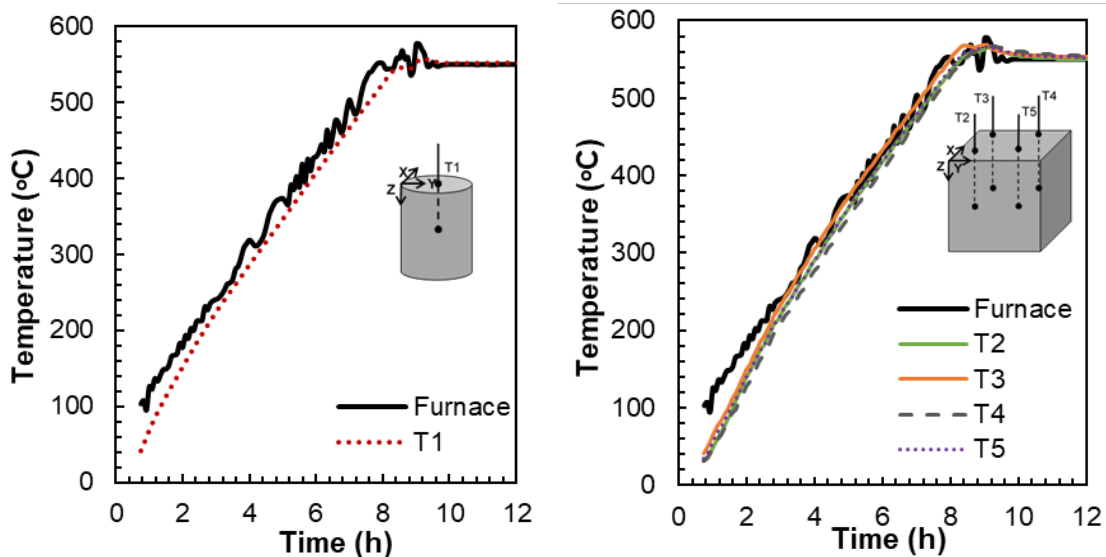


Figure 3.2: First dehydration stage: CYLINDRICAL and CUBIC samples.

3.2.2.2. Spalling risk

The risk of spalling concerning the sample geometry is appreciated in Figure 3.3. The evolution of temperature was recorded with the thermocouples in the prismatic sample. During the first 5 hours of testing, the thermal gradients between the furnace and the internal part of the sample increased achieving more than 100°C of difference. Thermocouple T8 recorded the highest difference because it distanced 75 mm from the heated surfaces, and this location was the critical point of the specimen. When the furnace was at 400°C the sample underwent spalling. At this time, T8 was at 250°C and the difference of temperature was 150°C in 75 mm. This generated high thermal stresses within the concrete and the material underwent spalling, as is shown in Figure 3.4. Despite having the same cross-section as the cubic sample, the thermal gradients were bigger in the prismatic one. Therefore, thermal gradients are not only influenced by the distance from the heat source but also by the geometry. On the other hand, ageing also influences the risk of spalling. Whereas the cubic sample was tested after 90 days, the prismatic had only 28 days of age and a larger dimension, which end up in a spalling phenomenon.

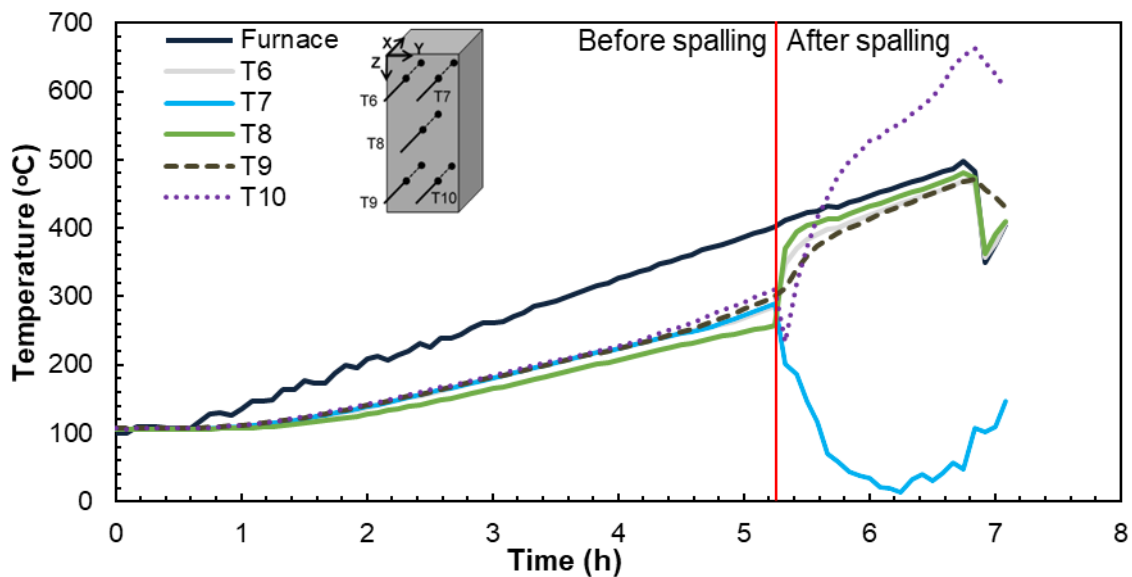


Figure 3.3: First dehydration stage: PRISMATIC sample.



Figure 3.4: Prismatic sample after the spalling phenomenon.

3.2.2.3. Effect of geometry in spalling risk

Analysing the three geometries made with the same type of concrete, Figure 3.5 shows the evolution of temperature inside the three geometries during the dehydration stage up to 550°C. Moreover, Table 3.4 quantifies the difference of temperature between the furnace and the thermocouple T1 (cylindrical), T4 (cubic) and T8 for the prismatic. The heating rate of the heat source (furnace) was fixed in 1°C/min but the real heating rate inside the samples was 0.9°C/min for the cylindrical and cubic and 0.6 for the prismatic geometry, determined from the temperature evolution over time in the core of the specimens. This is owing to internal stresses, which increase the risk of spalling when the sample size is increased. For that reason, the geometry and dimensions of the specimens should be considered when carrying out the dehydration process before starting the high temperature test.

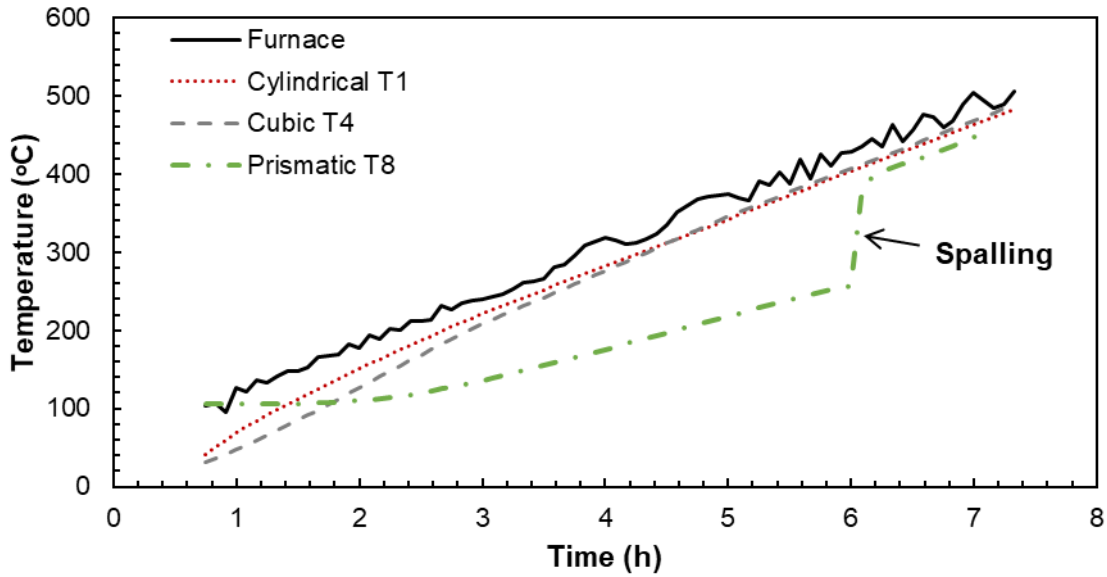


Figure 3.5: First dehydration stage for all geometries.

Several authors have evaluated the effect of the section size on concrete spalling. For the same concrete mix and heating rate ($1^{\circ}\text{C}/\text{min}$), a reduction of size by 50-75% eliminated the risk of spalling [13]. Kanéma et al. [5] also analysed the effect of size and observed that spalling happened only in large samples despite undergoing the same thermal gradients as the small ones. Liu et al. [6] give the explanation that smaller samples facilitate the escape of moisture out of the concrete and this induces lower pore pressure. In the present study, the thermal gradients were higher in the prismatic specimen (Table 3.4) and the spalling happened after being exposed to a high temperature difference for a long time (6 hours).

| Temperature difference, ΔT (°C) | | | | |
|---|------------|------------------|------------------|-----------------------|
| | Furnace | Cylindrical T1 | Cubic T4 | Prismatic T8 |
| Time (h) | T_{Furn} | ΔT_{cyl} | ΔT_{cub} | ΔT_{prism_2} |
| 1.5 | 150 | 37 | 63 | 57 |
| 3 | 240 | 19 | 32 | 87 |
| 4.5 | 335 | 22.5 | 24 | 115.5 |
| 6 | 428.5 | 24 | 24 | Spalling |
| 7.5 | 531 | 35 | 32 | |
| Heating rate (°C/min) | 1 | 0.9 | 0.9 | 0.6 |

Table 3.4: Temperature differences between the furnace and the core of the specimens

On the other hand, the temperature differences were bigger in the first heating instants because of thermal inertia (Table 3.4). At those moments, the furnace was being heated but the core of the material needed time to receive the heat. After that, the temperature difference decreased in both the cylindrical and cubic specimens whereas the prismatic sample continued increasing with the time of exposure, Figure 3.5.

In order to reduce the spalling risk during the first heating in case of using concrete in a TES infrastructure for a CSP Plant, the geometry must be taken into account. The spalling risk might be avoided by doing the first heating and commissioning process by steps and remain at plateaus of constant temperature until the core reaches a homogeneous temperature. Doing that, the temperature difference would be reduced and, hence, the risk of spalling too. An additional contingency is the incorporation of polypropylene fibres (PPF) and the use of more thermal stable materials in the concrete composition.

3.2.3. Partial conclusions on the spalling risk analysis

This initial study carried out helped to evaluate the influence of the concrete composition and geometry in the spalling phenomenon. The results of the investigation led to the following conclusions:

- The design of the concrete composition should include PPF as a contingency for avoiding the risk of spalling in the first heating and thermally stable materials.
- Not only the design of the concrete mix influence the risk of spalling but also the geometry. Despite having the same cross-section, the cubic and prismatic specimens the large sample underwent spalling because the temperature difference between the core and the external surface was higher.
- The ageing also influences the spalling risk and up-scaled concrete specimens.
- Appropriate commissioning during the first heating is essential for homogenising the temperature within the concrete and reduce the thermal gradients.

3.3. Durability of High Thermal Performance Concrete under thermal cyclic operation and suitability for CSP infrastructures

After the initial study carried out in the previous section, the aim of the experimental work performed in this section is to test different concrete compositions under the cyclic operation of a CSP Plant to evaluate the thermal response and the suitability for being used in the infrastructure of thermal energy storage.

3.3.1. Methodology of the durability of High Thermal Performance Concrete under thermal cyclic operation and suitability for CSP infrastructures

The procedure followed was firstly defining the thermal regime and doing a characterisation of the aggregates and cement so as to evaluate their thermal performance. After that, the design of the concrete compositions was carried out considering the thermal response of the aggregates and the addition of PPF as a contingency to avoid the spalling phenomenon. Finally, tests regarding the evolution of the mechanical and physicochemical properties before and after the thermal exposure were carried out.

3.3.1.1. Design of the thermal cycle

As it was explained in previous chapters, the role of concrete in infrastructures of thermal energy storage in CSP Plants may vary on its purpose as follows: structural element, storage or isolating component or a combination of both structural and storage material. In any case, concrete might be exposed at the extreme operating conditions of the HTF and will undergo the same variations of temperature. For that reason, the thermal cycle was designed to evaluate the behaviour of the material in the most severe operation with the temperature

ranging between the same limits of operation as the HTF. The purpose is to evaluate the variation of the thermo-mechanical properties after the thermal operation. The cycles designed need to reflect the charge and discharge processes, and in the most severe operating conditions, to ensure the safety of the system.

The thermal exposure of the concrete samples has been divided into 3 stages, according to the physicochemical changes that take place in the concrete, as is mentioned as follows: drying process, dehydration and thermal fatigue stage. Figure 3.6 shows the thermal cycles and stages. For the drying process, concrete loses all of the free water located in the pores. For such aim, concrete samples were dried up to 105°C for 72 hours, a duration that was established after carrying out many tests on samples with the same geometry and after verifying that all the free water was lost by weighting the samples. Secondly, the dehydration stage covers the heating from 105 to 300°C, in the case of CAC concretes. During this stage, the dehydration of CAC cement paste occurs and then the response of the cement is stable as is displayed in Table 3.6.



Figure 3.6: Thermal cycle and stages.

Figure 3.7 details the heating rates used for the dehydration and thermal fatigue stage. The first heating up to 550°C was made by following a rate of 1°C/min to reduce the risk of spalling. This risk is higher during the first heating of concrete due to the high thermal gradients between the external heated surface and the core of the element and the water pressures generated during the water vapour release. Once the material has been exposed to the maximum temperature and has undergone the chemical transformations, the risk of spalling is reduced. It is the reason why the following cycles can be made with a faster heating rate of 8°C/min. Finally, the thermal fatigue stage covers the subsequent heating and cooling cycles between 290-550°C, according to the minimum and maximum stable temperature of the Solar Salt [14, 15]. For evaluating the effect of the thermal fatigue in this study some samples were exposed to 1, 5, 10, 25 and 75 repetitive cycles. It is worth noting that the heating rates were selected to the geometry analysed to ensure that all the sample reaches the set temperature.

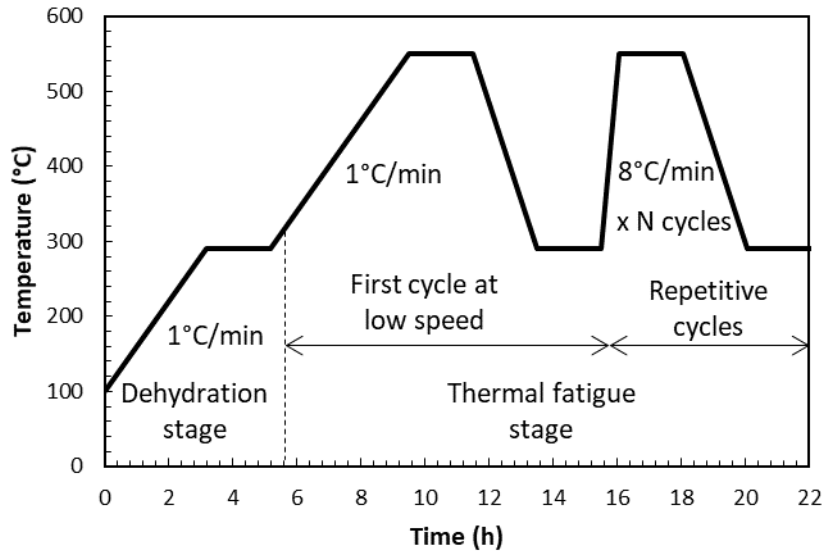


Figure 3.7: Detailed heating rates and repetitive cycles.

3.3.1.2. Materials and production of samples

Taking into account the operating regimes between 290-550°C mentioned above, a set of 5 concrete mixes were made with CAC cement due to its good refractory response at high temperatures [16]. The selection of the aggregates for the composition was made according to their thermal response evaluated through a characterisation.

The differences are related to the type of aggregates and their thermal response. Basalt aggregates from Pedrera Can Saboia (Spain) were used for their stable thermal response. Calcium aluminate aggregates called CAT are synthetic clinker aggregate based on CAC cement from Cement Molins (Spain). Finally, the waste slag came from São Domingos mine (Portugal) and it has high iron oxides content in its composition [17, 18]. Additionally, another composition was made with conventional siliceous aggregates to compare exclusively compressive strength and the micro-cracking analysis. Table 3.5 shows the aspect of both the sand and gravel aggregates used in the compositions.

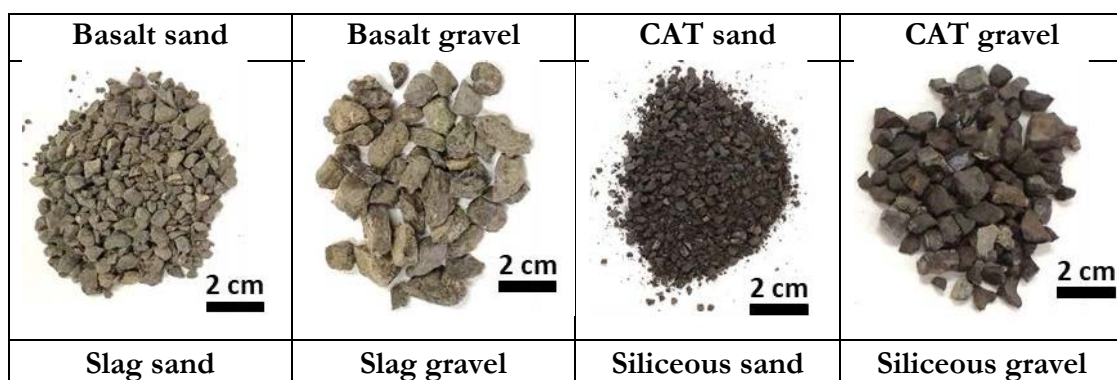
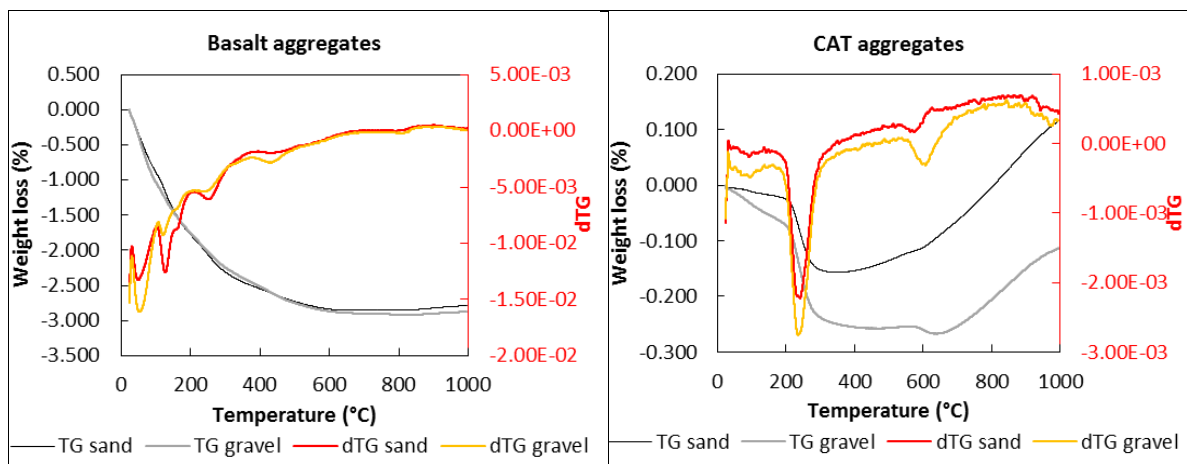




Table 3.5: Sand and gravel aggregates used in the compositions

The thermal response of the aggregates at high temperatures was tested through thermogravimetric analysis (ATD). This test analyses the weight loss of the component with the temperature and includes the temperature where the aggregates experience chemical transformations and changes in their components. The temperature at which those reactions take place identified by the differential thermogravimetric analysis (dTG). The test was determined in a TA Instrument, model TGA-DSC-DTA Q600 in powder samples.

Results of ATD and dTG of CAC cement and aggregates are displayed in Table 3.6. Basalt aggregates experience transformations up to 400°C with a weight loss of 3% which is stabilised at higher temperatures. CAT aggregates are more stable and present a variation of mass of 0.2% around 230°C. Their response is very similar to CAC cement with a peak of transformation at 230°C, which can be associated with the transformation of AH₃ [19]. Regarding the slag aggregates, they experienced transformations at 45°C, at 100°C, 230°C, 440°C, 610°C and at 770°C a significant and increasing weight loss for both sand and gravel, which are thought to be produced by the iron-silica compounds (at 230°C and 440°C) and because of the decomposition of calcite and carbonated phases at 670°C and 730°C [20, 21]. This process is especially significant after reaching 700-800°C, and the weight loss is more drastic in the case of the sand. However, for the application analysed in this thesis the waste slag loss a 4% up to 600°C.



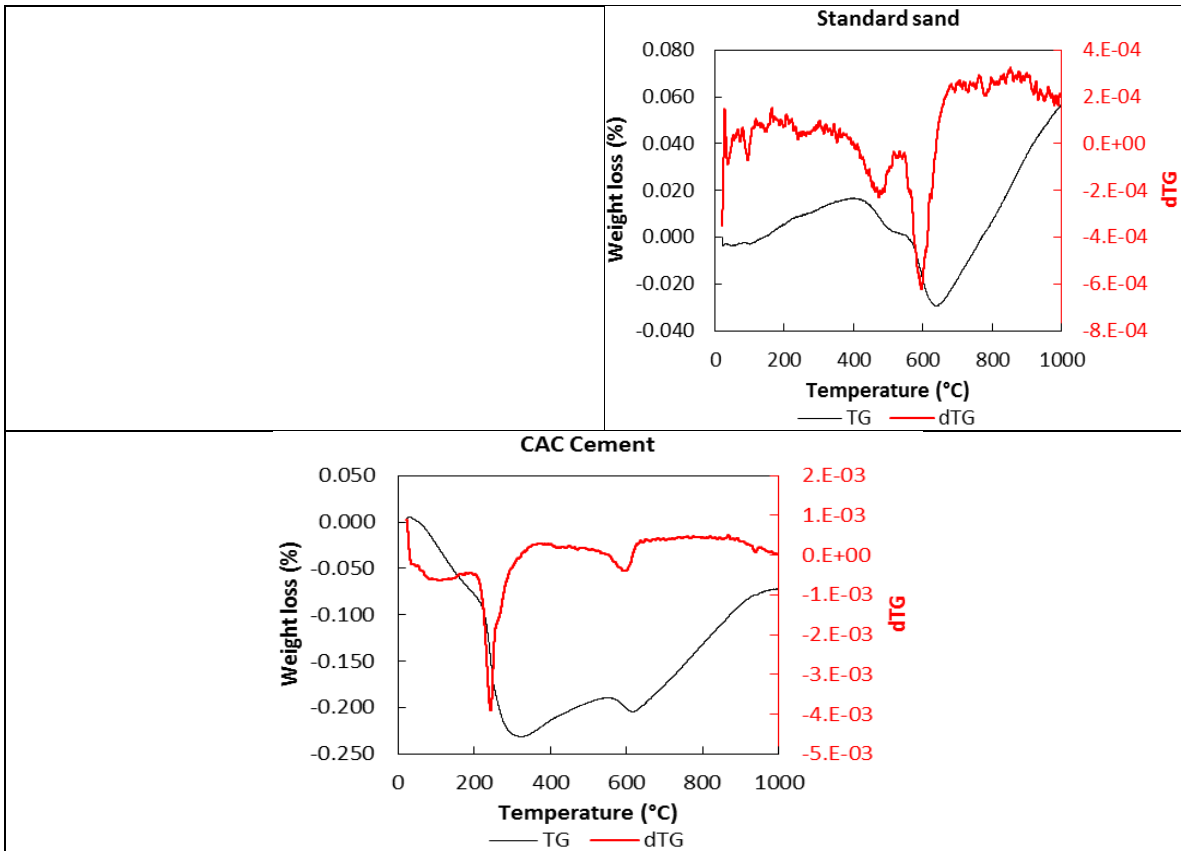


Table 3.6: TG/DTG analysed for basal sand and gravel, CAT sand and gravel, slag sand and gravel, siliceous sand and CAC cement.

Five concrete mixes were made using the aggregates mentioned above and CAC cement. The composition of the CAC cement used in this work is shown in Table 3.7. The concrete compositions analysed have the same volume of cement paste and aggregates to assure the comparability of results (Table 3.8). All of them have a water/cement (w/c) ratio of 0.43. The aggregates used in the five concrete compositions and the percentage of the type of aggregate vs the total volume of aggregates evaluated were: 1) a ternary mix combining basalt (43%), CAT (42%) and 15% of the waste slag named B-C-S15%, 2) binary mix combining basalt (49%) and CAT (51%) named B-C, 3) a mix containing 100% of CAT aggregates named C, 4) a ternary mix of basalt (35%), CAT (35%) and 30% of the slag, named B-C-S30% and 5) a 100% siliceous composition is also shown, but this concrete mix was only tested for comparing the compressive strength and the micro-cracking analysis. Polypropylene fibres (PPF) from Sika were added to all the concrete mixes to avoid the risk of spalling during the heating process at high temperatures. The fibres (diameter 18 µm, length 12 mm) melt at 165°C and vaporize at 350°C, creating voids within the cement paste and reducing the internal stresses produced for the steam evacuation at high temperatures [4, 22, 23].

| | Al_2O_3 | CaO | Fe_2O_3 | SiO_2 | MgO | Na_2O | K_2O | SO_3 |
|-----|-------------------------|--------------|-------------------------|----------------|--------------|-----------------------|----------------------|---------------|
| CAC | 40.3 | 37.43 | 15.2 | 4.4 | 0.47 | 0.16 | 0.14 | 0.06 |

Table 3.7: Composition of CAC cement (wt.%)

| | B-C-S 15% | B-C | C | B-C-S 30% | S |
|---|-------------|-------------|-------------|-------------|-------------|
| Cement CAC (kg/m ³) | 600 | 600 | 600 | 600 | 600 |
| Water (kg/m ³) | 258 | 258 | 258 | 258 | 258 |
| Gravel 1 - Siliceous 4-12 mm (kg/m ³) | 0 | 0 | 0 | 0 | 742 |
| Gravel 2 - Basalt 4-12.5 mm (kg/m ³) | 682 | 788 | 0 | 576 | 0 |
| Gravel 3 - CAT 3-10 mm (kg/m ³) | 0 | 0 | 885 | 0 | 0 |
| Gravel 4 - Slag 1-6.3 mm (kg/m ³) | 139 | 0 | 0 | 278 | 0 |
| Sand 1 - Siliceous 0-3 mm (kg/m ³) | 0 | 0 | 0 | 0 | 693 |
| Sand 2 - CAT 0.25-4 mm (kg/m ³) | 714 | 826 | 826 | 602 | 0 |
| Sand 3 - Slag 0.25-2 mm (kg/m ³) | 128 | 0 | 0 | 256 | 0 |
| Polypropylene fibres (kg/m ³) | 2 | 2 | 2 | 2 | 2 |
| Plasticizer Sikament 165 | 1 | 1 | 1 | 1 | 1 |
| <i>Water/cement (w/c)</i> | <i>0.43</i> | <i>0.43</i> | <i>0.43</i> | <i>0.43</i> | <i>0.43</i> |

Table 3.8: Concrete compositions

One concrete batch of 8 samples of each concrete composition was produced. Additionally, 4 extra samples of B-C-S15% were produced. The mixes were poured in cylindrical moulds of 75 mm of diameter and 150 mm of height and compacted using a compacting rod. To control the temperature in the core of the sample, one sample per concrete mix had a thermocouple K-type embedded in its geometric gravity centre with a distance to the external surface of 37.5 mm.

After preparing the mixes, all concrete samples were kept inside metallic moulds and covered with a plastic bag to avoid drying for 24 hours until hardening in a controlled temperature room at 20°C. After that, samples were demoulded and stored in a humidity chamber at 20°C and 95% of RH until the testing time for at least 7 days. After the curing stage, some specimens were cut in disks of around 20 mm of width and stored again in the humidity chamber until the testing time. The ageing of the samples before starting with the thermal exposure were: 9, 10, 8, 11 and 10 days for the type of concrete B-C-S15%, B-C, C, B-C-S30% and S, respectively.

3.3.1.3. Experimental setup for performing the high temperature tests

Due to the high number of samples to test (6 per concrete type and 10 for B-C-S15% mix), the performance was carried out in 4 furnaces, whose characteristics are detailed in Table 3.9. The drying process was performed exclusively in BINDER ED53 because its maximum operating temperature is 300°C. The dehydration and thermal fatigue cycles were performed in Thermolab Chamber furnace MLR11, SATER and Nabertherm N 20/H. The maximum temperature allowed in the three models are above 600°C and all of them have a controller able to do the heating process with a controlled heating rate. The differences among them are related to the cooling process, which can be controlled exclusively in Thermolab Chamber furnace MLR11. The cooling processes are natural draft in the furnaces SATER and Nabertherm N 20/H.

| Model | BINDER ED53 | Thermolab Chamber furnace MLR11 |
|---------------------------|---|--|
| Technical characteristics | Nominal temperature: 300°C Power: 1,2 kW Power supply: 230V 5.3A | Max. Temperature: 1100°C Power: 15 kW Power supply: 400V |
| Heating process | Drying process | Dehydration + Thermal fatigue stage |
| Photo |  |  |
| Model | SATER Horno eléctrico | Nabertherm N 20/H |
| Technical characteristics | Max. Temperature: 1150°C Power: 3 kW Power supply: 420V 13.6A | Max. Temperature: 1340°C Power: 6.5 kW Power supply: 400V 14A |
| Heating process | Dehydration + Thermal fatigue stage | Dehydration + Thermal fatigue stage |
| Photo |  |  |

Table 3.9: Furnaces and technical characteristics used in this study.

The furnaces Thermolab, SATER and Nabertherm present resistances in two lateral surfaces. Figure 3.8 shows the geometrical disposition of specimens inside the oven with their relative position to the electric resistances and the heat flow direction. This symmetrical disposition of specimens was decided to ensure that all the specimens experienced the same heat exposure. The central specimen, with the embedded thermocouple, controlled the temperature profile reached in the interior of the material. All temperature data were

recorded through a data acquisition system (Model: Agilent 349704A) directly by an external datalogger. This disposition was applied in the three furnaces and Figure 3.9 shows an example of the samples tested at SATER over.

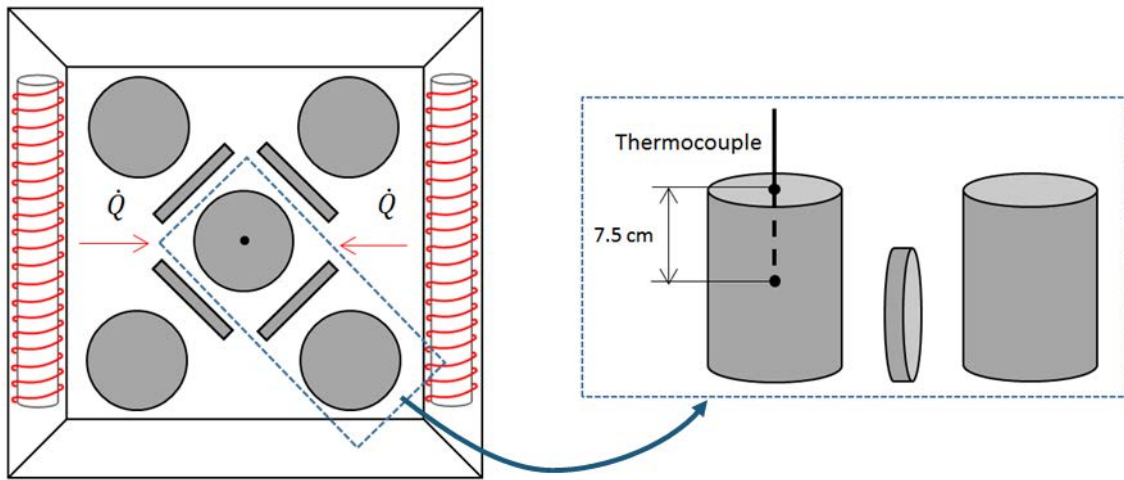


Figure 3.8. Position of the concrete cylinders and disks inside the oven (left) and detail (right).

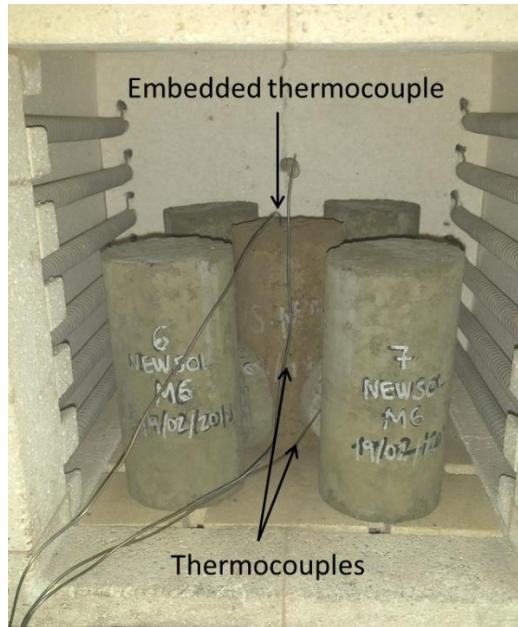


Figure 3.9: Experimental set-up in the SATER oven.

Samples were weighted before and after drying in an oven at 105°C for 72 hours. The weight measured after drying was selected as the reference for the weight loss after thermal cycles since the weight before drying will depend on the internal moisture content, which is a variable parameter that will vary with the exposure conditions. Figure 3.10 shows a photo of cylindrical and disks specimens drying in the oven. Enough space around all the samples was guaranteed to facilitate the evaporation.



Figure 3.10. Cylindrical samples and disks drying in the oven at 105°C.

Different mechanical, thermal and physicochemical tests were performed in this study and are summarised in Table 3.10. All the mixes were tested under 0, 1, 5 and 10 thermal cycles. Additionally, sample B-C-S15% was tested after 25 and 75 thermal cycles. During the thermal test, the evolution of the temperature in the geometric centre of the samples was recorded as well as the temperature of the furnaces by using K-type thermocouples. After the thermal cycles, the specimens were cooled down to room temperature inside the furnace without evacuating heat promptly, to avoid inducing high thermal gradients into the material. After that, the specimens were stored in a desiccator before the scheduled tests.

Compressive strength was tested following EN 12390-3:2009 in 2 cylinders of 150 mm of height for samples without thermal tests at 7 days and 28 days and after 1, 5 and 10 thermal cycles. Additionally, the samples exposed to 25 and 75 cycles for the B-C-S-15% were also tested. The mass was measured in both cylinders and disks specimens at initial conditions before the thermal test and after testing. Disks were used for measuring ultrasonic pulse velocity (UPV), porosity, microcracking analysis and electronic microscope (SEM) and X-ray diffraction (DRX). Table 3.10 summarises the tests performed and the geometry of the samples.

| Specimen | Test performed | Specimens tested |
|------------------------------------|---------------------------------------|---|
| Cylinder Φ 75 mm, H 150 mm | · Compressive strength · Mass loss | · 10/mix: 2 per thermal cycles: 0 (7d), 0(28d), 1, 5 and 10 +25, 75 cycles for a selected mix |
| Cylinder Φ 75 mm, H 150 mm | · Temperature inside the specimen | · 1/mix |
| Disk Φ 75 mm, H 20 mm | · Mass loss · UPV | · 8/mix: 2 per thermal cycles: 0, 1, 5 and 10 +25, 50 cycles for a selected mix |
| Disk Φ 75 mm, H 20 mm | · Microcracking | · 4/mix per thermal cycles: 0, 1, 5 and 10 +25, 75 cycles for a selected mix |
| Powder and sample with epoxy resin | · Porosity · SEM, DRX | · 2/mix: before/after cycles · 1/mix for a selected mix |

Table 3.10: Experimental campaign and specimens analysed in this study.

The devices employed for measuring the parameters are as follows. The temperature inside the concrete cylinders was recorded by a K-type thermocouple with an accuracy of $\pm 0.1^\circ\text{C}$. Additionally, the temperature of the furnaces was recorded with 2 thermocouples K-type with the same accuracy. The UPV was obtained by using a PUNDIT 7 CNSFARNELL with a nominal frequency of 54 kHz and a precision of $\pm 0.1 \mu\text{s}$. The measurements were made by using two p-wave transducers located in contact with the two parallel surfaces of the concrete disks. X-ray diffraction tests (DRX) were carried out on powder concrete with the equipment BRUKER AXS D8 Advance diffractometer with an RX Lynxeye super speed detector with Cu-K α radiation and a nickel filter. The samples were scanned from 5 to 45° at 20 angles with a step size of 0.02° and a counting time of 0.5 s/step.

According to the microstructure, it was investigated through SEM and it was performed using a Hitachi S-4800 scanning electron microscope in backscattered mode (BSEM). It was equipped with a BRUKER 5030 energy dispersive analyser under the following conditions: 20 kV accelerating voltages and a beam current of 20 μA . It was analysed with small concrete samples of around 20 mm embedded into an epoxy resin and polished before obtaining the images.

Regarding the microcracking analysis, an optical microscope Nikon SMZ-2T with a camera was used for taking the pictures at the centre of the disk on the parallel surfaces. After an initial study, it was decided to use two different zooms to evaluate the cracks and micro-cracks: a) one covering an area of $14.43 \text{ mm} \times 11.25 \text{ mm}$ for the definition of the pattern and crack area, and b) another covering an area of $4.81 \text{ mm} \times 3.75 \text{ mm}$ for a better measure of the crack width. In all the pictures, the red point indicates the position of that geometric centre. The number of pictures analysed was two pictures per sample for all the mixes and after 1, 5 and 10 thermal cycles to quantify the thermal fatigue effect in cracking. The software used for the analysis of the pictures is the open software GIMP®. With this software several parameters have been determined: the percentage of cracks and micro-cracks in a certain area and to examine the topography of cracks.

3.3.1.4. Safety measures

The equipments mentioned above were located in a laboratory dedicated exclusively to high temperature tests. For that reason, the laboratory is prepared with some safety measures and the people who work in the lab have different personal protective equipments (PPE). The laboratory has an air extractor fan and an air conditioner to evacuate the air heated in the room and reduce the temperature of the lab. Both equipments were operating when at least one oven was working.

Regarding the PPE, all laboratory workers should work with a lab coat and for high temperature tests they have to wear additional items. Refractory gloves and an apron for protection when they are placing heated samples in the oven. Those items protect from temperatures up to 500°C and follow the standards EN 388 3X3X and EN 407 44XXXX for the gloves and UNE-EN ISO 11612:15 for the apron. Additionally, if the temperature is higher than 100°C , people should wear a protective screen (SCOTT Safety IV 950TC SS 1 F39 HEAT) and safety boots.

3.3.2. Results of the durability of High Thermal Performance Concrete under thermal cyclic operation and suitability for CSP infrastructures

3.3.2.1. Evolution of mechanical properties

Mass variation

Regarding the mass variation (Figure 3.11) the first drop was produced after de drying process, reaching between 3 and 4% of weight variation for all concrete mixes due to the evacuation of the internal humidity and free water loss. After being exposed to 1, 5 and 10 thermal cycles, all mixes show similar losses, with slightly lower values of losses for the ternary mixes and the one with only CAT aggregates. The results for all compositions show that the biggest loss is produced during the dehydration of the cement paste and after the first heating up to 550°C, reaching values of mass losses that are stabilized for the performance up to 10 thermal fatigue cycles. The weight variation was also stabilized after a long-term performance of 75 thermal cycles for the B-C-S15%, as is shown in Figure 3.12.

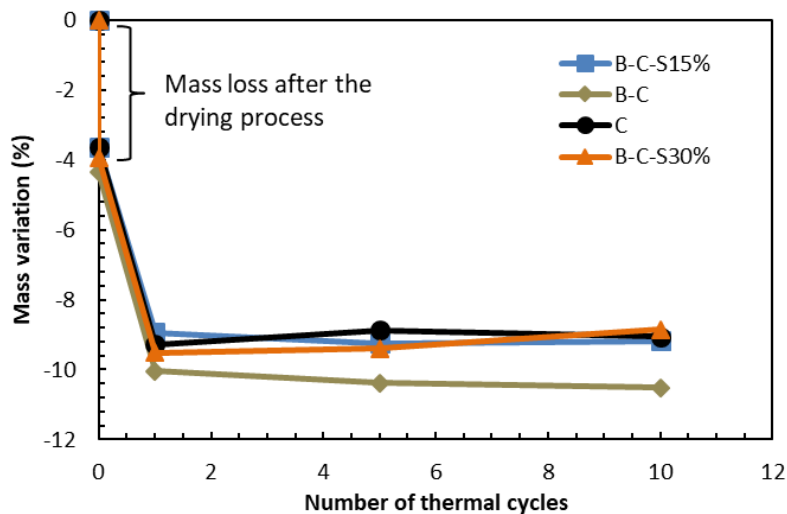


Figure 3.11: Mean value of mass variation after thermal cycles.

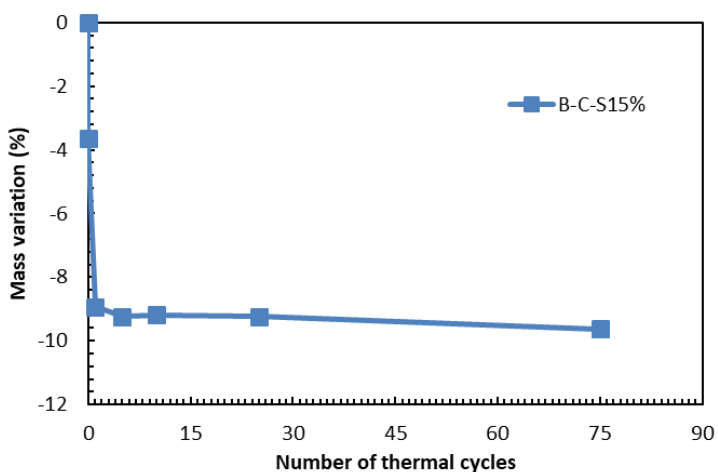


Figure 3.12: Mean value of mass variation at long-term for B-C-S15%.

Compressive strength

Before thermal exposure

Figure 3.13 shows the results of compressive strength at 7 and 28 days for the different mixes, showing that the best result in terms of strength was composition C with only CAT aggregates, achieving 66 MPa. Nevertheless, all of the mixes presented similar results among them and might be used. The differences found between 7 and 28 days are slightly, and this is because concrete made with CAC cement reaches almost all the resistance during the first 7 days [1].

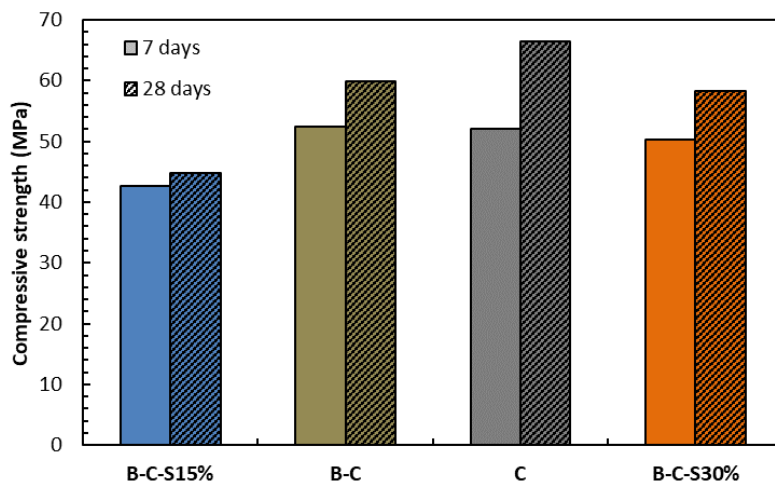


Figure 3.13: Compressive strength mean values at 7 and 28 days.

After thermal exposure

A severe strength loss was produced after the first cycle, and slight or non-detectable decreases were produced during the cycles (Figure 3.14). The mixes that maintain the highest percentage of the initial strength are ternary mixes with Basalt, CAT, and the waste slag (B-C-S15% and Basalt-CAT-Slag 30%). The inclusion of the slag aggregate led to a slight improvement in the thermal fatigue stage. The compressive strength of the ternary mixes after 10 thermal cycles was around 20 MPa, while the other mixes did not reach 20 MPa after the cycles.

John et al. [2] reported residual strength values after performing thermal cycles between 300 and 600°C of around 30% of the initial strength. Their study used siliceous, calcareous, and syenite aggregates. Those results are consistent compared with the siliceous aggregates used in this work. In this study, the mixes with basalt and CAT, only CAT aggregates, and especially, the ternary mixes, showed better retention of the mechanical properties, demonstrating their better thermal stability.

The B-C-S15% mix was selected to verify its long-term stability in terms of strength losses. The residual values of the compressive strength of the selected mix reached 17.15 MPa after 25 cycles and 14.9 MPa after 75 cycles. Thus, a decrease of around 5% of compressive strength took place between the tenth and the 75th cycles.

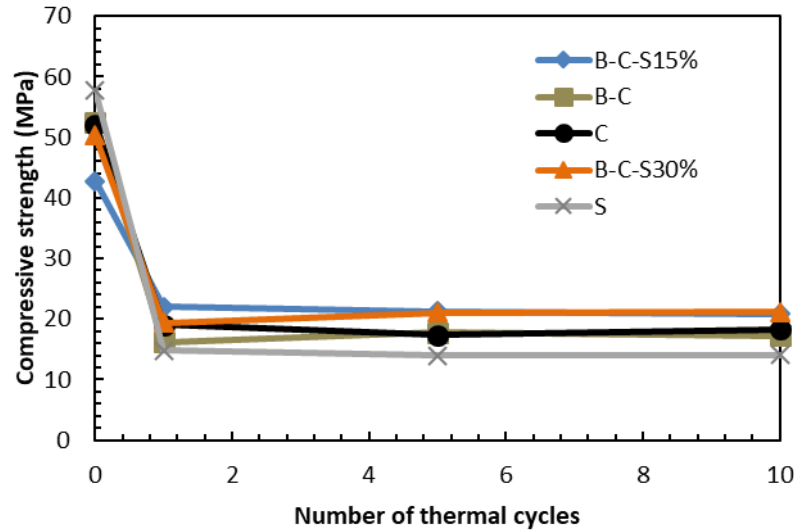


Figure 3.14: Compressive strength after 1, 5 and 10 thermal cycles.

Thermo-mechanical stability and long-term performance

For the five concrete types studied in this work, the regression curve between compressive strength and the number of thermal cycles was calculated. Good fittings ($R^2 > 0.90$) were obtained following potential and logarithmic curves. The potential regression equations obtained through this method were used to estimate an extrapolation of the compressive strength to the long term, as is shown in Figure 3.15. Considering that at the TES system each solar day implies one thermal cycle, after five years in service (1825 cycles), concrete strength is estimated to be 6.5 MPa in the lowest case (siliceous aggregates mix) and 12.55 MPa in the B-C-S15% mix. Similarly, after 25 years (9125 cycles), concrete strength is estimated as 5.25 MPa in the siliceous aggregates mix, and 11 MPa in the B-C-S15% mix. The results for the five mixes are displayed in Figure 3.15. Comparing these values with the literature, another previous study made with CAC concretes exposed to 75 thermal cycles between 290-550°C obtained a compressive strength of 10 MPa [1]. Another experiment with CAC concrete exposed to 30 thermal cycles between 300-600°C obtained compressive strength values between 9-12 MPa [2]. One study reported an experimental compressive strength after being exposed to 2250 thermal cycles (lifetime of six years) of 15 MPa [3]. All these results are consistent with the results of the five mixes analyzed in this study.

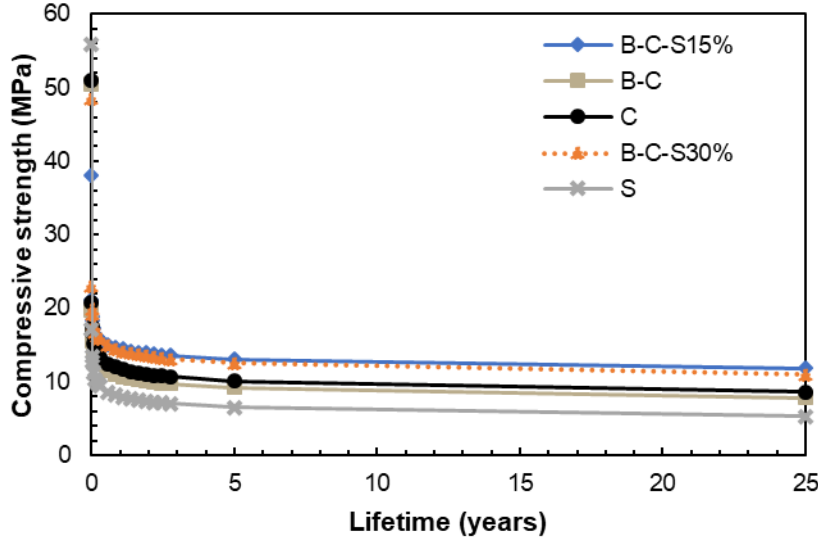


Figure 3.15: Evolution of the compressive strength estimated through the experimental results of this work, considering daily thermal cycles.

Elastic Modulus

The Elastic Modulus or Young Modulus is calculated from the velocity measured through the UPV. The evolution of velocity experienced for the different concrete compositions after being exposed to thermal cycles is shown in Figure 3.16-left. The biggest reduction in the parameter was experienced after the drying process for all of the mixes. The composition B-C-S30% experienced the highest decay after the drying stage (24% of its value) affecting negatively the performance of the thermal cycles. On the contrary, composition with only CAT aggregates (C) performs better with the thermal cycles, presenting a lower reduction in the parameter in comparison to the value before being tested (15% after drying process). The Elastic Modulus can be calculated from the following expression obtained by [24]:

$$E = \rho \cdot v^2 \cdot \frac{(1 + \mu) \cdot (1 - 2\mu)}{(1 - \mu)} \quad (1)$$

where:

E is the Elastic Modulus [MPa]

P is the density of the concrete mix [kg/m^3]

v is the velocity measured with ultrasounds [km/s]

μ is the Poisson coefficient [-]

Assuming $\mu = 0.2$ for concrete with a density equal to $2400 \text{ kg}/\text{m}^3$ the Elastic Modulus is obtained and the evolution after being exposed to thermal fatigue cycles is showed in Figure 3.16-right for the compositions up to 10 cycles and in Figure 3.17 for B-C-S15% after the long-term performance at 25 and 50 successive heating and cooling cycles. Once again the stabilization of mechanical properties after the first thermal cycle is proved.

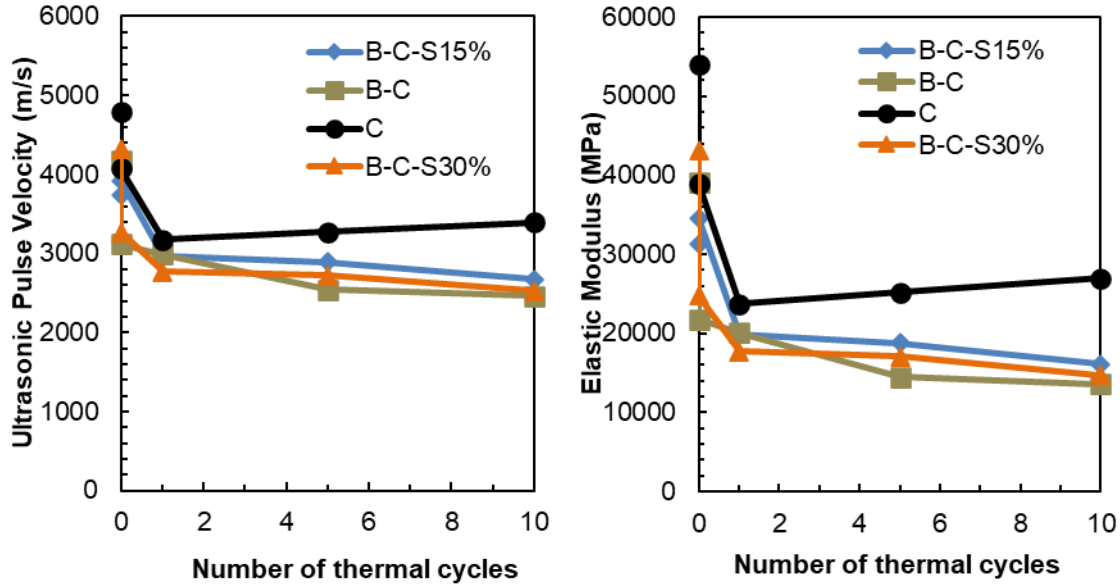


Figure 3.16: Evolution of UPV (left) and Elastic Modulus of concrete samples after thermal cycles.

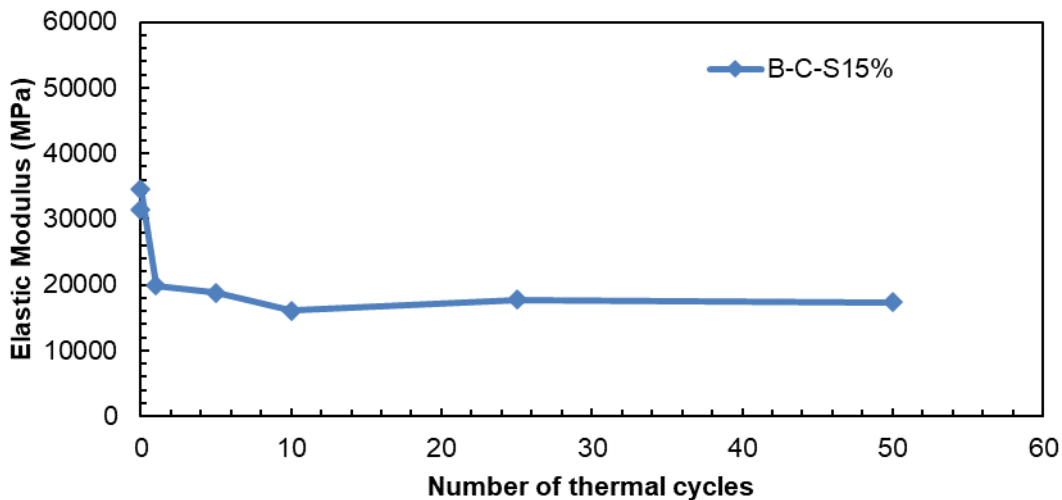


Figure 3.17: Evolution of Elastic Modulus for the B-C-S15% composition at long-term performance.

3.3.2.2. Micro-cracking analysis

The evolution of microcracks within the material is of interest because the creation of air gaps might affect negatively heat transfer. When a material is heated, the mechanism of heat transfer inside it is conduction. Nevertheless, if the material presents air gaps and cracks of considerable size, the convection mechanism of heat transfer will play another role. If those microcracks were high enough heat conduction would be affected and, hence, applications of thermal energy storage as well.

Micro-cracks mappings after different thermal cycles

For this analysis, the photos were taken at the centre of all of the samples and the micro-cracking mappings were obtained by using the open software GIMP®. Figure 3.18-left shows a screenshot of the software during the procurement process of the microcracking pattern for the composition B-C-S15% after being exposed to the first heating and cooling

cycle. On the right appears the real picture of the same concrete specimen with the mapping coloured in red.

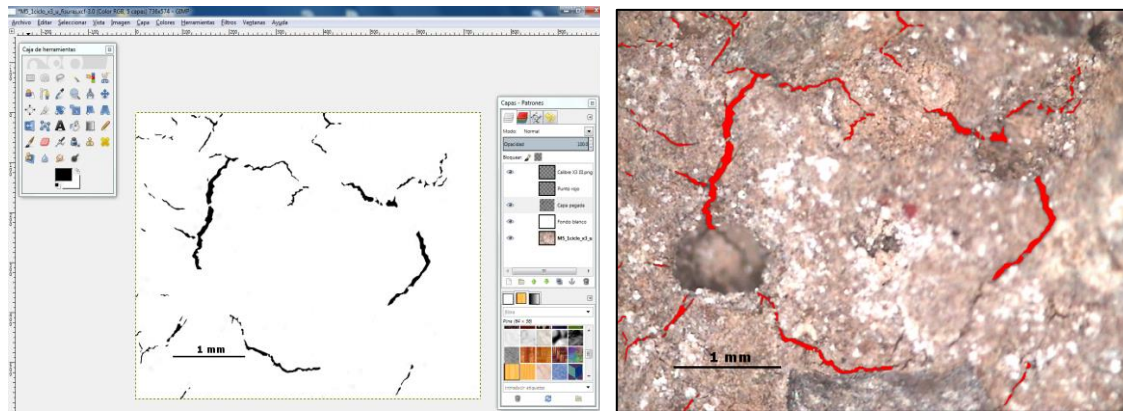


Figure 3.18: Procurement process of the crack mapping with software GIMP® (left) and real picture with coloured pattern (right) of composition B-C-S15% after being exposed to 1 thermal cycle.

The mappings of the microcracks found after 1, 5 and 10 cycles are collected in Table 3.11, Table 3.12, Table 3.13, Table 3.14 and Table 3.15 for the compositions B-C-S15%, B-C, C, B-C-S30% and S, respectively. Additionally, the evolution of cracks on the long-term performance was studied through the microcracking pattern of the ternary composition with 15% of the content of waste slag, and its mappings are shown in Table 3.11.

| Composition B-C-S15% | | |
|----------------------|---------|-----------------------|
| N cycles | Picture | Micro-cracks mappings |
| N=1 | | |
| N=5 | | |

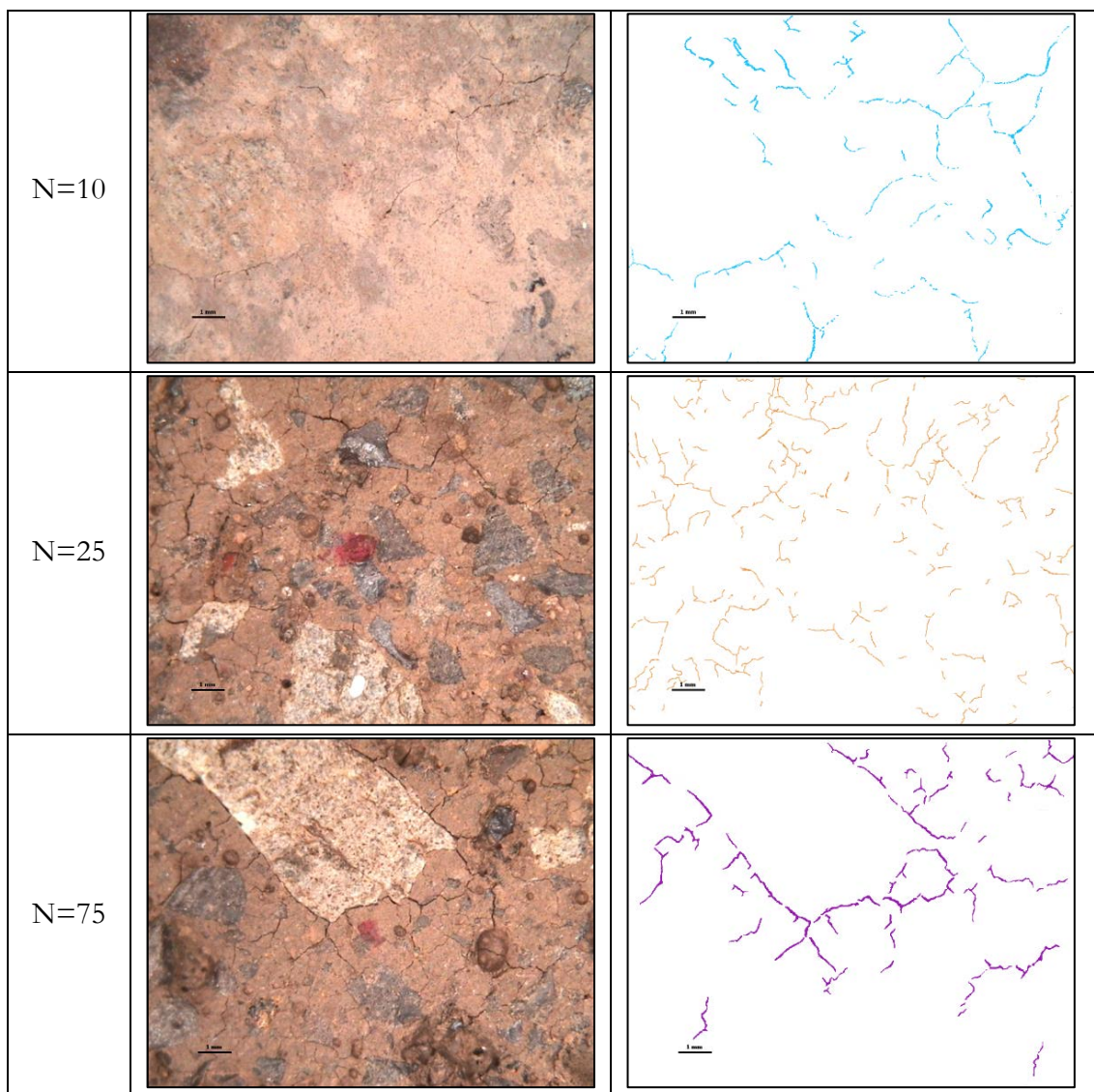
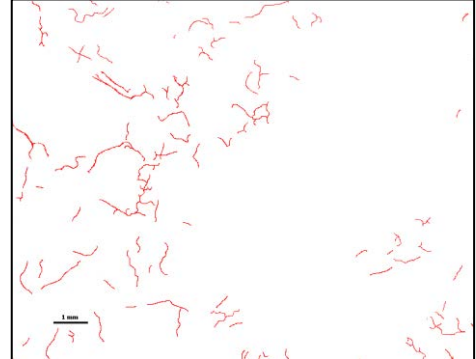


Table 3.11: Crack mappings of B-C-S15% in the centre of the samples after 1, 5, 10, 25 and 75 thermal cycles.

| Composition B-C | | |
|-----------------|---|--|
| N cycles | Picture | Micro-cracks mappings |
| N=1 |  |  |

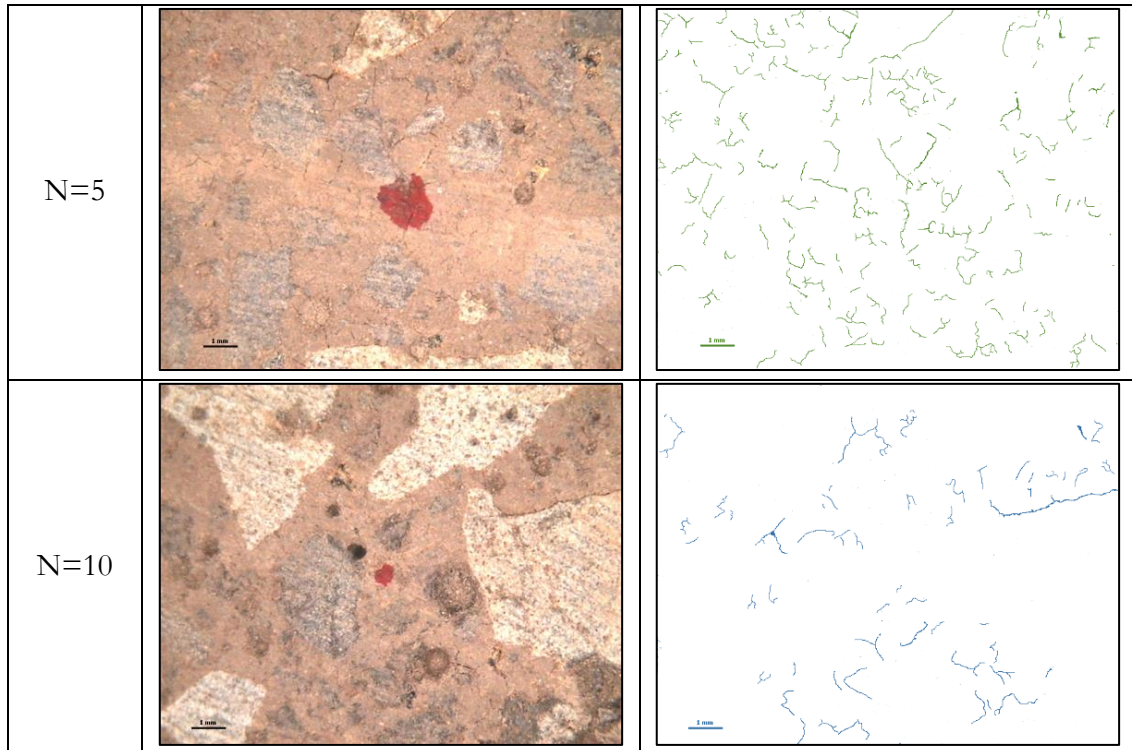
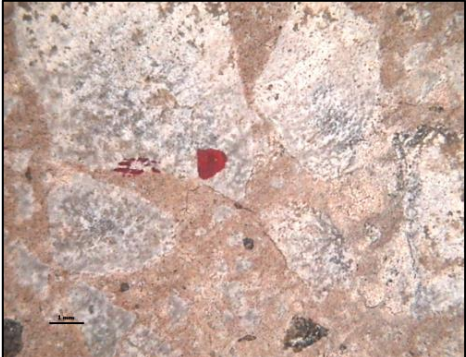
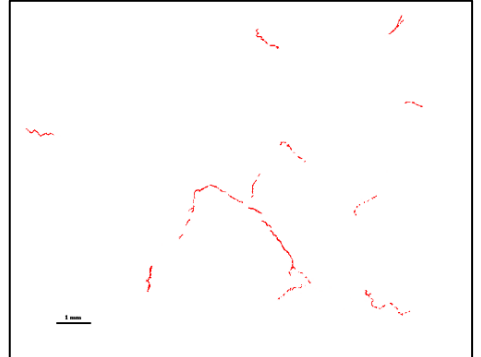
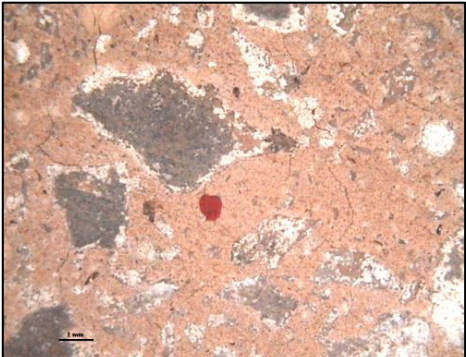
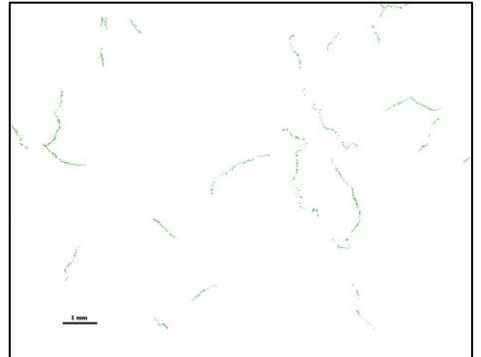


Table 3.12: Crack mappings of B-C in the centre of the samples after 1, 5, 10, 25 and 75 thermal cycles.

| Composition C | | |
|---------------|---|--|
| N cycles | Picture | Micro-cracks mappings |
| N=1 |  |  |
| N=5 |  |  |

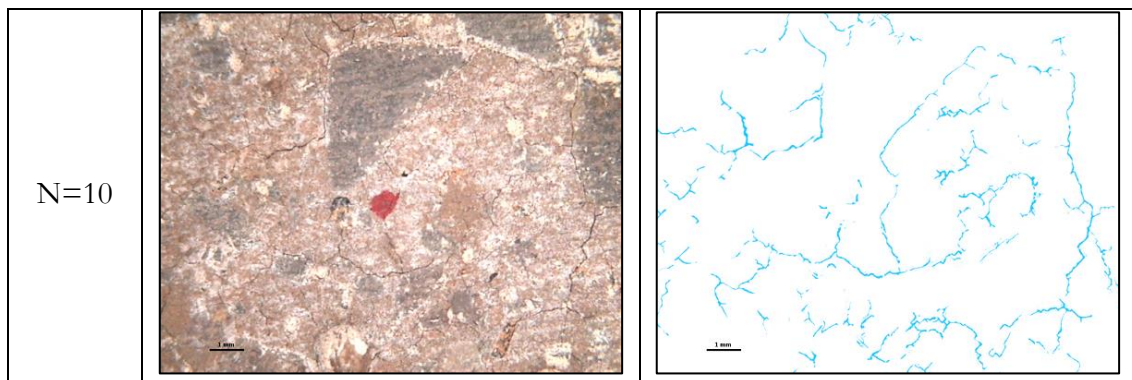


Table 3.13: Crack mappings of C in the centre of the samples after 1, 5 and 10 thermal cycles.

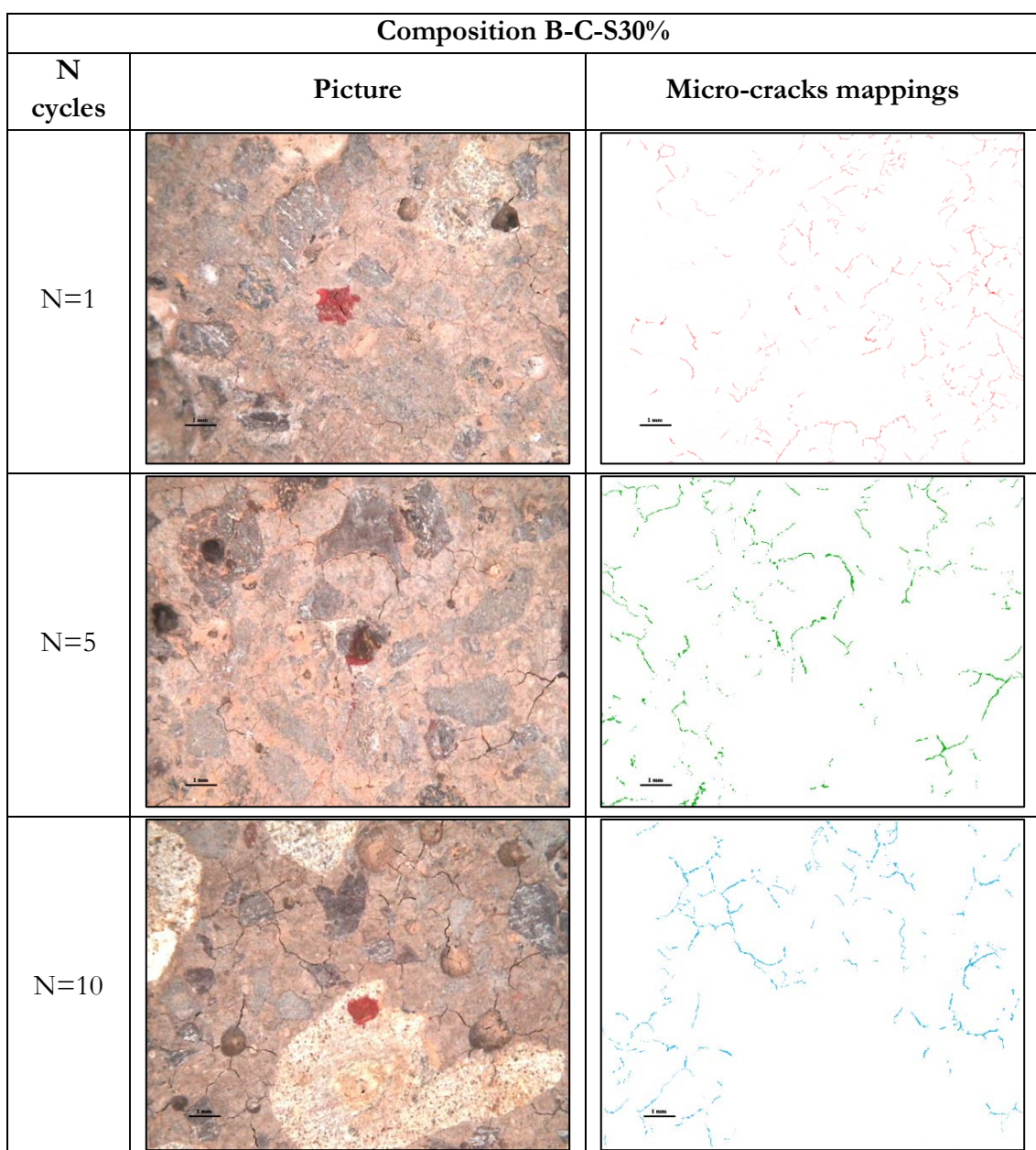


Table 3.14: Crack mappings of B-C-S30% in the centre of the samples after 1, 5 and 10 thermal cycles.

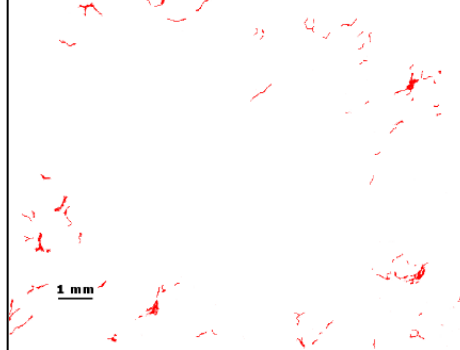
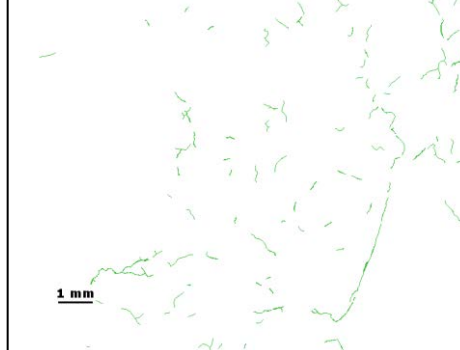
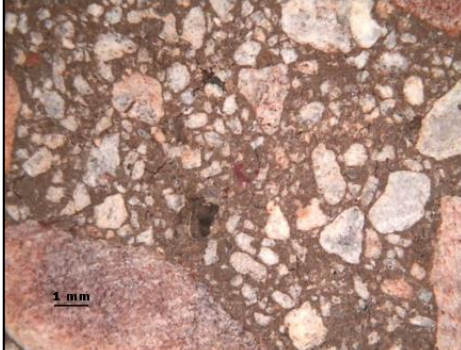
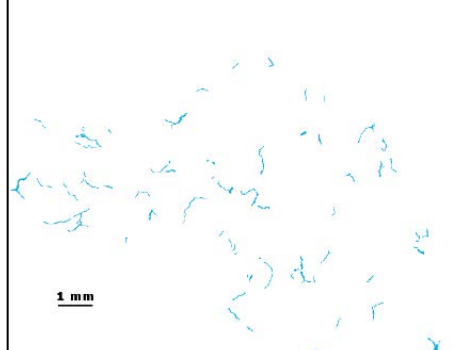
| Composition S | | |
|---------------|---|--|
| N cycles | Picture | Micro-cracks mappings |
| N=1 |  |  |
| N=5 |  |  |
| N=10 |  |  |

Table 3.15: Crack mappings of S in the centre of the samples after 1, 5 and 10 thermal cycles.

Based on the mappings shown above, a qualitative analysis can be made according to the shape of those cracks. In general terms, there are two types of cracks. While the first ones border the aggregates, the second ones are normal to them and their presence are more significant. The aggregates that present more cracks around them are basalt (the clear one) and the slag aggregate that can be appreciated because it shines and reflects the light. Those aggregates are more expansive than CAT aggregates and, thus, they have more cracks in regions closer to them. Basalt is the coarse aggregate and despite presenting low thermal expansion its bigger dimension produces cracks when it is changing its volume due to expansions while heating. On the contrary, the waste slag aggregate produces more cracking despite having a lower dimension. Indeed, it can be observed in the crack pattern of the ternary mix with more content of slag, composition B-C-S30% on Table 3.14.

Additionally, some pictures show pores and the cracks generated perpendicular to them: B-C-S15% (N=1, 25, 75), B-C (N=10), B-C-S30% (N=1, 5, 10) and S (N=10). The

pores are the locations where water and steam were evacuated during the heating. This process produced cracks, whose characteristics are similar to the ones produced by the expansion of aggregates.

Figure 3.19 shows the micro-cracks mappings performed for two of the analysed mixes, showing the random cracking pattern produced in the geometric centre of the concrete sample. The colours code is: **red** after 1 thermal cycle, **green** after 5 thermal cycles and **blue** after 10 thermal cycles. Furthermore, it is demonstrated that the area covered by the cracks is maintained similar when increasing the number of cycles for B-C-S15% while for C the area is increased with the number of cycles. It should be noted here that the samples used for each picture are different, and then, the natural dispersion of concrete produces different results in the cracking trends, due to the specific distribution of components in that area.

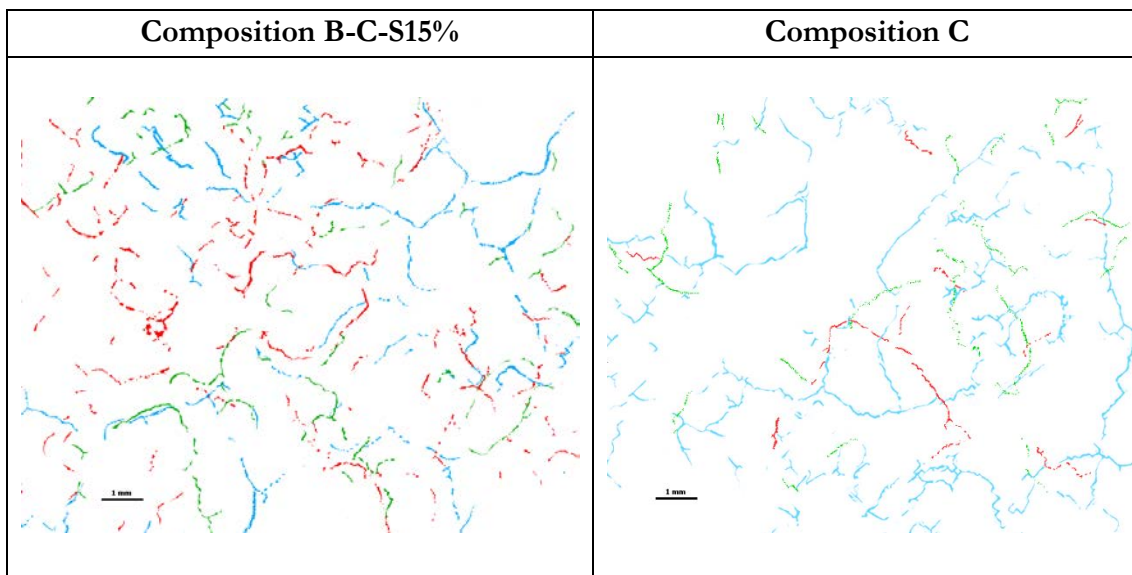


Figure 3.19: Comparison of micro-cracks mapping for B-C-S15% (left) and C (right).

Figure 3.20 shows the micro-cracks mappings for the short-term up to 10 thermal cycles (left) and for the long-term up to 75 thermal cycles (right). Both of them represent the ternary composition B-C-S15%. The colours code is in the left picture: **red** after 1 thermal cycle, **green** after 5 thermal cycles and **blue** after 10 thermal cycles, and in the right picture **orange** after 25 cycles and **purple** after 75 cycles.

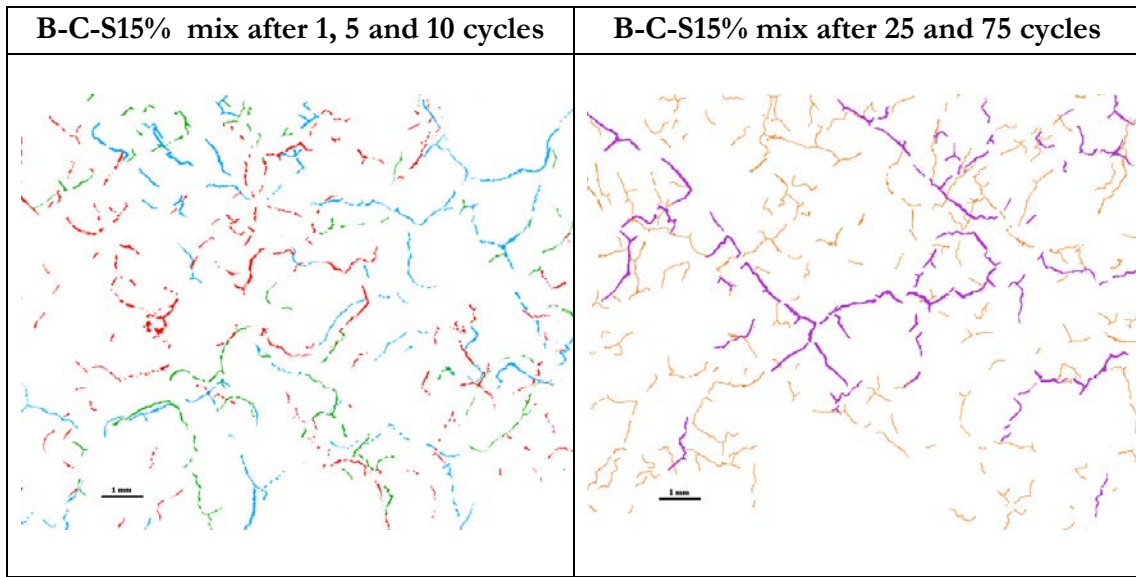


Figure 3.20: Comparison of micro-cracks mapping for B-C-S15% after 1 to 10 thermal cycles (left) and after 25-75 thermal cycles (right).

Regarding the quantification of the cracking, two parameters were chosen as the main factors that affect the durability of concrete: percentage of cracks obtained through the same area of a picture and the crack width.

The area covered by cracks in the centre of the sample has also been evaluated. The image of the central area covers 162.42 mm². The quantity of cracks has been expressed in the percentage of the area of the image. Figure 3.21-left shows the area covered by cracks for all of the compositions analysed with the number of cycles. The results show that all of the mixes experienced the area covered by cracks, which are maintained below 2.5% of the area of the image, with almost no variation when increasing the number of cycles. The percentage of microcracks obtained was below 1.10% in all cases. For the long-term performance, a stabilization of cracks with a percentage below 2% for B-C-S15% after being exposed to 75 cycles was detected (Figure 3.21-right). It should be noted here that the specimens used for each picture are different, and then, the natural dispersion of the components in concrete produces different results in the cracking trends. Results found in the literature for concrete with calcareous, silicon, and silico-calcareous aggregates showed higher values of percentage of microcracks in the area for the silico-calcareous (5.44%) and siliceous mixes (1.56%) after heating at 600°C [25]. Conversely, the calcareous mix had a 0.9% of microcracks, which is a similar value to those obtained in this study.

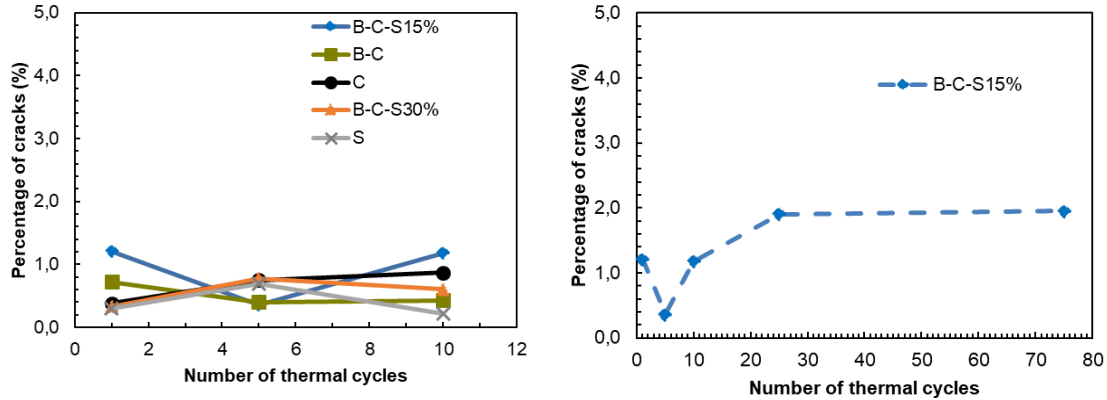


Figure 3.21: Crack area variation of the four concrete mixes after 1, 6, and 10 cycles, measured in % of an area of 162.42 mm^2 .

In addition, cracks were analyzed at different distances between the border and the centre of the cylindrical specimen (Figure 3.22). These photos seem to indicate that the crack area is higher in the central point; however, the evaluation of the crack area indicates that the percentage of cracks is almost the same independently of the position analysed (below 2%).

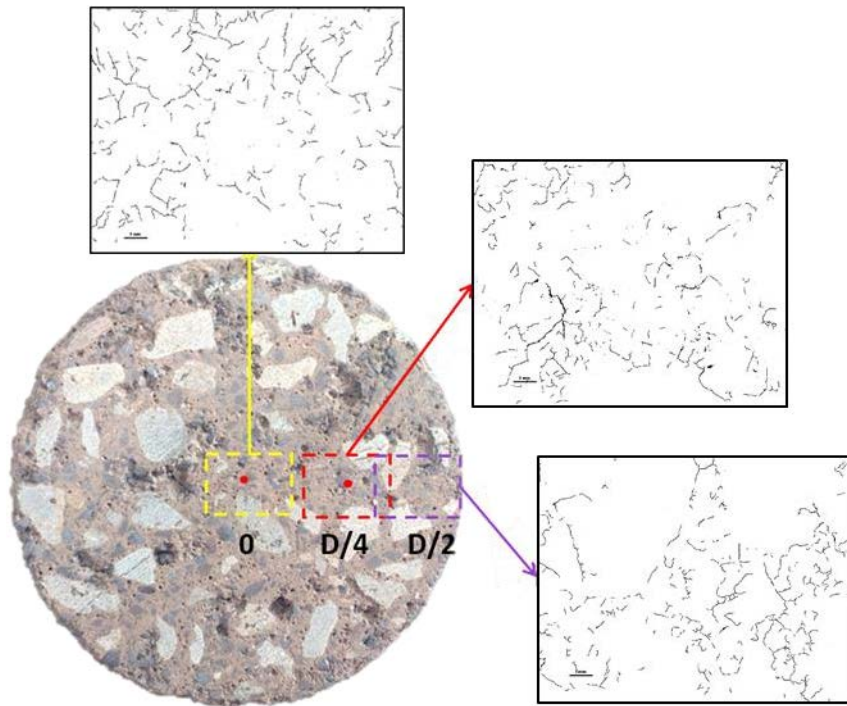


Figure 3.22: Pictures taken at different locations of the cylindrical specimen.

The maximum crack width was also quantified, and it is shown in Figure 3.23. The colours code is: red after 1 thermal cycle, green after 5 thermal cycles, blue after 10 thermal cycles, orange after 25 thermal cycles and purple after 75 thermal cycles. In all cases, the maximum crack widths remained under 0.08 mm, and generally below 0.05 mm, which are usual crack sizes for service conditions in concrete. The ternary mixes had a wider maximum crack width (0.08 mm), especially the mix with 15% of São Domingos Slag. The mixes with the narrower maximum crack width were B-C and C mixes, with maximum crack sizes below 0.025 mm and stabilized behaviour after the fatigue cycles.

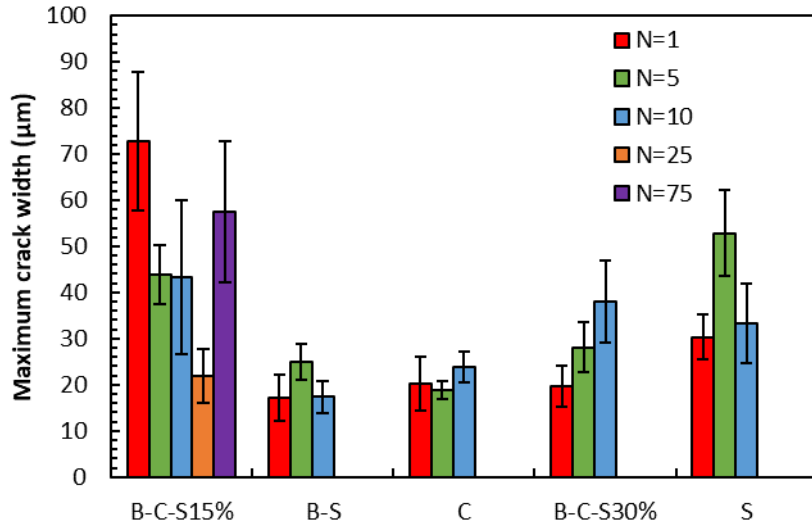


Figure 3.23: Maximum width cracks for B-C-S15%, B-S, C, B-C-S30% and S after thermal cycles.

Having said the above-mentioned analysis, it is worth noting that the pictures were taken at samples at residual condition once they had been cooled down to room temperature after the thermal test. As the behaviour of aggregates while heating is expansive whereas that of cement paste is shrinkage, at high temperature those cracks widths are supposed to be narrowed [26]. That is the reason why the microcracking might not be affecting the mechanisms of heat transfer at high temperature. Nevertheless, **Chapter 4** will prove this hypothesis by evaluating the thermal conductivity parameter at high temperatures up to 600°C.

Microstructure after thermal fatigue

Cracks were detected concentrated in the aggregates' interface, caused by the expansion of the aggregates and shrinkage of the paste at high temperatures. Figure 3.24 shows the cracks in the boundaries between the paste and the three types of aggregates after 5 thermal cycles obtained by electronic microscopy, as well as a general view with aggregates and cement paste. Cracks of constant size around 2 μm were detected around basalt aggregates, which is the largest size of aggregate used in this work. CAT aggregates had very distributed and thin cracks in their boundary. Slag aggregates also exhibited thin cracks in their boundary, but they were wider than the cracks produced around CAT aggregates. The composition of the cement paste was analyzed in terms of oxide content at several points and showed no significant differences with the paste before the thermal cycles.

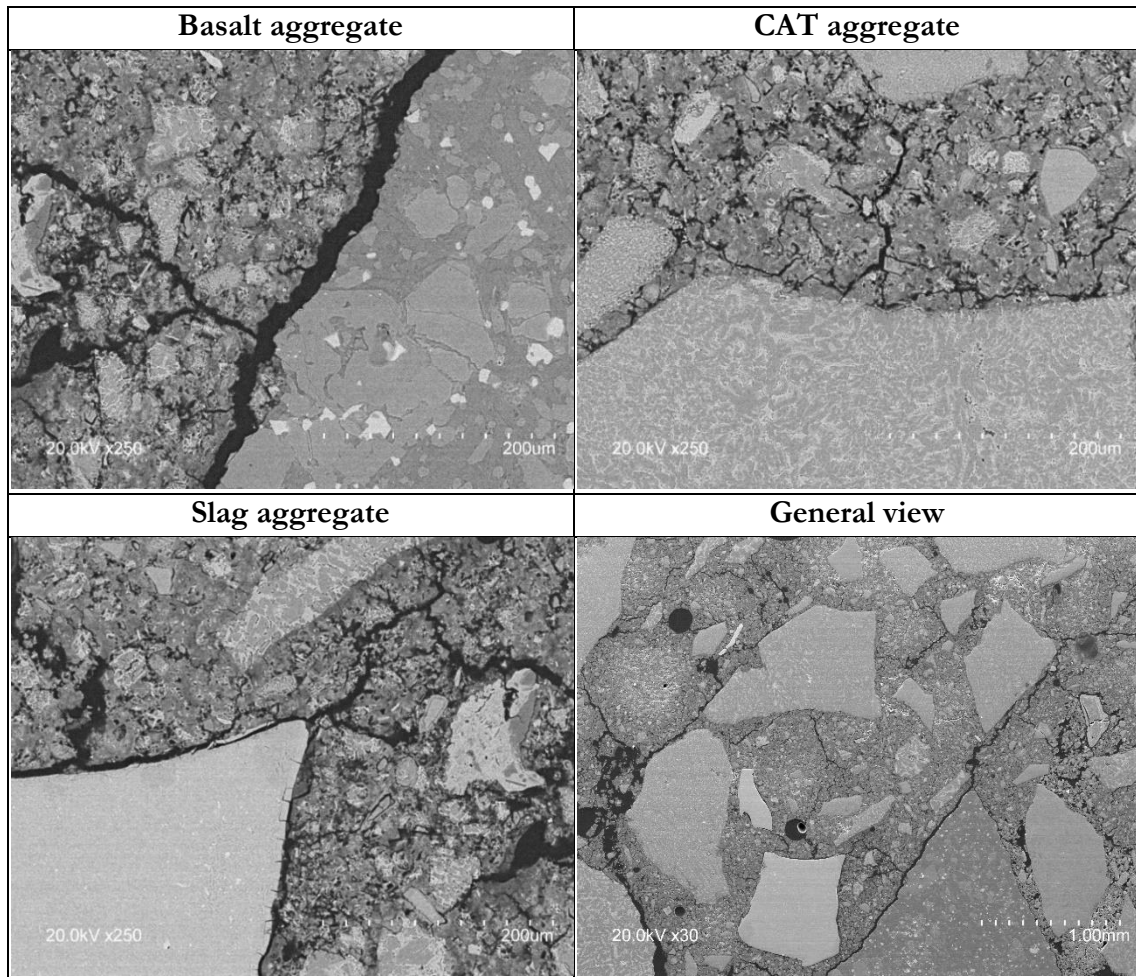


Figure 3.24: Cracks produced in the interfaces between the cement paste and the three aggregates after thermal cycles.

3.3.2.3. Physico-chemical performance

Mercury Intrusion Porosimetry (MIP)

Mercury Intrusion Porosimetry (MIP) tests were used to characterize the pore size distribution of all the concrete mixes, before and after thermal cycling. The results are displayed in Figure 3.25 before thermal cycles and after 1 and 10 cycles. Before the thermal cycles, most of the pores are capillary pores, with sizes around 1.6-2 μm (C, B-C-S15%, and B-C-S30%), while B-C has a slightly finer pore distribution (pores around 0.7 μm). Three mixes have a secondary peak of porosity produced in the range of 10-25 μm , associated with micropores. Conversely, C mix (only with CAT aggregates) showed no initial pores in that secondary region.

After thermal cycling, a new peak of porosity in the range of 24-27 μm size was found in all the concrete mixes, including the C mix. This range can be related to the presence of cracks (the size of the cracks from the image analyses ranges from 10 to 70 μm) and the vaporization of the polypropylene fibres (12 mm length and 18 μm diameter), as reported in the literature [4, 26].

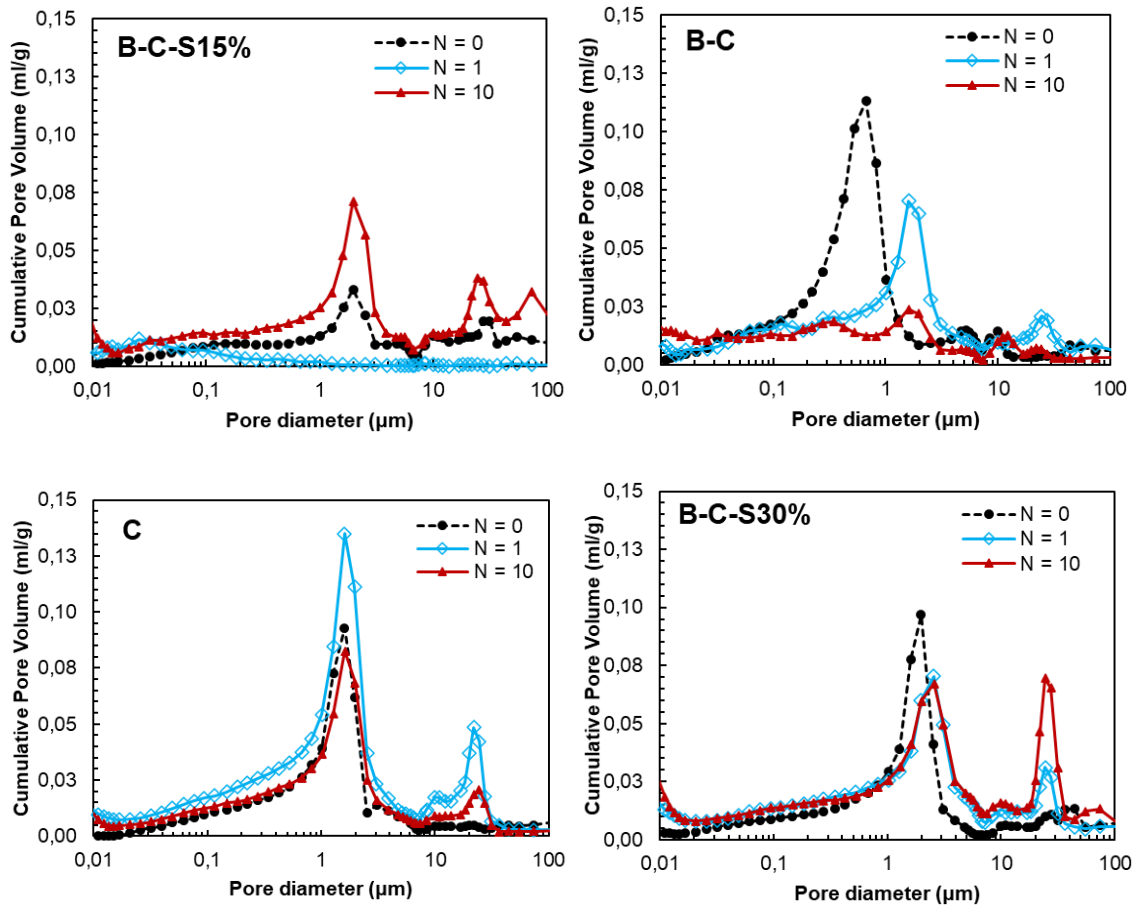


Figure 3.25: Pore size distribution for the four concrete mixes before and after thermal cycling.

X-Ray Diffraction (DRX)

X-ray diffraction performed on B-C-S15% concrete samples before thermal cycles but after drying at 105°C and, after 50 thermal cycles (Figure 3.26) show the presence of several phases, associated with the hydrated compounds (C_2AH_6 , CAH_{10} and AH_3), which disappear after the thermal cycles. The remaining phases are related with the spectra of unhydrated calcium aluminate (CA and C_{12}A_7), produced by both the unhydrated cement and the CAT aggregates, but also quartz originated in the basalt aggregates, which are rich in silicon, and calcite, which can be formed due to the calcium-rich cement paste. Other compounds that were identified in the Slag aggregate such as fayalite, petedunnite or maghemite could be influencing these spectra.

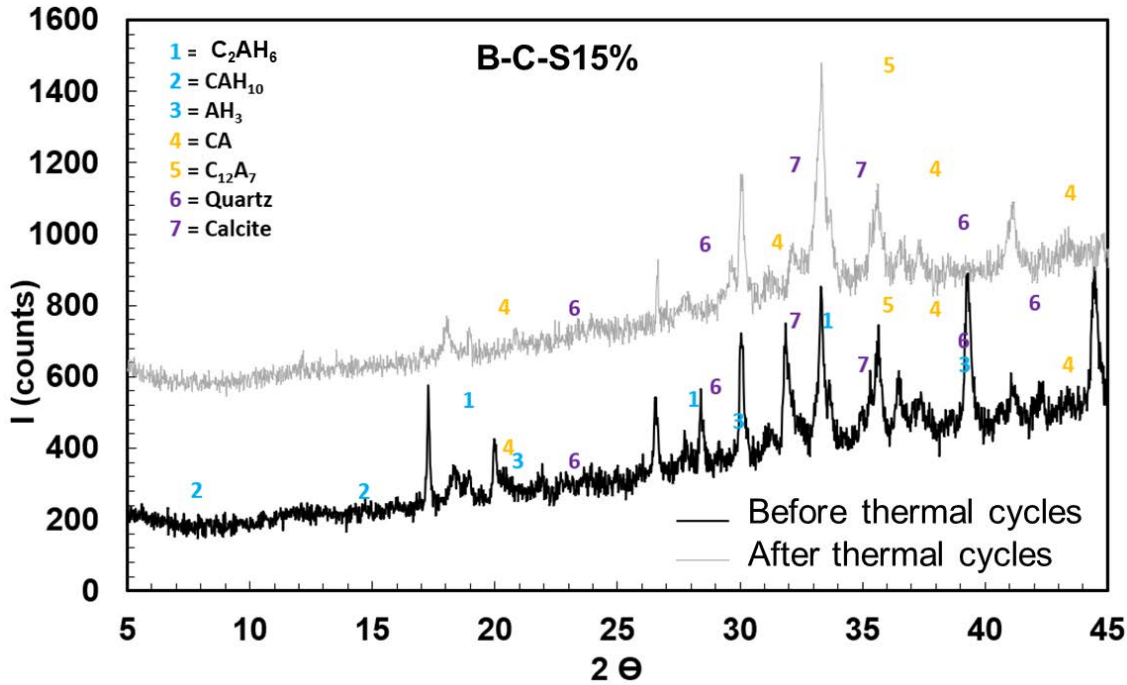


Figure 3.26: X-ray diffraction results of B-C-S15% mix before and after the thermal cycles.

Concrete ATD/dTG before and after thermal cycles of the selected concrete

A thermogravimetric analysis (ATD) of concrete samples before and after suffering thermal cycles, including differential thermogravimetry analysis (dTG). The results obtained are displayed in Figure 3.27, showing clear differences between the samples before or after the thermal cycles, as also reported in the literature [1]. The dried concrete shows mass losses (TG curve) of around 15% in total at 1000°C, most of them occurring between 200 and 300°C. During the drying process at 105°C, internal moisture and part of the water binded in $Al_2O_3 \cdot xH_2O$ are lost, that is the reason why no peaks are obtained in that range of temperatures. Afterwards, the peaks in the dTG curve show transformations, which are produced by the dehydration of CAH_{10} and C_2AH_8 between 120 to 200°C and by dehydration of AH_3 from 200 to 240°C. In fact, the endothermic peak obtained at 270°C, also took place in the ATD/dTG of the unhydrated CAC and CAT aggregates.

According to the sample exposed to 50 thermal cycles, it shows also progressive mass loss with the temperature but reaching a total variation of 5% at 1000°C. Some transformations have been detected in the dTG, but of a lesser magnitude. These transformations take place before reaching 200°C, which could be produced by small moisture uptake of the dried samples, and at 425°C and 725°C, which can be associated with the waste Slag aggregates transformations and CAT/CAC respectively, due to its similarities with their dTG curves.

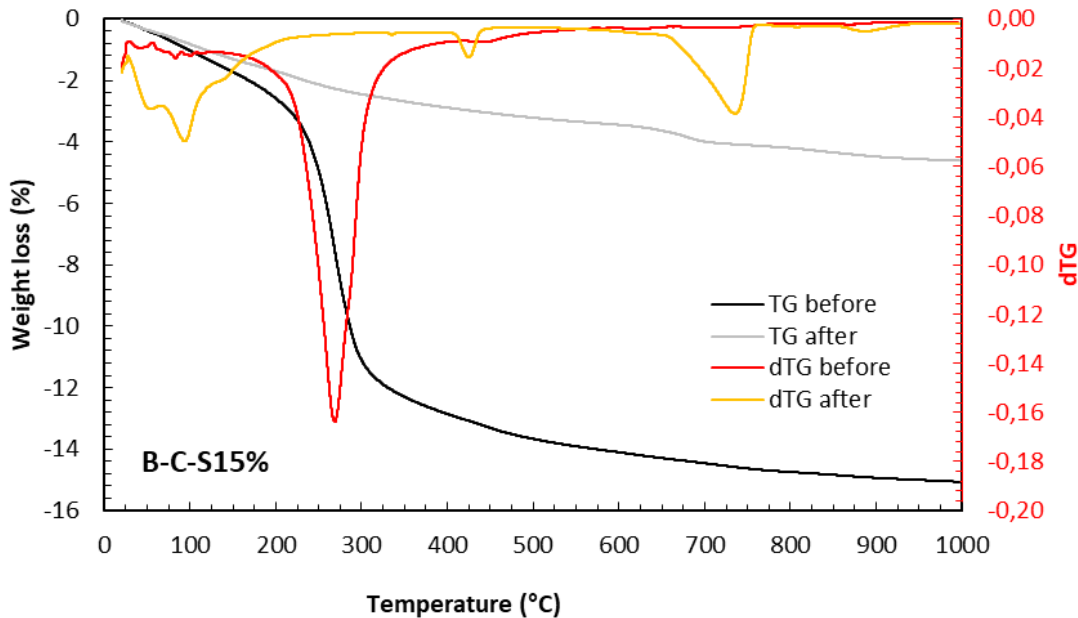


Figure 3.27: ATD/dTG results for mixes before and after the thermal cycles.

3.3.2.4. Suitability of concrete as a thermal energy storage material

Despite being concrete mixes with the same w/c ratio, cement, type of aggregates, and almost the same ageing, their results differ. The type of aggregate influences the overall thermal and mechanical response when the material is exposed to high temperatures. However, the parameters evaluated have shown that all of the mixes are stable to thermal cycles and, hence, the compositions might be used for TES infrastructures.

Comparing the mechanical properties after thermal cycles, the following issues can be highlighted. The mass variation is very similar in all the mixes. The compressive strength of the ternary mixes B-C-S15% and B-C-S30% are those with the lowest losses (around 20MPa after 10 thermal cycles), while the siliceous (S) has the highest strength drop (around 15 MPa after 10 thermal cycles). Regarding the Elastic Modulus, C mix is the only one that maintains higher stiffness after the thermal cycles. On the other hand, cracking is increased in the ternary mixes in terms of area covered by cracks, and also in terms of crack width. Then, the most beneficial mixes in terms of cracking are the binary mix B-C and C mix with basalt and CAT and the mix with only CAT aggregates, respectively.

Nevertheless, the thermal properties are of importance for TES infrastructures working under high temperature regimes because they influence the overall thermal performance. For that reason, a deeper study in this field is needed and is included in the following **Chapter 4**.

3.3.3. Partial conclusions on the design and performance of High Thermal Performance Concrete

The use of concrete in Thermal Energy Storage structures can produce a significant benefit. However, it is a challenge that needs specific approaches to achieve high stability under thermal cycles at high temperatures. Using special types of binders, such as CAC, as well as thermally stable aggregates and proper size distribution, can mitigate the drawbacks of the

use of concrete at high temperatures. Based on the results presented in this work, the following conclusions can be drawn:

- Thermal cycles produced significant changes in the properties of the concrete types analyzed. The most significant degradation was produced after the first thermal cycle. After the thermal fatigue stage, the properties were only slightly degraded with each thermal cycle.
- After the thermal cycles, when using basalt, CAT, and São Domingos Slag aggregates, the compressive strength loss obtained was between 60-70% of the initial strength. When using siliceous aggregates, the compressive strength loss obtained was around 75%. In all cases, the mass loss produced after the thermal cycles ranges between 5.5 and 6.5% of the initial mass.
- The pore size distribution obtained after the thermal cycles showed a peak of porosity in the range of 24-27 μm , which is related to the presence of microcracks and the vaporization of the polypropylene fibres.
- The microcracking analysis showed that the area covered by cracks remains < 1% of the area analyzed, showing maximum crack widths below 80 μm after the thermal cycles performed.
- The concrete mixes analysed are recommended for thermal energy storage applications because of the stabilization of the mechanical and physicochemical properties in the long-term performance. However, the evolution of the thermo-physical properties with temperature and with thermal cycles needs a deeper investigation.

(Chapter 4 on page 79)

3.4. References

- [1] M. C. Alonso, J. Vera-Agullo, L. Guerreiro, V. Flor-Laguna, M. Sanchez and M. Collares-Pereira, "Calcium aluminate based cement for concrete to be used as thermal energy storage in solar thermal electricity plants," *Cement and Concrete Research*, vol. 82, pp. 74-86, 2016. Available: <http://www.sciencedirect.com/science/article/pii/S0008884615003075>. DOI: <https://doi.org/10.1016/j.cemconres.2015.12.013>.
- [2] E. John, M. Hale and P. Selvam, "Concrete as a thermal energy storage medium for thermocline solar energy storage systems," *Solar Energy*, vol. 96, pp. 194-204, 2013.
- [3] D. Laing, C. Bahl, T. Bauer, M. Fiss, N. Breidenbach and M. Hempel, "High-temperature solid-media thermal energy storage for solar thermal power plants," *Proc IEEE*, vol. 100, (2), pp. 516-524, 2011.
- [4] M. Zeiml, D. Leithner, R. Lackner and H. A. Mang, "How do polypropylene fibers improve the spalling behavior of in-situ concrete?" *Cement and Concrete Research*, vol. 36, (5), pp. 929-942, 2006. Available: <http://www.sciencedirect.com/science/article/pii/S0008884605003376>. DOI: <https://doi.org/10.1016/j.cemconres.2005.12.018>.
- [5] M. Kanéma, P. Pliya, A. Noumowé and J. Gallias, "Spalling, Thermal, and Hydrous Behavior of Ordinary and High-Strength Concrete Subjected to Elevated Temperature," *J. Mater. Civ. Eng.*, vol. 23, (7), pp. 921-930, 2011. . DOI: 10.1061/(ASCE)MT.1943-5533.0000272.
- [6] J. Liu, K. H. Tan and Y. Yao, "A new perspective on nature of fire-induced spalling in concrete," *Construction & Building Materials*, vol. 184, pp. 581-590, 2018. . DOI: 10.1016/j.conbuildmat.2018.06.204.
- [7] J. Mindegua, H. Carré, P. Pimienta and C. La Borderie, "Experimental discussion on the mechanisms behind the fire spalling of concrete," *Fire Mater.*, vol. 39, (7), pp. 619-635, 2015. . DOI: 10.1002/fam.2254.
- [8] R. J. Connolly, "The spalling of concrete in fires," *Aston University. United Kingdom*, 1998.
- [9] H. L. Zhang and C. T. Davie, "A numerical investigation of the influence of pore pressures and thermally induced stresses for spalling of concrete exposed to elevated temperatures," *Fire Saf. J.*, vol. 59, pp. 102-110, 2013. . DOI: 10.1016/j.firesaf.2013.03.019.
- [10] C. Parrado, A. Marzo, E. Fuentealba and A. G. Fernández, "2050 LCOE improvement using new molten salts for thermal energy storage in CSP plants," *Renewable and Sustainable Energy Reviews*, vol. 57, pp. 505-514, 2016. Available: <http://www.sciencedirect.com/science/article/pii/S1364032115015312>. DOI: <https://doi.org/10.1016/j.rser.2015.12.148>.
- [11] (Last visited on 21-03-02). *CORDIS European Commission. Long Lasting Reinforced Concrete for Energy Infrastructure under Severe Operating Conditions.* Available: <https://cordis.europa.eu/project/id/685445/es>.

- [12] (Last visited on 21-03-02). LORCENIS Webpage. Available: <https://www.sintef.no/projectweb/lorcenis/>.
- [13] K. Hertz, "Heat-induced explosion of dense concretes," *Technical University of Denmark, Institute of Building Design*, 1984.
- [14] A. Bonk, M. Braun, V. A. Sötz and T. Bauer, "Solar Salt – Pushing an old material for energy storage to a new limit," *Applied Energy*, vol. 262, pp. 114535, 2020. Available: <http://www.sciencedirect.com/science/article/pii/S0306261920300477>. DOI: <https://doi.org/10.1016/j.apenergy.2020.114535>.
- [15] V. A. Sötz, A. Bonk, J. Forstner and T. Bauer, "Molten salt chemistry in nitrate salt storage systems: Linking experiments and modeling," *Energy Procedia*, vol. 155, pp. 503-513, 2018. Available: <http://www.sciencedirect.com/science/article/pii/S1876610218309767>. DOI: <https://doi.org/10.1016/j.egypro.2018.11.030>.
- [16] Z. P. Bažant, M. F. Kaplan and Z. P. Bazant, "Concrete at high temperatures: material properties and mathematical models," 1996.
- [17] R. Pérez-López, A. M. Álvarez-Valero, J. M. Nieto, R. Sáez and J. X. Matos, "Use of sequential extraction procedure for assessing the environmental impact at regional scale of the São Domingos Mine (Iberian Pyrite Belt)," *Applied Geochemistry*, vol. 23, (12), pp. 3452-3463, 2008. Available: <http://www.sciencedirect.com.biblioteca5.uc3m.es/science/article/pii/S0883292708002874>. DOI: <https://doi-org.biblioteca5.uc3m.es/10.1016/j.apgeochem.2008.08.005>.
- [18] H. Freitas, M. N. V. Prasad and J. Pratas, "Plant community tolerant to trace elements growing on the degraded soils of São Domingos mine in the south east of Portugal: environmental implications," *Environment International*, vol. 30, (1), pp. 65-72, 2004. Available: <http://www.sciencedirect.com.biblioteca5.uc3m.es/science/article/pii/S0160412003001491>. DOI: [https://doi-org.biblioteca5.uc3m.es/10.1016/S0160-4120\(03\)00149-1](https://doi-org.biblioteca5.uc3m.es/10.1016/S0160-4120(03)00149-1).
- [19] L. Fernández-Carrasco, J. Rius and C. Miravittles, "Supercritical carbonation of calcium aluminate cement," *Cem. Concr. Res.*, vol. 38, (8), pp. 1033-1037, 2008. Available: <http://www.sciencedirect.com/science/article/pii/S0008884608000811>. DOI: <https://doi.org/10.1016/j.cemconres.2008.02.013>.
- [20] J. Dweck, P. M. Buchler, A. C. V. Coelho and F. K. Cartledge, "Hydration of a Portland cement blended with calcium carbonate," *Thermochimica Acta*, vol. 346, (1), pp. 105-113, 2000. Available: <http://www.sciencedirect.com/science/article/pii/S004060319900369X>. DOI: [https://doi.org/10.1016/S0040-6031\(99\)00369-X](https://doi.org/10.1016/S0040-6031(99)00369-X).
- [21] M. Castellote, C. Alonso, C. Andrade, X. Turrillas and J. Campo, "Composition and microstructural changes of cement pastes upon heating, as studied by neutron diffraction," *Cem. Concr. Res.*, vol. 34, (9), pp. 1633-1644, 2004. Available: <http://www.sciencedirect.com/science/article/pii/S0008884603002291>. DOI: [https://doi.org/10.1016/S0008-8846\(03\)00229-1](https://doi.org/10.1016/S0008-8846(03)00229-1).
- [22] P. Kalifa, G. Chéné and C. Gallé, "High-temperature behaviour of HPC with polypropylene fibres: From spalling to microstructure," *Cem. Concr. Res.*, vol. 31, (10), pp. 1487-1499, 2001. Available:

[http://www.sciencedirect.com/science/article/pii/S0008884601005968.](http://www.sciencedirect.com/science/article/pii/S0008884601005968) DOI:
[https://doi.org/10.1016/S0008-8846\(01\)00596-8.](https://doi.org/10.1016/S0008-8846(01)00596-8)

[23] X. Liu, G. Ye, G. De Schutter, Y. Yuan and L. Taerwe, "On the mechanism of polypropylene fibres in preventing fire spalling in self-compacting and high-performance cement paste," *Cem. Concr. Res.*, vol. 38, (4), pp. 487-499, 2008. Available: <http://www.sciencedirect.com/science/article/pii/S0008884607002931>. DOI:
<https://doi.org/10.1016/j.cemconres.2007.11.010>.

[24] R. Huete-Fuertes, P. Rubio-de-Hita and C. Rodríguez-Liñán, "Aplicación de los métodos de ultrasonidos a la verificación de materiales de construcción," *Publicaciones De La Universidad De Navarra*, 1993.

[25] Z. Xing, A. Beaucour, R. Hebert, A. Noumowe and B. Ledesert, "Influence of the nature of aggregates on the behaviour of concrete subjected to elevated temperature," *Cement and Concrete Research*, vol. 41, (4), pp. 392-402, 2011. Available: <http://www.sciencedirect.com/science/article/pii/S0008884611000068>. DOI:
<https://doi.org/10.1016/j.cemconres.2011.01.005>.

[26] P. Pimienta, R. J. McNamee and J. Mindegua, *Physical Properties and Behaviour of High-Performance Concrete at High Temperature*. Springer, 2018.

Chapter 4

Thermal properties of concrete at high temperatures for thermal energy storage applications: experimental analysis

This chapter aims at analysing the evolution of the thermal properties of concrete exposed to temperatures up to 600°C and after thermal cycling. First, in *section 4.1* the importance of the evolution of thermal properties with temperature for analysis of heat transfer was highlighted. Furthermore, the structure of analysis carried out on the thermal properties was presented.

Second, *section 4.2* presents an initial analysis of thermal parameters such as thermal conductivity, volumetric heat capacity and thermal diffusivity, which were measured on different concrete compositions before and after been exposed to thermal cycles.

Later, *section 4.3* thoroughly describes the protocol developed for measuring the thermal conductivity at high temperatures up to 600°C and after repetitive cooling and heating cycles. The results were displayed on different compositions as well as the expressions and microstructure after the thermal cycles.

By the end of the chapter, some conclusive remarks on the evolution of the thermal parameters with temperature were provided in *section 4.4*.

4.1. Introduction

The analysis of heat transfer is essential for TES systems. The purpose of these infrastructures is to store energy and ensure a suitable overall efficiency in energy storage. Indeed, a TES infrastructure needs for keeping the energy stored and minimizing the energy losses to the surroundings. Hence, the heat transfer analysis for applications of thermal energy storage at high temperatures is of interest to predict the appropriateness of the whole system under operating conditions.

As it was explained in **Chapter 2**, thermal conductivity is the parameter that governs the conduction mechanism of heat transfer and it gives the relation between the heat flux and the thermal gradients that take place between the core and the external surface of the material [1]. Additionally, some authors have reported the temperature dependence of the thermophysical properties of the storage materials with the overall thermal performance of the storage systems [2]. That is the reason why a better knowledge in the evolution of the parameter with the thermal exposure in the materials used for store and insulate energy is essential.

Taking into account the changes in the mechanical and physicochemical properties of concrete analysed in **Chapter 3**, the thermal parameters of concrete when is exposed to heat should also experience some changes because of that. However, the formulation of this concept (TRL 2) needs to be experimentally proved (TRL 3) and it is the objective of the present chapter.

The lack of thermal conductivity tests on concretes up to 600°C and the need to improve the input data in CTES numerical models made necessary this experimental study. Besides, the evolution of the thermal parameter under successive thermal fatigue cycles between the temperature regime 300-600°C has only been analysed in one study [3] for two concrete types.

The main objective of this study is to analyse the evolution of thermal conductivity of concrete at high temperatures, up to 600°C and after repetitive thermal cycles between 300-600°C, to simulate working conditions as close as possible in a thermocline tank for TES in a CSP Plant. The thermal properties were analysed in two steps:

1. Characterisation of the thermal changes in concrete after the thermal exposure to high temperatures, with measurements at room temperature once the samples have been cooled down to room temperature. This initial study will improve the maturity of the technology from a formulation of the concept TRL 2 to the experimentally proof of it, achieving a TRL 3.

2. Characterisation of the thermal conductivity of concrete at high temperature, as well as to define a test protocol for measuring this parameter at high temperature. This deeper study will allow also the validation of the protocol at the laboratory, with an improvement in the Technology Readiness Level up to TRL 4.

4.2. Thermal properties of concrete after exposure at high temperature cycling

The changes in the mechanical and physicochemical parameters of concrete due to the exposure at high temperatures and after thermal cycles between 290-550°C (**Chapter 3**) highlighted the importance of knowing the effect in the thermal parameters.

The first analysis of the thermal properties was carried out at IETcc-CSIC with the measurement of the thermal conductivity of concrete once the material had been exposed to thermal cycles and the samples were cooled down to room temperature. Additionally, the PhD candidate was in brief research stay at the University of Évora (Portugal), in the Renewable Energies Chair. Both institutions were partners of the H2020 “NewSOL” project, and the stay aimed to share knowledge on the thermal properties of concrete. During the

stay, the heat capacity and thermal diffusivity were measured in concrete samples at residual conditions, after being exposed to thermal cycles.

4.2.1. Experimental procedure

4.2.1.1. Materials

Five concrete mixes were made using the aggregates mentioned in **Chapter 3** and CAC cement. The concrete compositions analysed have the same volume of cement paste and aggregates to assurance the comparability of results (Table 4.1).

| kg/m³ | B-C-S 15% | B-C | C | B-C-S 30% | S |
|------------------------------|------------------|-------------|-------------|------------------|-------------|
| Cement CAC | 600 | 600 | 600 | 600 | 600 |
| Water | 258 | 258 | 258 | 258 | 258 |
| Gravel 1 - Siliceous 4-12 mm | 0 | 0 | 0 | 0 | 742 |
| Gravel 2 - Basalt 4-12.5 mm | 682 | 788 | 0 | 576 | 0 |
| Gravel 3 - CAT 3-10 mm | 0 | 0 | 885 | 0 | 0 |
| Gravel 4 - Slag 1-6.3 mm | 139 | 0 | 0 | 278 | 0 |
| Sand 1 - Siliceous 0-3 mm | 0 | 0 | 0 | 0 | 693 |
| Sand 2 - CAT 0.25-4 mm | 714 | 826 | 826 | 602 | 0 |
| Sand 3 - Slag 0.25-2 mm | 128 | 0 | 0 | 256 | 0 |
| Polypropylene fibres | 2 | 2 | 2 | 2 | 2 |
| Plasticizer Sikament 165 | 1 | 1 | 1 | 1 | 1 |
| <i>Water/cement (w/c)</i> | <i>0.43</i> | <i>0.43</i> | <i>0.43</i> | <i>0.43</i> | <i>0.43</i> |

Table 4.1: Concrete compositions

One concrete batch of 8 samples of each concrete composition was produced. Additionally, 4 extra samples of B-C-S15% were produced. The mixes were poured in cylindrical moulds of 75 mm of diameter and 150 mm of height and compacted using a compacting rod. After preparing the mixes, all concrete samples were kept inside metallic moulds and covered with a plastic bag to avoid drying for 24 hours until hardening in a controlled temperature room at 20°C. After that, samples were demoulded and stored in a humidity chamber at 20°C and 95% of RH until the testing time for at least 7 days. After the curing stage, some specimens were cut in disks of around 20 mm of width and stored again in the humidity chamber until the testing time. The ageing of the samples before starting with the thermal exposure were: 9, 10, 8, 11 and 10 days for the type of concrete B-C-S15%, B-C, C, B-C-S30% and S, respectively.

4.2.1.2. Thermal regime

The thermal exposure of the concrete samples has been divided into 3 stages, according to the physicochemical changes that take place in the concrete, as is mention as follows: drying process, dehydration and thermal fatigue stage defined in **Chapter 3**. For the drying process, the concrete samples were dried up to 105°C for 72 hours. Secondly, the first thermal cycle was done heating at 1°C/min up to 290°C, where the temperature was maintained 2 hours to homogenise the temperature in the whole specimens. After that, the heating process up

to 550°C was done following the same heating rate and then the temperature was maintained constant 2 hours to ensure that the whole sample reaches the set temperature. After that, the sample was cooled down to 290°C in 2 hours and then the subsequent heating and cooling cycles between 290–550°C were performed with a faster heating rate of 8°C/min. For evaluating the effect of thermal fatigue in this study, the samples were exposed to 1, 5, 10, 25 and 75 repetitive cycles.

After the heating cycles, the samples were cooled down to room temperature and stored in a hermetic plastic bag that is placed in a desiccator until the measuring of the thermal parameters.

4.2.1.3. System description

The test system for measuring thermal conductivity comprised of various components. The electrical furnace used is from *Eurotherm* and has 15 kW of power, and the model of the chamber furnace is MLR11 305/16. The maximum operating temperature of the oven was 1100°C and it has a control system able to carry out the heating and cooling cycles with controlled rates. The concrete samples were disks of 75 mm of diameter and 20 mm of height. In summary, the test comprises of the following components: furnace, disk samples of concrete, K-type thermocouples and a data acquisition system, whose experimental setup were shown in **Chapter 3**.

The equipment used for measuring the thermal conductivity was QTM-700 from Kyoto Electronics Manufacturing (Figure 4.1). The equipment for measuring thermal conductivity had two different probes: one to measure the thermal parameter at room temperature and another for measuring at high temperatures, up to 1000°C. The probe covers a rectangular surface of 100×40 mm. This equipment is based on the ‘Hot wire’ method and measures the increase in temperature produced when an electrical current passes through the wires. The thermal conductivity measurements have an accuracy of ± 0.001 W/(m·K).

Regarding the measures taken at the University of Évora, the equipment used was ISOMET, model 2104 from Applied Precision, shown in Figure 4.2. It also follows the physic principle of the ‘Hot wire’ method, but this equipment measures jointly the volumetric heat capacity and the thermal diffusivity of the material. The probe covers a circular section of 4 cm of diameter.



Figure 4.1: Equipment QTM-700 and probe for measuring at room temperature.



Figure 4.2: Equipment ISOMET (model 2104) and probe for measuring at room temperature.

4.2.2. Results and discussion

4.2.2.1. Before thermal tests

The thermal conductivity (Figure 4.3) was measured at room temperature for wet and dried states (after removing the free water from the pores in samples heated for 72 hours at 105°C). In wet conditions, all mixes show values of thermal conductivity between 1.16 and 1.26 W/(m·K) with only slight differences, except for the siliceous sample (S) whose thermal conductivity reaches 2.5 W/(m·K) due to the more conductive aggregates. However, since each sample may have different internal humidity due to their compositions, the values in dried conditions without thermal cycles will be more representative of the thermal conductivity of the mixes. In fact, at dried conditions, a considerable difference between the mixes has been detected, with C (mix with CAT aggregates) showing the best thermal conductivity and B-C-S30% and S showing the biggest drop in the thermal parameter.

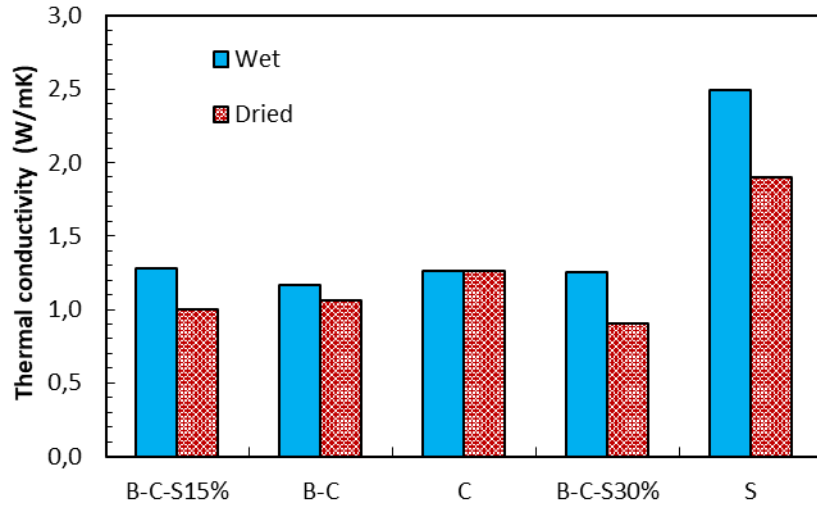


Figure 4.3: Thermal conductivity in wet and dried states.

Regarding the heat capacity and diffusivity of these concrete compositions (Figure 4.4), the binary mix (B-C) had the highest heat capacity and lowest diffusivity, while the mix with CAT aggregates (C) reached both heat capacity and diffusivity high values.

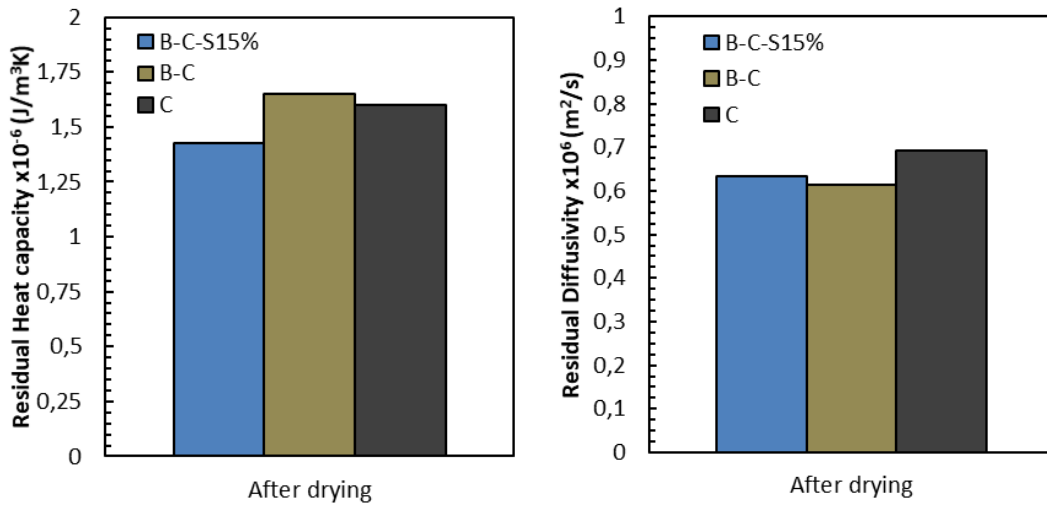


Figure 4.4: Residual heat capacity (left) and diffusivity (right)

4.2.2.2. After thermal tests

Concrete disks were exposed to 1, 5 and 10 thermal cycles and the thermal conductivity were measured after the cooling down of the samples to room temperature (Figure 4.5). The two points at 0 cycles represent the values obtained at the initial condition with moisture, and after being dried at 105°C since the presence of humidity contributes to the thermal conductivity. The mix that obtained the higher thermal conductivity is the mix with siliceous aggregates. However, it is also the mix with the highest drop, around 50% of the initial conductivity measured at wet conditions. In comparison, the rest of the mixes followed the same trend with higher stability and with global decreases of only 30-35%. Again, the critical loss of properties was produced during the drying and after 1 thermal cycle (with decreases of around 18-30%), whereas during the thermal fatigue stage, the decreases are less significant

(7-12%). The thermal conductivity values obtained when using the thermally stable aggregates before drying range between 1 and 1.3 W/(m·K). The values after the thermal cycles are, on average, 0.81 W/(m·K) for the B-C-S15%, 0.67 W/(m·K) for the B-C mix, 0.89 W/(m·K) for the C mix, 0.76 W/(m·K) for the B-C-S30% mix and 1.2 for the S mix. Additionally, the ternary composition B-C-S15% was measured after being exposed to 25, 50 and 75 cycles and the stabilization of the thermal parameter was reached as well (Figure 4.6).

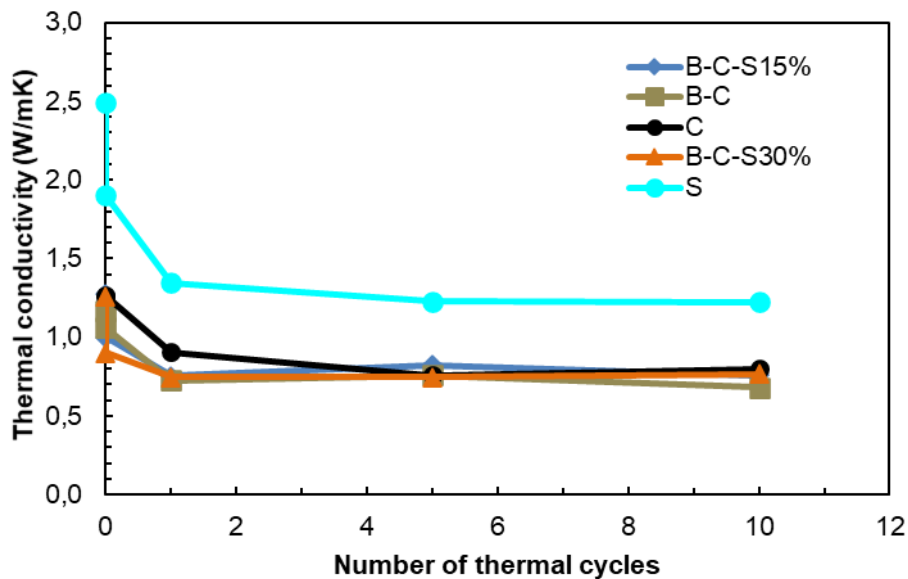


Figure 4.5: Evolution of thermal conductivity of all compositions after 0, 1, 5 and 10 thermal cycles.

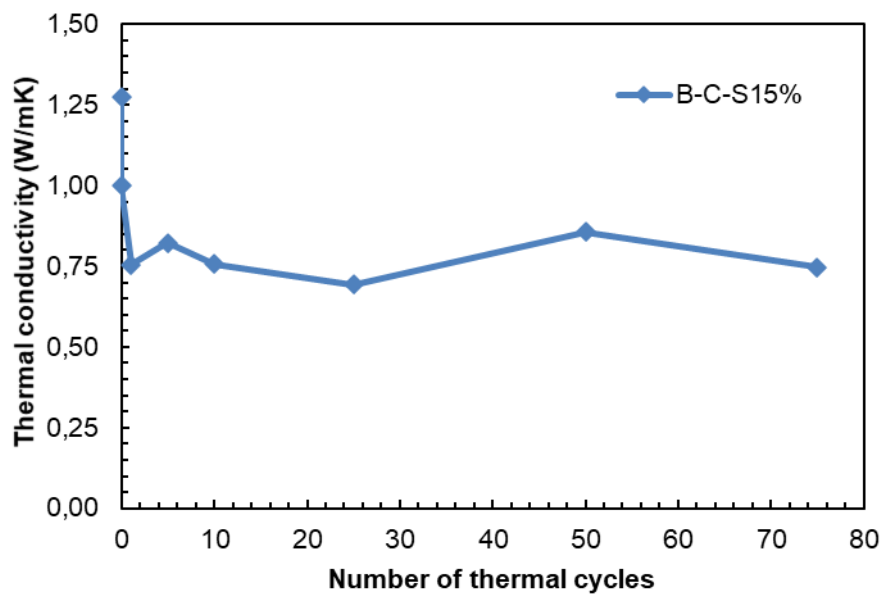


Figure 4.6: Evolution of thermal conductivity after a long-term performance of B-C-S15% composition.

The evaporation of water in the pores and dehydration of the cement paste caused the loss in thermal conductivity after the first thermal cycle. This process causes a substitution of the internal water by air inside the material. The thermal conductivity of water

is higher than that of the air, with values of $0.607 \text{ W}/(\text{m}\cdot\text{K})$ and $0.02551 \text{ W}/(\text{m}\cdot\text{K})$, respectively, at room temperature [1]. Additionally, dehydration and thermal cycling will also produce cracks in concrete (air gaps). Consequently, dehydrated concrete will necessarily have lower thermal conductivity. Once the material suffered the first thermal cycle and the changes in its microstructure, the thermal cycling stage does not have a relevant effect on the values of thermal conductivity measured in residual conditions.

The evolution of thermal conductivity with the temperature depends on the concrete composition and, especially, on the aggregates' type. Most studies published reported decreases in the thermal conductivity with the temperature [4-6], especially when using limestone or quartzite aggregates, and slight increases were reported when using lightweight aggregates [4].

For concrete elements for TES applications, a balance between high thermal conductivity and good stability of aggregates are usually the desired parameters, but heat capacity and diffusivity are also parameters of interest for some applications. While the first one gives an idea of the energy storage capacity into the material, the second quantifies the velocity of heat transport along with the material. This is important for solar energy applications because the heat source is intermittent, and the storage turn the renewable source into dispatchable energy. Therefore, concrete as a thermal energy storage material must capture the greatest amount of energy in the shortest time with less damage within the material. This is achieved with a balance between the thermophysical properties of its compounds.

The values of volumetric heat capacity and diffusivity obtained before and after 5 thermal cycles are displayed in Figure 4.7. The results of volumetric heat capacity indicate a small decrease of around 5-7% after the thermal cycles when compared to the values obtained in wet conditions. In comparison, thermal diffusivity decreased around 30%, similar to the decrease produced in the thermal conductivity, which is consistent with the results reported in the literature [4]. Thermal diffusivity experienced significant changes in the binary composition containing basalt and CAT aggregates (B-C) and the one containing 100% CAT (C). The thermal parameter experienced decreases of around 35-40% of its dried value after being exposed to thermal cycles. The ternary mix B-C-S15% experienced a more stable response, with a variation of around 20% after being exposed to thermal cycles.

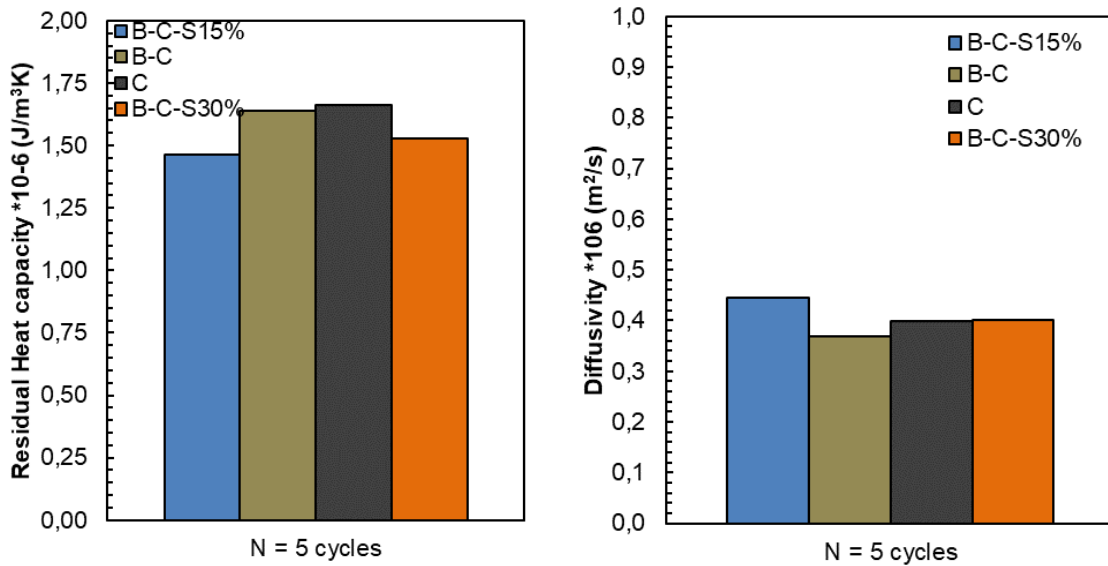


Figure 4.7: Residual values of heat capacity and diffusivity after 5 thermal cycles.

4.2.3. Partial conclusions on the evolution of thermal parameters measured at room temperature

The thermal conductivity, volumetric heat capacity and thermal diffusivity experienced changes after cycles but measured at residual conditions. The following conclusions can be drawn:

- Thermal conductivity is similar in all the mixes with initial values around 1-1.20 W/(m·K), and residual values after the thermal cycles around 0.80 W/(m·K). The only mix with higher thermal conductivity is that with siliceous aggregates (S), which maintains a thermal conductivity of 1.25 W/(m·K) after the thermal cycles. The thermal conductivity decreased between 30-35% after the first thermal cycle in the composition B-C-S15%. This decay reached a drop of 50% of its initial value in the siliceous composition.
- The volumetric heat capacity experienced a slower decrease in its value when the concrete was exposed to thermal cycles, achieving between 1.5-1.6·10⁶ J/(m³·K) after being exposed to 5 thermal cycles.
- The highest capacity after thermal cycles comes from the C mix with CAT aggregates and the binary mix without the waste slag. On the other hand, the higher diffusivity is obtained by the ternary mixes B-C-S15%, B-C-S30% followed by C concrete composition.
- Thermal diffusivity experienced significant changes in the binary composition containing basalt and CAT aggregates (B-C) and the one containing 100% CAT (C). The thermal parameter experienced decreases of around 35-40% of its dried value after being exposed to thermal cycles. The ternary mix B-C-S15% experienced a more stable response, with a variation of around 20% after being exposed to thermal cycles. The values of diffusivity ranged between 0.4-0.5·10⁻⁶ m²/s.

4.3. Thermal properties of concrete at high temperature and during cycling

The initial and previous results indicate that the most significant changes are related to the thermal conductivity when concrete is exposed to high temperatures up to 550°C. However, this variation was detected at residual conditions when concrete was cooled down to room temperature. In a real TES infrastructure, as the tanks for storing molten salts, the temperature is always cycling between the temperatures of operation. For that reason, a deeper analysis of the evolution of thermal conductivity with temperature is fundamental for evaluating the overall thermal performance of the TES configuration.

Different concrete compositions were studied with a different type of aggregates, using CAC cement and incorporating polypropylene fibres. The study was divided into two parts: 1) the first part related to the first heating up to 600°C where the effect of the aggregates and the heating rates were evaluated, and 2) the second part that comprises the effect of the thermal fatigue between 300-600°C under service conditions and the final cooling down to room temperature.

4.3.1. Methodology

4.3.1.1. Materials

A set of five concrete mixes made of CAC cement and different aggregates type were analysed. The concrete compositions analysed had the same water/cement (w/c) ratio and aggregates volume (Table 4.2). The CAC was used due to its refractory properties and good response at high temperatures and during heating cycles [6]. The aggregates used in the five concrete mixes studied are: 1) fine CAT aggregate (named 1-C); 2) basalt aggregate (2-B); 3) a ternary mix combining basalt, CAT and a waste Slag from *São Domingos* mine [7, 8] (3-B-C-S); 4) calcareous aggregate (4-CAL); and 5) siliceous sand (5-S).

| kg/m³ | 1-C | 2-B | 3-B-C-S | 4-CAL | 5-S |
|-----------------------------|------------|------------|----------------|--------------|------------|
| Cement CAC | 600 | 600 | 600 | 600 | 600 |
| Water | 258 | 258 | 258 | 258 | 258 |
| Aggr. 1 – Basalt 0-6 mm | 0 | 1568.5 | 691 | 0 | 0 |
| Aggr. 2 - CAT 0.25-4 mm | 1736.5 | 0 | 745 | 0 | 0 |
| Aggr. 3 - Slag 0.25-2 mm | 0 | 0 | 133 | 0 | 0 |
| Aggr. 4 – Slag 3-7 mm | 0 | 0 | 141 | 0 | 0 |
| Aggr. 5 – Calcareous 0-6 mm | 0 | 0 | 0 | 1456.4 | 0 |
| Aggr. 6 - Siliceous 0-3 mm | 0 | 0 | 0 | 0 | 1456.4 |
| Polypropylene fibres | 0 | 0 | 2 | 0 | 0 |
| Plasticizer | 0.9 | 0.9 | 0.9 | 0.9 | 0.9 |
| <i>Water/cement (w/c)</i> | 0.43 | 0.43 | 0.43 | 0.43 | 0.43 |

| Strength class | C70/85 | C60/75 | C45/55 | C50/60 | C40/50 |
|----------------|--------|--------|--------|--------|--------|
|----------------|--------|--------|--------|--------|--------|

Table 4.2: Mix compositions used in this work.

One concrete batch of each concrete composition was produced. The mixing process consisted of these steps: 1) mixing the solid materials, aggregates and cement, for five minutes, 2) introduction of water with the plasticizer already diluted in it for one minute, 3) mixing during three minutes, 4) introduction of the polypropylene fibres during one minute, and 4) mixing during one minute. The mixes were poured inside prismatic moulds of $40 \times 40 \times 160 \text{ mm}^3$ and compacted using a compacting rod. Since the size of the largest aggregates (7 mm) is smaller than 1/5 of the wide of the concrete sample (40 mm), the homogeneity of the material is ensured. Specimens were demoulded 24 hours after casting and left in a humidity chamber at 95 % of relative humidity and 20°C until the age of testing.

4.3.1.2. System description

A test protocol to measure properly the evolution of thermal conductivity at high temperatures (up to 600°C) and during cyclic operation (during charging and discharging) has been designed. The test system for measuring the thermal conductivity comprised of various components, as is shown in Figure 4.8 and Figure 4.9. The electrical furnace used is from *Eurotherm* and has 15 kW of power, and the model of the chamber furnace is MLR11 305/16. The maximum operating temperature of the oven was 1100°C and it has a control system able to carry out the heating and cooling cycles with controlled rates. The equipment used for measuring the thermal conductivity was QTM-700 from Kyoto Electronics Manufacturing. This equipment is based on the hot wire method and measures the increase in temperature produced when an electrical current passes through the wires. The high-temperature probe of thermal conductivity is located between two concrete samples that are placed inside the oven, as shown in Figure 4.8. The wires of the probe are connected to the equipment outside the furnace. Those wires were protected with ceramic covers in the region close to the door in order to insulate the connections from the metallic parts of the furnace. The thermal conductivity measurements have an accuracy of $\pm 0.001 \text{ W}/(\text{m}\cdot\text{K})$. To control and monitor the evolution of the temperature inside the concrete, one temperature sensor (K-type thermocouple) was embedded in the geometrical centre of the sample. Another two temperature sensors were located inside the furnace to follow the thermal response and to record the evolution of temperature at the external surface of the samples. The calibrated K-type thermocouples have accuracy in line with the specification of $\pm 0.1^\circ\text{C}$. All temperature data were collected and recorded through a data acquisition system (Model: Agilent 34970A) directly by an external data logger. In summary, the test comprises of the following components: furnace, two concrete samples, high-temperature thermal conductivity probe, K-type thermocouples and data logger (Figure 4.8 and Figure 4.9).

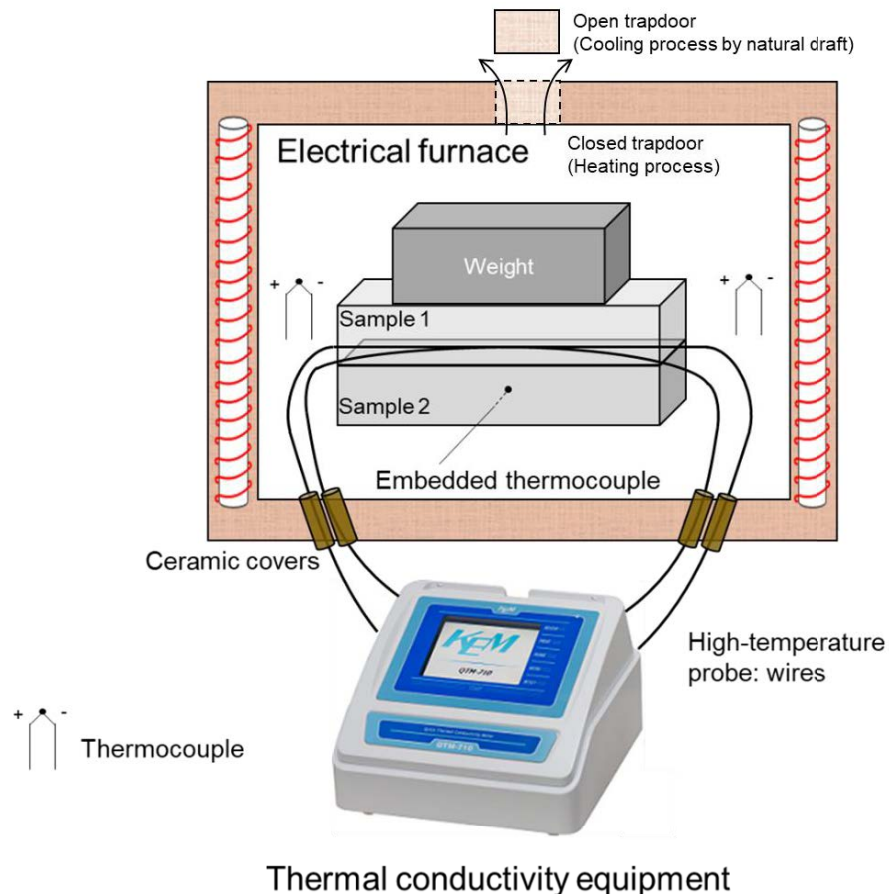


Figure 4.8: Graphical layout of the test facility and equipment.

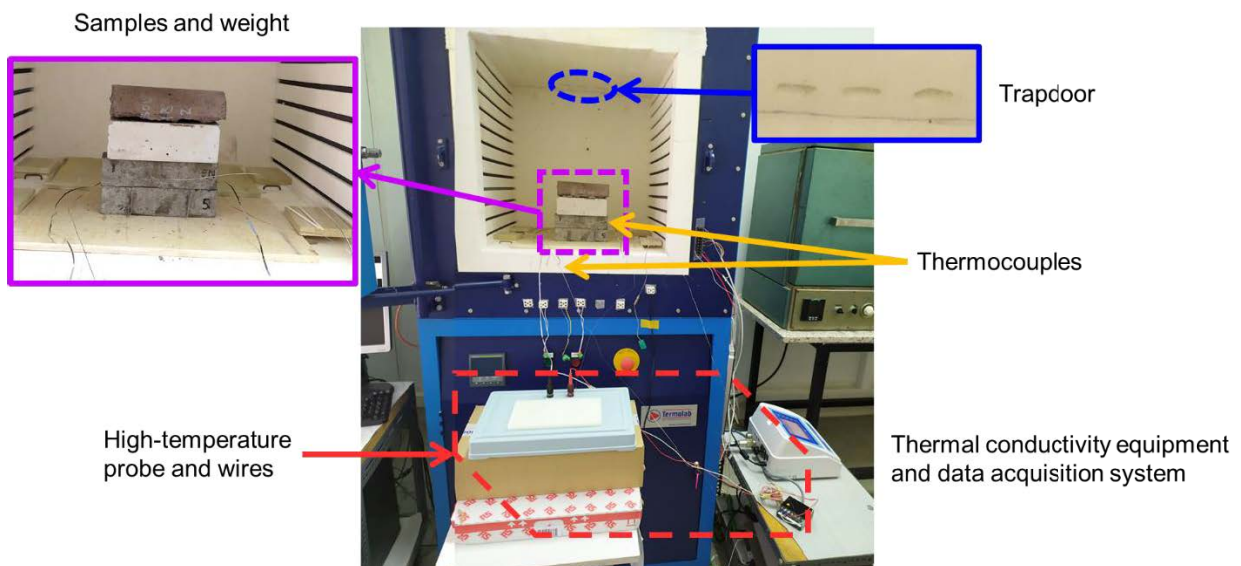


Figure 4.9: Experimental set-up of the real test facility.

The equipment for measuring thermal conductivity had two different probes: one to measure the thermal parameter at room temperature and another for measuring at high temperatures, up to 1000°C. The room temperature probe covers a surface of 100×40 mm and the high temperature probe covered an area of 160×40 mm. Both probes cover a wide

region of the surface of the concrete specimens. The values of thermal conductivity at room temperature were measured with both probes to compare their measures.

The lack of standardized tests methods for measuring the parameter at temperatures up to 600°C made it necessary to develop a protocol taking into account the physicochemical changes that take place within the concrete while the material is being heated and cooled down. Two identical concrete samples of 40×40×160 mm³ were needed for carrying out the test. The sample located at the bottom has a thermocouple embedded for recording the evolution of temperature in the centre of the specimen. An additional weight placed over the samples is needed to achieve full contact among the two samples and the probe.

Before start measuring, the wires of the high-temperature probe had to be calibrated. The wires used were able to measure up to 1000°C, but the sensors started to suffer damage from temperatures above 600°C. For that reason, the wires were calibrated before starting each test to ensure that they were not damaged.

To obtain an accurate measurement, the system needed to achieve constant temperature along both concrete surfaces in contact. For that reason, a time of 30 minutes after the furnace reached the target temperature was needed in order to homogenize the temperature in the concrete samples in the processes of heating and cooling. Once those 30 minutes were elapsed, the thermal conductivity test started. The measures were discrete and the time for measuring was established in 60 seconds. During this time, the oven has to be under steady-state conditions to obtain an accurate value. If the electrical resistances of the furnace switched on at the end of the 60 seconds testing time, the transient conditions affected the value of thermal conductivity measured and the result had to be discarded. During these transient conditions, the convection inside the oven affected the measurement and the value was mainly affected by air-forced convection instead of the conduction within the solid medium. To obtain a more representative value of thermal conductivity, ten measurements at each temperature were taken, and only stable measures were considered.

4.3.1.3. Thermal regime

The evolution of the thermal parameters at the operating temperatures regime is of relevant importance to assess the heat transfer within the concrete structure and for determining the real energy storage. For that purpose, this study deals with the maximum operating regime of the HTF in CSP Plants, commonly molten salts between 300 and 600°C. For that reason, the thermal conductivity was measured during the first heating up to 600°C and in successive heating and cooling cycles between 300-600°C.

The thermal conductivity has been measured during the thermal exposure of concrete, which has been divided into three stages: drying, dehydration and thermal fatigue stage.

Firstly, the concrete samples were dried up to 105°C for 72 hours. In this stage, the loss of free water in the pores takes place. The time of 72 hours was established after carrying out many tests on samples with the same geometry and after verifying that all the free water was lost by weighting the samples. Secondly, the dehydration stage covers from 105 to 300°C, in the case of CAC concretes. During this stage, the dehydration of cement paste occurs.

Finally, the thermal fatigue stage covers the subsequent heating and cooling cycles between 300-600°C.

The thermal conductivity was measured every 100°C from room temperature to 600°C during the first heating. During the first cooling stage, samples were cooled down to 300°C using the same temperature step. The second heating was performed up to 600°C again, measuring thermal conductivity every 100°C. Finally, the samples were cooled down to room temperature and the thermal parameter was evaluated at 400, 200 and 25°C. All heating rates were programmed at 1°C/min. Regarding the cooling process, the oven controlled the evacuation of the heat using a trapdoor located at the top of the furnace, which was detailed in Figure 4.8 and Figure 4.9. The control system of the furnace regulated the degree of openness of the trapdoor. When the temperature had to decrease in more than 10°C than the theoretical programmed temperature, the furnace opened the trapdoor completely. For that reason, the furnace experienced a cooling process by following a natural draft. The thermal cycle and the stages are detailed in Figure 4.10, and the measurements were performed at the temperature plateaus. The drying stage (**blue** surface) covers the first heating up to 100°C during the first 72 hours of testing. After that, the first heating (1H) up to 600°C was performed (**red** area). During this heating, the dehydration of the CAC at 300°C takes place (dashed line). The thermal fatigue stage follows the cycle with a first cooling (1C) down to 300°C (**violet** surface), a second heating (2H) up to 600°C (**orange** surface) and a second cooling (2C) down to room temperature (**purple** surface). The duration of one complete test lasted 10 days.

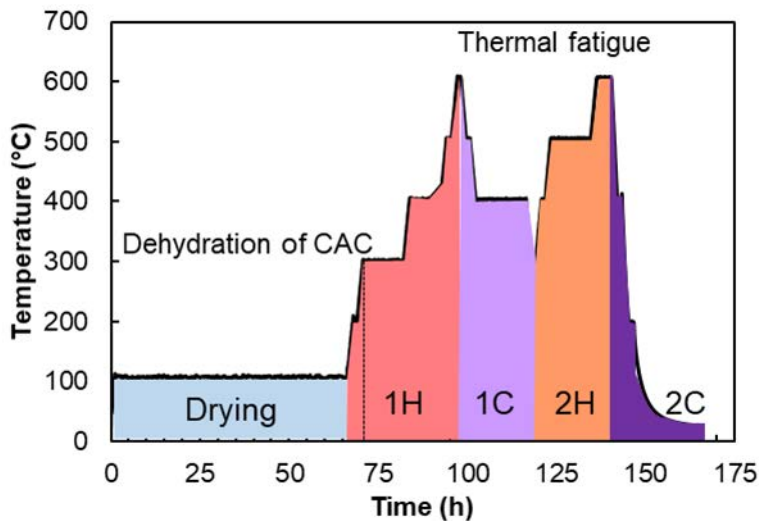


Figure 4.10: Thermal cycle with the stages in different colours.

The output parameters measured were the thermal conductivity, the temperature of the furnace, and the temperature in the core of the concrete samples. The experimental test was carried out in the five concrete mixes in order to evaluate the effect of the type of aggregates. Two samples per concrete mix were tested at the same time. An additional test was performed for the evaluation of the effect of the heating rate on the 3-B-C-S mix at 0.5°C/min.

Additionally, microscopic analysis was carried out when the samples were cooled down to room temperature, following the 2C process, with a similar procedure as the one

defined in **Chapter 3**. Some pictures were taken at the surface of the samples by using an optical microscope (model SZ61TR from OLYMPUS) with a resolution of $\pm 1 \mu\text{m}$. The crack width was measured with the software OLYMPUS Stream Essentials in order to quantify the effect of the thermal exposure in all the concrete mixes.

4.3.1.4. Methodology for data analysis

The probes of the thermal conductivity equipment need to be calibrated before starting the test. The calibration procedure is carried out at room temperature using the patterns of different materials provided by the manufacturer. The calibration procedure consists of measuring the thermal conductivity of some patterns whose thermal conductivity is known for a selected current of the equipment. The calibration is done when the probe achieves three measures with a standard deviation lesser than 3% and a mean value similar to the value of the pattern.

After that, the test started with the thermal regime explained in Figure 4.10. A set of 10 measurements were carried out at every single temperature once the material reached the equilibrium in the temperature located in the centre of the specimen. The weighted mean was taken from the right measurements and was the estimation of the real value. The uncertainties (U) were calculated and evaluated following the instructions summarised in [9]. The first step is the calculation of the standard deviation (σ) following the equation:

$$\sigma = \sqrt{\frac{\sum_{i=1}^n (X_i - \bar{X}_n)^2}{n - 1}} \quad (2)$$

Where σ is the standard deviation and is half of the U at 95% of confidence stated for each measurement X_i . The mean value is \bar{X}_n and n is the number of measurements carried out at different stages of temperature.

The uncertainty (U) of the measurements were obtained by expression in the following equation:

$$U_x = \frac{2}{\sqrt{\sum_{i=1}^n \frac{1}{\sigma_i^2}}} \quad (3)$$

4.3.2. Results and discussion

4.3.2.1 Characterisation of intrinsic thermal conductivity of concretes: before heating at room temperature

Figure 4.11 shows a comparison between the thermal conductivity measured with both probes: the room temperature probe (RT) and the high temperature probe (HT). The measures were carried out when samples were taken from the humidity chamber at room temperature. The values measured with the two probes show significant differences between them because the high-temperature probe is not appropriate for measuring the thermal conductivity at low temperature. This suggests the importance to employ an adequate probe system for the measurement of this parameter. The results obtained with the two probes display a linear dependence. Being the thermal conductivity measured at room temperature,

k_{RT} , and the ones measured at high temperature, k_{HT} , the relation between them is shown in Figure 4.11, with a coefficient of determination, $R^2=0.9525$.

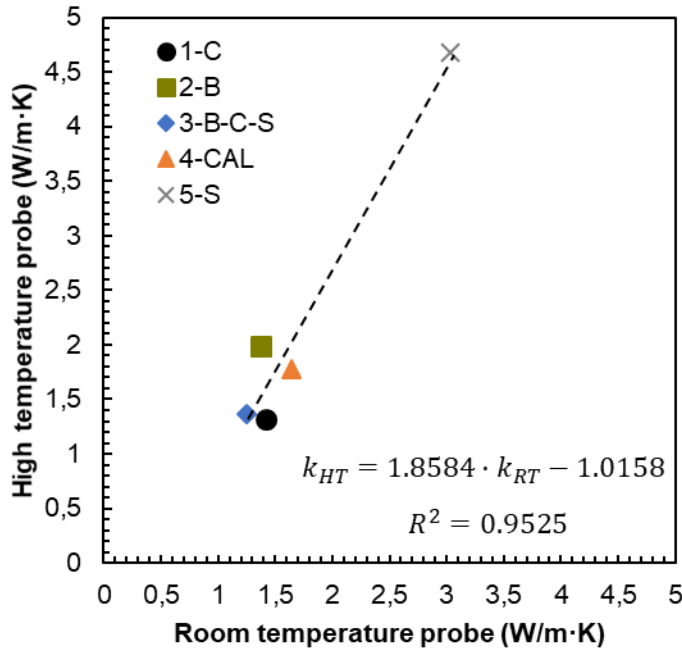


Figure 4.11: Thermal conductivity at room temperature measured with the two probes.

4.3.2.2. Characterisation of thermal conductivity of concretes at high temperature: First heating from ambient to 600°C

Figure 4.12 shows the evolution of thermal conductivity measured during the first heating up to 600°C. The legend shows the first heating (1H) followed by the name of the concrete mix. The values at room temperature represented in the chart are the ones measured with the high temperature probe to make a better comparison among them by using the same probe of measure.

The results obtained show that thermal conductivity decreases with temperature, especially for the siliceous mix. Thermal conductivity experienced the highest loss after drying the concrete at 105°C for 3 days. Basically, the loss of evaporable water during drying up to 105°C decreases thermal conductivity because the air replaces water in concrete pores, as was explained in the previous section when comparing results at wet and dried conditions. From temperatures below 100°C, thermal conductivity is supported by both solids and liquids within the material. When the temperature exceeds 100°C, the conduction is mainly supported by the solids inside the material. Additionally, the temperature affects the creation of air gaps and microcracking inside the material. That is the main reason why the parameter decreases during heating up to 105°C.

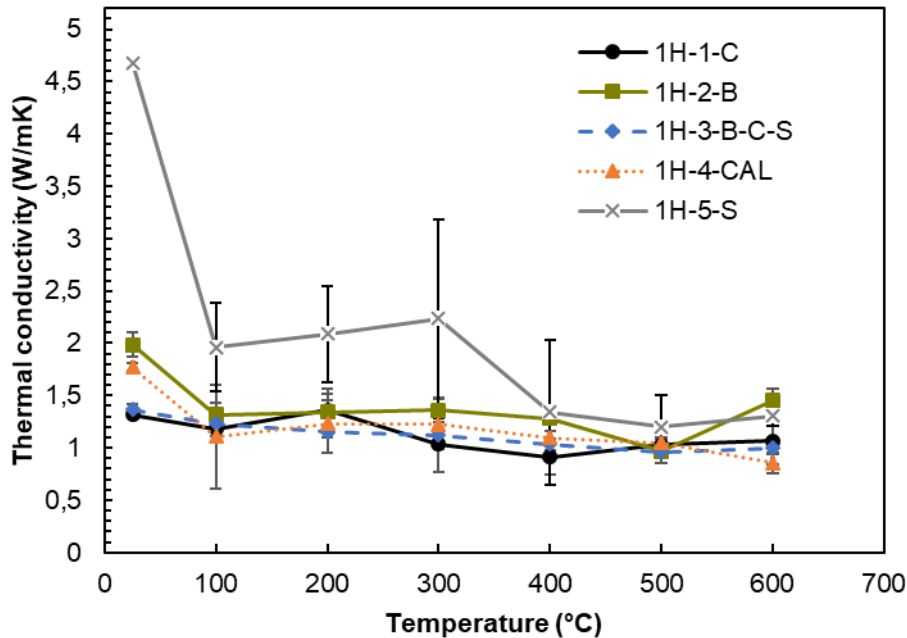


Figure 4.12: Evolution of thermal conductivity up to 600°C for the CAC concrete mixes.

When the samples were heated up to the maximum temperature of 600°C, CAC concretes experienced decreases in the thermal parameter due to the dehydration of the cement pastes (up to 300°C for the CAC [10]) and the volumetric changes that take place due to the shrinkage of the cement paste and the expansion of the aggregates [6]. The results indicate that the thermal response of the concrete is influenced by the thermal response of the aggregates and the mix design. The biggest reduction of thermal conductivity took place in the siliceous mix (5-S) when heating up to 100°C, achieving values of nearly 2 W/(m·K). Many authors reported a similar decrease when heating up to 300°C [11, 12], but the test was done continuously and the drop was linear, which indicates the importance of giving time to homogenise the temperature and to produce the physicochemical changes in the whole specimen. Concrete with calcareous aggregates (4-CAL) also experienced a significant decay of conductivity when heating up to 100°C. More stable aggregates such as basalt (2-B) experienced the lowest drop up to 100°C and then the thermal response remained almost constant.

The decreasing trend in the thermal conductivity is consistent with many tests on concrete at high temperature carried out by different authors [3, 6, 12, 13], highlighting the aggregates effect and the degree of saturation of the concrete. In this research, the siliceous mix (5-S) experienced the highest scattering, but this dispersion was verified as originated by the probe. On the contrary, another literature reported an increase of the thermal conductivity with temperature when adding graphite [14], but that would be a property of special material.

In this work, thermal conductivity change with the temperature has been compared with the results of other studies in Figure 4.13.

The research articles [15, 16] measured the evolution of thermal conductivity at high temperatures for their use in CTES. In these investigations, tests to measure thermal

conductivity were carried out up to 400 and 450°C, respectively but with different initial conditions. Moreover, in both projects, the type of cement and aggregate composition are not described by the authors. In the case of [15], the thermal conductivity of concrete was measured after being exposed at 430°C for 100h, obtaining values of around 1.92-1.78 W/(m·K) at 300 and 400°C, respectively. In [16], the thermal conductivity of concrete was measured after a simultaneous drying and dehydration process at 400°C, obtaining 1.2 W/(m·K).

Other studies that reported values at high temperatures analysed: a) two Normal Strength Concretes (NSC) with OPC cement and siliceous and calcareous aggregates, named OPC-NSC-S and OPC-NSC-C, respectively [17], and b) a Self-Compacting Concrete (SCC) with PP fibres (OPC-SCC-PPF) [18].

Figure 4.13 shows the evolution of the thermal conductivity at high temperature measured in the concrete mixes of this work and the results obtained in the literature for [15], [16], the NSC [17] and the SCC [18] concretes. Additionally, the limits of thermal conductivity given in Eurocode 2 [19] are represented in the chart. It is worth noting that Eurocode 2 curves are adjusted from tests of concrete structures under fire conditions and take into consideration only the moisture transport. However, it is one of the most relevant resources of thermal conductivity and, for that reason, it was included in Figure 4.13.

The curves obtained for the mixes analysed in this work are in accordance with those reported in the literature. Regarding the siliceous concretes, both compositions (OPC-NSC-S and 5-S) experienced the highest drop when are heated up to 100°C, but the lack of measured values at 600°C in the literature made it not possible to compare the second decrease between 400-600°C. The calcareous mixes experienced a lesser decrease at high temperatures in both tests up to 300°C, however, they may not be appropriate for operating up to 600°C, as reported in this work. The calcareous mix (4-CAL) experienced a decrease in the parameter of 20% when was heated from 400 to 600°C.

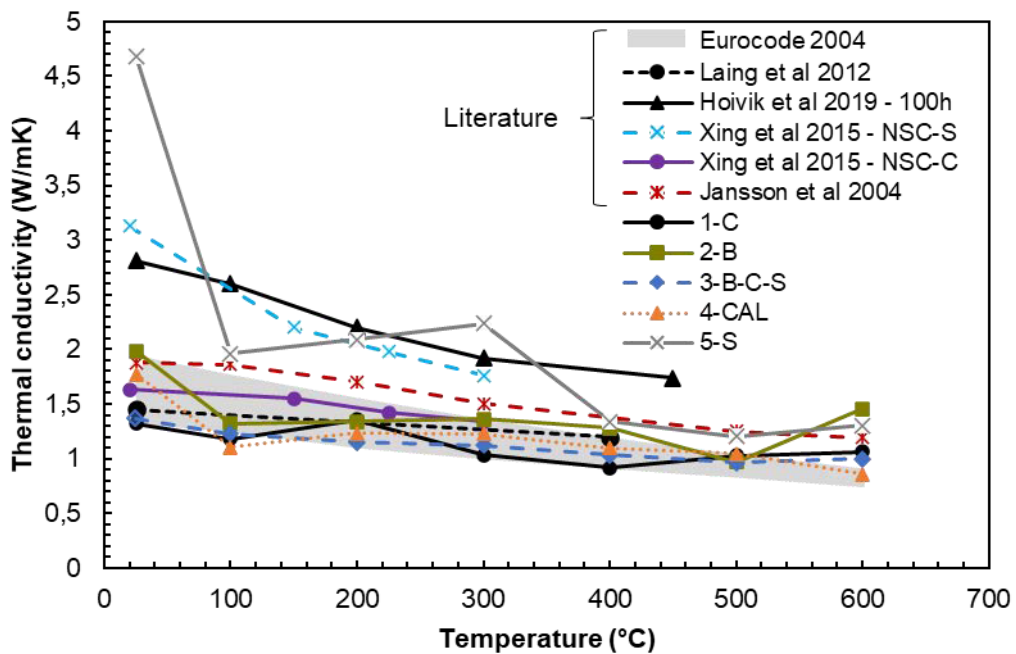


Figure 4.13: Measured thermal conductivity of CAC concretes and comparison to concretes from the literature [15-19].

To sum up, the mixes 1 to 3 analysed in this study can work properly up to 600°C without significant variation of the thermal conductivity between 300-600°C and showing low dispersion. Their thermal behaviour is almost steady under the cyclic operating conditions, as will be shown later. In contrast, the mixes containing calcareous and siliceous aggregates experienced the biggest losses and high variations of thermal conductivity (-30% for 4-CAL and -40% for 5-S) at temperatures above 300°C. The results obtained in this work do not support their use for CTES applications under operating temperatures up to 600°C.

Uncertainty analysis

There exist a discrepancy of results obtained with the high temperature probe among the siliceous 5-S and the other concrete mixes. It is worth noting that the boundary conditions in all tests were the same and the changes were mainly produced by the different materials tested. The repetition of the tests was done following the same procedure, i.e., the calibration process, thermal regime, heat source, power and thermal conductivity probes. The uncertainties in engineering experiments were described as “variable but deterministic” and are the errors that change during an experiment [9]. In fact, the author highlighted that in experiments including heat transfer and high temperature the source of errors might be produced for several factors such as system disturbance effects or interactions between the system and the sensor among others. For that reason, these conceptual disturbances difficult to find the connection between the estimation and the source of error.

Table 4.3 shows the mean values and the interval of the uncertainty of thermal conductivity for the first heating. The 5-S experienced bigger variation at high temperatures. Several sources might have been caused the errors such as the creation of air gaps due to microcracks in the material. The cracks affect negatively the thermal conductivity, and the probe is very sensitive to changes in the thermal performance. On the other hand, a previous

study showed that siliceous mixes lose more mass during the drying stage due to water evaporation, indicating that the high value of thermal conductivity at room temperature was owing to higher humidity in the composition [3]. The humidity might be altered the wires of the probe and for that reason, the measurements from 100 to 600°C showed the biggest variation in the repeated measurements.

| Material | 100°C | 200°C | 300°C | 400°C | 500°C | 600°C |
|-----------------|----------------|----------------|----------------|----------------|----------------|----------------|
| 1-C | 1.18 ± 0.20 | 1.35 ± 0.26 | 1.03 ± 0.17 | 0.92 ± 0.07 | 1.03 ± 0.22 | 1.06 ± 0.24 |
| 2-B | 1.32 ± 0.52 | 1.34 ± 0.61 | 1.36 ± 0.32 | 1.28 ± 0.64 | 0.97 ± 0.16 | 1.45 ± 0.77 |
| 3-B-C-S | 1.23 ± 0.47 | 1.15 ± 0.33 | 1.12 ± 0.24 | 1.04 ± 0.15 | 0.96 ± 0.11 | 0.99 ± 0.14 |
| 4-CAL | 1.11 ± 0.28 | 1.23 ± 0.24 | 1.23 ± 0.13 | 1.09 ± 0.12 | 1.04 ± 0.10 | 0.86 ± 0.10 |
| 5-S | 1.96 ± 0.45 | 2.08 ± 0.95 | 2.23 ± 0.68 | 1.34 ± 0.30 | 1.20 ± 0.10 | 1.30 ± 0.11 |

Table 4.3: Mean values and uncertainties of thermal conductivity for the first heating up to 600°C.

Effect of the aggregates

Not only the thermal conductivity of the aggregates is important but also the thermal expansion. More thermal expansive aggregates might induce a higher risk of microcrack formation, and this effect is increased because of the shrinkage of the cement paste [6]. The $\Delta L/L_0$ experienced by the aggregates up to 600°C ranges from 0.5-1.5% depending on the type of aggregate and the cement paste varies from -1 to -2% of length change [6]. The cracks are originated from 100°C and when the temperature rises the density of cracks is increased, as reported in [20]. The appearance of cracks implies the creation of gaps within the material and, thus, the creation of another thermal resistance inside the material. In dry conditions, these interstices are filled with air, whose thermal conductivity differs orders of magnitude from the solid medium. Heat transfer is affected because there is not only conduction but convection also as mechanisms of transporting the heat.

Siliceous aggregates are more thermally conductive but also expansive. The CTE grows with the temperature, as reported in [6]. As a consequence, a concrete mix with siliceous aggregates can be more prone to crack under certain conditions [3, 21]. In fact, in this study, the 5-S mix experienced another significant drop in the thermal conductivity at temperatures between 300 and 400°C, achieving similar values of thermal conductivity than compositions with more thermally stable and less heat conductive aggregates. On the other hand, thermal conductivity is not only affected by the generation of cracks but also by changes in the crystallinity in the aggregates, as was reported in [22].

Effect of the heating rate

Additionally, another test was done in the 3-B-C-S mix for evaluating the effect of using different heating rates: 0.5 and 1°C/min. The results (displayed in Figure 4.14) indicate that using these two heating rates the evolution of the thermal conductivity followed the same

pattern: i) decrease when heating up to 100°C, ii) slightly increase at 200°C, iii) another decrease at 300°C, and iv) slight decrease or constant value when heating up to 600°C. This test shows that the heating rate may have some effects on the measured thermal conductivity, but the trend is maintained. In this research, the heating rate of 1°C/min was selected, since it is a commonly used heating rate [20, 23].

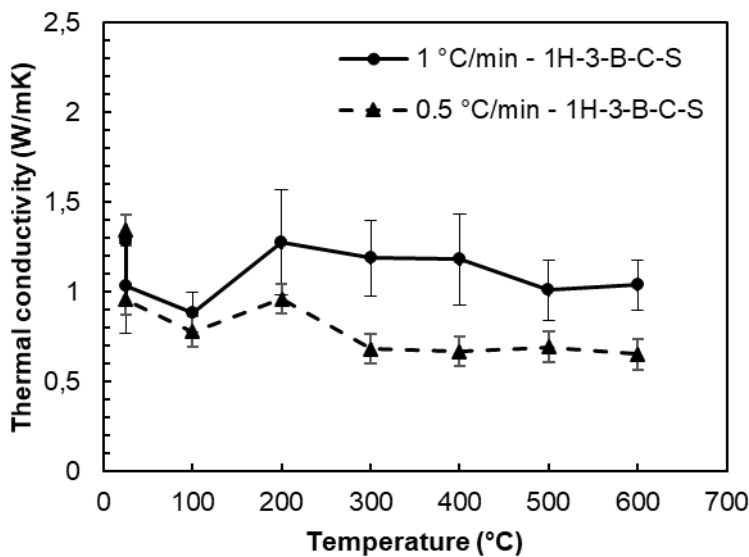


Figure 4.14: Evolution of thermal conductivity up to 600°C for the 3-B-C-S with different heating rates.

4.3.2.3. Thermal fatigue stage (cycles from 300 to 600°C)

This section presents the evolution of thermal conductivity when temperature ranged between the operating regime (300-600°C). The code used for the different stages was: first heating up to 600°C (1H); first cooling from 600 to 300°C (1C); second heating from 300 to 600°C (2H) and the second cooling down to room temperature (2C). The legend shows the previous code followed by the type of cement, CAC and the type of aggregate: C (CAT), B (basalt), B-C-S15 (basalt, CAT and Slag), CAL (calcareous) and S (siliceous). The results are presented in two subsections related to the heating and cooling processes. Both sections show graphs including the first processes (1H or 1C) with solid lines and the second processes (2H or 2C) represented with dashed lines.

Effect of the heating in the thermal fatigue cycles from 300 to 600°C (1H and 2H)

Figure 4.15 shows the evolution of thermal conductivity during the two heating processes up to 600°C in all concrete mixes. Whereas the first heating is a process mainly influenced by physicochemical changes, the successive heating cycles are expected to be affected by the degradation of the material due to thermal fatigue.

The specimens followed the same pattern during the first heating (1H) and during the second heating (2H). In the second heating, the thermal conductivity decreased until reaching the same previous value obtained at 600°C during the first heating. The mixes recorded similar values at 600°C in both heating cycles, but the siliceous composition (5-S) had a decrease of 7 % with respect to the thermal conductivity obtained in the first heating. Despite this slight difference, the experimental tests have proved similar patterns and stability during the cycles performed.

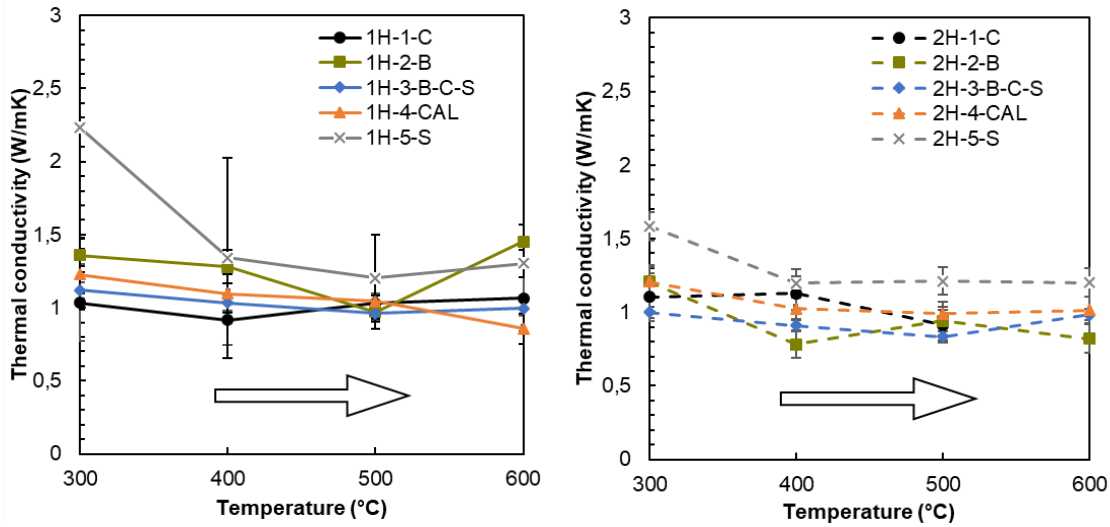


Figure 4.15: Evolution of thermal conductivity when heating from 300°C to 600°C during the 1H and 2H for the CAC concrete mixes.

The experimental tests showed a slow degradation of thermal conductivity that seems to stabilize, but the long-term performance is not demonstrated in this work. Cyclic operating conditions above the 3rd thermal cycle are not reproducible at lab-scale with the setup of this study, since the time of testing of each sample exceeded 10 days and the degradation of the wires of the high-temperature probe made it not possible to obtain accurate measurements at longer testing times.

Regarding the variation between the two heating processes, Figure 4.16 shows the percentage of modification experienced by the concretes at the same temperature of testing. There exists a stabilization between 400 and 500°C with a variation lesser than 10% in all cases excluding the basalt composition. When the temperature increased up to 600°C, the calcareous mix experienced another significant drop, with a percentage of change of nearly 20%, whereas the other mixes remained with changes around 10%.

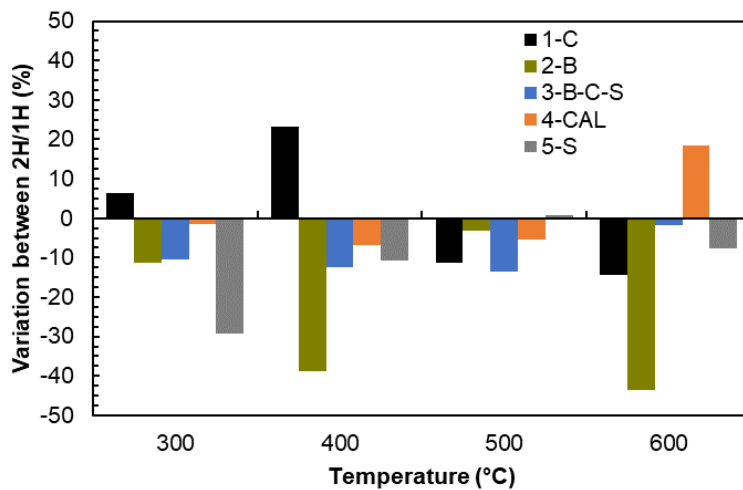


Figure 4.16: Percentage of variation between the two heating processes.

Effect of the cooling in the thermal fatigue cycles from 600 to 300°C (1C and 2C)

The evolution of thermal conductivity during the two cooling processes is shown in Figure 4.17. Thermal conductivity of the concrete mixes might be assumed constant within the fatigue tests between 300-600°C only for the ternary mix. Despite having more thermal stable aggregates, the basalt mix (2-B) test showed scattered values, in this case, due to the damage of the high-temperature wires while testing. The mix with calcareous aggregates in 4-CAL obtained the highest variability of the thermal conductivity. When the temperature decreased to 300°C, there was a slight recovery of the thermal conductivity in all the mixes, which was more notable for the 4-CAL (40%) and 5-S (22%) mixes. In the second cooling down to room temperature, calcareous and siliceous mixes recovered between 15-30% of the value of thermal conductivity at 600°C, while the mix with basalt aggregates experienced a decrease of 8% and the ternary mix showed almost constant values.

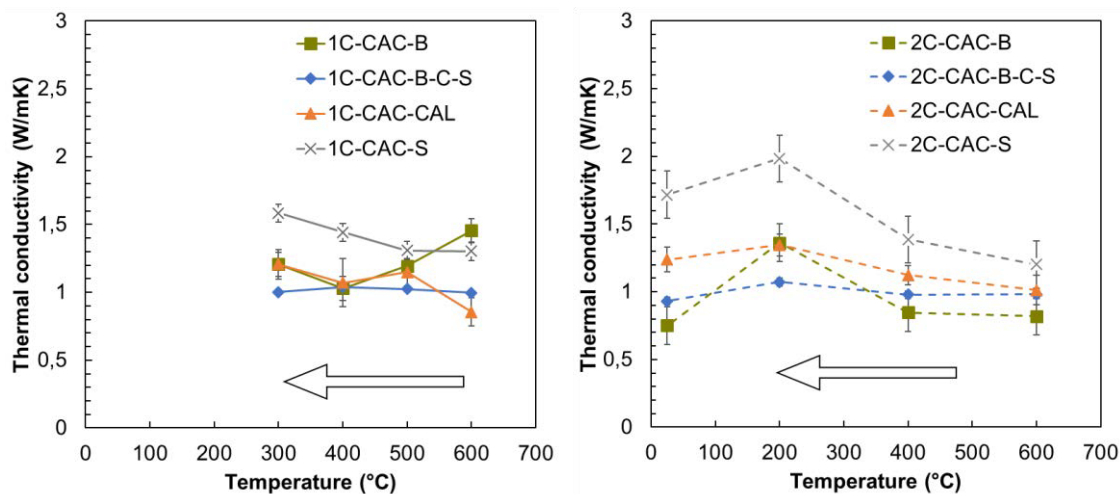


Figure 4.17: Evolution of thermal conductivity when cooling from 600°C to 300°C (1C) and from 600 to 25°C (2C) for the CAC concrete mixes.

In the literature, several authors reported that the thermal conductivity remained almost constant when concrete was cooled down [18, 24]. In one study [18], the values were measured by using the transient plane source for an SCC concrete with PPF, and the temperatures analysed when cooling were 500, 200 and 20°C, and these differences do not allow a fair comparison with the tests carried out in this work.

Regarding the variation in the cooling processes, Figure 4.18 shows the percentage of modification experienced by the concretes at the same temperature of testing. The most significant is the variation of the thermal conductivity at room temperature between the value before and after the test, ranging between 25-45% for the concrete mixes. For temperatures of 200 and 400°C, the changes were below 8% in the mixes, excluding the basalt composition.

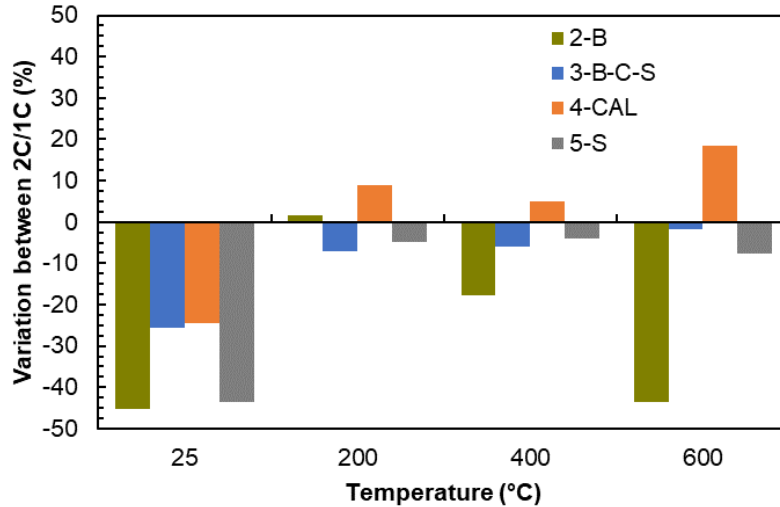


Figure 4.18: Percentage of variation between the two cooling processes.

4.3.2.4. Microstructure after the thermal fatigue stage

Figure 4.19 shows an example of a picture taken on the surface of one 5-S concrete sample after two thermal cycles. The crack width values are included in different locations of the picture. The widths were measured ten times in all concrete compositions. The microcracks appeared close to the pores and in the interface between the cement paste and the aggregates. It is important to note that those cracks are the result of the thermal test because the pictures were taken at residual conditions. At higher temperatures, during real operating conditions, when aggregates are increasing their volume, the cracks might be even lower than the ones represented in Figure 4.19.

Regarding the microcracks, all concrete mixes experienced cracks of widths below 80 µm (Figure 4.20). The mixes with calcareous and siliceous aggregates (4-CAL and 5-S) experienced the biggest microcracks with mean values of 15 and 55 µm, respectively. The biggest cracks found in the 5-S explained the highest decay in the thermal conductivity experienced by this concrete mix compared to the other materials tested. According to the more stable aggregates, the ternary mix (3-B-C-S) and basalt composition (2-B) experienced the narrower crack widths with values below 10 µm and 12 µm, respectively. These results are in accordance with other values reported in the literature for residual conditions, whose concretes experienced cracks between 50-80 µm after one thermal fatigue cycle between 290-550°C [25].



Figure 4.19: Example of microscopic analysis after the thermal exposure for the 5-S composition (each value of “length” indicates the crack width measured at the point indicated).

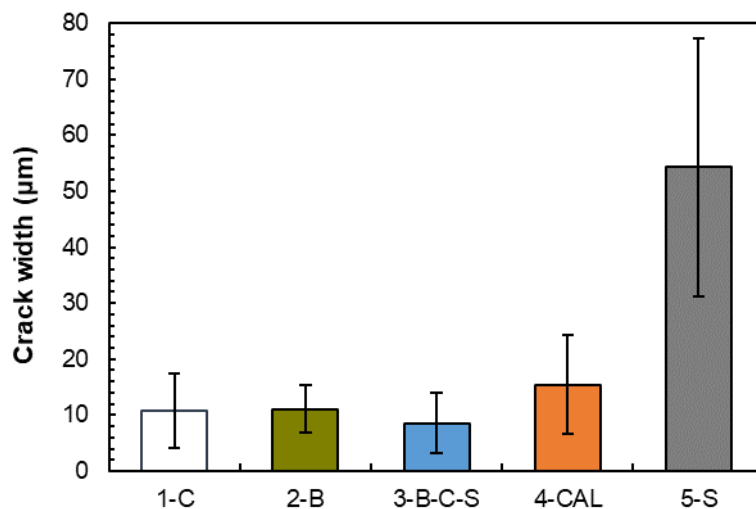


Figure 4.20: Crack width for the concrete mixes after the thermal cycle.

4.3.2.5. Relationships for thermal conductivity at high temperatures

Recently, the number of simulations of CTES has increased due to its suitability for working at high temperatures. However, the evolution of concrete thermal conductivity at temperatures up to 600°C is required to be used for those simulations and to improve the knowledge and the results of the heat transfer theoretical models.

To provide new information in this matter, this work aims to provide equations to calculate thermal conductivity as a function of temperature based on the experimental results

obtained at high temperatures. Five compositions of CTES have been tested using CAC cement and different aggregates. The formulas for the thermal conductivity were obtained by curve fitting and are collected in **Appendix A**. These relationships can be used as an input for numerical heat transfer models at high temperatures. This study has allowed the validation of the protocol at the laboratory, with an improvement in the Technology Readiness Level up to TRL 4.

Figure 4.21 shows the evolution of thermal conductivity of the 3-B-C-S mix with the temperature for the 2 thermal cycles, differentiating the heating and cooling stages. The curves were obtained from the fitted equations collected in **Appendix A** and followed a polynomial equation of second order. The evolution of thermal conductivity highlights the dependence with the temperature for the range of operation of applications of CSP Plants. For that reason, assuming a constant value may not be suitable for making predictions on the overall thermal performance of certain applications of concrete working at high temperatures.



Figure 4.21: Evolution of thermal conductivity of 3-B-C-S with temperature for successive heating and cooling processes obtained from fitted equations.

Regarding the stability of the thermal parameter during the long-term operation, additional thermal cycles are needed to make an appropriate prediction. With the present data available in this work, a linear regression was made to have a first approach on the stabilization of the thermal conductivity at both 300 and 600°C along with the thermal fatigue cycles. The prediction for the 3-B-C-S mix is shown in Figure 4.22. For this concrete composition working under heating and cooling cycles between 300 and 600°C the stabilization of thermal conductivity would be reached around the 10th cycle, achieving a value of 0.95 W/(m·K) at 600°C and 1.01 W/(m·K) at 300°C. Nonetheless, this preliminary model needs further verification with additional experimental tests, which could not be performed due to the limitations in the durability of working at high temperatures of the available wires for this research. Additional research aiming to add insights in this matter should target at least 10 cycles to verify if the thermal conductivity equation converges.

Anyway, the long-term performance should be tested at up-scaled levels in a real prototype of CTES in a CSP, since the data available of the behaviour of this material at operating conditions is still scarce.

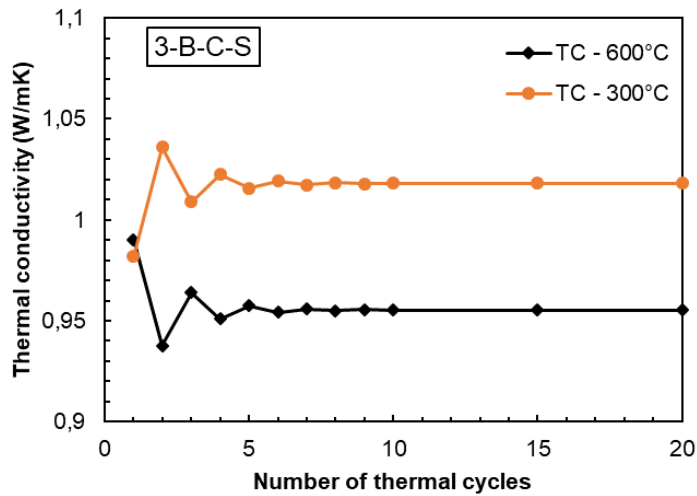


Figure 4.22: Estimation of thermal conductivity at 600°C during the thermal cycles of 3-B-C-S concrete mix.

In summary, assuming a constant value of thermal conductivity in simulations of heat transfer when concrete is exposed to high temperatures seems not accurate, at least for the first thermal cycles. After a certain number of thermal cycles (estimated around 10 cycles), the equation describing thermal conductivity change with temperature between 300 and 600°C may stabilize, which in case of being confirmed experimentally, would smooth the modellers task.

4.3.3. Partial conclusions on the evolution of thermal conductivity at high temperature

In this chapter, the evolution of the thermal conductivity at high temperatures of different concrete compositions exposed up to 600°C and during repetitive thermal cycles was carried out. In particular, an analysis of the effect on the aggregates, heating rate and the thermal fatigue under service operation between 300-600°C has been analysed in detail. Based on the experimental results presented in this work, the following conclusions can be drawn:

- The thermal conductivity of concrete at high temperatures depends on the concrete mix and the aggregates. At room temperature, the values of thermal conductivity range for most of the concrete studied between 1.2-2 W/(m·K), range obtained in concretes with calcareous, basalt, CAT and their combinations of aggregates. The use of siliceous aggregates improved thermal conductivity.
- In all the mixes, the biggest loss in the thermal conductivity takes place during the drying stage due to the loss of free water. When heating up to 600°C, the siliceous mix experienced the biggest drop ($\downarrow 50\%$) in the thermal conductivity compared to its initial value, while CAT and ternary mixes displayed more stable behaviour.
- In the first cooling down to 300°C, the thermal conductivity of most concrete mixes does not vary significantly, but siliceous and calcareous mixes recovered between 20-

40% of the value at 600°C. In the second heating, the thermal conductivity achieves again the previous values at the equivalent temperatures. The last cooling produced a slight recovery in the thermal conductivity when samples were cooled at 200°C in mixes using siliceous, calcareous and basalt aggregates whereas the other mixes maintained the same value of the thermal parameter.

- The concrete mixes analyzed, excluding the siliceous mix, are recommended for thermal energy storage applications with temperatures between 290-550°C (as expected in TES systems with molten salts as HTF), because of the stabilization of their thermophysical properties.
- The assumption of constant thermal conductivity in simulations of CTES is not appropriate for the first operating cycles and has to be decided depending on the concrete compounds. For longer-term cycles, further research is needed.
- The development has allowed the validation of the protocol at the laboratory, with an improvement in the Technology Readiness Level up to TRL 4.

(Chapter 5 on page 111)

4.4. References

- [1] F. P. Incropera, *Introduction to Heat Transfer*. (5th ed. ed.) Hoboken, NJ: Hoboken, NJ : John Wiley & Sons, 2006.
- [2] C. R. C. Rao, H. Niyas and P. Muthukumar, "Performance tests on lab-scale sensible heat storage prototypes," *Applied Thermal Engineering*, vol. 129, pp. 953-967, 2018. Available: <http://www.sciencedirect.com/science/article/pii/S1359431117353991>. DOI: <https://doi.org/10.1016/j.applthermaleng.2017.10.085>.
- [3] T. Lucio-Martin, M. Roig-Flores, M. C. Alonso and L. Guerreiro, "Evolution of thermal conductivity on CAC concrete at high temperatures and during thermal fatigue tests." vol. Proceedings of the 6th International Workshop on Concrete Spalling due to Fire Exposure, 2019.
- [4] U. Schneider, "Concrete at high temperatures—a general review," *Fire Saf. J.*, vol. 13, (1), pp. 55-68, 1988.
- [5] V. Kodur and W. Khalil, "Effect of Temperature on Thermal Properties of Different Types of High-Strength Concrete," *J. Mater. Civ. Eng.*, vol. 23, (6), pp. 793-801, 2011.
- [6] Z. P. Bazant and M. F. Kaplan, *Concrete at High Temperatures: Material Properties and Mathematical Models*. Longman, 1996.
- [7] R. Pérez-López, A. M. Álvarez-Valero, J. M. Nieto, R. Sáez and J. X. Matos, "Use of sequential extraction procedure for assessing the environmental impact at regional scale of the São Domingos Mine (Iberian Pyrite Belt)," *Applied Geochemistry*, vol. 23, (12), pp. 3452-3463, 2008. Available: <http://www.sciencedirect.com.biblioteca5.uc3m.es/science/article/pii/S088329270800284>. DOI: <https://doi-org.biblioteca5.uc3m.es/10.1016/j.apgeochem.2008.08.005>.
- [8] H. Freitas, M. N. V. Prasad and J. Pratas, "Plant community tolerant to trace elements growing on the degraded soils of São Domingos mine in the south east of Portugal: environmental implications," *Environment International*, vol. 30, (1), pp. 65-72, 2004. Available: http://www.sciencedirect.com.biblioteca5.uc3m.es/science/article/pii/S016041200300149_1. DOI: [https://doi-org.biblioteca5.uc3m.es/10.1016/S0160-4120\(03\)00149-1](https://doi-org.biblioteca5.uc3m.es/10.1016/S0160-4120(03)00149-1).
- [9] R. J. Moffat, "Describing the uncertainties in experimental results," *Exp. Therm. Fluid Sci.*, vol. 1, (1), pp. 3-17, 1988.
- [10] V. Antonovič, J. Kerienė, R. Boris and M. Aleknevičius, "The Effect of Temperature on the Formation of the Hydrated Calcium Aluminate Cement Structure," *Procedia Engineering*, vol. 57, pp. 99-106, 2013. Available: <http://www.sciencedirect.com/science/article/pii/S1877705813007455>. DOI: <https://doi.org/10.1016/j.proeng.2013.04.015>.
- [11] Y. Collet, "Etude des Propriétés du Béton soumis à des Températures Elevées," *Ann Trav Publics Belg*, (4), 1977.

- [12] A. Millard and P. Pimienta, *Modelling of Concrete Behaviour at High Temperature. State-of-the-Art Report of the RILEM Technical Committee 227-HPB*. Springer, 2019.
- [13] Z. Xing, A. Beaucour, R. Hebert, A. Noumowe and B. Ledesert, "Influence of the nature of aggregates on the behaviour of concrete subjected to elevated temperature," *Cement and Concrete Research*, vol. 41, (4), pp. 392-402, 2011. Available: <http://www.sciencedirect.com/science/article/pii/S0008884611000068>. DOI: <https://doi.org/10.1016/j.cemconres.2011.01.005>.
- [14] C. Guo, J. Zhu, W. Zhou and W. Chen, "Fabrication and thermal properties of a new heat storage concrete material," *J. Wuhan Univ. Technol. -Mat. Sci. Edit.*, vol. 25, (4), pp. 628-630, 2010. . DOI: 10.1007/s11595-010-0058-3.
- [15] N. Hoivik, C. Greiner, J. Barragan, A. C. Iniesta, G. Skeie, P. Bergan, P. Blanco-Rodriguez and N. Calvet, "Long-term performance results of concrete-based modular thermal energy storage system," *Journal of Energy Storage*, vol. 24, pp. 100735, 2019. . DOI: 10.1016/j.est.2019.04.009.
- [16] D. Laing, C. Bahl, T. Bauer, M. Fiss, N. Breidenbach and M. Hempel, "High-temperature solid-media thermal energy storage for solar thermal power plants," *Proc IEEE*, vol. 100, (2), pp. 516-524, 2011.
- [17] Z. Xing, A. Beaucour, R. Hebert, A. Noumowe and B. Ledesert, "Aggregate's influence on thermophysical concrete properties at elevated temperature," *Construction and Building Materials*, vol. 95, pp. 18-28, 2015. Available: <http://www.sciencedirect.com/science/article/pii/S095006181530057X>. DOI: <https://doi.org/10.1016/j.conbuildmat.2015.07.060>.
- [18] R. Jansson, "Measurement of concrete thermal properties at high temperature," *Proceedings from the Fib Task Group*, vol. 4, pp. 2-3, 2004.
- [19] European Committee for Standardisation, (CEN), *Eurocode 2: Design of Concrete Structures - Part 1-2: General Rules - Structural Fire Design*. Brussels: 2004.
- [20] P. Pimienta, R. J. McNamee and J. Mindegua, *Physical Properties and Behaviour of High-Performance Concrete at High Temperature*. Springer, 2018.
- [21] S. P. Senadheera and D. G. Zollinger, "Influence of coarse aggregate in portland cement concrete on spalling of concrete pavements," 1996.
- [22] Y. S. Touloukian, R. W. Powell, C. Y. Ho and P. G. Klemens, "Thermophysical Properties of Matter - The TPRC Data Series. Volume 2. Thermal Conductivity - Nonmetallic Solids," 1971.
- [23] M. C. Alonso, J. Vera-Agullo, L. Guerreiro, V. Flor-Laguna, M. Sanchez and M. Collares-Pereira, "Calcium aluminate based cement for concrete to be used as thermal energy storage in solar thermal electricity plants," *Cement and Concrete Research*, vol. 82, pp. 74-86, 2016. Available: <http://www.sciencedirect.com/science/article/pii/S0008884615003075>. DOI: <https://doi.org/10.1016/j.cemconres.2015.12.013>.

[24] K. Ödeen and Å Nordström, "Thermal properties for concrete at high temperatures," *Statens Provningsanstalt, Brandtekniska Laboratoriet, Stockholm*, 1972.

[25] M. C. Alonso and J. Puentes, "Self-Compacted Concrete with Self-Protection and Self-Sensing Functionality for Energy Infrastructures," *Materials*, vol. 13, (5), pp. 1106, 2020.

This page has been intentionally left blank.

Chapter 5

Monitoring of the commissioning of concrete before the CSP operation

The present chapter deals with the commissioning of a concrete infrastructure before starting with the operation at high temperatures of the facility. With such aim, the problem with the moisture content of the concrete was presented in *section 5.1*, as well as the changes that are produced within the material during the drying process when it is exposed to high temperatures.

Later in this chapter, we will propose a methodology for following the drying process by monitoring the structure and evaluating the evolution of the drying in real time. This methodology, explained in *section 5.2*, was applied in different compositions and its particularities are provided in *section 5.3*.

At the end of this chapter, in *section 5.4*, some conclusions related to the monitoring of concrete during the drying process at high temperatures before the operation at higher temperatures are given.

5.1. Introduction: Moisture content preconditioning

The need for appropriate commissioning of a concrete infrastructure before start operating the facility at high temperatures is essential. The present thesis has proved the changes in the thermophysical and chemical parameters with temperature and suitable commissioning of the concrete will have an impact on the further operation of the infrastructure.

On the other hand, as was dealt in **Chapter 3**, the risk of spalling increases when concrete is being heated due to the release of water and the evaporation of this component [1] and the thermal gradients between the surface exposed to heat and the core, which originates stresses and pore pressures fire [2-4]. Although the contingency of incorporating spalling retarders agents, such as Polypropylene fibres (PPF) that were included in the designs of concretes (**Chapter 3**), the verification of drying and dehydration processes of concrete at high temperature is fundamental before the commissioning and operation of the concrete

infrastructure in the CSP Plant. The temperatures and, hence, the thermal gradients can be followed easily by embedding thermocouples within the concrete infrastructure. Nevertheless, the monitoring of the moisture content of the concrete and the evaporation and evacuation of the water is not trivial in a facility of large dimensions. That is the reason why the concrete needs to be dried accurately before the testing at high temperatures.

The electrical resistance of concrete is a parameter that can be used for determining the interconnections between the pores inside the material and the level of saturation. The concrete is a compound and porous material and the electrical resistance is highly dependant on the moisture content and, thus, the degree of saturation of the pores. Therefore, the electrical resistance can show more conductive or isolating electrical properties when the parameter measured reaches low or high values, respectively. The measure of the electrical resistance is thought to be another parameter for detecting the level of drying of the concrete (TRL 2). The goal is to detect the free water loss out of concrete when the material is being heated. Initially, the pores of the concrete contain water and while the material is being heated, the water is substituted by air/vapour. As the water is more electrically conductive, once the material is dried, the concretes become less conductive and, hence, the electrical resistance increase. At this step, the material can be assumed completely dried and has no free water inside.

The protocols followed at the lab scale needs to be adapted for following the drying process in a real structure, independently of the type of concrete, geometry and dimensions. This chapter provides the commissioning of a test protocol for measuring the electrical resistance at high temperature during the drying stage for different types of concrete. The aim is to prove whether the concept (TRL 2) is able to follow the drying process at the laboratory, achieving an improvement in the technology up to TRL 4. The suitability of this test protocol for the commissioning of the drying process of concrete infrastructures is analysed.

5.2. The methodology of the drying process

This test aims to determine the evolution of the drying process when concrete is exposed to high temperatures. With such an aim, the experimental protocol described in this chapter follows the evolution of mass and electrical resistance with temperature.

The expressions of variations of mass depending on temperature will be of interest in modelling the behaviour of concrete exposed to heat. For that purpose, different types of concrete were tested under temperatures up to 600°C to go deeper in the drying process and the mass variations which take place at higher temperatures due to the processes of drying (loss of free water) and dehydration of cement paste and for the thermal cycling tests during cycles of heating and cooling (charge and discharge of thermal energy).

Additionally, thermal conductivity is measured before and after the drying process, as well as the changes in the pores due to the evaporation of water that takes place in the process.

5.2.1. Materials

A set of four concrete mixes were evaluated made of CAC and OPC cements. The mixes were made using different type of aggregates and concrete admixtures to evaluate differences

in thermal and electrical performance. The dosages of the concrete mixes are not given because some of them are commercial products. Nonetheless, the following characteristics of them are mentioned: 1) Ultra-High-Performance Fibre Reinforcement Concrete, namely UHPFRC, is a concrete that presents high compressive strength (140–150 MPa) [5], made of OPC, siliceous sand and steel fibres; 2) Normal Strength Concrete, namely OPC-Core, made of OPC, siliceous aggregates and both steel and polypropylene fibres; 3) an Insulating concrete, namely OPC-Insulating, made of OPC and expanded polystyrene (EPS) and 4) the CAC-Ternary mix, made of CAC and basalt, CAT and Slag aggregates and polypropylene fibres, whose dosage is shown in **Chapter 3** and **4**.

The specimens were cast in prismatic moulds of $40 \times 40 \times 160$ mm³ and were cured in a humidity chamber at 95% of relative humidity and 20°C until the age of testing.

5.2.2. Methodology

5.2.2.1. System description

To evaluate the drying stage, the electrical resistance parameter was measured as well as the evolution of the temperature in the core of the sample over time and the mass loss. Three samples per type of concrete of $40 \times 40 \times 160$ mm³ were needed for performing the tests. One of them had a K-type thermocouple embedded for recording the temperature inside the material; another had two metallic grids embedded, to register the electrical resistance and the other one was free of sensors, for the mass evaluation. The final aspects of the three types of samples used for carrying out the tests are shown in Table 5.1.

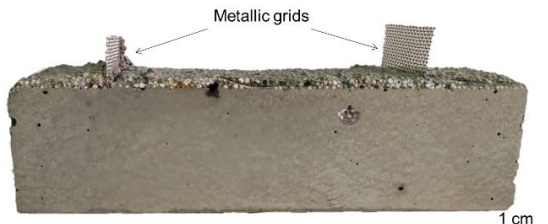
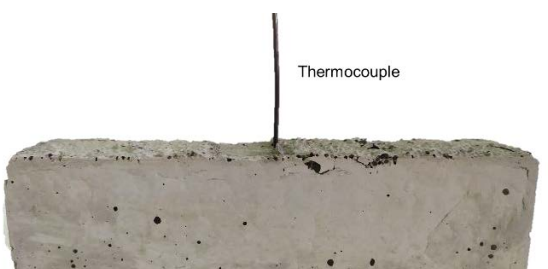
| Description | Picture of the sample |
|--|--|
| Instrumented with 2 metallic grids for measuring the electrical resistance. |  <p>Metallic grids</p> |
| Instrumented with a thermocouple for recording the evolution of the temperature in the core. |  <p>Thermocouple</p> |
| Empty for measuring the evolution of mass. |  |

Table 5.1: Instrumentation of samples for carrying out the tests.

Two options are considered based on changes in the physical properties of the concrete (electrical resistance and mass loss) to identify the level of drying. The test system comprises various components. Two electric furnaces were needed, one of them included the samples instrumented with thermocouples and metallic grids and another contained the empty samples. The electrical furnace containing the instrumented specimens is from Eurotherm and has 15 kW of power, and the model of the chamber furnace is MLR11 305/16. The maximum operating temperature of the oven was 1100°C and it has a control system able to carry out the heating and cooling cycles with controlled rates. The smaller electric furnace that contained the samples that were not instrumented is from SATER and has 1 kW of power with a maximum operating temperature of 1300°C, able to perform heating and cooling cycles at a fixed heating rate.

For measuring the electrical resistance parameter, a data acquisition unit was used. The model was Agilent 34970A and the data were recorded continuously by using the module Keysight 34901A. The equipment gives the electrical parameter because it can be recorded by opening one channel of the module directly. The range of measure varies between 0 to $10^8 \Omega$. The measure of the electrical resistance is done between two metallic grids embedded in the concrete samples of $40 \times 40 \times 160 \text{ mm}^3$. While the electrical resistance is measured continuously, the mass loss is a discrete measure. The equipment for measuring the evolution of mass was a balance, model CENT-2 from Gibertini Europe and it has an accuracy of $\pm 0.1 \text{ g}$.

The output parameters measured were: temperatures inside the samples and within the furnace, the evolution of mass and the electrical resistance. Additionally, 2 thermocouples were included inside the furnaces to follow the evolution of the temperature inside them. The calibrated K-type thermocouples have an accuracy of $\pm 0.1^\circ\text{C}$. All temperature data were collected and recorded through a data acquisition system (Model: Agilent 34970A) directly by an external data logger. The complete system was placed inside the furnace and the setup is shown in Figure 5.1 and Figure 5.2. Remarkably, the samples UHPFRC were placed inside a metallic mesh because of its risk of spalling, as can be appreciated in Figure 5.2-left.

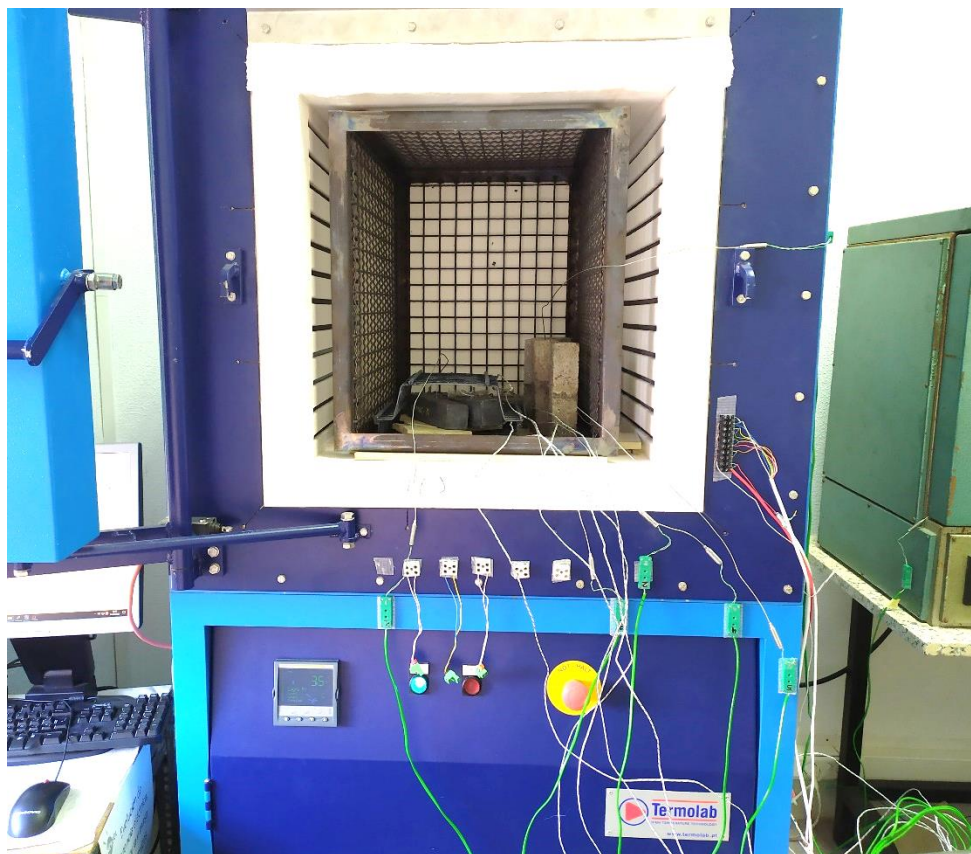


Figure 5.1: Picture of the furnace with instrumented samples.



Figure 5.2: left) detail of metallic mesh containing UHPFRC samples and right) picture of empty samples.

5.2.2.2. Thermal regime

Two different tests were implemented in order to determine the evolution of the thermal and electrical parameters with the temperature:

- 1) Test 1: Evolution of parameters up to 600°C and during thermal cycles.

The evolution of the parameters with temperature was evaluated for a first heating up to 600°C and for thermal cycles between 300-600°C, whose cycle and stages are illustrated in Figure 5.3. For the thermal exposure, three stages were analysed: i) drying up to 105°C for 72

hours, simulating the loss of free water (underlined below), ii) the dehydration of the cement pastes and first heating up to 600°C (in **bold** below) and iii) thermal cycles between 300-600°C (in *italics* below). The sequence of temperatures evaluated was: 25-105-**200**-**300**-**400**-**500**-**600**-500-400-300-400-500-600-400-200-25°C.



Figure 5.3: Thermal cycle and stages

- 2) Test 2: Evolution of the parameters during a drying stage up to 29 weeks.

This test aimed to determine the time at which the material was completely dried, having the heat source at 105°C. For that purpose, the evolution of the free water loss was followed by measuring the electrical resistance (continuously) and the mass at different stages of drying, focusing the beginning of the test for having better accuracy. The punctual measures of mass were obtained: hourly at 0, 0.5h, 1h, 2h, 2.5h, 3h, 3.5h, 4h, 4.5h, 5h, 5.5h, 6h and after 24h, 25h, 26h, 27h, 28h; daily up to 900h and then, weekly up to 29 weeks and 5000 hours.

In both tests, the level of drying was obtained through the following expression:

$$\text{Level of drying (\%)} = \frac{m_i - m_0}{m_e - m_0} \cdot 100 \quad (4)$$

where:

m_i mass in the instant i (g)

m_0 mass at the beginning of the test (g)

m_e mass at the end of the drying stage (g)

Additional parameters were measured such as the thermal conductivity and porosity before and after the drying process. The thermal conductivity equipment was QTM-700 from Kyoto Electronics Manufacturing, whose characteristics were described in **Chapter 4**. Regarding the porosity, it was identified by mercury intrusion porosimetry (MIP). The MIP measurements were conducted by using Micrometrics Autopore IV 9500 porosimeter.

Table 5.2 summarises the tests carried out in the four concrete mixes before the thermal exposure, during the drying and thermal cycling stage and at residual conditions once the samples were cooled down to room temperature.

| | Initial conditions | Drying stage | Thermal cycling stage |
|---------------|---------------------------|---------------------------|---|
| Test 1 | - Mass | <u>96 hours at 105°C:</u> | <u>1st heating up to 600°C and cooling and heating cycles between 300-600°C:</u> |
| | | - Mass loss | |
| | | - Percentage of mass loss | |
| | | - Electrical resistance | - Mass loss with the temperature. |
| | Initial conditions | Drying stage | Residual conditions |
| Test 2 | - Mass | <u>29 weeks at 105°C:</u> | - Thermal conductivity |
| | - Thermal conductivity | - Evolution of mass loss | - Porosity |
| | - Porosity | - Percentage of drying | |
| | | - Electrical resistance | |

Table 5.2: Summary of the tests carried out in this chapter.

Additionally, for the COVID-19 situation, some protective measures were included in the protocol of safety measures mentioned in **Chapter 3**. When a person enters at the laboratory, the use of the hydroalcoholic gel was mandatory. Furthermore, all the surfaces must be cleaned with isopropyl alcohol, including the computer and the surfaces of the furnaces. Also, after the work carried out in the laboratory, all of the tools and surfaces were cleaned again with isopropyl alcohol.

5.3. Results and discussion

5.3.1. Test 1: Evolution of parameters for the drying + thermal cycling process up to 600°C

5.3.1.1. Drying stage – 72 h at 105°C

Mass loss

Figure 5.4 shows the percentage of drying at different testing times for all the specimens tested up to 72 hours at 105°C. Regarding the CAC-Ternary concrete, around 70% of the mass was lost for the first 6 hours of exposure at 105°C. According to the OPC-Core and OPC-Insulating, both mixes experienced similar patterns of water loss, being the first 24 hours the period where most water went out of concrete. After 24 hours of starting the test, all concrete mixes lost nearly 90% of the mass lost during drying except the OPC-UHPFRC. In that case, the water loss was evacuated in 55% the first 24 hours of the test, but the material remained losing water up to 96 hours, which might mean that OPC-UHPFRC is not

completely dried and might continue to experience a decrease in the mass for longer exposure times.

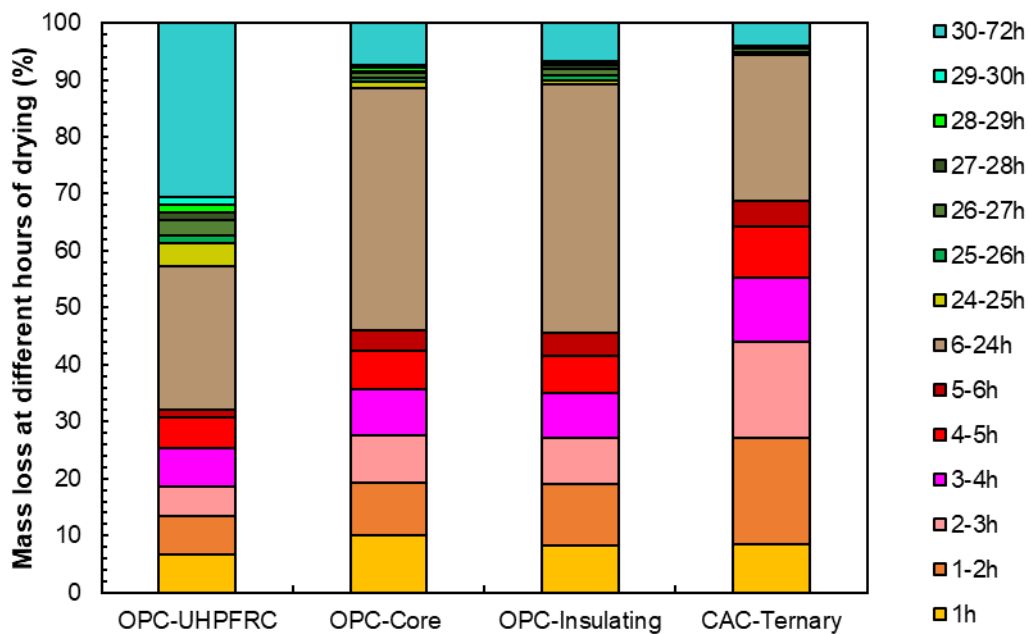


Figure 5.4: Mass loss at different hours of the drying stage for the five materials tested.

Figure 5.5-left represents the percentage of cumulative mass lost in time. OPC-Insulating material was the composition that experienced the biggest loss in the mass, achieving a value of 12%. The high value of mass lost is due to the particularities of this material, which contains exclusively a high content of cement paste and EPS. However, the particularities of the EPS in the material are explained in the following sections. The mixes CAC-Ternary and OPC-Core experienced a mass loss of around 4% and the OPC-UHPFRC a 1.2% of the mass variation. The percentage or level of drying is shown in Figure 5.5-right. The level of drying was above 90% after 24 hours in most cases excluding OPC-UHPFRC.

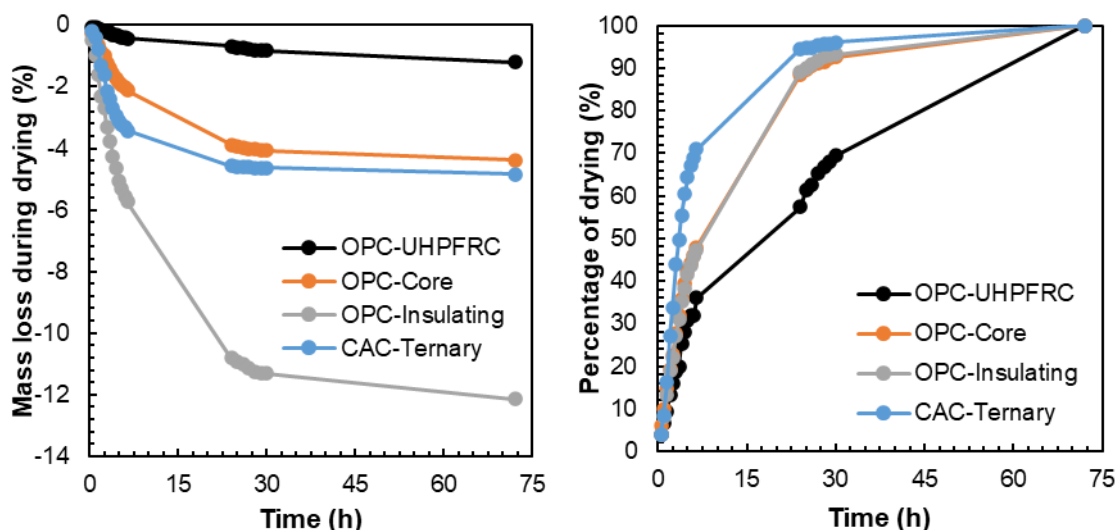


Figure 5.5: left) Evolution of mass during drying and right) level of drying during the testing time.

Electrical resistance during the drying process

Figure 5.6-left shows the evolution of the electrical resistance with temperature for the four materials tested. The electrical resistance decreased in all cases while the concretes were being heated from room temperature up to 100°C because the water located in the pores are mainly liquid and, hence, it is highly electrically conductive. When the material is being heated, the water inside the pores increases its electrical conductivity and for that reason, the materials underwent a decrease in the electrical resistance, as both parameters are proportionally inverse [6]. When the temperature reaches 100°C in the core of the samples, the water comes out of concrete and the electrical resistance increased exponentially due to the vaporization. Therefore, the measure of this parameter allows for detecting free water loss.

Figure 5.6-right shows the evolution of electrical resistance with the testing time. After around 2 hours of starting the test, the electrical resistance started increasing because the whole samples arrive at 100°C. From that moment, the pores of the concrete that initially contained water were substituted by air/vapour while the concretes were being heated. As the water is more electrically conductive, once the material is dried, the concretes become less conductive and, hence, the electrical resistance increase. The drop in the electrical resistance reached 3 and 4 orders of magnitude for CAC-Ternary and OPC-Core and OPC-Insulating, respectively before the measures were out of range at $1.2 \cdot 10^8 \Omega$. In the case of OPC-UHPFRC, the parameter underwent just an increase of 1 order of magnitude, achieving $1.9 \cdot 10^4 \Omega$ after being exposed at 105°C for 72 hours.

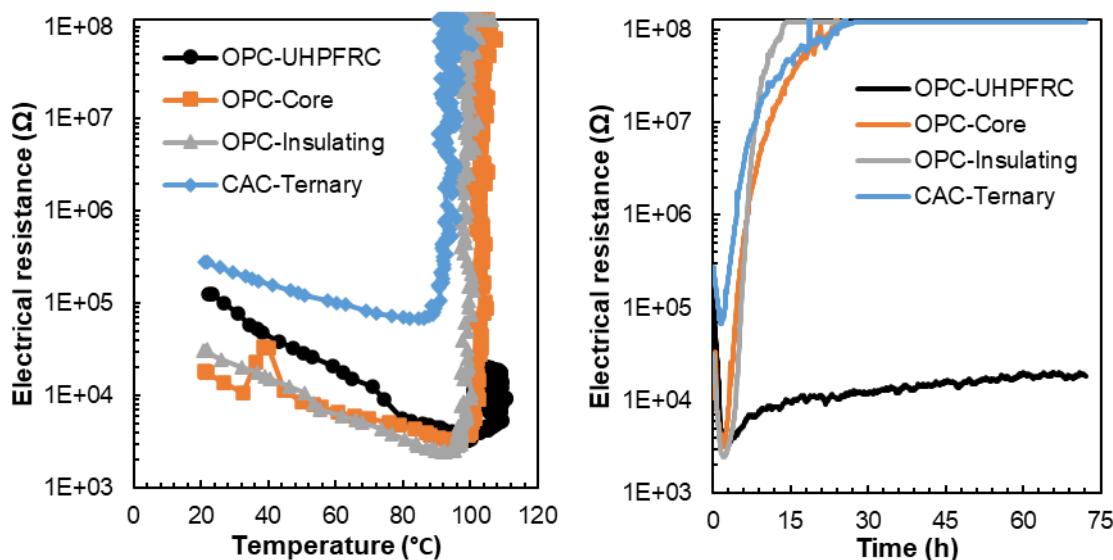


Figure 5.6: Evolution of the electrical resistance: left) with the temperature and right) with the testing time.

The question at this point is whether the material is completely dried and has lost all the free water during the drying process. To verify the level of drying detectable with the equipment, Figure 5.7 shows the evolution of both the electrical resistance and the percentage of drying during the time. CAC-Ternary lost almost all the free water during the first 24 hours after being exposed at 105°C, reaching a percentage of drying of 95%. Moreover, up to this point, there exists a change in the measure of electrical resistivity. Once the material does not have liquid water in the pores, it becomes more insulating to the electrical current flow. Consequently, electrical resistivity achieves higher values and become

out of the range of measurement for the equipment used. The parameter is considered adequate to follow the drying process. The same explanation can be applied to OPC-Core and OPC-Insulating. However, the characteristics of each material make that the free water loss detectable with the equipment was above 90% of the drying process in those materials. However, the OPC-UHPFRC experienced a slower drying process. It could mean that the material has not arrived at the equilibrium in the mass loss and, thus, the drying process is not completed. Another reason why this material underwent slower increases in the electrical resistance is that the free water might be in a lower proportion comparing to the other components of the concrete, due to the low proportion of water used to the high content of cement in this type of concretes [5]. For these reasons, the changes experienced by the material owing to the water loss are not detectable at short drying ages and, hence, the electrical resistance is governed by other components like the steel fibres and the siliceous sand.

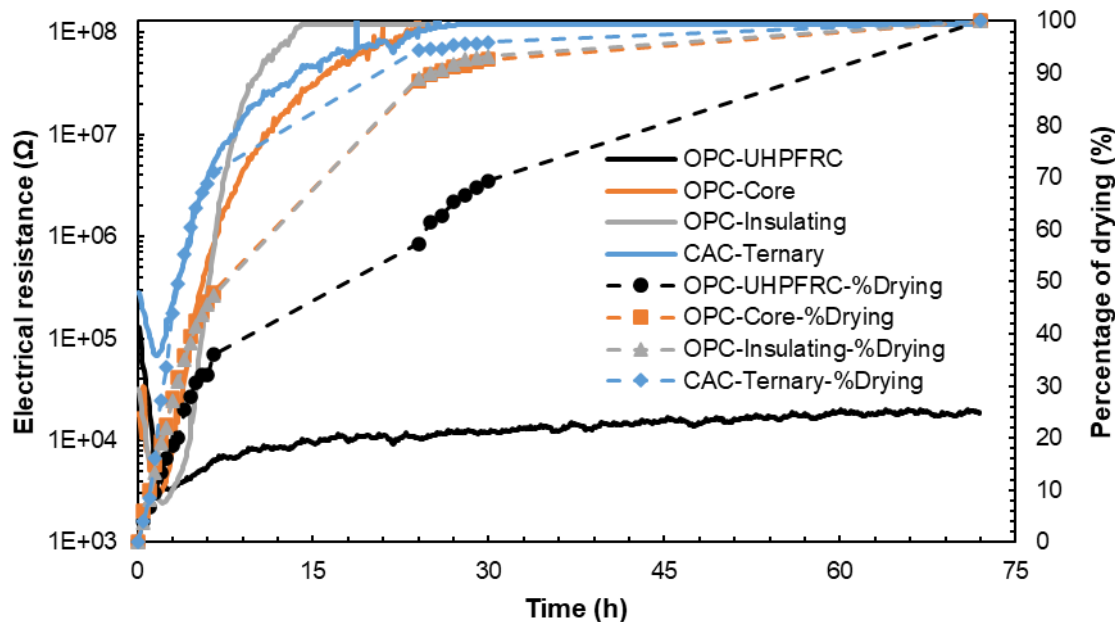


Figure 5.7: Electrical resistance and percentage of free water loss during drying.

5.3.1.2. Evolution of parameters for the thermal cycling stage

Mass loss

Figure 5.8 shows the mass lost during the first heating up to 600°C all of the samples, excluding the OPC-UHPFRC, which underwent spalling when the temperature of the heat source was 300°C. This material did not include PPF in its components and it was a dense material as well. It is worth noting that a significant majority of the mass variation took place after the heating phase for the OPC specimens and nearly half of the total value for the CAC concrete. Additionally, when the temperature increased up to 400°C, the specimens had lost more than 90% of the total mass loss. Regarding the OPC-UHPFRC, experienced a higher loss of mass when it was being exposed to 200 and 300°C, meaning that the concrete was not completely dried when the heating up to the maximum temperature started.

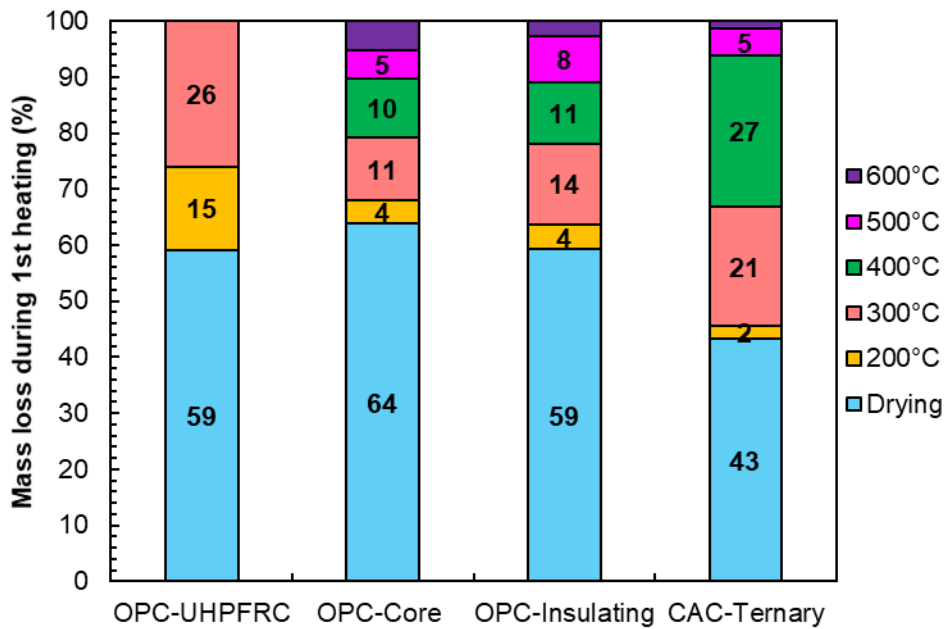


Figure 5.8: Mass loss during the first heating at different temperatures up to 600°C.

On the other hand, the evolution of the mass loss in the thermal cycles when the temperature ranged between 300-600°C is shown in Figure 5.9. In all cases, the total mass lost was reached during the first heating up to the maximum temperature. The thermal cycling did not produce a loss of mass in conventional types of concretes such as CAC-Ternary and OPC-Core. Nevertheless, thermal cycling increased 1% of the mass variation in the insulating material. This material underwent the highest loss of mass, but it was because one of its components, Expanded Polystyrene (EPS) beads were evaporated during the heating.

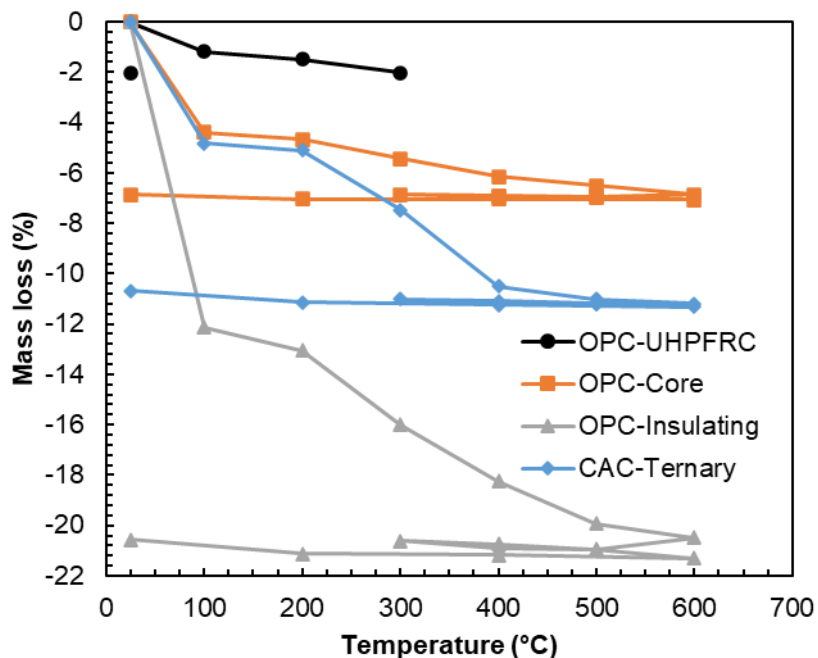


Figure 5.9: Cumulative mass loss during the first and successive heating and cooling cycles.

According to the OPC-UHPFRC, the sample experienced the spalling phenomenon when the temperature of the furnace was at 300°C. Figure 5.10 shows the final aspect of the samples after suffering from spalling. As those samples were placed inside another metallic grid, the spalling phenomenon did not affect the other samples either to the inside of the furnace. Analysing the images of the sample, the type of explosion was originated at the core of the sample. The presence of steel fibres maintained the shape of the initial specimen and small pieces of it were spread inside the furnace. Nevertheless, the material did not have PPF and, therefore the risk of spalling could not be avoided. The specimen underwent a spalling, meaning that the sample was not completely dried.

It highlights the importance of taking into account the particularities of each type of material. The importance of including PPF in the composition is once again demonstrated to avoid the risk of spalling. It does not make sense to have a strict protocol with fixed times for the drying process because the thermal response of different types of concrete is highly influenced by its components, as well as for its geometry. For that reason, following the drying in real time is essential before operating infrastructures of any kind of concrete and geometry.



Figure 5.10: Images of the OPC-UHPFRC after suffering from a spalling phenomenon.

5.3.2. Test 2: Evolution of parameters during the complete drying process at 105°C

5.3.2.1. Drying stage – up to 29 weeks at 105°C

Mass loss

In order to go deeper in the evolution of the drying process of the concrete, this test was carried out maintaining 105°C for 29 weeks to achieve an equilibrium in the variation of mass experienced by the water/vapour release. The results of the weekly percentage of drying are displayed in Figure 5.11. Whereas OPC-Core, OPC-Insulating and CAC-Ternary achieved the equilibrium in the first week of thermal exposure, the OPC-UHPFRC lost 37% of the

total mass loss during the first week. The percentage of drying was decreasing every week up to reach 2% of variation after being exposed to 105°C for 24 weeks. From that moment, the mass was stabilised, but the test continued up to 29 weeks to ensure that the material did not experience more variation of mass.

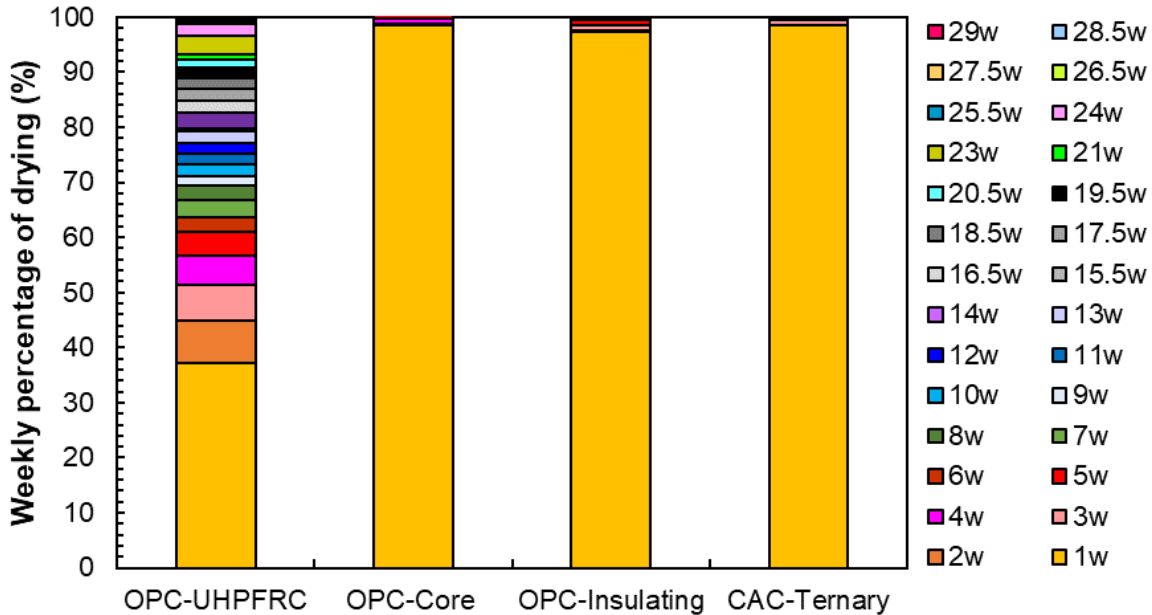


Figure 5.11: Percentage of drying at different times of testing.

Figure 5.12-left shows the evolution of cumulative mass lost during the testing time. The results in OPC-Core, OPC-Insulating and CAC-Ternary are similar to the ones reached in Test 1 for a drying process of 72 hours. The loss of mass achieved was around 4% in the case of OPC-Core and CAC-Ternary and 12% for the OPC-Insulating. However, OPC-UHPFRC reached the equilibrium after being exposed at 105°C more than 4000 hours later. At this point, the cumulative mass lost was 4.36% in the whole drying process. Comparing this value with the one experienced by the specimen that underwent spalling (1.2%) highlights the importance of having a concrete infrastructure correctly dried before operating at higher temperatures. In the previous case, the sample was only dried in 27% of the total and that is the reason why it spalled. Indeed, it is worth noting that the characteristics of each material influence the thermal response and, hence, the protocols need to be adapted for each type of material.

Figure 5.12-right represents the percentage of drying and again brings to light that the type of material conditions the evacuation of the water and vapour out of the concrete. Particularly, the case of OPC-UHPFRC was a concrete especially dense and with a high content of steel fibres inside [5]. Consequently, the drying process was produced more slowly than the other types tested.

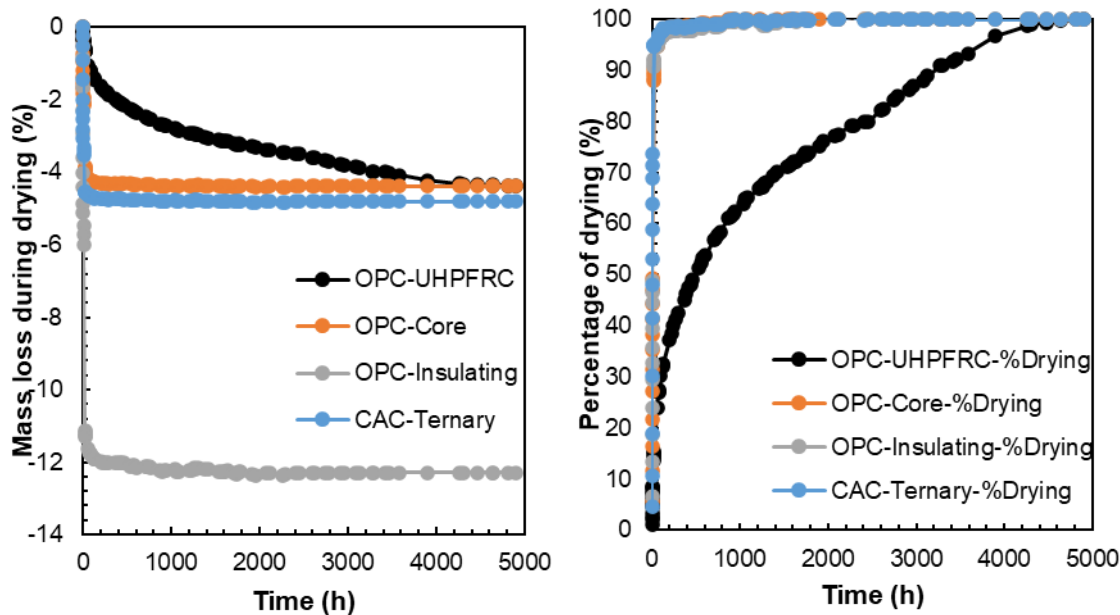


Figure 5.12: left) Evolution of mass loss during drying and right) level of drying during the testing time.

Electrical resistance during the drying process

Figure 5.13 represents the evolution of the electrical resistance in time. The conventional concretes experienced a faster drop of the magnitude of 4 orders of magnitude in less than 100 hours whereas the OPC-UHPFRC registered the same drop after 4000 hours of testing. The electrical resistance puts again in evidence the slower drying of this material compared to the other specimens.

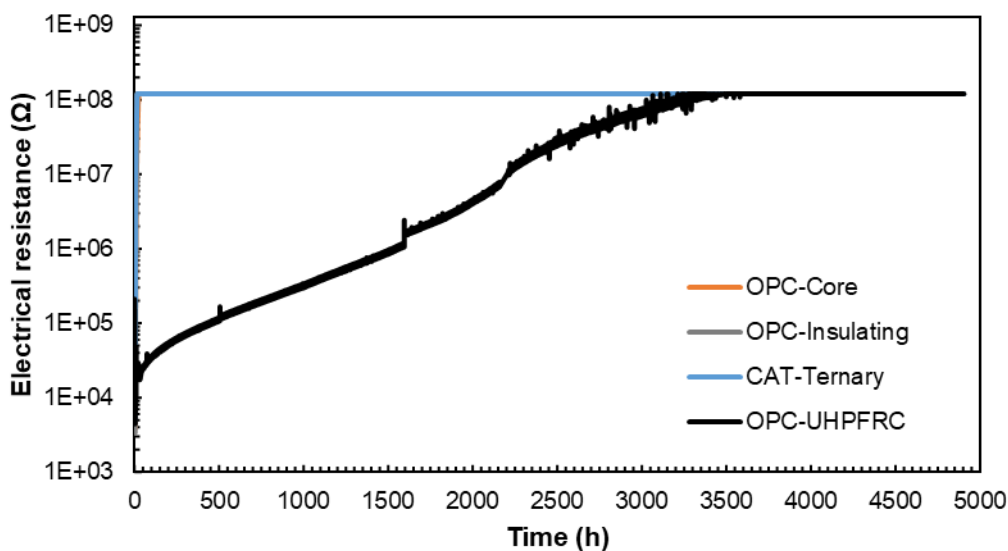


Figure 5.13: Evolution of electrical resistance during the test.

Suitability of the electrical resistance for detecting the drying stage

The previous results have proved that both the mass and the electrical resistance are parameters that can follow the evacuation of water/vapour of concrete when it is being heated. Nonetheless, a small concrete sample can be weighted but it is not the case of a large

infrastructure. Additionally, as was commented before, the electrical resistance is a parameter that is measured continuously whereas the mass weight is a discrete value. Figure 5.14 and Figure 5.15 represents the evolutions of the electrical resistance and percentage of drying for the conventional type of concretes and the OPC-UHPFRC, respectively. The evolutions are very similar as both parameters experienced changes within similar periods.

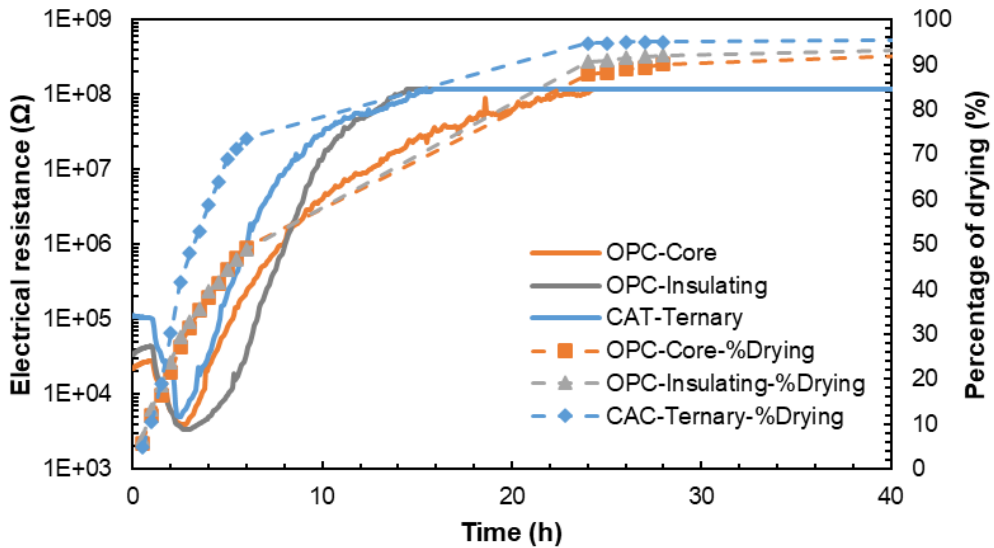


Figure 5.14: Evolution of electrical resistance and the percentage of drying of conventional concretes.

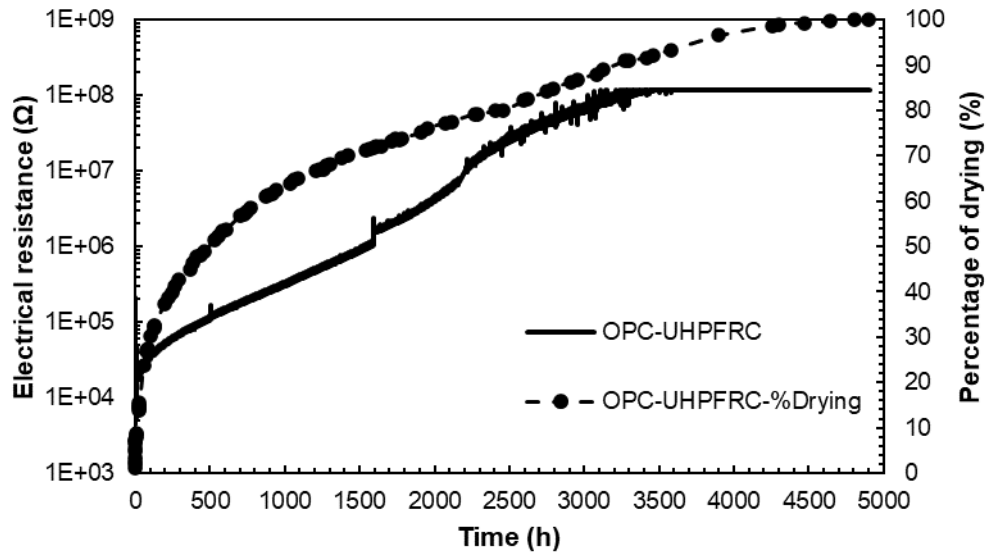


Figure 5.15: Evolution of electrical resistance and the percentage of drying of OPC-UHPFRC.

Analysing the curves of the drying process, the water was evacuated outside the material following a logarithmic expression and this expression is only possible to be determined after the end of the drying stage. For that reason, the importance of the electrical parameter rises to know the exact moment at which the material is dried during the test. The question at this point is what level of drying is measurable by following the electrical resistance? To answer this question, the expression of the percentage of drying with time is needed and the curves for each material are shown in the following equations:

1- OPC-UHPFRC:

$$\text{Level of drying (\%)}: 12.018 \cdot \ln[t(h)] - 15.87 \quad (5)$$

2- OPC-Core:

$$\text{Level of drying (\%)}: 9.698 + 22.939 \cdot \ln[t(h)] \quad (6)$$

3- OPC-Insulating:

$$\text{Level of drying (\%)}: 10.832 + 23.074 \cdot \ln[t(h)] \quad (7)$$

4- CAT-Ternary:

$$\text{Level of drying (\%)}: 21.94 + 22.459 \cdot \ln[t(h)] \quad (8)$$

On the other hand, variations of the electrical resistance were measured up to 24.51, 14.76, 16.18 and 3631.3 hours for OPC-Core, OPC-Insulating, CAC-Ternary and OPC-UHPFRC, respectively. Substituting those times in the previously adjusted expressions, the level of drying theoretically measurable with the electrical resistance parameter would be 83, 73, 85 and 82.64% for OPC-Core, OPC-Insulating, CAC-Ternary, and OPC-UHPFRC respectively. Nonetheless, analysing the charts represented in Figure 5.14 and Figure 5.15, the level of drying measured continuously with the electrical resistance is increased above 90% for OPC-Core, CAC-Ternary and OPC-UHPFRC. Regarding the OPC-Insulating, the percentage is smaller because this sample experienced a faster drying and the punctual mass results were obtained after 6 hours of reaching the maximum value of the electrical resistance.

5.3.2.2. Comparison between initial and residual conditions

Thermal conductivity

Figure 5.16 shows the evolution of thermal conductivity in blue before the thermal exposure; red after the dehydration process, measured at high temperature and grey at residual conditions after the cooling process of the samples. Additionally, the sample OPC-UHPFRC that underwent the spalling phenomenon was also measured at residual conditions.

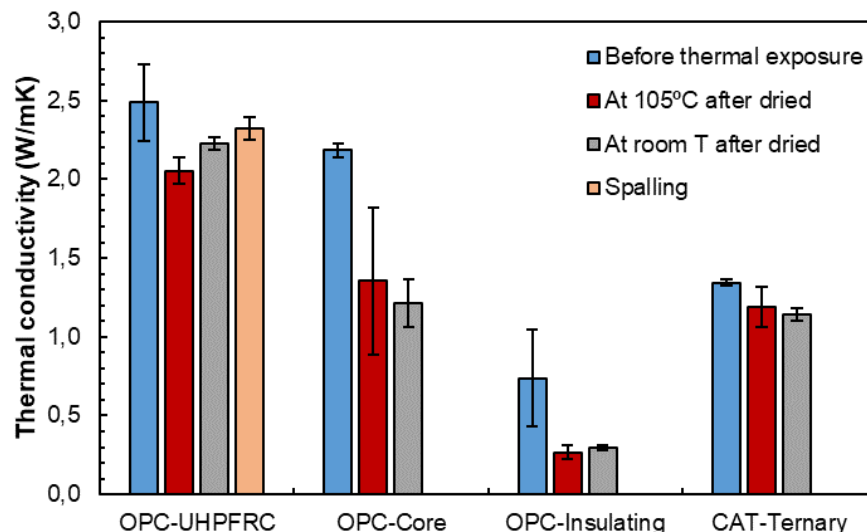


Figure 5.16: Thermal conductivity before and after dried, at high and room temperature.

The general trend is that the thermal conductivity decreases during the dehydration process due to the substitution of water by air in the pores of the concrete, as was explained in more detail in **Chapter 4**. The differences found between the measures taken after drying are related to the probes for measuring at high temperature and room temperature. Additionally, once the samples are cooled down, the values of thermal conductivity minimally recover in some cases, but the differences are very narrowed.

OPC-UHPFRC and OPC-Core recorded the highest values of thermal conductivity before the thermal exposure. As both materials contain steel fibres, the conductivity increases due to these components. The presence of fibres is 4 times higher in the OPC-UHPFRC than in OPC-Core and the material is denser and presents a compressive strength 2 times higher. The high content in steel fibres, 160 kg/m^3 reported by the authors in [5], made that this type of concrete experienced a smaller decrease ($\approx 25\%$) in the thermal conductivity once the material was completely dried, achieving values above $2 \text{ W/(m}\cdot\text{K)}$. In contrast, OPC-Core reached dried values of $1.35 \text{ W/(m}\cdot\text{K)}$, representing a decrease of 40% of its initial value under moisture conditions.

The CAT-Ternary composition is the more stable composition analysed. Despite having an initial thermal conductivity below $1.35 \text{ W/(m}\cdot\text{K)}$, the material reached a dried value of $1.18 \text{ W/(m}\cdot\text{K)}$, recording a decrease of 12% compared to the initial thermal conductivity.

Regarding the OPC-Insulating, the material presents the highest decay ($\downarrow 65\%$) in the thermal conductivity value, comparing to the initial value. Taking into account its components, cement paste and Expanded Polystyrene (EPS), the changes after 105°C might be related to the EPS because the cement paste is not dehydrated at this temperature. Regarding the thermal degradation of the EPS, some authors reported that the polymer beads collapse when the temperature reaches $110\text{-}120^\circ\text{C}$ and those beads stars melting and vaporizing at 160°C and 275°C , respectively [7]. Having this in mind, the unique explanation for the decrease in the thermal conductivity is the water. During the mixing and pouring of concrete, the EPS bead would catch water and maintained humidity inside them. With the exposure at 105°C , the water was lost and, for that reason the thermal conductivity decreased. Additionally, Figure 5.17 illustrates the aspect of the OPC-Insulating sample before (left) and after (right) the drying phase. Initially, there exist some pores in the cement paste and the EPS beads are well integrated into the cement paste. When the sample was dried, the EPS beads are diminished in size and some of them have collapsed, in the same way, that was reported in [7].



Figure 5.17: Cross-section of OPC-Insulating (left) before and right) after the drying process.

Porosity and pore volume

The results of the pore size distribution obtained through MIP before and after the drying process are displayed in Figure 5.18. Before the thermal exposure, the most pores in OPC-UHPFRC and OPC-Insulating are capillary pores with sizes between 1.2-2.5 μm . OPC-Core and CAC-Ternary present thinner pore size distribution with pores around 0.5 and 0.25, respectively. Additionally, OPC-UHPFRC, OPC-Insulating and CAC-Ternary reached another peak in regions with a pore diameter between 12-18 μm originated by micropores. On the other hand, OPC-UHPFRC presents the third peak in regions of 25-40 μm that might be related to the absence of steel fibres (13 mm of length and 20 μm of diameter) when the sample was obtained from the core of the specimen.

After the drying process, the pores found had bigger diameters. OPC-UHPFRC, OPC-Core and CAC-Ternary present more capillary pores after drying (1.6-3 μm). Also, the micropores were found in all the types of concrete for diameters of pore between 10-16 μm . Another peak was reached in the CAC-ternary around 40 μm that would be related to the presence of microcracks generated for the evacuation of water/vapour outside concrete. However, the previous crack analysis reported in **Chapter 3** concludes that no significant cracks were generated during the drying process. Indeed, the result obtained here might be produced during the obtention of the small sample for doing the MIP test.

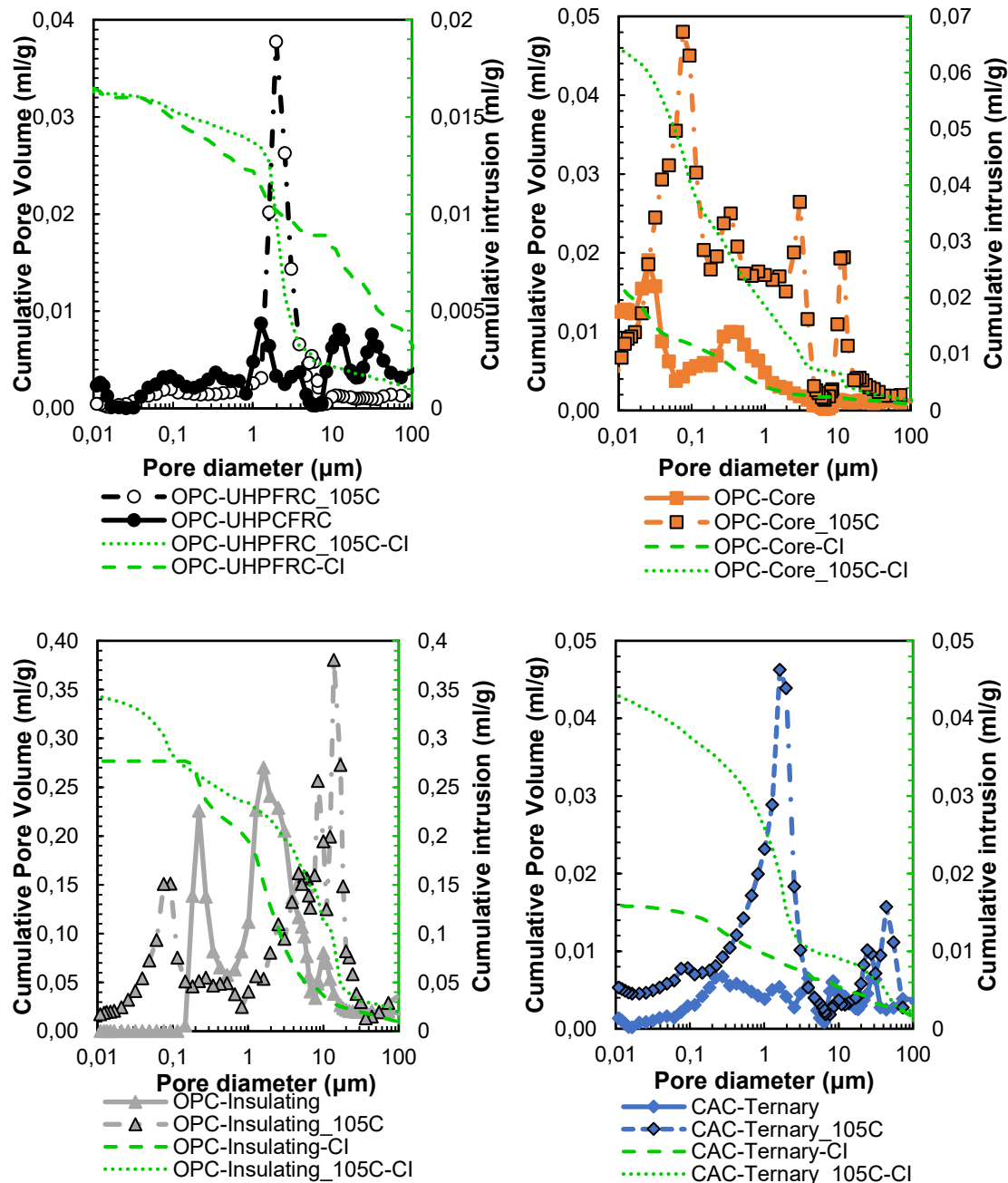


Figure 5.18: Cumulative pore volume for the four concrete compositions before and after the drying process.

Finally, the total porosity was obtained for the four concrete types before and after the thermal test and it is displayed in Figure 5.19. Excluding OPC-UHPFRC, in all cases, the total porosity was increased after the drying process, which is in accordance with the increase in the diameters of the pores previously commented. OPC-Insulating is an insulating material with a high content of pores of water and EPS. When the material is dried, the porosity increased 10% and achieved a total porosity of 43%. Regarding OPC-Core and CAC-Ternary, the values are similar because both are conventional concretes. The porosity increased from 6% to 14% for OPC-Core and from 4% up to 11% CAC-Ternary. Regarding OPC-UHPFRC, the total porosity was similar before and after drying because the material is dense with less quantity of pores than the other materials. However, the changes in the

pore diameter (Figure 5.18) during drying reflect the effect of the heating with the increase in the capillary pores.

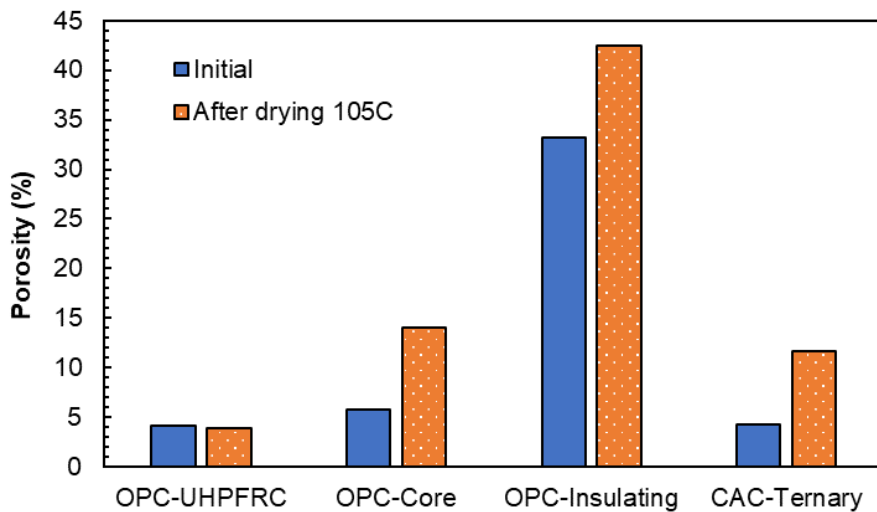


Figure 5.19: Total porosity before and after the drying process at 105°C.

5.4. Conclusions

This chapter has developed a methodology for following the evolution of the level of drying of concrete when it is exposed to high temperatures (105°C) and the variation of mass at temperatures up to 600°C and during thermal cycling. The results found in this chapter allows applying this methodology at large-scale infrastructures of concrete such as the ones in the energy field. The methodology described here started from a concept (TRL 2) and ended with the validation of the protocol at the laboratory, improving the level of maturity up to TRL 4.

The following conclusions can be drawn:

- The methodology developed regarding the measure of the electrical resistance for following the drying process continuously has been validated at the lab scale and can be applied for preconditioning large-scale infrastructures of concrete before the operation at high temperatures.
- It has been proved that the particularities of every material highly influence its thermal response and, thus, to the loss of water and vapour released during the drying process. For that reason, monitoring the drying process in real time is essential for ensuring the level of drying of a concrete material.
- While conventional concretes such as OPC-Core, OPC-Insulating and CAC-Ternary reached the equilibrium of drying at 72 hours, losing most of the water during the first 24 hours, OPC-UHPFRC needed 24 weeks for achieving the same equilibrium in samples of the same dimensions.
- The level of drying detectable with the measure of the electrical resistance was above 90% of the total mass lost and it was verified for all the concretes tested.
- The continuous measure of the electrical resistance permits following the drying process for a heating process and, hence, can avoid the spalling phenomenon.

- Additionally to the monitoring of the drying process, some conclusions can be drawn from the evaluation of other parameters:
 - The total mass loss was reached in the first heating up to the maximum temperature (600°C) for all concrete types, being the drying stage the one that underwent more than 50% of the total mass loss for all of the concretes tested. The thermal cycling did not produce an additional mass variation.
 - The thermal conductivity decreased with the drying process and the decay is less pronounced in the OPC-UHPFRC due to the high content of steel fibres.
 - The total porosity increased in all cases nearly 10% during the drying process as well as the diameters of pores due to the creation of micropores in all of the concretes tested.

(Chapter 6 on page 133)

5.5. References

- [1] Y. Fu, Y. Fu, L. Li and L. Li, "Study on mechanism of thermal spalling in concrete exposed to elevated temperatures," *Mater. Struct.*, vol. 44, (1), pp. 361-376, 2011. . DOI: 10.1617/s11527-010-9632-6.
- [2] Z. P. Bazant, "Analysis of pore pressure, thermal stresses and fracture in rapidly heated concrete," *International Workshop on Fire Performance of High-Strength Concrete*, 1997.
- [3] G. A. Khoury, C. E. Majorana, F. Pesavento and B. A. Schrefler, "Modelling of heated concrete," *Magazine of Concrete Research*, vol. 54, (2), pp. 77-101, 2002.
- [4] W. Nechnech, F. Meftah and J. M. Reynouard, "An elasto-plastic damage model for plain concrete subjected to high temperatures," *Eng. Struct.*, vol. 24, (5), pp. 597-611, 2002. . DOI: 10.1016/S0141-0296(01)00125-0.
- [5] A. Martínez-Ibernón, M. Roig-Flores, J. Lliso-Ferrando, E. J. Mezquida-Alcaraz, M. Valcuende and P. Serna, "Influence of Cracking on Oxygen Transport in UHPFRC Using Stainless Steel Sensors," *Applied Sciences*, vol. 10, (1), pp. 239, 2020.
- [6] M. B. Heaney, "Electrical conductivity and resistivity," *Electrical Measurement, Signal Processing, and Displays*, vol. 7, (1), 2003.
- [7] S. Mehta, S. Biederman and S. Shivkumar, "Thermal degradation of foamed polystyrene," *J. Mater. Sci.*, vol. 30, (11), pp. 2944-2949, 1995.

Chapter 6

Up-scaling and preconditioning of a section of a thermocline tank

The present chapter describes the construction of an up-scaled section of a thermocline tank made of concrete. This work aims to improve the knowledge on the use of concrete for TES infrastructures at an up-scaled level. To begin, *section 6.1* mentions the improvements in the technology readiness level related to CTES developed in the previous chapters of this thesis and the need for enhancing the experiences at an up-scaled level.

Secondly, *section 6.2* describes the methodology followed for the construction of the mock-up, including the instrumentation of the concrete and the other layers. Furthermore, the thermal regime for following the drying process of the concrete layer and the connections for monitoring the electrical resistance continuously are explained.

Later, *section 6.3* includes the results from both the construction phase and the thermal performance for the drying and dehydration stage of the mock-up section.

Finally, *section 6.4* gives some lessons learned from the up-scaled construction and preconditioning of the mock-up section of a thermocline tank and *section 6.5* summarises conclusive remarks of the chapter.

6.1. Up-scaling from lab-scale to a mock-up section of a thermocline tank

The studies carried out in **Chapters 3, 4 and 5** on different types of concrete at the lab scale proved that the use of concrete for a TES infrastructure is possible. The chapters also provided the evolution of the thermal and electrical performance of concrete at high temperatures and under thermal cycling. Indeed, the experimental investigation in **Chapter 5** demonstrated one way of doing the commissioning of concrete at high temperatures as an essential step before starting the operation of a CSP Plant. Nonetheless, the question at this point is whether those results at lab-scale (TRL 3-4) can be up-scaled to a large scale of a concrete infrastructure or not. Indeed, it is the aim of this chapter, improving the Technology Readiness Level evaluated in **Chapters 3, 4 and 5** to a TRL 5.

Additionally, the lack of experiences in real prototypes of thermocline tanks highlighted in **Chapter 2** made it necessary to develop and complete the knowledge on the thermal performance of the concrete for an up-scaled mock-up of a thermocline tank. Furthermore, the use of concrete as an element for those molten salts tanks is a novelty and the performance is unknown up to date. Focussing on this thermocline section, the CAC concrete layer is the most critical point owing to the physical and chemical transformations that take place at high temperatures [1-5]. For that reason, the heat flux effect was assessed in two stages: 1) drying + dehydration step, explained in **Chapter 6** and 2) thermal cycling curve during the operation of the thermocline mock-up, explained in **Chapter 7**. During the first stage, concrete loses the free water that is placed in the pores at temperatures above 100°C, and most of the binding water in the hydrated solid phases up to 300°C. The vapour water generated increases the pore pressure and, in combination with the thermal stresses generated in the concrete, can undergo a spalling phenomenon with a collapse of the infrastructure [2, 6-8]. When the temperature reaches 300°C, the CAC cement paste finishes the dehydration [9] and as the temperature increases, the variations in volume take place due to the shrinkage of the cement paste and expansion of aggregates [1, 2, 4, 5].

The aim was to demonstrate if the knowledge acquired in the laboratory could be extrapolated to a large scale and, thus, give some lessons learned from both the construction and operation of the thermocline prototype. It includes the optimization of the heating of the concrete tank and the preconditioning to avoid the spalling phenomenon of the concrete during the first heating while the infrastructure is being put into service at high temperature. Owing to the fact that this stage is one of the riskiest, the present section shows and develops experimental study tests and monitoring methods to be applied in the concrete prototype tank to ensure that will be operated appropriately.

For the reasons mentioned above and under the frame of the H2020 project “NewSOL” where the present thesis was developed, a mock-up section of a thermocline tank made of concrete was developed in collaboration with industrial partners such as ACCIONA, AIMEN and Cements Molins. The mock-up was built and tested at ACCIONA’s workshop; the research centre AIMEN was responsible for designing and monitoring the mock-up with special sensors located in the concrete layer and Cements Molins, which is not a partner in NewSOL Project, participated with the supply of the CAC cement and CAT aggregates. It is important to note that despite this development were done jointly with the above-mentioned contributors, the results showed in this chapter are related exclusively to the data information recorded with the monitoring systems under the responsibility of CSIC (monitoring of the temperature with thermocouples located in each component of the mock-up section and the electrical resistance in the concrete layer) and all the analysis of the information collected with these systems has been done by CSIC.

Comparing dimensions of the lab-scale small samples and the mock-up, the up-scaled volume factor is increased ($V \times 585.9$), as it is summarised in Table 6.1, and the demonstrated issues and the pending validation at large-scaled are summarised as follows:

1. Lab-scale: developed in **Chapters 3, 4 and 5** ($V \times 1$, TRL 3-4).

Demonstrated the possibility of using concrete for TES infrastructures, its evolution of thermal and mechanical properties after high temperatures as well as it

was defined a protocol for doing the commissioning of concrete before the operation at high temperatures. Those developments allow achieving a TRL 3-4.

2. Up-scale: Mock-up of a section of a thermocline tank ($V \times 585.9$, TRL 5).

Verification and validation of the previous protocols at an up-scaled section and provide lessons learned for a real prototype of thermocline tank. The NewSOL project will finish the study with the construction and operation of a prototype in the facilities of the Evora Molten Salts Platform (EMSP) from the University of Évora (Portugal). Currently, the CTES prototype is under construction and the last stage of the project will allow achieving a TRL 6-7.

| | Concrete dimensions | Up-scaled volume factor |
|-------------------------------|---|-------------------------|
| Lab-scale | $40 \times 40 \times 160 \text{ mm}^3$ | $V \times 1$ |
| Up-scale (mock-up) | $1000 \times 500 \times 300 \text{ mm}^3$ | $V \times 585.9$ |

Table 6.1: Dimensions and up-scale volume factor between the samples tested in this thesis.

The present chapter contains the definition of the mock-up section of the tank and the instrumentation of all of the layers. Additionally, includes the preconditioning of the concrete before the operation at high temperatures and the validation of the electrical parameter for following the advance of the drying process. At the end of the chapter, some lessons learned from the up-scaled mock-up are included.

6.2. Methodology

In this study, a mock-up section of a thermocline tank of dimensions $1525 \times 1700 \times 1600 \text{ mm}^3$, with a concrete volume of $300 \times 500 \times 1000 \text{ mm}^3$, has been investigated in terms of assessing the evolution of thermal parameters by monitoring them with conventional thermocouple sensors located between the layers across the tank. The section of the thermocline tank comprises different layers from the heat source to the external surface, as follows:

- Firstly, heating mats simulating the heat coming from the molten salts.
- Secondly, a steel liner working as a container for the molten salts with a thickness of 10 mm.
- Thirdly, an air gap of 15 mm of width for allowing the thermal expansion of the steel liner during the operation.
- Fourthly, a concrete layer as a structural element of the infrastructure able to withstand high temperatures and finally, an insulating material of 600 mm of width to minimize the heat losses to the surroundings.

The schematic position of the layers of the system, with the dimensions in millimetres, are shown in Figure 6.1. The acronyms used in the schema are referred to as the heating mats as a Higher Heating Mat (HHM) and Lower Heating Mat (LHM); to the steel liner (SL), air gap (AG), the CAC concrete layer (CAC) and insulation (I). The thermal power is expressed as \dot{Q} [W].

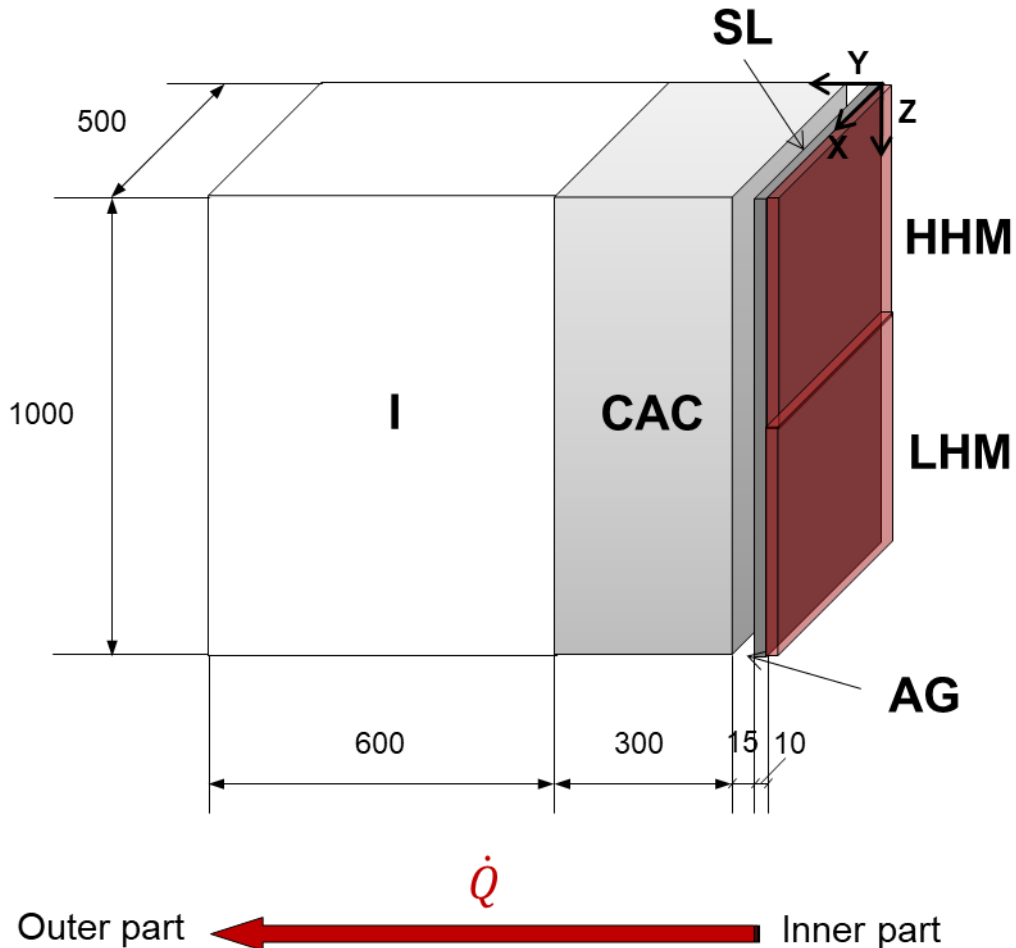


Figure 6.1: Layers of the mock-up section of a thermocline tank.

The layers shown in Figure 6.1 were located above an expanded clay with a sand compacted bed of 250 mm of height and the whole system was isolated with Rockwool so as to reduce heat losses to the environment. The top part of the mock-up was insulated with 350 mm of insulating (Rockwool). Finally, the whole system was insulated around with a thickness of Rockwool of 600 mm to minimise the heat transfer losses to the environment.

Regarding the type of concrete, the selected concrete mix was the optimized solution found in **Chapter 3** and in [3], whose detailed concrete dosage and main properties are summarised in Table 4.2.

| | kg/m ³ |
|-----------------------|-------------------|
| Cement CAC | 600 |
| Water | 258 |
| Basalt gravel 4-12 mm | 682 |
| Slag gravel 3-7 mm | 139 |
| CAT sand 0-3 mm | 714 |
| Slag sand 0.25-2 mm | 128 |

| | |
|--|------|
| Polypropylene fibres (PPF) | 2 |
| Plasticizer | 0.9 |
| <i>Water/cement (w/c)</i> | 0.43 |
| <i>Slump (mm)</i> | 170 |
| <i>Compressive strength at 7d (MPa)</i> | 50.6 |
| <i>Compressive strength at 28d (MPa)</i> | 53.5 |

Table 6.2: Composition and properties of the concrete layer.

6.2.1. Instrumentation of the mock-up

The aim is to evaluate the thermal performance of an up-scaled section of a thermocline tank as well as to have effective monitoring of the thermal performance of the mock-up during the commissioning. For this purpose, the whole system was instrumented with K-type thermocouples located between the layers of the mock-up and also embedded in the concrete layer to record and quantify the temperature profile across the full section. The schematic position of the thermocouples placed between the different layers (IL 1, IL 2, IL 3) and embedded in the concrete are shown in Figure 6.2. The coordinates with respect to the reference system (located in Figure 6.2) where the temperatures were recorded are shown in Table 6.3.

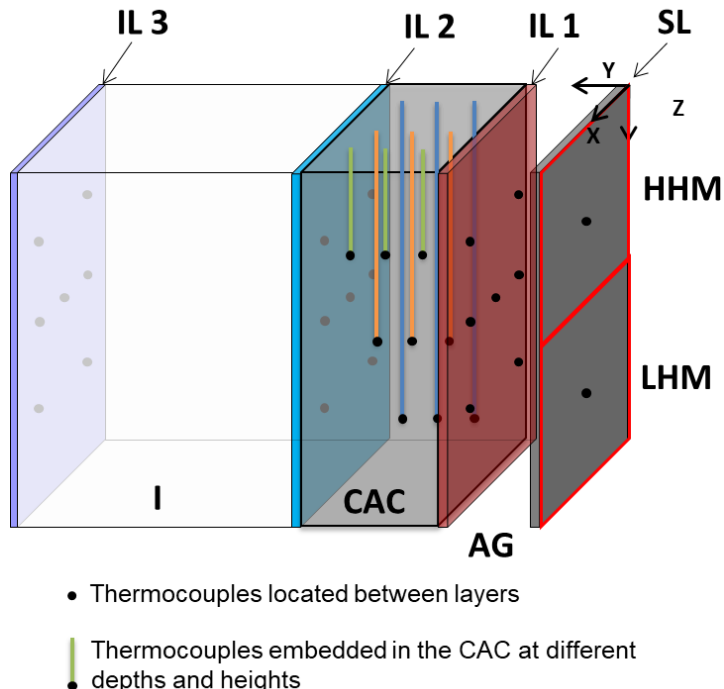


Figure 6.2: Location of thermocouples in the mock-up

| Location | Coordinates (mm) | | |
|----------|------------------|---|-----|
| | X | Y | Z |
| HHM | 250 | 0 | 250 |
| LHM | 250 | 0 | 750 |

| | | | |
|---|-----|-----|-----|
| IL1 (AG with closer external surface CAC) | 120 | 25 | 250 |
| | | | 500 |
| | | | 750 |
| | 230 | 25 | 500 |
| | | | 250 |
| | | | 500 |
| Embedded in CAC | 400 | 25 | 750 |
| | | | 270 |
| | | | 185 |
| | 100 | 270 | 85 |
| | | | 270 |
| | | | 185 |
| | 270 | 365 | 85 |
| | | | 270 |
| | | | 185 |
| IL2 (farther external surface of CAC with insulation) | 100 | 325 | 85 |
| | | | 250 |
| | | | 500 |
| | 270 | 380 | 750 |
| | | | 500 |
| | | | 250 |
| | | | 500 |
| | | | 750 |
| IL3 (Farther external surface of insulation) | 100 | 925 | 750 |
| | | | 500 |
| | | | 250 |
| | 270 | 380 | 500 |
| | | | 250 |
| | | | 500 |
| | | | 750 |

Table 6.3: Coordinates of the thermocouples placed in the mock-up.

Additionally, the evolution of the electrical resistance was measured in deep of the concrete with respect to the heat source. With such aim, the electrical resistance was measured in metallic sheaths embedded in the concrete a different depths with respect to the heat source, located at 80, 160 and 240 mm. The connections were made by using a wire able to withstand high temperatures, which were connected to the metallic sheaths by using a metallic connector to ensure a suitable assembly. A total of 5 connections were done between the mentioned depths with respect to the heat source as can be appreciated in the view from the top of the concrete layer, whose schema is shown in Figure 6.3. Connections C1, C2 and C3 record the evolution of the electrical resistance and, hence, the drying process between 80-160 mm of depth with respect to the heat source. On the other hand, connections C4 and C5 register the same parameter between 160-240 mm of depth with respect to the heat source.

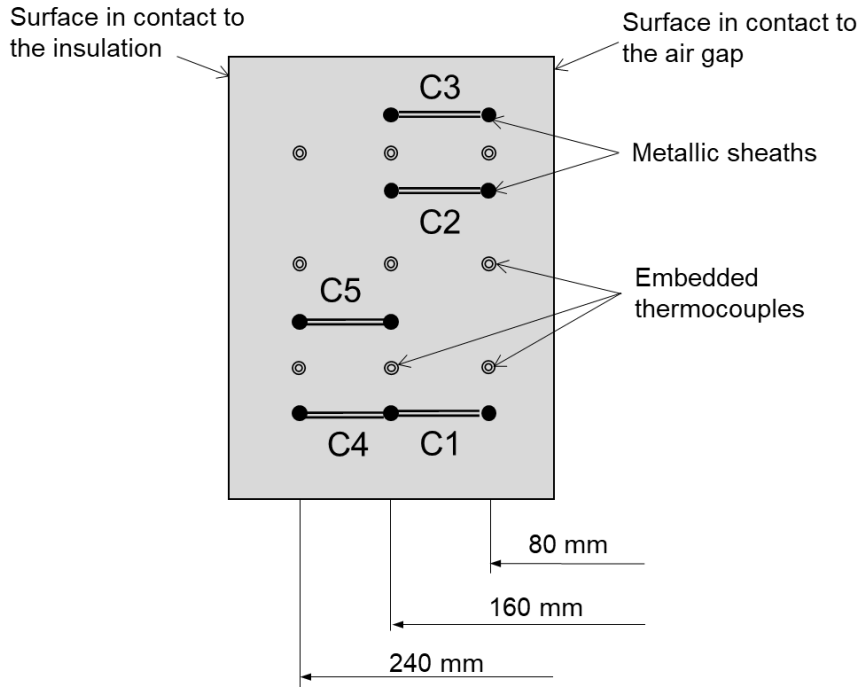


Figure 6.3: Schematic representation of the electrical connections at the top of the concrete layer.

Other types of equipment were used for performing the test. Two electrical heating mats were used to simulate the heat source from the molten salts to the walls of the tank. The model was SHX from Europe Heaters and have 4212 W of power and 240 V [10]. Those heating mats were connected to a control system able to make the heating and cooling processes with a controlled time and heating rates. The controller was model DUAL LOOP CONTROLLER RE 92 and the accuracy achieved in the programmed temperature of the heat source was $\pm 1^\circ\text{C}$. The measurements of temperature with the calibrated K-type thermocouples have an accuracy of $\pm 0.1^\circ\text{C}$. All temperature data collected by conventional thermocouples and the electrical resistance were recorded with a data acquisition system (Model: Agilent 34970A).

The output parameters measured during the test were the temperature across all layers of the mock-up at 3 heights (250, 500 and 750 mm) with thermocouples and the electrical resistance measured between 80-160 mm and 160-240 mm in the concrete layer.

6.2.2. Thermal regime

Focussing on this mock-up, the CAC concrete layer is the most critical point owing to the physical and chemical transformations that take place at high temperatures and that were defined in **Chapters 3 and 4**. The commissioning of the mock-up before starting with the cycling needs for drying and dehydrating the concrete layer to avoid the spalling phenomenon and achieve suitable preconditioning of the system. It includes the dehydration of cement paste to stabilise the transformations in cement paste before the operation with heating and cooling cycles. Before starting with the thermal performance, the concrete needs maturity of at least 28 days. The ageing was 188 days for the present study.

The thermal process for the drying and dehydration stage of the CAC concrete layer is shown in Figure 6.4. Firstly, the temperature increases up to 105°C with a heating rate of

$1^{\circ}\text{C}/\text{min}$ to produce the loss of most free water of concrete in the pores. The drying process and the temperature of 105°C are maintained for 24 hours. After that, to produce the dehydration of the cement paste, two plateaus of constant temperature at 250 and 350°C are established to make the temperature homogeneous and to avoid high thermal gradients within the concrete layer. The time at the plateaus is established in 24 hours and the heating rates are $1^{\circ}\text{C}/\text{min}$.

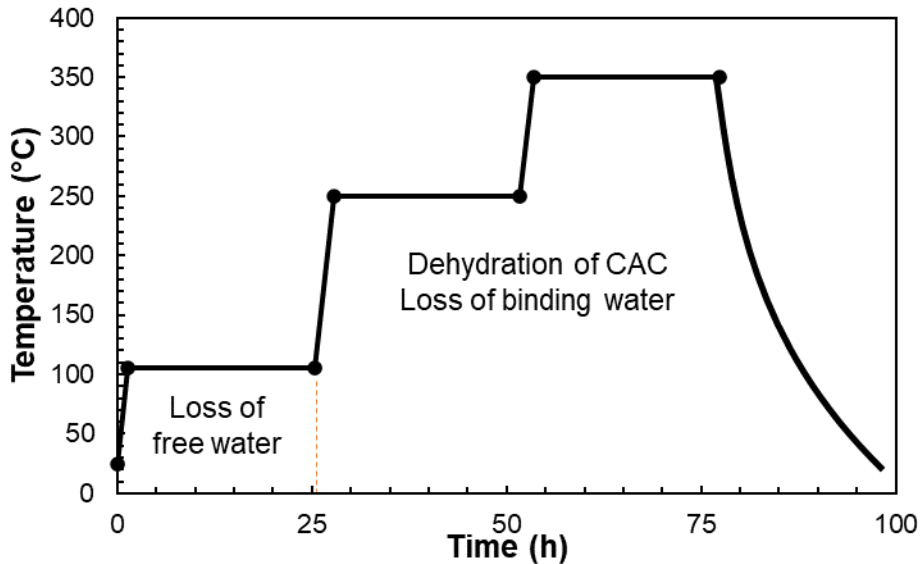


Figure 6.4: Drying and dehydration curve.

6.3. Results

6.3.1. Construction of the concrete layer

The first step was to build the concrete layer, at the Workshop from ACCIONA. The optimized mix detailed in Table 4.2 was sized up to 230 litres and it was poured in a wood mould with the dimensions of the concrete layer and instrumented with thermocouples. The fresh properties of the concrete related to the initial workability were 150-170 mm that maintained the fluidity after 40 minutes of casting. Figure 6.5: shows some pictures of the mould with thermocouples and the appearance of the fresh concrete.

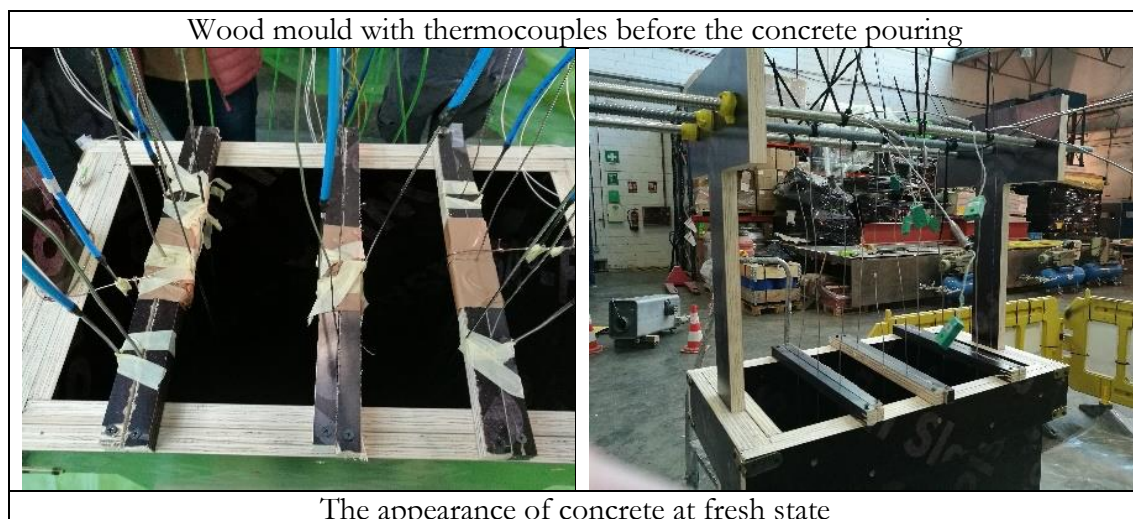




Figure 6.5: Pictures of the mould and appearance of fresh concrete.

During the setting and hardening period, the thermocouples embedded in the concrete specimen were recording the evolution of the temperature at different heights and positions. Figure 6.6 shows the evolution of temperature inside the concrete recorded by thermocouples during the hardening and first hydration stage of the CAC cement. The hardening of concrete is the process that takes place when fresh concrete is converted into a solid material. Regarding the hydration of the CAC, it recorded a peak at 10 hours between 90 and 110°C, depending on the location of the sensor. The highest temperature was reached in the geometric centre of the specimen (thermocouple 5) as expected due to the difficulty to release the heat to the environment. The peak during the setting of the CAC cement paste fits the one obtained during the calorimetry test for a sample without admixtures for this type of cement, whose top value was achieved 9 hours after pouring [11]. It is important to note that after the casting of concrete, the system was covered with Rockwool because of winter weather conditions. For that reason, the heat during the setting was not evacuated quickly. In a real structure of concrete, the peak of hydration would depend on the volume and geometry of the structure, but it will be lower because the structures are not isolated. However, this experience was useful to determine the construction phases of a real tank structure made of concrete.

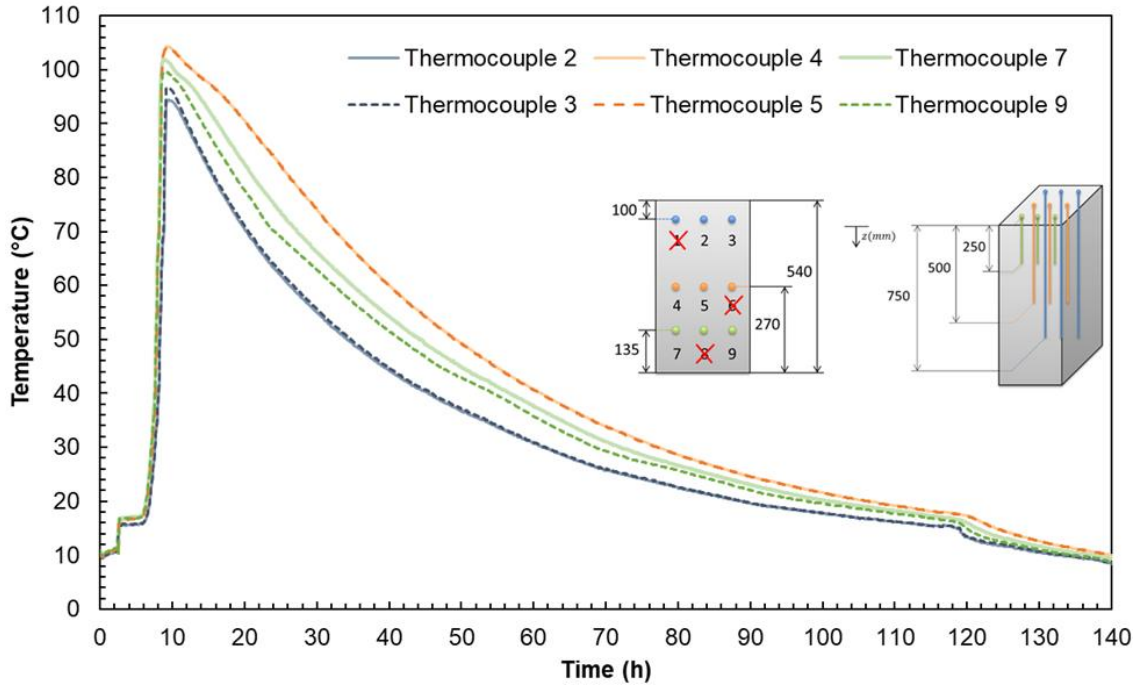


Figure 6.6: Evolution of temperature within concrete during the hydration and hardening.

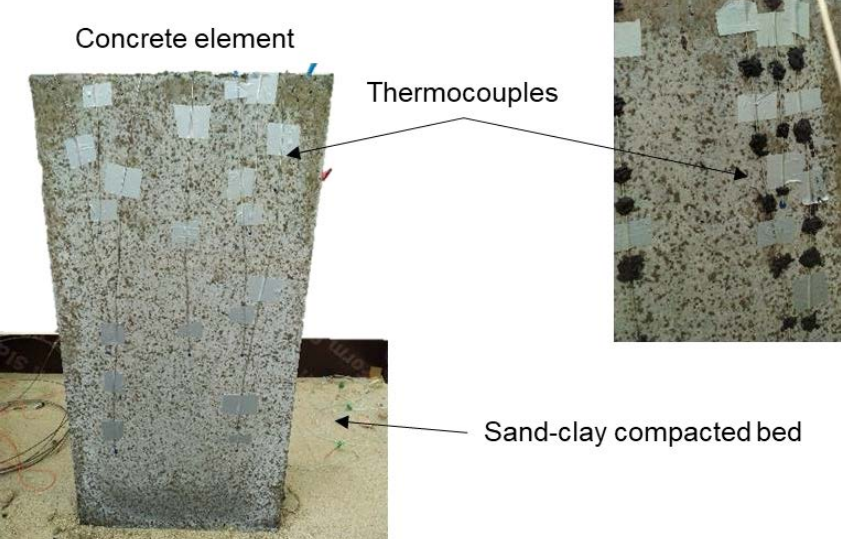
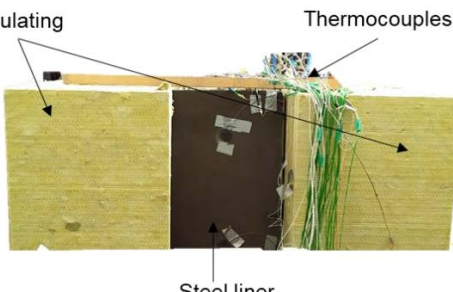
After the setting and hardening, the mechanical properties of the concrete were measured in 3 cylindrical samples of 150 mm of diameter and 300 mm of height through the compressive strength after 7 days. The samples were produced with the same concrete that the concrete layer. The mean value achieved was 48 MPa, which was in accordance with the optimal composition designed. The final aspect of the concrete layer is shown in Figure 6.7.

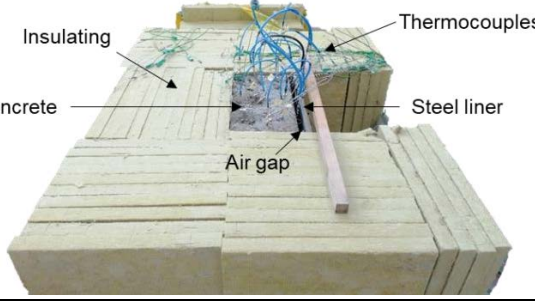
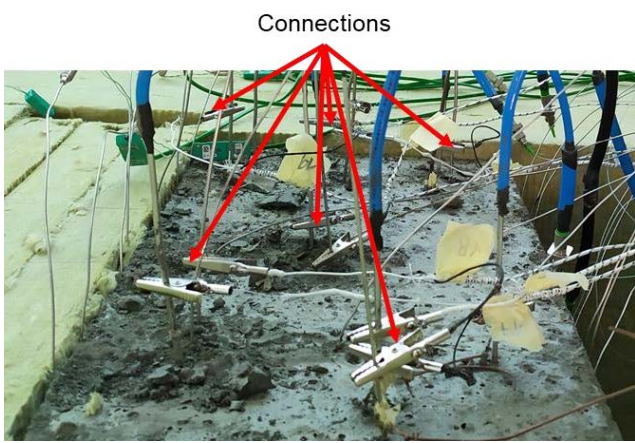
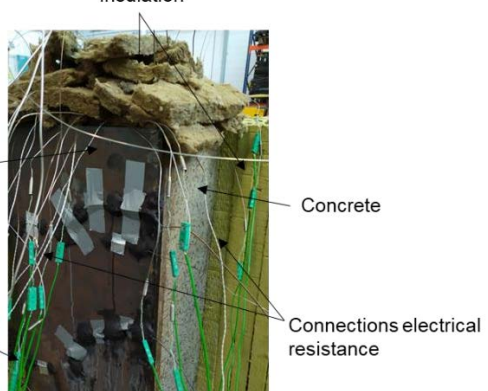


Figure 6.7: Final aspect of the concrete layer with the embedded sensors.

6.3.2. Final arrangement of the mock-up

Firstly, the CAC layer was placed above an expanded clay with compacted sand foundation and then, some thermocouples were located in the interface layers to record and quantify the temperature profile across the full section. The details of the sand-clay compacted bed and the location of thermocouples on the surface of the concrete is shown in step 1 from Figure 6.8. After that, the insulating system was placed around the concrete layer as well as the steel liner, maintaining the air gap between them. The details after placing those components figures in step 2 from Figure 6.8. The third step was to make the connections of the electrical resistance at the top of the concrete layer by using wires able to withstand temperatures up to 600°C. Once the connections were done accordingly and verified, the top of the concrete layer was insulated, as is reflected in step 4. The following step was to place the heating mats in the correct place in contact with the steel liner (step 5). Finally, the whole system was isolated with Rockwool so as to reduce heat losses to the environment. The final disposition of the mock-up section of a thermocline tank is shown in step 6.

| Assembly of the mock-up | |
|--|---|
| Step 1: Concrete layer with thermocouples on the Surface and sand-clay compacted bed | |
| |  <p>Concrete element</p> <p>Thermocouples</p> <p>Sand-clay compacted bed</p> |
| Step 2: Steel liner, air gap and insulation around the concrete layer | |
| Frontal view |  <p>Insulating</p> <p>Thermocouples</p> <p>Steel liner</p> |

| | |
|---|--|
| View from the top |  |
| Step 3: Connections for measuring the electrical resistance | |
| |  |
| Step 4: Insulation of the top of the concrete | |
| |  |
| Step 5: Location of the heating mats | |

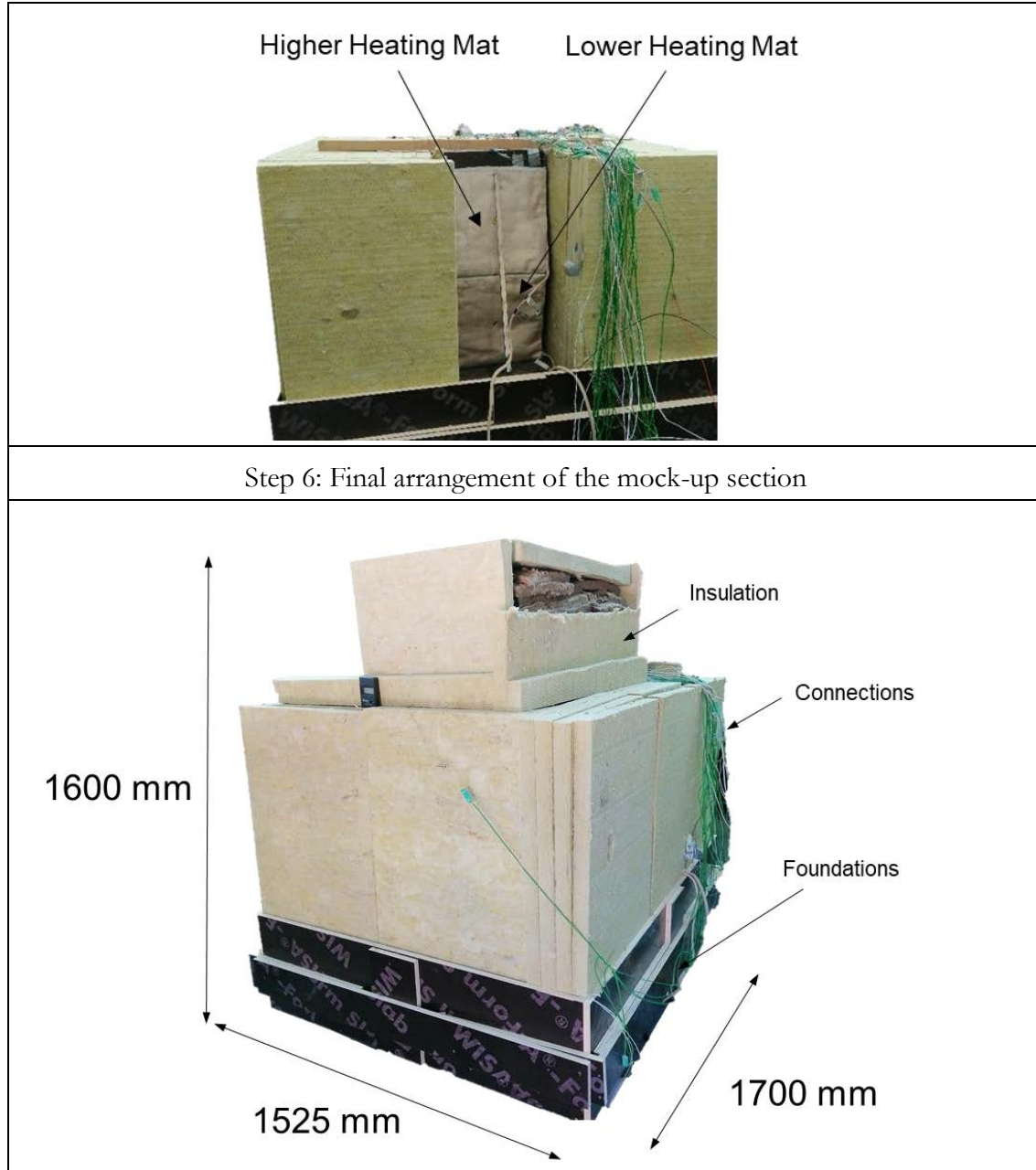


Figure 6.8: Assembly of the mock-up section of a thermocline tank.

6.3.3. Thermal performance

6.3.3.1. Evolution of temperatures across the mock-up

Figure 6.9 shows the evolution of temperature for the 150 hours of drying and dehydration stage across all the layers of the mock-up section. The temperatures of the layers are represented in: **black** for the heating source (heating mats); **red** after the air gap in the external closer surface of the CAC layer to the heat source; **light blue** after the CAC layer; **dark blue** after the insulating layer and **violet** for recording the temperature at the bottom of the mock-up, simulating the temperature in the foundations. The temperature recorded at the top (250 mm), middle (500 mm) and bottom (750 mm) are represented with a continuous line, a dashed line and a dotted line, respectively and for all the layers.

Focusing on the concrete layer Figure 6.10 shows the evolution of temperature for the 150 hours of drying and dehydration stage across the concrete layer. The temperatures are represented in: **black** for the heat source; **red** for the surface of the concrete exposed to the air gap, **orange**, **yellow** and **green** for positions inside the concrete at different depths (85, 185 and 270 mm, respectively); and finally, **light blue** for the external surface of the CAC layer in contact to the Rockwool. To have a more representative effect on the temperature evolution across the layers, the temperature differences have been represented between layers across the mock-up for the three heating steps: 105, 250, 350°C (Figure 6.11).

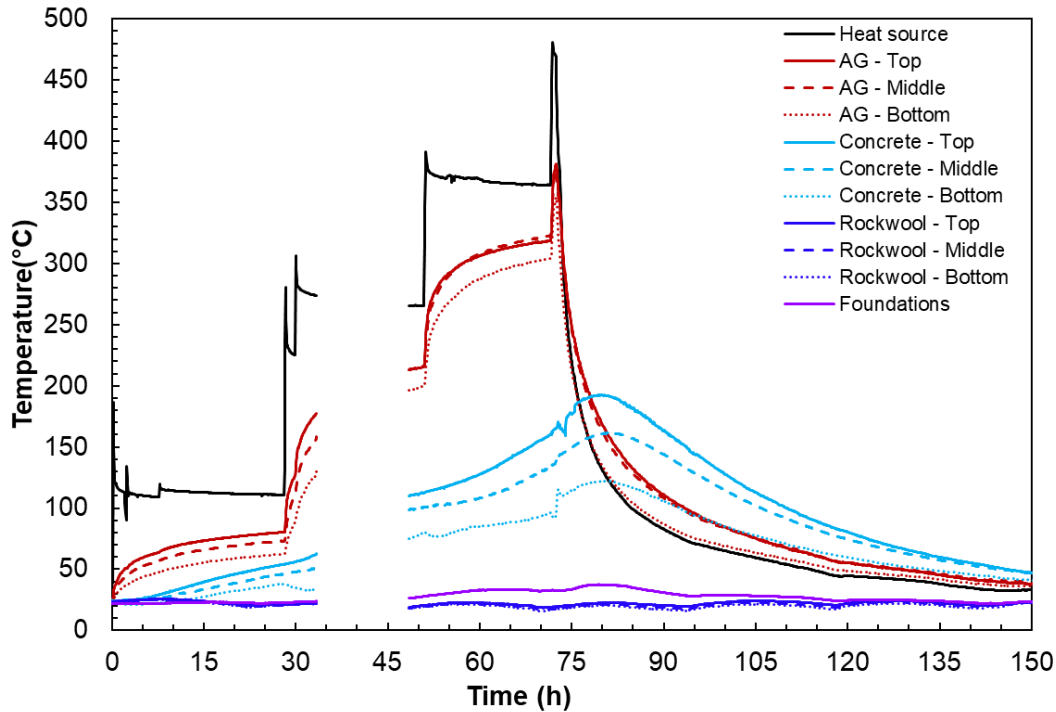


Figure 6.9: Evolution of temperature in the layers of the mock-up of a thermocline section. Drying and dehydration stage.

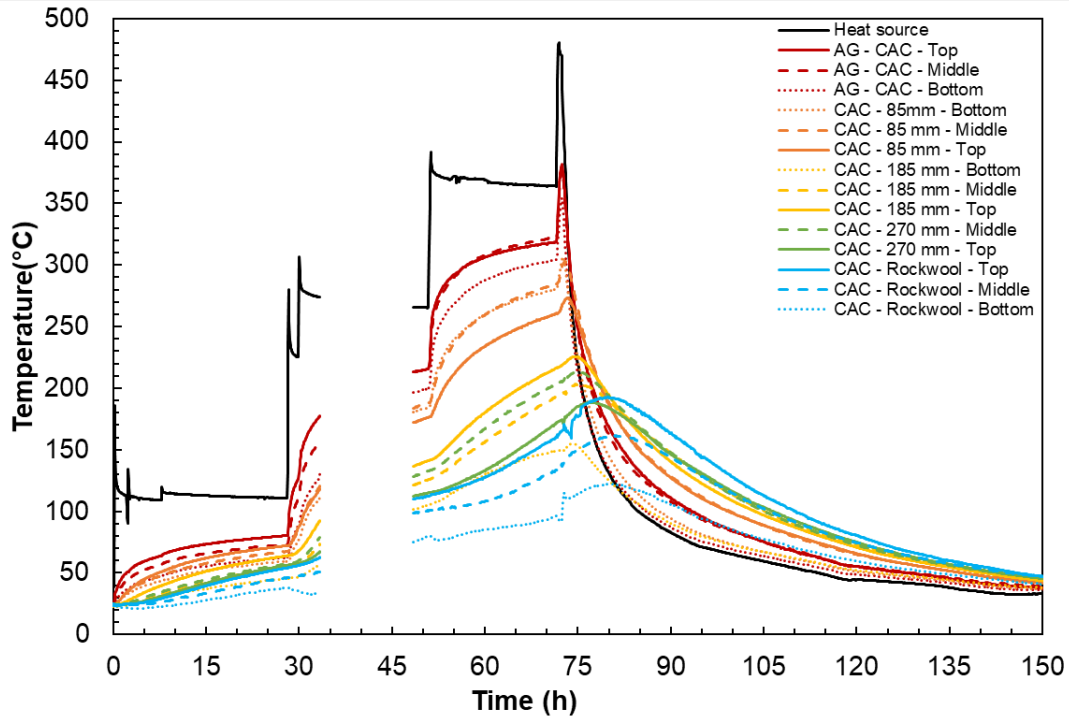


Figure 6.10: Evolution of temperature in the layers of the mock-up of a thermocline section. Drying and dehydration stage.

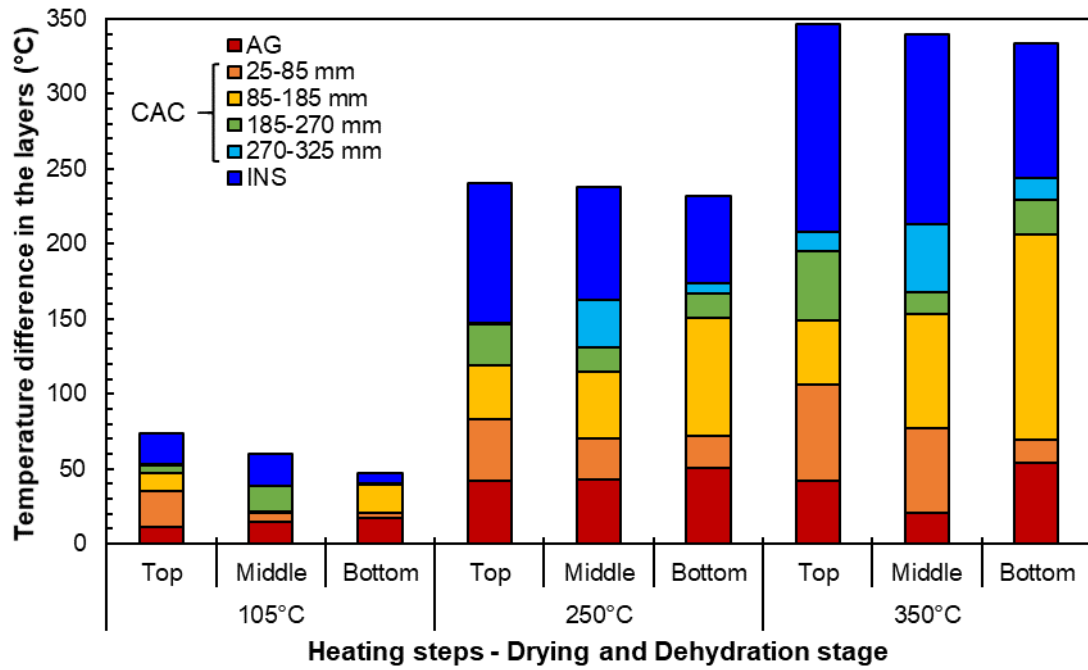


Figure 6.11: Temperature differences in the layers of the mock-up of a thermocline section. Drying and dehydration stage.

The test lasted 150 hours including both heating and cooling processes. The temperatures were not recorded for the period comprised between 35 and 45 hours due to a problem with the data acquisition system, but the thermal test continued and then the issue with the data recording was solved. The following conclusions at every layer can be drawn:

1) **Air Gap:** It is remarkable the “air gap effect” because the highest temperature difference took place within the 50 mm between the steel liner and the surface of the CAC concrete (ΔT_{AG}). Moreover, the heat convection in the air gap was appreciated because the temperature was higher in the upper part due to heat air convection currents. Air with higher temperature has a lower density and tends to go up and that is the reason why the mock-up layers experienced the highest temperatures at the top. For that reason, the ΔT_{AG} was higher at the bottom ($\approx 50^{\circ}\text{C}$) whereas in the upper part reached $\leq 35^{\circ}\text{C}$.

2) **Concrete:** The maximum temperature achieved in the concrete layer was among 200-300°C and the temperature difference within the material (ΔT_{CAC}) was 150°C. At the top, the highest difference of temperatures was achieved in the first 60 mm of CAC concrete. Owing to the convection effect in the air gap, this zone was exposed to higher temperatures and underwent the highest heat effect. At the middle and the bottom, when the temperature increased up to 300-450°C the highest temperature differences were obtained between 85-185 mm of depth. At the time to stop the test, the concrete was being heated but the heat did not arrive at the farther region. Basically, the concrete would have needed more time to homogenize the temperature inside and, for that reason, the highest temperature differences were obtained at those depths.

3) **Insulation:** the heat that arrived at the external part of the insulation was very small because the thermocouples recorded almost the same temperature evolution of the workshop. As the heat was lost from this layer to the ambient, the temperature at the external surface should be higher than the temperature of the workshop. However, the recorded temperature was between 20-22°C in both cases and a better accuracy should have been achieved by using thermocouples with more precision and better calibration.

4) **Foundations:** the temperature sensors located below the mock-up in the sand bed did not register temperatures above 40°C.

The evolution of the temperature across the mock-up from the heat source to the end of the Rockwool is shown in Figure 6.12. The temperature experienced the biggest drop across the CAC concrete layer, which acts as an insulating layer as well. Comparing different heights, the top and middle part followed a similar response in the concrete, but the convection effect is more significant at the top. The insulation ensures low temperature at the further position, which will be close to the structural concrete in the real thermocline tank.

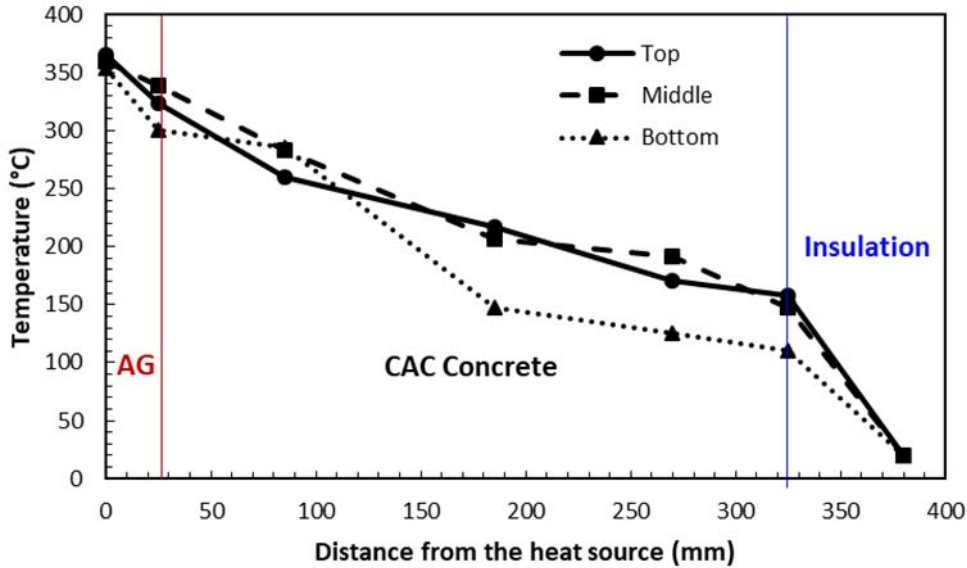


Figure 6.12: Evolution of temperature along with the heat source at the end of the drying and dehydration stage.

6.3.3.2. Evolution of the electrical resistance

The evolution of the electrical resistance recorded in the 5 connections is displayed in Figure 6.13. The electrical resistance follows the same pattern explained in **Chapter 5** for lab-scale samples. Firstly, the parameter decreases up to 30 hours of starting the test due to the high volume of concrete for heating. From that moment, the electrical resistance increases meaning that the concrete layer was losing water from the pores. The rise in the electrical parameter was more significant in regions closer to the heat source as can be seen in the electrical response of connections C1, C2 and C3. At deeper regions, between 160-240 mm, the electrical resistance started increasing its value at 60 hours and the increase was slower. That is the reason why the curves of connections C4 and C5 experienced a smaller slope.

Regarding the monitoring at different depths, Figure 6.14 shows the evolution of electrical resistance, as well as the temperature inside the concrete at the two levels of depths evaluated: 80-160 and 160-240 mm. Regarding the region closer to the heat source (80-160 mm), the concrete reached 100°C after 30 hours of starting the thermal exposure, reaching electrical resistance values between 1-3 kΩ. By contrast, at depths between 160-240 mm the temperature registered 100°C after 60 hours, reaching electrical resistance values of 2-4 kΩ. From that moment, the electrical resistance started growing due to the loss of water and, hence, the drying process. After 75 hours, the electrical resistance was among 238-455 kΩ at depths 80-160 mm, whereas the further region (160-240 mm) was reaching values below 30 kΩ. In this way, the level of drying of the concrete layer was lower in that region.

To conclude, the protocol for measuring the drying process of concrete developed in **Chapter 5** has been validated for monitoring the evolution of the loss of water of concrete exposed to heat. Additionally, the protocol allows the monitoring of the drying process at different depths of a concrete infrastructure at large dimensions. Therefore, the industrial application of the protocol and device developed reaches a TRL 5 because the technology

has been validated in a relevant simulated environment such as this mock-up section of a thermocline tank.

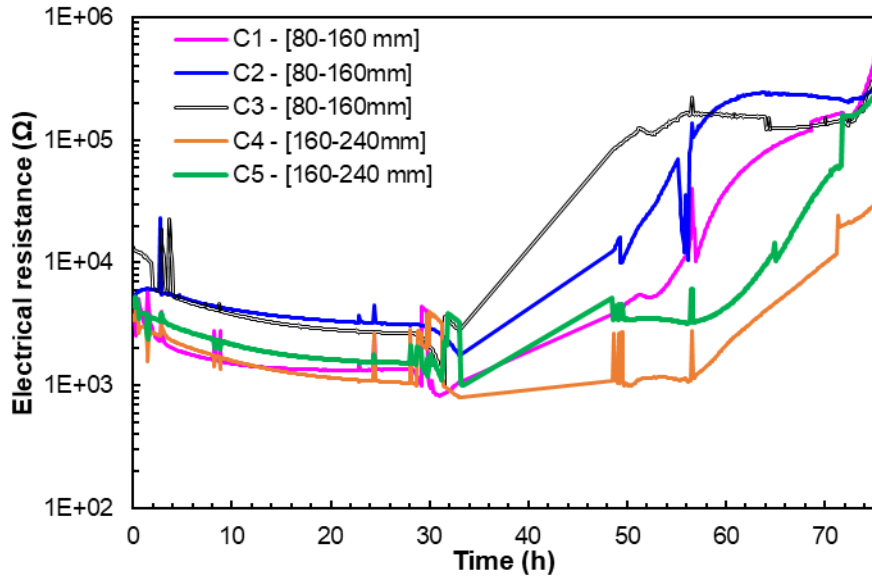


Figure 6.13: Evolution of the electrical resistance of the 5 connections during the drying and dehydration stage.

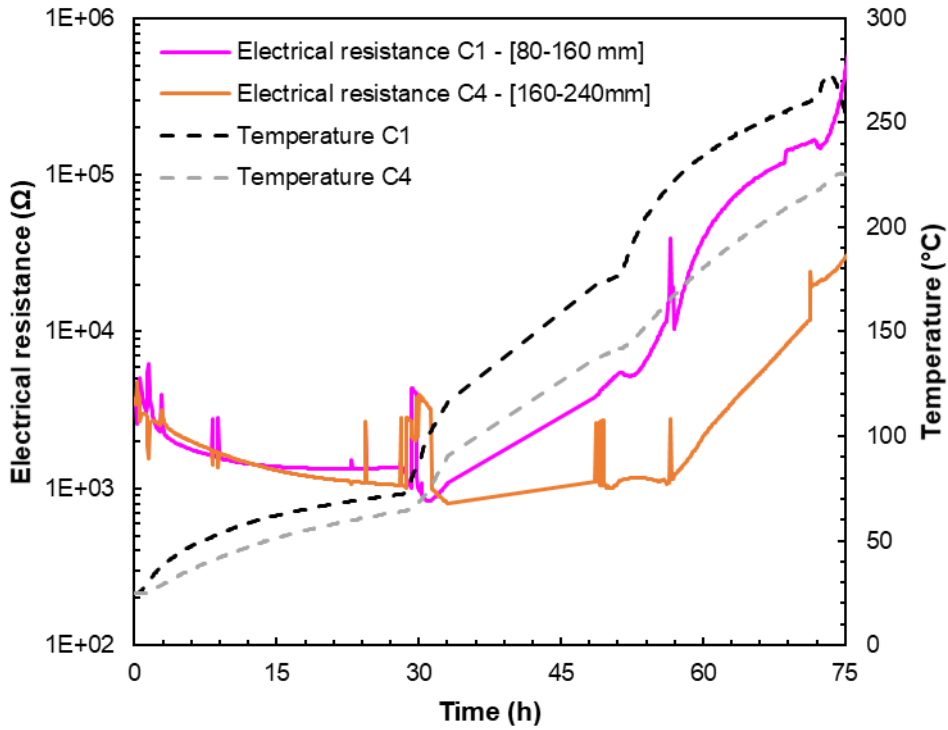


Figure 6.14: Evolution of electrical resistance and temperature inside the concrete for the 2 levels of depth.

6.4. Lessons learned

This section deals with some comments and lessons learned from the construction and commissioning of the mock-up section of a thermocline tank.

Regarding the construction, the most relevant lesson learned has been the high temperatures reached within the concrete layer during the setting period. The temperatures

in the core achieved peak values around 110°C after 10 hours of pouring the concrete into the mould. The peak recorded during the hardening process was elevated because the specimen was isolated with Rockwool due to the low temperature when the element was built in winter. This experience was useful to determine the construction phases of a real tank structure made of concrete. A recommendation of pouring the concrete by phases in a real tank is given so as to reduce the peak of temperature. Additionally, the phases of pouring the concrete should be delayed at least 24 hours to ensure that the poured concrete in the first phase has allowed the cooling down to the ambient temperature.

The thermocline tank needs to be heated before filling the tank with molten salts to commissioning the system for the high temperature reducing risks such as high thermal gradients in the layers that could induce high internal pressures and affect the mechanical performance of the concrete layer or even increase the risk of spalling. Another reason for doing the pre-heating during the commissioning is to minimize the heat losses from the salts to the surroundings in order to avoid a temperature decrease, which will produce the freeze of the molten salts. The temperature of the pre-heating process has to be chosen accordingly to the configuration of the layers and the temperature of the cold salt melted in the tank.

On the other hand, the protocol developed in **Chapter 5** allows the monitoring of the drying process at different depths of a concrete infrastructure at large dimensions. Therefore, the industrial application of the protocol and device developed reaches a TRL 5 because the technology has been validated in a simulated relevant environment such as this mock-up section of a thermocline tank.

Finally, the concrete layer has been demonstrated as an insulating material due to the high temperature difference withstood. Owing to this fact, using concrete in a real tank would allow reducing the thickness of insulating material and, hence, the cost of the whole thermal energy storage infrastructure. However, the appropriateness of this concrete layer during the cyclic performance of a CSP Plant will be evaluated in **Chapter 7**.

6.5. Conclusions

In this chapter, the construction and commissioning of a mock-up section of a thermocline tank made of concrete were carried out. The evolution of the thermal response of different layers subjected to a heat source was studied. The analysis of the commissioning of the mock-up exposed to high temperatures has been analysed, as well as the protocol for monitoring the drying process in a large scale concrete infrastructure. Based on the experimental results presented in this work, the following conclusions can be drawn:

- A mock-up of a section of a thermocline tank was built. It includes a concrete layer made of the optimized concrete mix developed in **Chapter 3**, up-scaled up to 230 litres.
- A recommendation of pouring the concrete by phases in a real tank is given so as to reduce the peak of temperature reached during the setting period.
- A pre-heating process of the thermocline during the commissioning is needed to reduce risks such as high thermal gradients in the layers that could induce high internal stresses and affect the mechanical performance.

- The protocol developed in **Chapter 5** allows the monitoring of the drying process at different depths of a concrete infrastructure at large dimensions. Therefore, the industrial application of the protocol and device developed reaches a TRL 5 because the technology has been validated in a simulated relevant environment such as the mock-up section of a thermocline tank.
- The CAC concrete element has been able to withstand accurately the operation under regimes of high temperatures. For that reason, its use as an insulating element in thermal energy storage tanks is highly recommended for both the thermal response and the reduction of costs.
- The insulation with Rockwool after the CAC concrete and the expanded clay with sand compacted foundation experienced temperatures below 40°C, reducing heat transfer losses to the exterior.

(Chapter 7 on page 155)

6.6. References

- [1] Z. P. Bažant, M. F. Kaplan and Z. P. Bazant, "Concrete at high temperatures: material properties and mathematical models," 1996.
- [2] P. Pimienta, R. J. McNamee and J. Mindegua, *Physical Properties and Behaviour of High-Performance Concrete at High Temperature*. Springer, 2018.
- [3] M. Roig-Flores, T. Lucio-Martin, M. C. Alonso and L. Guerreiro, "Evolution of thermo-mechanical properties of concrete with calcium aluminate cement and special aggregates for energy storage," *Cem. Concr. Res.*, vol. 141, 2021. . DOI: 10.1016/j.cemconres.2020.106323.
- [4] T. Lucio-Martin, M. Roig-Flores, M. Izquierdo and M. C. Alonso, "Thermal conductivity of concrete at high temperatures for thermal energy storage applications: Experimental analysis," *Solar Energy*, vol. 214, pp. 430-442, 2021. . DOI: 10.1016/j.solener.2020.12.005.
- [5] T. Lucio-Martin, M. Roig-Flores, M. C. Alonso and L. Guerreiro, "Evolution of thermal conductivity on CAC concrete at high temperatures and during thermal fatigue tests." vol. Proceedings of the 6th International Workshop on Concrete Spalling due to Fire Exposure, 2019.
- [6] J. Mindegua, P. Pimienta, A. Noumowé and M. Kanema, "Temperature, pore pressure and mass variation of concrete subjected to high temperature — Experimental and numerical discussion on spalling risk," *Cement and Concrete Research*, vol. 40, (3), pp. 477-487, 2010. Available: <http://www.sciencedirect.com/science/article/pii/S0008884609002944>. DOI: <https://doi.org/10.1016/j.cemconres.2009.10.011>.
- [7] M. Zeiml, D. Leithner, R. Lackner and H. A. Mang, "How do polypropylene fibers improve the spalling behavior of in-situ concrete?" *Cement and Concrete Research*, vol. 36, (5), pp. 929-942, 2006. Available: <http://www.sciencedirect.com/science/article/pii/S0008884605003376>. DOI: <https://doi.org/10.1016/j.cemconres.2005.12.018>.
- [8] William, K., Lee, K.K., Xi, Y., Xotta, G., Salomoni, V., "Explosive spalling of concrete materials under extreme environments," in *2nd International Workshop on Concrete Spalling due to Fire Exposure* Anonymous Delft, The Netherlands: 2011, pp. 227-236.
- [9] V. Antonovič, J. Kerienė, R. Boris and M. Aleknevičius, "The Effect of Temperature on the Formation of the Hydrated Calcium Aluminate Cement Structure," *Procedia Engineering*, vol. 57, pp. 99-106, 2013. Available: <http://www.sciencedirect.com/science/article/pii/S1877705813007455>.
- [10] (Last visited on 20-10-05). *Mantas calefactoras flexibles de alta temperatura para curado de composites*. Available: [http://santiescoin.com/resistencias-flexibles-2/mantas-calefactoras-flexibles-de-alta-temperatura-para-curado-de-composites/](http://santiescoin.com/resistencias-flexibles-2/mantas-calefactoras-flexibles-de-alta-temperatura-para-curado-de-composites/mantas-calefactoras-flexibles-de-alta-temperatura-para-curado-de-composites/).
- [11] M. d. M. Alonso, M. Palacios and F. Puertas, "Effect of Polycarboxylate–Ether Admixtures on Calcium Aluminate Cement Pastes. Part 2: Hydration Studies," *Ind Eng Chem Res*, vol. 52, (49), pp. 17330-17340, 2013. . DOI: 10.1021/ie401616f.

This page has been intentionally left blank.

Chapter 7

Thermal performance of a section of a thermocline tank and post-analysis of the concrete layer

To validate the thermal operation of the mock-up of a thermocline tank made of concrete, this chapter describes the thermal performance simulating the limits of operation of a TES in a CSP Plant.

To begin, *section 7.1* presents the monitoring of the operation and summarises the limits of operation of different molten salts in order to fix the operation of the mock-up.

Later, *section 7.2* describes the methodology followed related to the thermal operation and explains the performance of the heat source used in the thermal test. Additionally, includes a brief explanation of the tests carried out after the thermal performance, once the mock-up was disassembled in order to evaluate the concrete layer.

Section 7.3 includes results and discussion of the operation at high temperatures and the characterisation of the concrete layer after the thermal exposure. The experience gained led to learning some lessons related to the operation of the mock-up section of a thermocline tank, which are included in *section 7.4*.

Finally, *section 7.5* includes the conclusive remarks on the operation reported in the present chapter.

7.1. Monitoring of the thermal performance of the up-scaled mock-up

The lack of experiences using concrete as an element in real tanks of molten salts commented in **Chapter 2** made it necessary to go deeper in the knowledge on the thermal performance of a prototype including a concrete layer. With such aim and under the frame of the European H2020 project “NewSOL”, a mock-up section of a thermocline tank was built to validate the results obtained at lab-scale (TRL 3-4) in a simulated environment of a TES system to reach a TRL 5.

The optimization of the concrete composition developed during **Chapters 3 and 4** and in research articles [1-3] revealed the physicochemical transformations of the concrete at high temperatures. Additionally, it was demonstrated that the effect of thermal cycling has not a negative impact on the thermophysical and mechanical properties of the concrete under regimes of temperatures up to 550°C for small lab-scale samples.

Focusing on the mock-up of a section of a thermocline tank, the construction and commissioning were defined in **Chapter 6**, where some lessons learned were given for taking into account in the construction of a real prototype. As it was advanced in **Chapter 6**, the thermal cyclic operation of the mock-up is included in the present chapter. Having done the commissioning of the mock-up and reduced the risk of spalling, the infrastructure can be operated at high temperatures.

The thermal cycle covers the subsequent heating and cooling cycles that a thermocline tank will experience due to the incoming and outgoing of the molten salts. The temperatures of the heated and cooled molten salts vary depending on several factors such as the type of salt and the CSP technology. Regarding the concentrating technology, the temperatures for storing energy varies for Parabolic Trough technology, which ranges between 280-400°C, and in the case of Solar Tower Plants, the temperature is increased up to 550°C [4]. According to the molten salts, recent studies analysed new types of mixes to achieve low melting points and higher temperature stability to improve the properties of the fluid and, hence, the thermal energy storage [5]. The commonly-used Solar Salt present a high melting point around 220°C and some researchers are focused on reducing this temperature and, hence, the cost of the storage [5-7].

Several studies have demonstrated the reduction of the melting point down to 100-120°C in ternary and quaternary mixes [8-11], but the thermal stability of the salts is also reduced up to 480-500°C [8, 11]. On the other hand, a novel ternary molten salt was patented by YARA with a melting point of 131°C and it can be operated with a minimum temperature of 170°C and a maximum temperature limited up to 500°C [12].

Having this context in mind, the limits of the operating temperatures of the heat source of the mock-up were established in 200 and 500°C so as to cover the new advances in the molten salts and to prove the energy storage that can be applied to the solar concentrating technology.

The present chapter contains the results of the monitoring during the thermal cyclic operation of the mock-up section of a thermocline tank. Furthermore, it includes a deeper characterisation of the concrete layer after the thermal test and its appropriateness for being used in infrastructures of TES at high temperatures. At the end of the chapter, some lessons learned from the operation of the up-scaled mock-up are included.

7.2. Methodology

7.2.1. Thermal cycle

The setup and equipments used are the same as the ones mentioned in **Chapter 6** for the mock-up of the thermocline tank. The thermal cyclic operation simulated in the mock-up covers the repetitive heating and cooling cycles between 200 and 500°C. The goal is to

simulate the performance of a thermocline tank where the hot and cold molten salts are placed in the same tank. For that reason, the process of charging and discharging the heat is of importance to perform the evolution of the thermocline zone where the heated and cold salts are together. As the test is carried out with two heating mats and they have two control systems, they can be operated at different temperature regimes.

The charging and discharging process of a thermocline tank can be simulated in the mock-up with the two heating mats as it is shown in Figure 2.5. The initial state is the end of the drying and dehydration curve when the heat source was at 350°C and the air gap at 300°C. The charging process starts from the top and the heated molten salts come into the tank from the upper part and the cold ones go out of the tank from the bottom. Therefore, the HHM was heated up to 500°C while the LHM remained constant. After that, the LHM was heated up to 500°C to simulate a thermocline fully charged. It remained at the maximum temperature for 4 hours and then the discharging process was simulated. The discharge is produced backwards, and the heated molten salts go out of the tank from the top and the cold salts come into the tank from the bottom. Given this process, firstly the LHM was cooled down to 200°C and then the HHM is cooled down to the minimum temperature. Once both heating sources are at 200°C the thermal curve is repeated to simulate the thermal cycling stage.

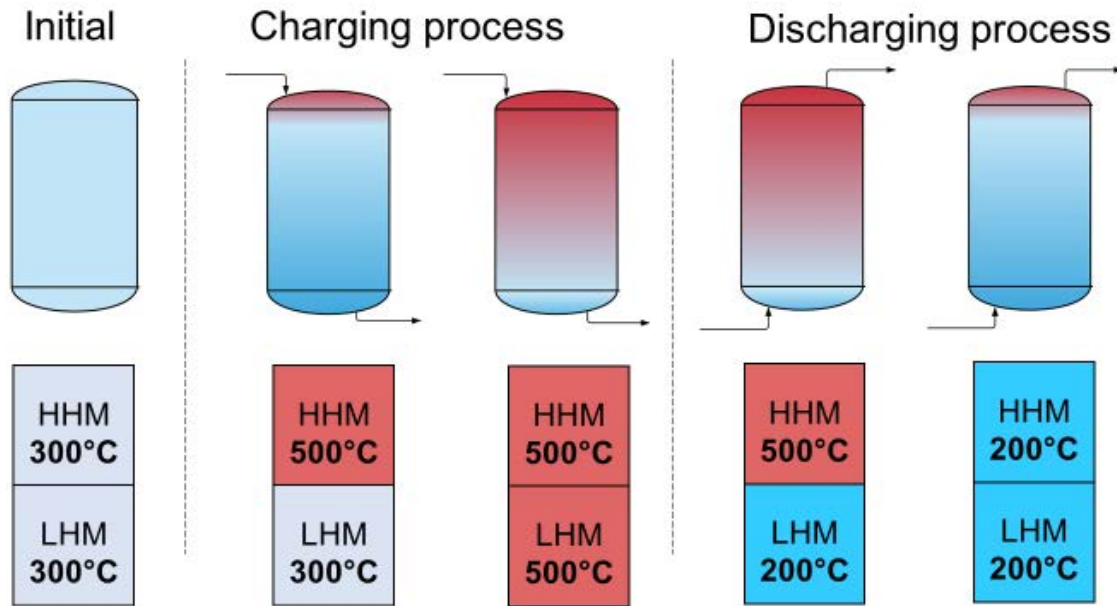


Figure 7.1: Simulated thermal cycling process operation of the mock-up in the heating mats.

Figure 7.2 shows the thermal cycle followed for the thermal cycling stage. The plateaus of temperature were maintained for 4 hours so as to achieve 1 daily cycle. The first heating process was made in order to achieve 300°C in the air gap. Regarding the cooling process, it followed a natural draft. The availability of the workshop for doing the cyclic test was 5 days. It was the reason for doing 3 repetitive complete cycles.

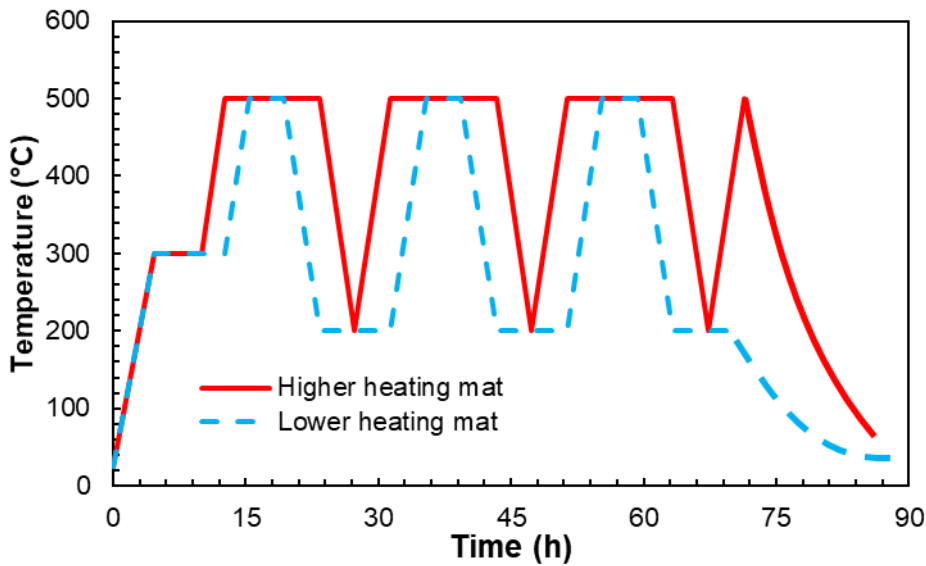


Figure 7.2: Thermal cycling curve

The output parameters measured during the test were the temperature across all layers of the mock-up at 3 heights (250, 500 and 750 mm) with thermocouples and temperature and the electrical resistance measured between 80-160 mm and 160-240 mm in the concrete layer.

7.2.2. Characterisation of the concrete layer after the thermal exposure

Some analyses were made in the concrete after the thermal regime in order to evaluate its appropriateness as a CTES at high temperatures. For that purpose, firstly a visual analysis of the surface of the concrete was carried out. Secondly, some concrete drills were obtained to have a better knowledge of the heat effect in the core of the concrete. The location of the samples was chosen according to the position of the thermocouples and they were obtained at three different levels: 250, 500 and 750 mm from the top and equidistant. A total of 9 core samples of 85 mm of diameters and 300 mm of height were obtained. Additionally, samples 2, 5 and 8 were cut in 10 disks of 20 mm, as is shown in the schema of Figure 7.3.

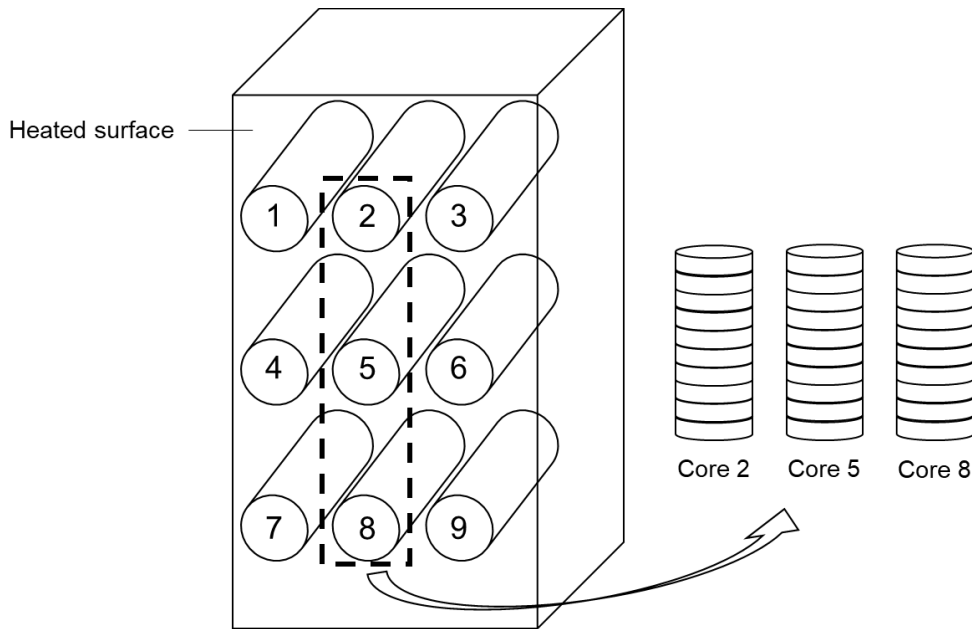


Figure 7.3: Position of the drilled core samples of the concrete

The tests that were performed are classified into two categories: visual analysis and physicochemical characterisation and are summarised in Table 7.1 and Table 7.2, respectively including the identification of the samples. Regarding the dimensions, the core samples 3, 6 and 9 were cut in 2 cylinders (85 mm of diameter and 145 mm of height) and samples 2, 5 and 8 were cut in 10 disks of 85 mm of diameter and 20 mm of height.

| Core samples | Visual analysis | | |
|------------------|-----------------|---------------------|----------------|
| | Colour profile | Location of sensors | Micro-cracking |
| Left: 1,4,7 | X | X | - |
| Middle: 2,5,8 | X | X | X |
| Right: 3,6,9 | X | X | - |

Table 7.1: Tests of visual analysis of core samples.

| Core samples | Physicochemical characterisation | | | | | | |
|------------------|----------------------------------|----------------------|-----|------------------------|----------|--------|--------|
| | Compressive strength | Thermal conductivity | UPV | Electrical resistivity | Porosity | DRX | ATD |
| Left: 1,4,7 | - | - | - | - | - | - | - |
| Middle: 2,5,8 | - | X | X | X | X | - | - |
| Right: 3,6,9 | X | X | X | X | - | Core 3 | Core 3 |

Table 7.2: Tests of physicochemical characterisation of core samples.

Firstly, the evolution of the colour profile, the location of sensors and a micro-cracking evaluation was done. For that purpose, the optical microscope SZ61TR from

OLYMPUS with a resolution of $\pm 1 \mu\text{m}$ was used for taking the pictures. Regarding the microcracking analysis, the software OLYMPUS Stream Essentials was employed to quantify the microcracks width. The tests executed for the physicochemical characterisation were: compressive strength, the evolution of thermal conductivity and electrical resistivity along with the depth, Ultrasonic Pulse Velocity (UPV), accessible water porosity, X-ray diffraction (DRX) and thermogravimetric analysis (ATD).

Five powder samples were obtained to analyse the DRX and ATD at different depths from the heated surface as follows: 10, 60, 150, 200 and 290 mm. The aim was to detect the chemical transformations in the cement paste across the concrete and the samples were obtained from core 2.

The devices employed for measuring the parameters are as follows: the thermal conductivity equipment was model QTM-700 from Kyoto Electronics Manufacturing, with an accuracy of $\pm 0.001 \text{ W}/(\text{m}\cdot\text{K})$. The UPV was obtained by using a PUNDIT 7 CNSFARNELL with a nominal frequency of 54 kHz and a precision of $\pm 0.1 \mu\text{s}$. The measurements were made by using two *p-wave* transducers located in contact with the two parallel surfaces of the concrete disks. The electrical resistivity was obtained from AUTOLAB PGSTAT 302 N Metrohm and it was measured with two metallic grids located in the parallel surfaces of the concrete disks. X-ray diffraction tests (DRX) were carried out on powdered concrete with the equipment BRUKER AXS D8 Advance diffractometer with an RX Lynxeye super speed detector with Cu-K α radiation and a nickel filter. The samples were scanned from 5 to 45° at 20 angles with a step size of 0.02° and a counting time of 0.5 s/step. ATD was determined in a TA Instrument, model TGA-DSC-DTA Q600. Finally, the accessible porosity for water in concrete was measured in core samples 2, 5 and 8. The accessible porosity gives the relation between the volume of pores accessible for water and the apparent volume of the sample. The protocol for calculating the porosity followed was UNE 83980. A precision hydrostatic balance was needed for performing the test, model CENT-2 from Gibertini Europe that has an accuracy of $\pm 0.1 \text{ g}$.

7.3. Results and discussion

7.3.1. Thermal cyclic operation of the mock-up

7.3.1.1. Evolution of temperatures across the mock-up

The thermal cycling test consisted of three repetitive heating and cooling cycles, which lasted 75 hours and a cooling process down to the room temperature. As the test started in another working week that the drying and dehydration stage mentioned in **Chapter 6**, the test starts from room temperature. That is the reason why the first heating was made in order to achieve a temperature of 300°C in the air gap to simulate the operating condition after the drying and dehydration stage. Once the air gap reached the target temperature, the first cycle started and the heating process up to 500°C was made according to the procedure described in Figure 7.2. Figure 7.4 shows the evolution of temperature for the duration of the test across all the layers of the mock-up. The temperatures of the layers follow the same colour pattern that was explained in **Chapter 6**. The temperatures of the layers are represented in: **black** for the heating source (heating mats); **red** after the air gap in the external closer surface of the CAC layer to the heat source; **light blue** after the CAC layer; **dark blue** after the

insulating layer and **violet** for recording the temperature at the bottom of the mock-up, simulating the temperature in the foundations. The temperature recorded at the top (250 mm), middle (500 mm) and bottom (750 mm) are represented with a continuous line, a dashed line and a dotted line, respectively and for all the layers.

Focusing on the concrete layer Figure 7.5 shows the evolution of temperature for the 150 hours of drying and dehydration stage across the concrete layer. The temperatures are represented in: **black** for the heat source; **red** for the surface of the concrete exposed to the air gap, **orange**, **yellow** and **green** for positions inside the concrete at different depths (85, 185 and 270 mm, respectively); and finally, **light blue** for the external surface of the CAC layer in contact to the Rockwool.

The temperature differences across all the layers of the mock-up are represented in Figure 7.6 for three scenarios as follows: the first heating up to reach 300°C in the air gap (initial condition for starting the cycling, time = 3h), and the maximum and minimum operating temperatures when the heat source was at 500°C (time = 40h) and 200°C (time = 50h), respectively.

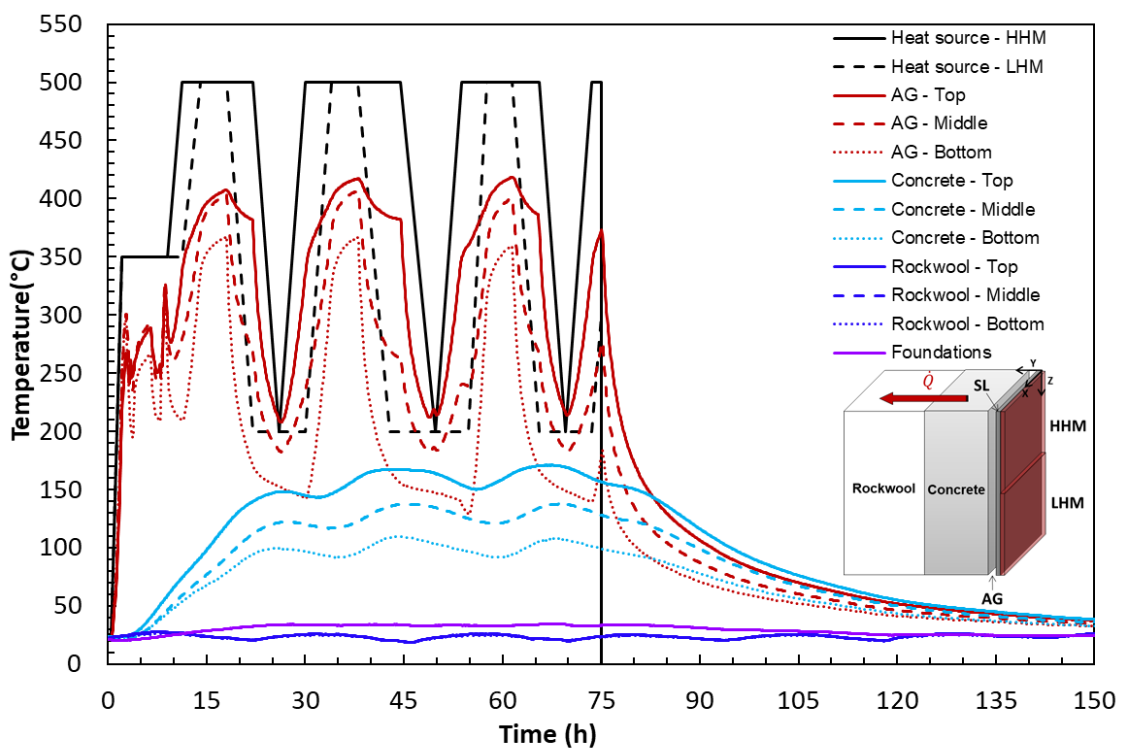


Figure 7.4: Evolution of temperature in the layers of the mock-up of a thermocline section. Thermal cycling stage.

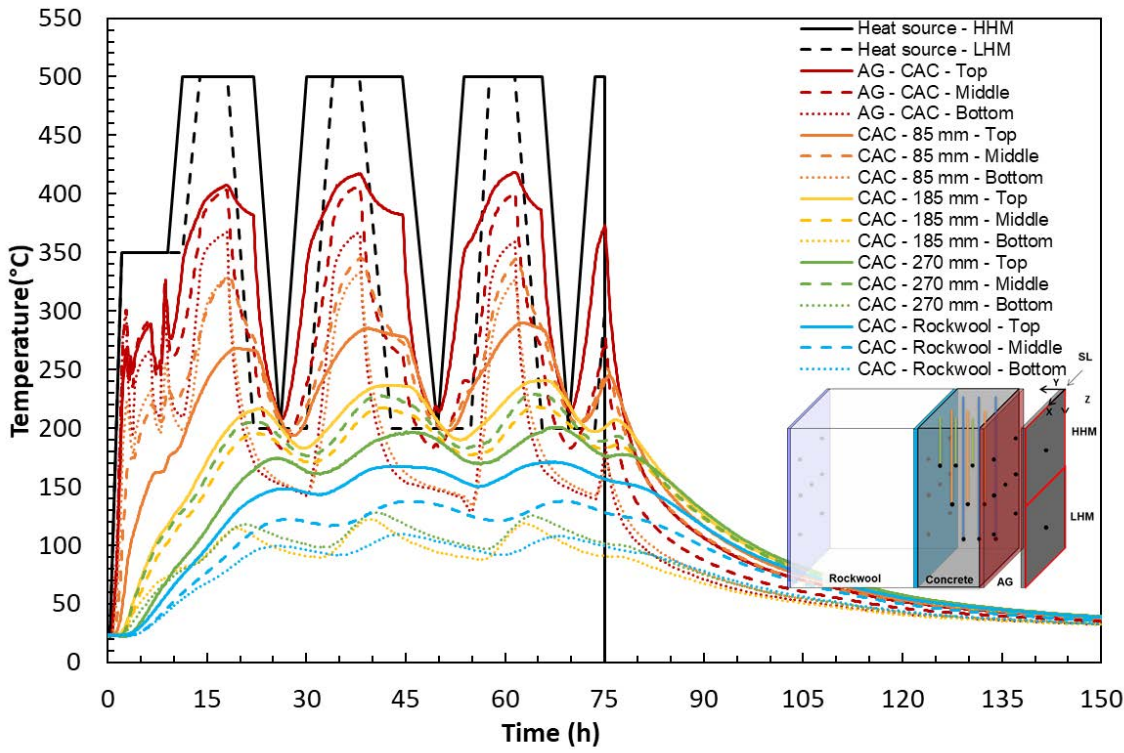


Figure 7.5: Evolution of temperatures in the concrete layer. Thermal cycling stage.

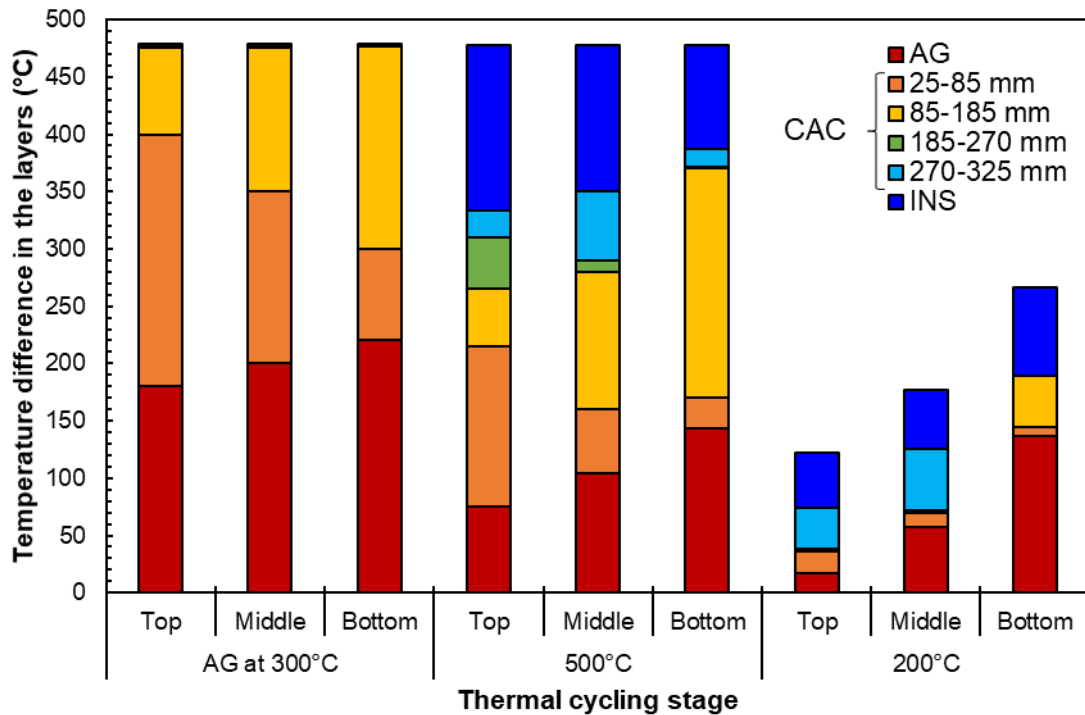


Figure 7.6: Temperature differences in the layers of the mock-up. Thermal cycling stage.

The results of the thermal cycling stage highlighted the following issues that are of interest for carrying out the thermal performance of a thermocline tank.

1) **Air gap:** Again, the role of the air gap is notable. The effect is even higher because the cycles did not allow homogenising the temperature. Those values were above 200°C whereas the top achieved a maximum ΔT of 175°C at the beginning of the heating when the AG was heated to achieve 300°C before performing the thermal cycles from 200-500°C. When the heat source was operating at 500°C, the closer CAC surface was at 420°C at the top and 375°C at the bottom. For the minimum temperature of the cycles (200°C), the temperature differences were slightly lower due to the thermal inertia during the cooling process. The convection heat transfer mechanism that took place in the air gap region was detected between thermocouples located at 500 mm of different height. The convection heat flow from the bottom to the top of the mock-up accelerates the heat losses from the tank to the surroundings. It is worth noting that for a thermocline tank concept having an air gap between layers is not suitable because part of the energy stored is lost.

2) **Concrete:** The maximum temperature achieved in the concrete was 350°C and the temperature differences within the material (ΔT_{CAC}) was 250°C. It is worth noting that the closest CAC region (60 mm) to the air gap experienced the highest difference of temperature of 150°C. Despite undergoing such high difference in temperatures, the concrete layer withstood the cycling properly and its use as both structural and insulating layer was proven.

3) **Insulation:** Operating at the maximum temperature during the cycles did not increase the temperature at the external part of the insulation. The first 3 hours of heating when the test started did not increase the temperature in the Rockwool. Regarding the temperature differences, they were similar when the mock-up was being performed both at 200°C and 500°C.

4) **Foundations:** The thermocouples located in the expanded clay with compacted sand bed did not register temperatures above 40°C. Owing to this fact, there were not heat transfer losses from the mock-up to the soil.

Moreover, two temperature profiles within the layers are shown in: first, when the thermal cycle was at 500°C (time = 40h) and second when the thermal cycle was at 200°C (time = 50h). The evolution of the temperature across the mock-up from the heat source to the end of the Rockwool when the heat source was at 500°C and 200°C are shown in Figure 7.7 and Figure 7.8, respectively. The temperature experienced the biggest drop across the concrete layer when the mock-up was operating at the maximum temperature. Comparing different heights, the top and middle part followed a similar response in the concrete, but the convection effect is more important at the top, as it was explained before. When the heat source was at 200°C, regions closer to the heat source (the air gap) lost energy more quickly, reducing the temperature faster than the regions of concrete located at a deeper distance due to the thermal inertia. The concrete lost energy to the surroundings for the top and the air gap. For that reason, regions closer to the air gap reduced their temperature faster than the further ones and this explains why the top and middle remained almost constant along with the distance of the concrete.

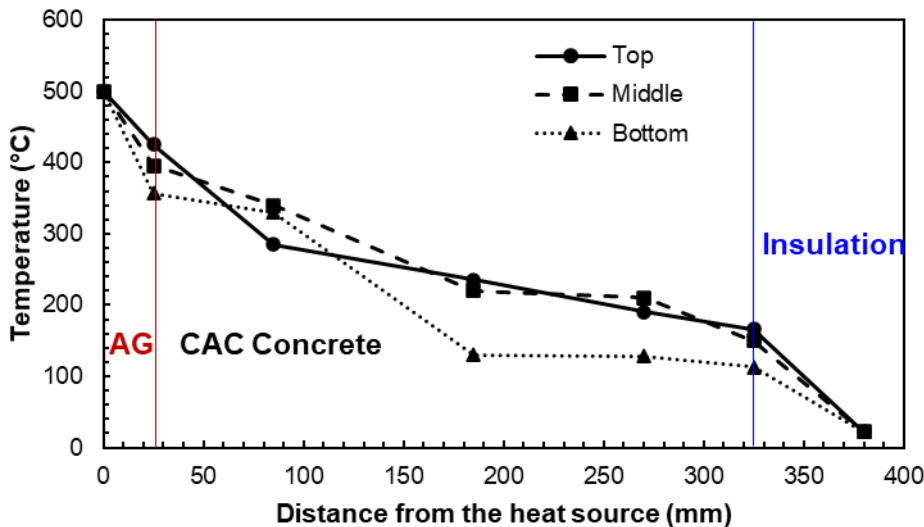


Figure 7.7: Evolution of temperature along with the heat source when the mock-up was operating at 500°C.

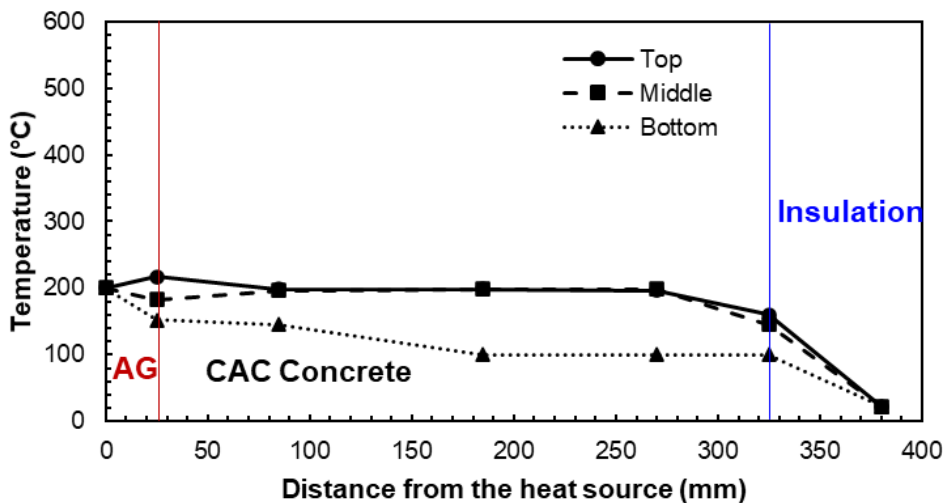


Figure 7.8: Evolution of temperature along with the heat source when the mock-up was operating at 200°C.

7.3.2. Characterisation of the concrete layer after the thermal test

7.3.2.1. Visual analysis and obtention of drilled core samples

Figure 7.9 shows some pictures that were taken to the different surfaces of the concrete element once the mock-up was disassembled. The material did not show visual cracks on the surfaces (left and centre) after being exposed to heat and no visual damage was detected. Therefore, the appropriateness of the CAC concrete designed for the tank wall is once again demonstrated. Regarding the appearance of the thermocouples, they were correctly stuck to the CAC concrete surface after the end of the thermal exposure as can be shown in Figure 7.9-right.

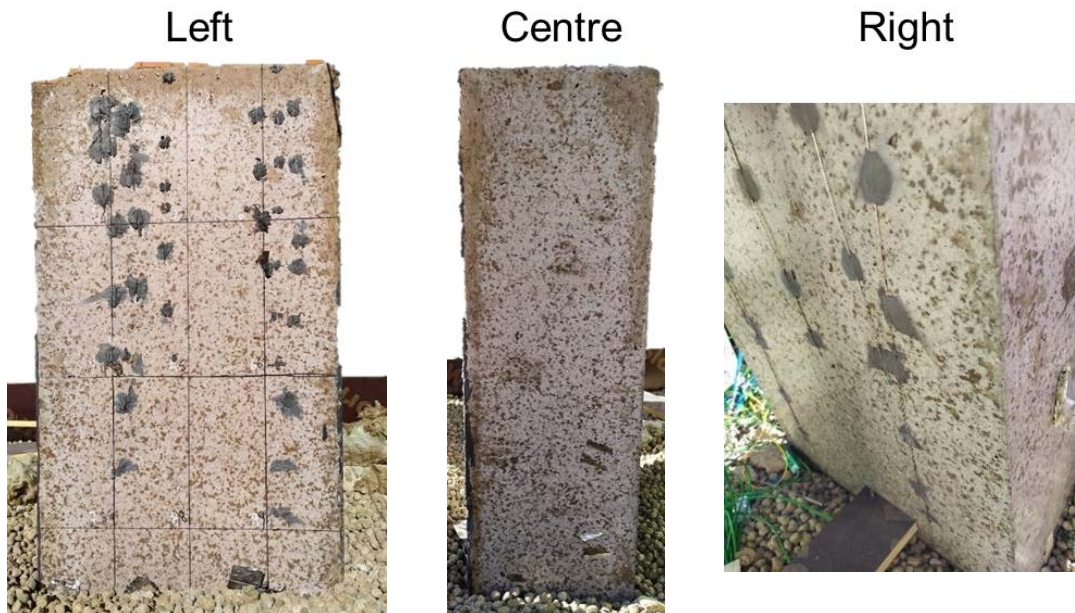


Figure 7.9: Pictures taken on the concrete element after thermal exposure.

In addition, after the visual analysis, 9 drilled core samples were taken so as to evaluate the heat effect across the concrete at 3 heights: 250, 500 and 750 mm and equidistant (Figure 7.10-left). The aspect of the element once the samples were extracted appears in Figure 7.10-centre. The final aspect of the drilled core samples is shown for core sample 1 in Figure 7.10-right.

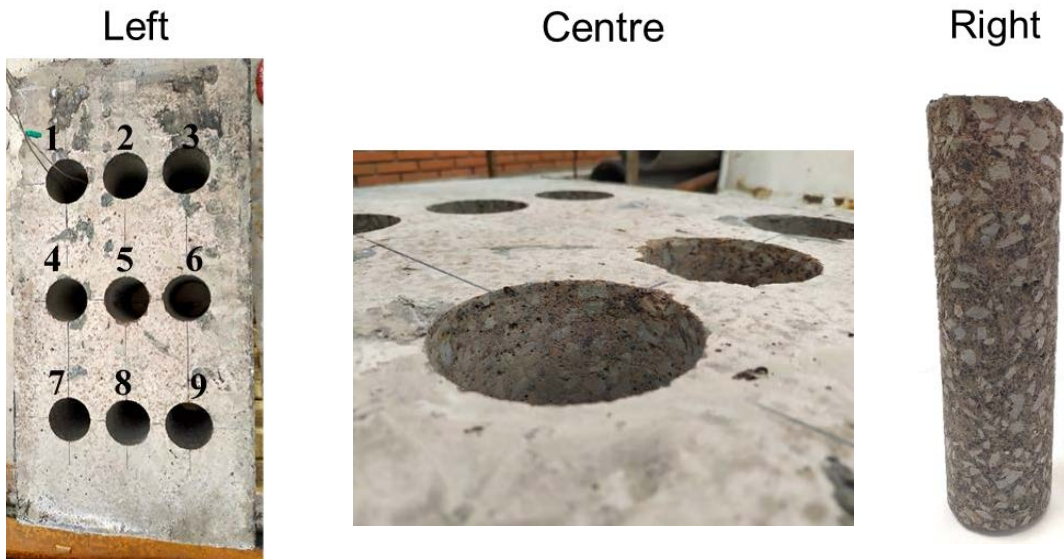


Figure 7.10: Position of the drilled core samples (left), extracted from the element (centre) and core sample 1 (right).

Deviations of the location of sensors and thermocouples

The location of thermocouples was identified in the 9 core samples obtained in the concrete. Some of them were identified in the right position and others were missing, indicating that those sensors were moved during casting. The position was measured with a calliper and the

coordinates for core sample 1 are shown in Table 7.3. The sensor input is referred to as the top of the core section and the sensor output to the bottom part of the section. The position of the sensors identified on the other core samples is in **Appendix B**. Figure 7.11 shows a picture of core sample 1 with 2 thermocouples identified: T7 and T8. The thermocouple 9 was not localized in the core sample, which means that it was moved from the theoretical position during the concrete pouring process and vibration. On the other hand, Figure 7.11 shows 3 additional sensors (FBG-A, FBG-S2, FBG-E) related to the fibre optic sensors that AIMEN, another project partner, put in the concrete. Nevertheless, the position of those sensors was also identified, but they are not included in the results of the present PhD thesis.

| | Theoretical position | | | Measured value | | | | | |
|--------|----------------------|-----|----------|----------------|-----|-------|---------------|-----|-----|
| | Coordinates | | | Sensor input | | | Sensor output | | |
| | X | Y | Z | X_1 | Y_1 | Z_1 | X_2 | Y_2 | Z_2 |
| Core 1 | 375±42.5 | | 250±42.5 | | | | | | |
| T9 | 365 | 60 | 250 | Not localized | | | Not localized | | |
| T8 | 365 | 160 | 250 | 396 | 124 | 213.7 | Not localized | | |
| T7 | 365 | 245 | 250 | 368.2 | 210 | 208.6 | Not localized | | |

Table 7.3: Coordinates of sensors localized in core sample 1



Figure 7.11: Identification of sensors of core sample 1.

Colour changes after heating

Some authors confirm that when concrete is exposed to heat the material experiences a colour change that varies with the temperature reached [13, 14]. For that reason, the colour profile allows for identifying the deepness of concrete affected by the temperature. The CAC concrete of the mock-up also follows a series of colour change under the temperature that moves from a greyer dark colour at initial to a pinkness after 500°C. The concrete colour profiles were obtained on the surface of the nine drilled core samples. Around 20 pictures were taken by using an optical microscope in order to obtain the profile and to determine the change in the colour. The depth of colour change is related to the maximum temperature achieved in the concrete and, hence, to the chemical transformations of the cement paste due to dehydration. Figure 7.12 shows an example of the profile in core sample 2 from the heated surface (left) to the cooler part (right). The profile represents the first 62.23 mm where the colour change can be appreciated. The depth of colour change is shown in Figure 7.13. Concrete located in the upper part (level 250 mm from the top) underwent a higher depth of colour change. The heat came across a higher depth of concrete, around 60 mm whereas the samples located in the lower part (level 750 mm from the top) experienced a colour change within the first 12 mm.

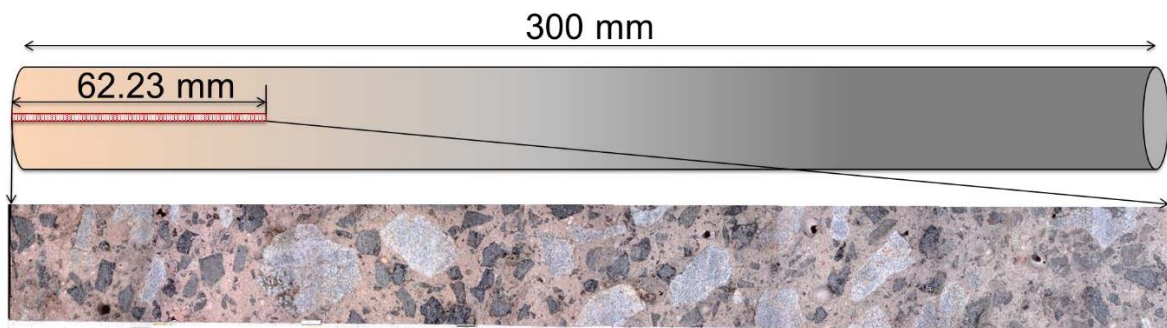


Figure 7.12: Colour profile of the core sample 2 in 62.23 mm.

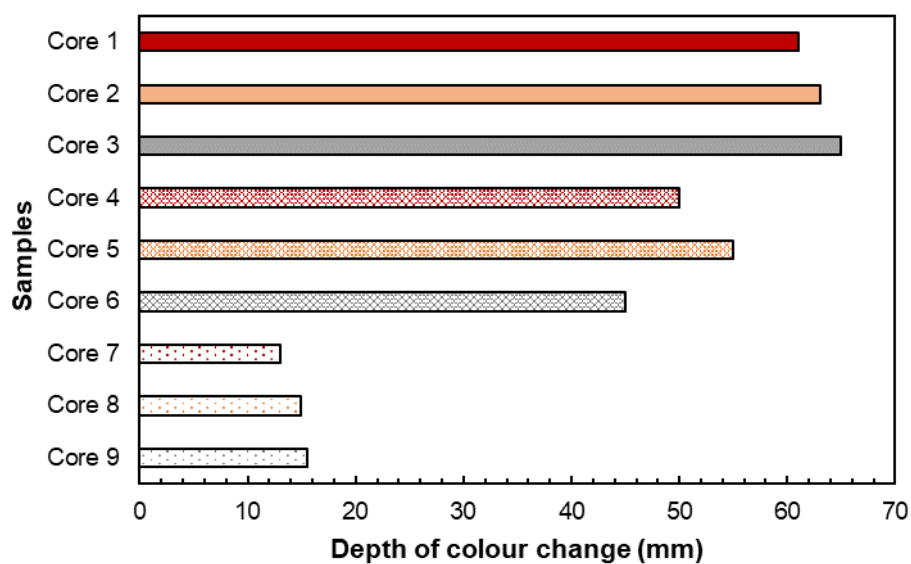


Figure 7.13: Depth of colour change of all core samples.

Micro-cracking analysis

This analysis was made on the micro-cracks generated along with the depth of the concrete layer of the mock-up. The images were taken for all of the concrete disks from core samples 2, 5 and 8 in-depth and the crack width was measured in all of them. Figure 7.14 summarises the mean value of the crack widths. On samples located at the top of the mock-up (core 2), the width slightly increases when the distance ranges from 75 to 125 mm, but the micro-cracks are around 30-45 µm. According to the samples located at the middle (core 5), the widths also increase from 50 to 120 mm ranging from 10 to 60 µm. On the contrary, sample 8 located at the bottom show scattered values but in any case, are the lowest. Those values are in accordance with the micro-crack measurements obtained from different lab-scale studies of CTES [15] as well as the ones obtained in **Chapters 3 and 4** and in [1, 3], whose cracks were lower to 80 µm. Nonetheless, the up-scaled concrete structure did not achieve the maximum temperature in deep and the micro-cracks might be created due to the thermal gradients.

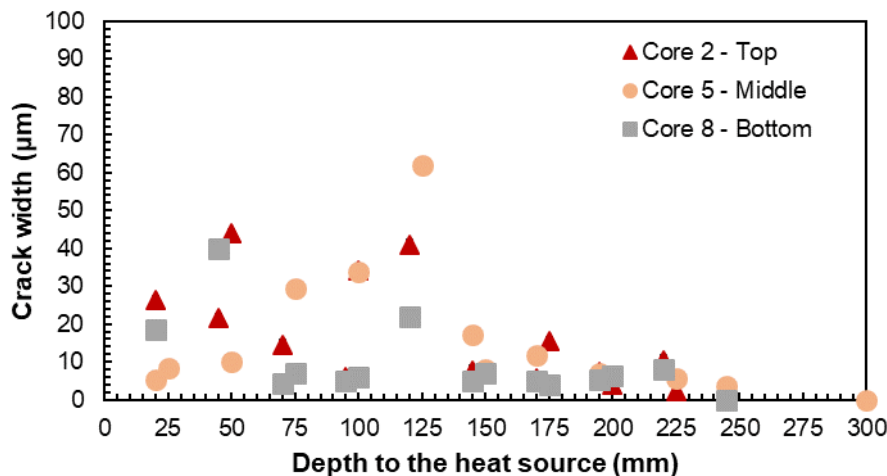


Figure 7.14: Crack width with depth from the heat source.

7.3.2.2. Physicochemical characterisation

Mechanical properties: Compressive strength, UPV and Elastic Modulus

The compressive strength and UPV were measured in the core samples located on the right (3, 6 and 9) and the Elastic Modulus was calculated and are represented in Figure 7.15. The Elastic Modulus was obtained by using the equation (1) presented in **Chapter 3**. Results indicate that the zones located close to the heat source (0-150 mm) were more affected and, hence, the compressive strength was lower than the cooler zones (150-300). Regarding the lower sample (9), the values differ but this could be explained because of the variability of the material. According to UPV, the same explanation can be applied. On the other hand, the UPV was measured on core samples located in the middle (2, 5 and 8) and across the depth of the concrete from the heated surface to the coolest region in samples of width around 20 ± 2 mm (Figure 7.16). Results show scatter but two conclusions can be drawn: i) Depths up to 120 mm from the heat source follow the same pattern and the samples located in the upper part had lower velocity, in the same way, that samples located on the right (3, 6 and 9), ii) from 125 to 300 mm the velocity in the lower sample (8) is always higher because

the heat did not arrive and samples 2 and 5 (top and middle, respectively) experienced almost the same values but with higher dispersion.

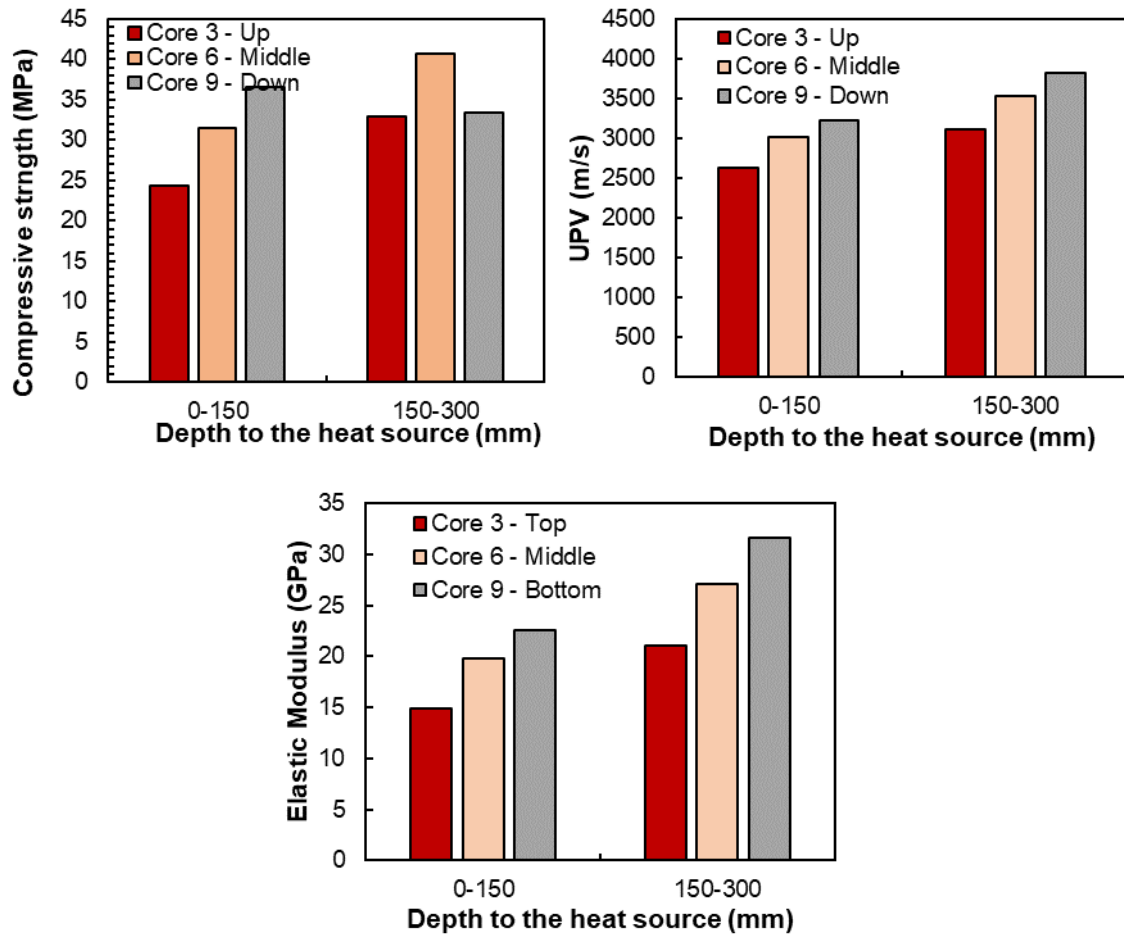


Figure 7.15: top-left) Compressive strength, top-right) UPV and bottom) Elastic modulus in core samples 3, 6 and 9.

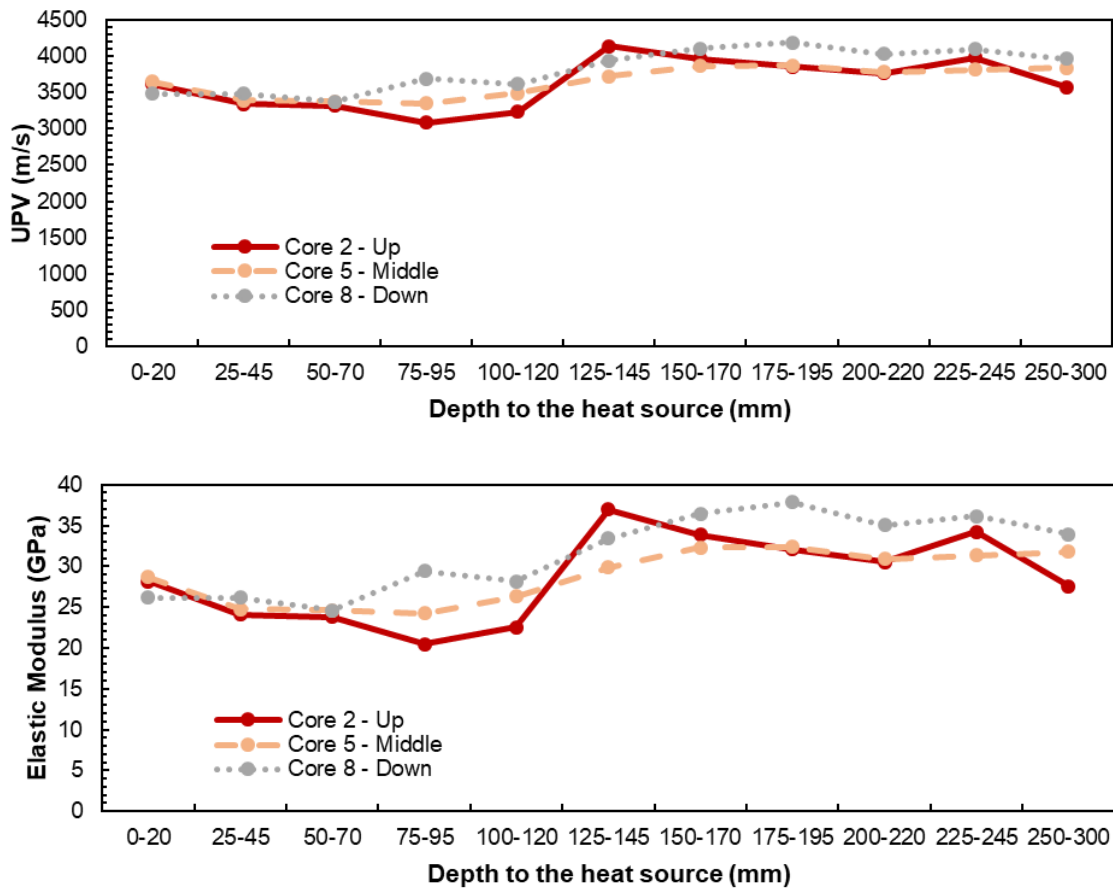


Figure 7.16: top) UPV and bottom) Elastic modulus in core samples 2, 5 and 8 along with the depth of the concrete to the heat source.

Thermal and electrical properties

Figure 7.17 shows the thermal conductivity (left) and the electrical resistivity (right) measured on drilled core samples 3, 6 and 9. The closest region to the heat source (0 mm) experienced the lowest value of thermal conductivity because the concrete was completely dried and dehydrated. At a higher distance to the heated surface, the thermal conductivity was higher because at those locations the temperature was lower and the concrete did not undergo complete dehydration. The value is almost the same at 300 mm in the coolest surface and the high temperature did not arrive at the external surface of the concrete layer. Regarding the electrical resistivity, the samples located near the heat source have higher electrical resistivity than the ones located at 150-300 mm. The reason is that the concrete is more dried and, hence, less electrically conductive. Moreover, the effect of the convection heat transfer mechanism might be detected because the values of electrical resistivity are higher in sample 3 than the core samples 6 and 9. What it does mean is that the upper part of the CAC concrete was more dehydrated because of heat flow.

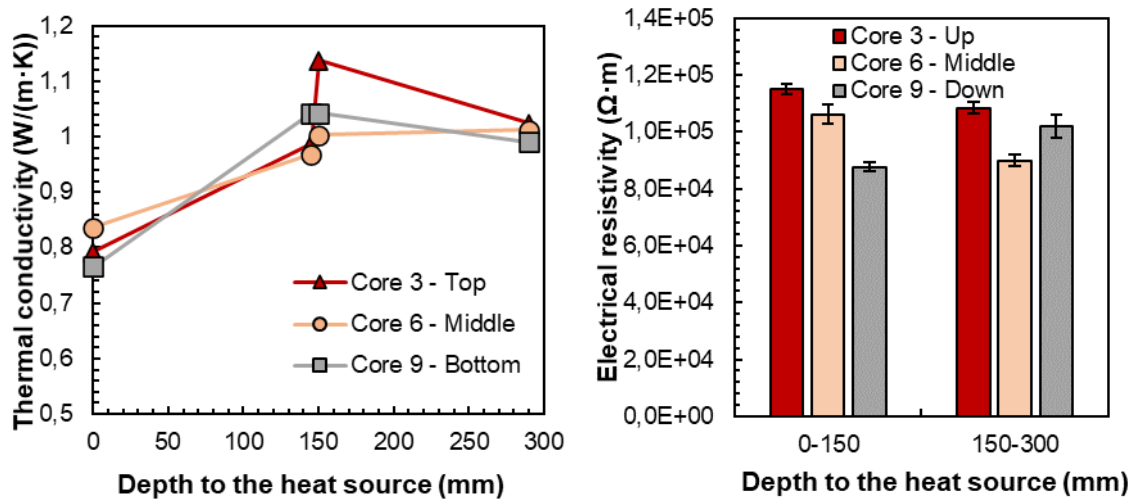


Figure 7.17: left) Thermal conductivity and right) electrical resistivity of samples 3, 6 and 9.

The evolution of the thermal conductivity in depth is shown in Figure 7.18 for the core samples 2, 5 and 8 located in the middle of the mock-up. A black line was added at 1 W/(m·K) because this value is the thermal conductivity of CAC concrete once the material has been dried. Other two dash lines were added representing the standard deviation of the value measured dried. The three samples followed a growing trend in depth because the regions closer to the heat source were more dried than the farther ones. Values below 1 W/(m·K) might mean that those regions have been exposed to higher temperatures and the concrete is completely dried and dehydrated. The drying depth was lower in sample 8 located at the bottom (75 mm), and higher in sample 5 (100 mm) and sample 2 (125 mm). Those values for drying are in accordance with regions of colour change (Figure 7.13). They are not exactly the same because the colour change is related to the dehydration of cement paste, which takes place at higher temperatures, but the pattern is the same in both cases.

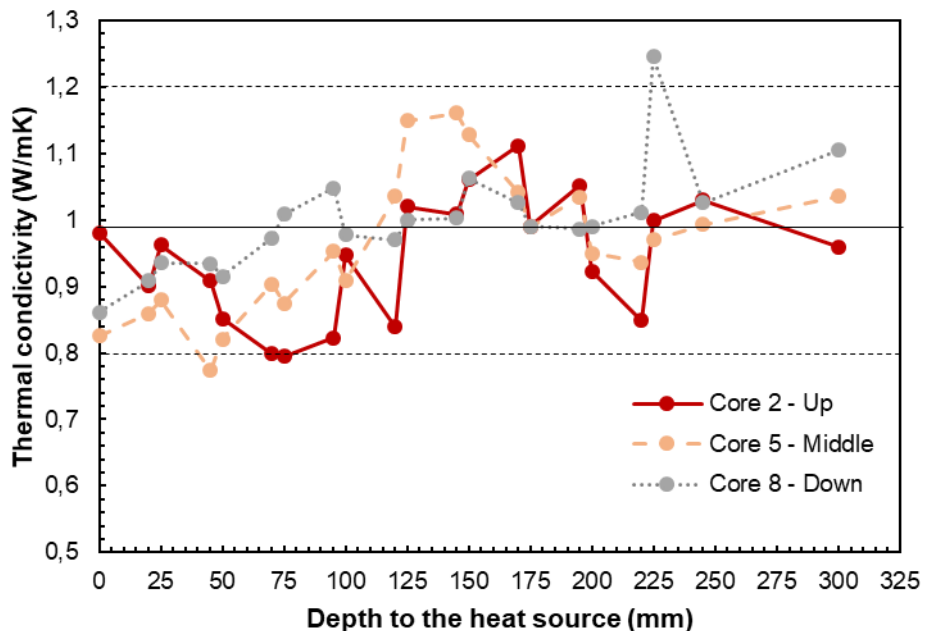


Figure 7.18: Evolution in the depth of thermal conductivity of samples 2, 5 and 8.

Accessible porosity for water in concrete

Figure 7.19 shows the changes in the porosity with the depth of concrete. Core 2, located at the top, experienced the highest porosity because the temperature profile through core 2 achieved a higher temperature and higher dehydration level of cement paste. The core 5, located at the middle, followed the same pattern but with lower porosity. Regarding the core 8, it is remarkable the decrease in the second half of the sample, from 150 to 300 mm, achieving 15.5% of porosity at the end.

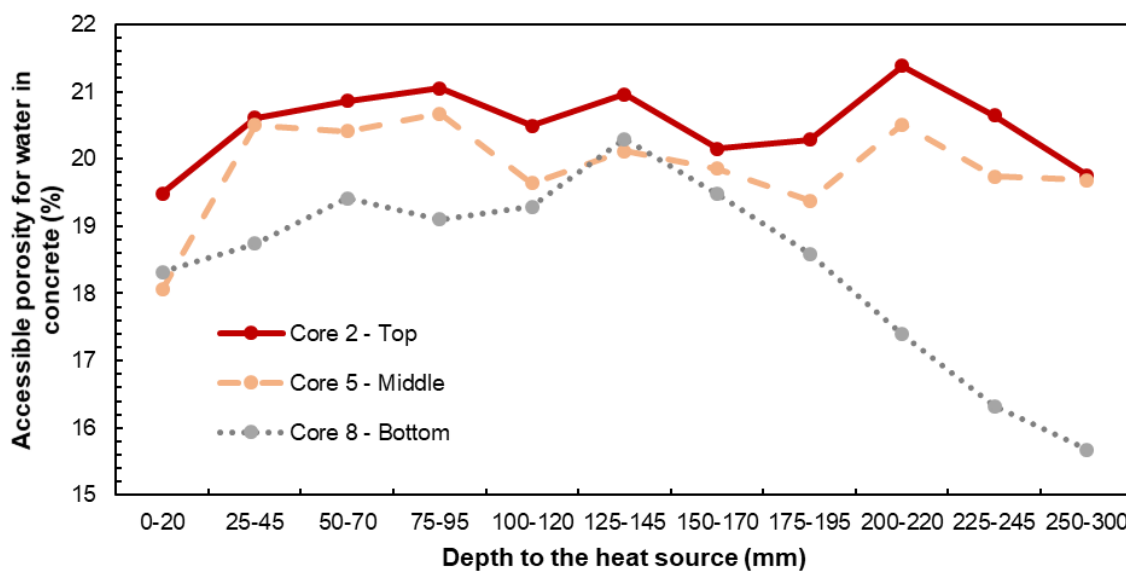


Figure 7.19: Evolution in the depth of accessible porosity of samples 2, 5 and 8.

Microstructural changes: DRX and TG/ATD

X-ray diffraction performed on concrete powder samples (Figure 7.20) show the presence of several phases associated with the hydrated compounds (C_2AH_6 , CAH_{10} and AH_3), which disappear after being exposed to heat at 10 and 60 mm. For deeper samples, the presence of the hydrated compounds indicates that the cement paste was not fully dehydrated and the temperatures at those locations were lower to 300°C. The remaining phases are related with the spectra of unhydrated calcium aluminate (CA and $C_{12}A_7$), produced by both the unhydrated cement and the CAT aggregates, but also quartz originated in the basalt aggregates, which are rich in silicon, and calcite, which can be formed due to the calcium-rich cement paste. Those phases might be appreciated at 60, 150, 200 and 290 mm and indicate that the concrete was not dehydrated at those positions.

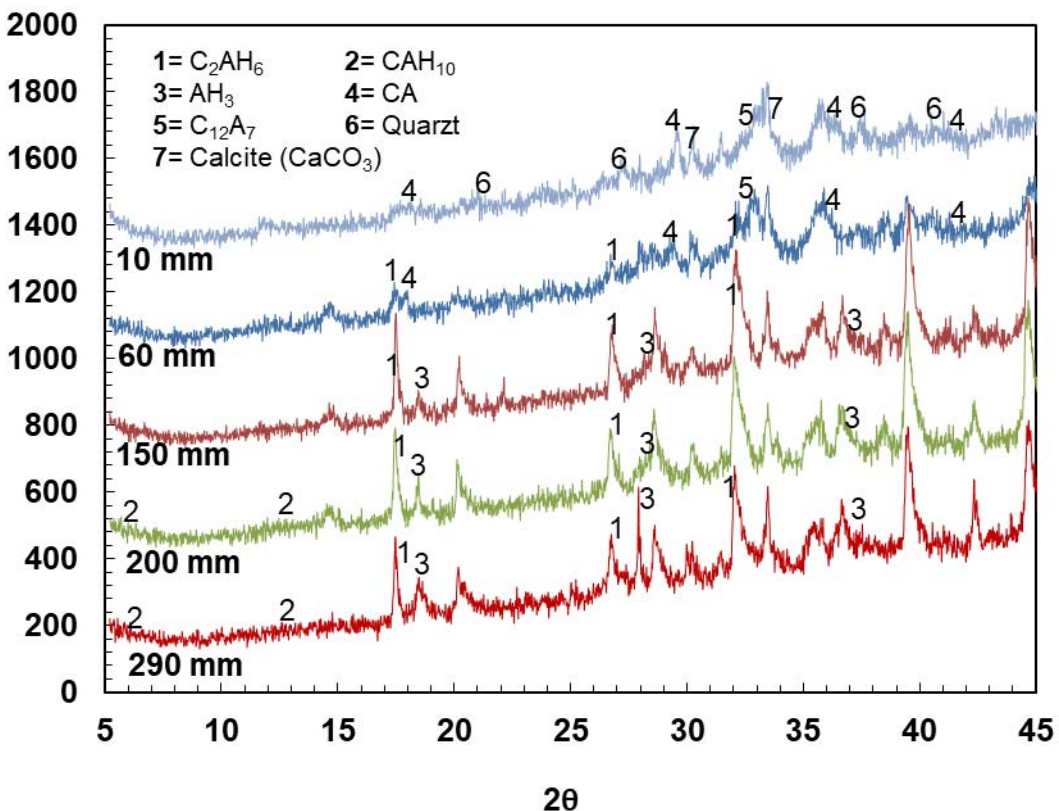


Figure 7.20: DRX results of CAC concrete samples at 10, 60, 150, 200 and 290 mm from the heated surface.

The results are displayed in Figure 7.21 at 10, 60, 150, 200 and 290 mm from the heated surface. The peaks in the dTG curve show transformations produced by dehydration of CAH_{10} and C_2AH_8 between 120-200°C, dehydration of AH_3 between 200-240°C and decomposition of C_2AH_6 between 200-250°C. Other transformations at 450-500°C and 700°C might be associated with Alentejo Slag Aggregates and calcium carbonate, respectively as it was commented in **Chapter 3**. The results show clear differences between the samples located at 10 and 60 mm and the other ones. The weight loss was 5.6% and 6.67% for samples located at 10 and 60 mm, respectively. Those samples experienced a lower peak of transformation at 270°C, indicating that most of the CAC were dehydrated in the thermal performance of the mock-up. On the contrary, samples at 150, 200 and 290 mm experienced a loss of 10.01%, 10.48% and 11.96 %, respectively. Samples located at a deeper distance from the heat source underwent a higher peak of transformation, which indicates that the cement was not dehydrated in those regions.

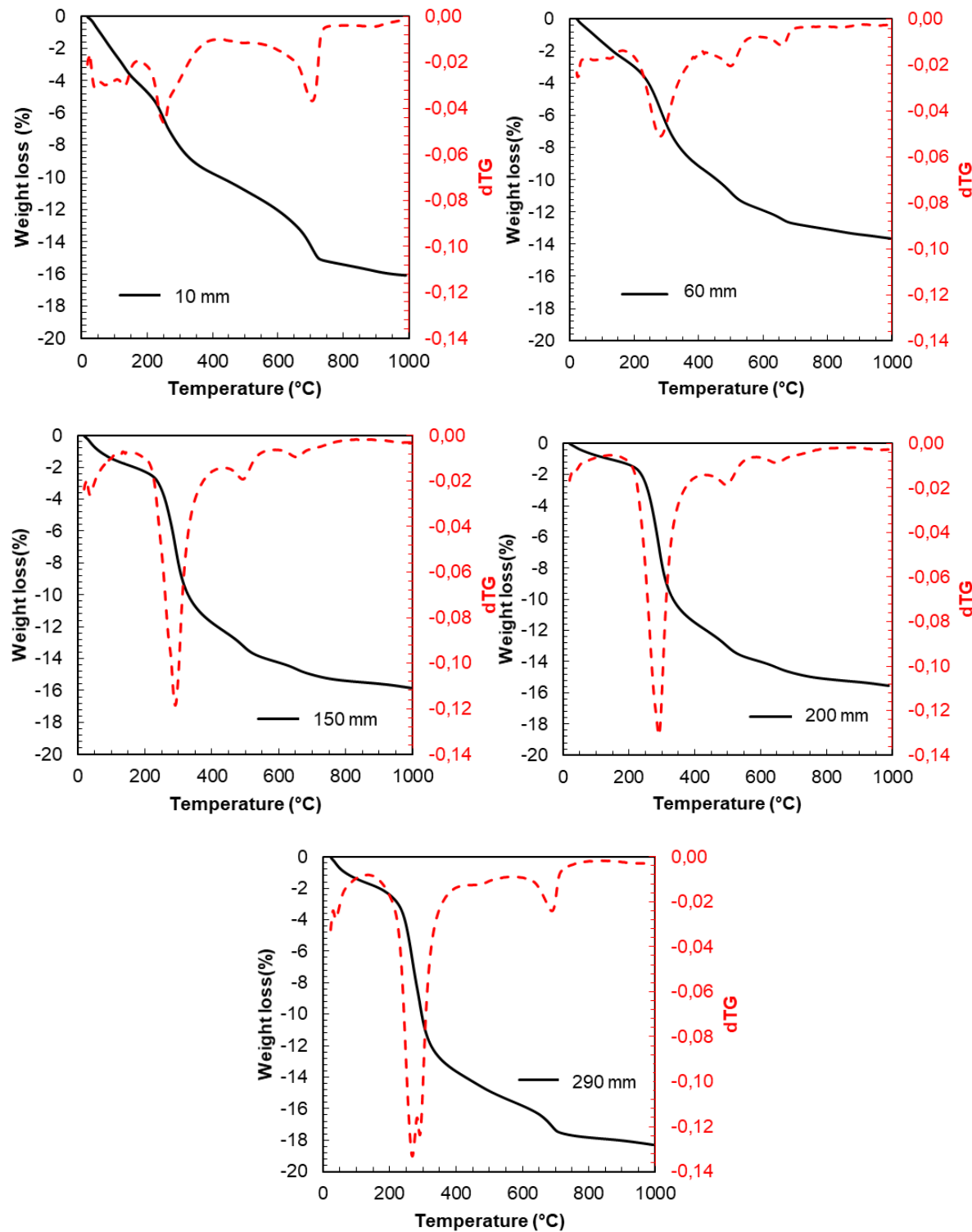


Figure 7.21: TG/DTG analyses for CAC concrete powder located at different depths: top) 10 and 60 mm, middle) 150 and 200 mm and bottom) 290 mm.

7.4. Lessons learned and thermocline discussion

Proceeding in the same way as in **Chapter 6**, this section presents some comments and lesson learned from the operation of the mock-up of a thermocline tank section.

The temperature of the first heating was established at 350°C for achieving 300°C in the air gap and the surface of the concrete layer in order to achieve the same conditions as the ones obtained at the last heating step of the commissioning curve. However, in a real prototype of a tank, both process (commissioning and operation) would be separated because the process of filling the tank with molten salts should be done after the commissioning. As the particularities in the preconditioning and filling process depend on the TES system and geometry, here some general details are included. The tank should be preheated before the entrance of the melted salts in the tank. There exists a wide range of types of molten salts, which presents different melting points and temperatures of stability, as was mentioned in subsection *7.1. Monitoring of the thermal performance of the up-scaled mock-up*. The temperature of the preheating should be fixed according to the type of the salt and should be higher than its melting point in order not to freeze the salts when they are incoming into the tank.

Regarding the operation of the thermocline, the successive heating and cooling cycles have highlighted the thermal inertia of the system. It is the air gap the unique layer that underwent the variations of temperature of the heat source. The highest decrease in temperature was found in the concrete. Therefore, the CAC concrete element has been able to withstand accurately the cyclic operation under regimes of high temperatures. For that reason, its use as an insulating element in thermal energy storage tanks is highly recommended for both the thermal response and the reduction of costs. This advance of using concrete as a thermal energy storage material was also reported by many authors at lab-scale [1, 16-18]. Nevertheless, in this study, a novel concept of using concrete as an insulating layer for tanks containing molten salts has been demonstrated for an up-scale achieving a TRL 5. The outcomes demonstrate that the configuration of TES analysed can be used in systems operating up to 500°C, and in the technology of Parabolic Trough collectors.

According to the limitations of the technology of the thermocline concept, it is important to note that the air gap experienced thermal gradients between top and bottom owing to the convection heat flow effect. Heat tends to go up and that is the reason why the temperature recorded at the top was always above 50°C higher than the one recorded 500 mm below. This outcome was found in just 500 mm of height, so the effect might be even higher in real thermocline tanks whose heights would be bigger than 10 metres, from simulations carried out by many authors [19-21].

The convection heat flow accelerates the heat transfer losses and for a thermocline tank concept, having an air gap is not the most efficient because the ratio cost vs energy is reduced. Nonetheless, the gap is needed from the mechanical point of view because the tank filled with molten salts will expand during the operation, reducing the width of the air chamber. The negative effect of the air gap analysed in this mock-up could be reduced in a real tank due to the thermal expansion, and as a consequence, the loss of thermal energy to

the top would be reduced. For those reasons, a balance between the geometry, construction phase and the thermal operation of the infrastructure must be found.

The negative effect of the air gap might be reduced with a redesign of the air chamber so as to minimize the convective heat flow and, thus, the discharge of energy from the bottom to the top of the tank. Some baffles might be included in the geometry with the purpose of changing the direction of the air flow and avoid the generation of the convection currents. Nevertheless, the baffles should be made of a material resistant to high temperatures and able to withstand changes in the volume of the steel tank due to the thermal expansion. Those requirements complicate the geometry and the construction process of the tank. However, a solution must be found because the relevance of this negative effect will be even higher in real tanks with bigger dimensions.

Comparing the 2-tank and thermocline concepts, the thermocline zone where the temperature drop is located causes exergy losses due to the contact of two fluids at different temperatures. Narrower thermocline zones produce lower exergy losses, as was reported by [22, 23]. Indeed, it affects efficiency compared to 2-tank technology, which does not present exergy losses because it has no temperature difference.

On the other hand, the present mock-up operation has arisen the issue of thermal losses due to the convection process within the air gap. Having said that, despite the cost has been reported to be lower in the thermocline configuration [19, 24, 25], in terms of energy efficiency the benefits do not overcome the results of the 2-tanks storage.

7.5. Conclusions

The operation under cyclic regimes of temperature between 200-500°C has been reported in this chapter. The evolution of the thermal response of different layers subjected to the cyclic heating and cooling cycles was studied. Furthermore, some physicochemical tests were performed on concrete core samples obtained after the thermal operation once the mock-up was disassembled. Based on the results presented in this work the following conclusions can be drawn:

- An initial heating process of the tank is needed before the entrance of the melted salts in the tank with a temperature higher than the melting point in order not to freeze the salts when they are incoming into the tank.
- The convection heat transfer mechanism in the air gap highly influence the evacuation of heat from the bottom to top, reaching differences of temperature near 50°C in a mock-up of 1 m height).
- The convection heat flow accelerates the heat transfer losses and for a thermocline tank concept, having an air gap is not the most efficient because the ratio cost vs energy is reduced. Nonetheless, the gap is needed from the mechanical point of view because the tank filled with molten salts will expand during the operation.
- A balance between the geometry, construction phase and the thermal operation of the infrastructure must be found.
- The characterisation of the CAC concrete layer after the thermal test have demonstrated that:

- The closest region of CAC from the heated surface (first 60 mm of concrete) experienced ΔT_{CAC} of 150°C with no damage within the concrete. The maximum temperature of concrete was 350°C but the material did not present cracks.
- CAC concrete was completely dried up to 125 mm from the heated surface (Thermal conductivity and profiles of colour change).
- CAC concrete was dehydrated up to 60 mm from the heated surface (DRX-TG/DTA).
- The region of CAC affected by heat was from 0 to 150 mm from the heat source (Compressive strength and UPV).
- Micro-cracks (10-60 μm) appeared up to 125 mm from the heated surface due to dehydration and the temperature difference.
- The CAC concrete layer has been withstood accurately the operation under regimes of high temperatures. For that reason, its use as an insulating element in thermal energy storage tanks is highly recommended for both the thermal response and the reduction of costs.
- The novel concept of using concrete as an insulating layer for tanks containing molten salts has been demonstrated for an up-scale achieving a TRL 5. The outcomes demonstrate that the configuration of TES analysed can be used in systems operating up to 500°C, and in the technology of Parabolic Trough collectors.

(Chapter 8 on page 181)

7.6. References

- [1] M. Roig-Flores, T. Lucio-Martin, M. C. Alonso and L. Guerreiro, "Evolution of thermo-mechanical properties of concrete with calcium aluminate cement and special aggregates for energy storage," *Cem. Concr. Res.*, vol. 141, 2021. . DOI: 10.1016/j.cemconres.2020.106323.
- [2] T. Lucio-Martin, M. Roig-Flores, M. C. Alonso and L. Guerreiro, "Evolution of thermal conductivity on CAC concrete at high temperatures and during thermal fatigue tests." vol. Proceedings of the 6th International Workshop on Concrete Spalling due to Fire Exposure, 2019.
- [3] T. Lucio-Martin, M. Roig-Flores, M. Izquierdo and M. C. Alonso, "Thermal conductivity of concrete at high temperatures for thermal energy storage applications: Experimental analysis," *Solar Energy*, vol. 214, pp. 430-442, 2021. . DOI: 10.1016/j.solener.2020.12.005.
- [4] G. Peiró, C. Prieto, J. Gasia, A. Jové, L. Miró and L. F. Cabeza, "Two-tank molten salts thermal energy storage system for solar power plants at pilot plant scale: Lessons learnt and recommendations for its design, start-up and operation," *Renewable Energy*, vol. 121, pp. 236-248, 2018. . DOI: 10.1016/j.renene.2018.01.026.
- [5] M. Vaka, R. Walvekar, P. Jagadish, M. Khalid, N. M. Mubarak and H. Panchal, "High-temperature molten salts optimisation using mixture design for energy storage application," *Journal of Energy Storage*, vol. 32, pp. 101981, 2020. . DOI: 10.1016/j.est.2020.101981.
- [6] A. Gil, M. Medrano, I. Martorell, A. Lázaro, P. Dolado, B. Zalba and L. F. Cabeza, "State of the art on high temperature thermal energy storage for power generation. Part 1—Concepts, materials and modellization," *Renewable and Sustainable Energy Reviews*, vol. 14, (1), pp. 31-55, 2010.
- [7] A. G. Fernández, S. Ushak, H. Galleguillos and F. J. Pérez, "Thermal characterisation of an innovative quaternary molten nitrate mixture for energy storage in CSP plants," *Solar Energy Mater. Solar Cells*, vol. 132, pp. 172-177, 2015. Available: <https://www.sciencedirect.com/science/article/pii/S0927024814004437>. DOI: <https://doi.org/10.1016/j.solmat.2014.08.020>.
- [8] C. Y. Zhao and Z. G. Wu, "Thermal property characterization of a low melting-temperature ternary nitrate salt mixture for thermal energy storage systems," *Solar Energy Materials and Solar Cells*, vol. 95, (12), pp. 3341-3346, 2011. Available: <http://www.sciencedirect.com.biblioteca5.uc3m.es/science/article/pii/S0927024811004478>. DOI: <https://doi-org.biblioteca5.uc3m.es/10.1016/j.solmat.2011.07.029>.
- [9] N. Ren, Y. Wu, C. Ma and L. Sang, "Preparation and thermal properties of quaternary mixed nitrate with low melting point," *Solar Energy Mater. Solar Cells*, vol. 127, pp. 6-13, 2014. Available: <https://www.sciencedirect.com/science/article/pii/S0927024814001871>. DOI: <https://doi.org/10.1016/j.solmat.2014.03.056>.
- [10] R. I. Olivares and W. Edwards, "LiNO₃–NaNO₃–KNO₃ salt for thermal energy storage: Thermal stability evaluation in different atmospheres," *Thermochimica Acta*, vol. 560, pp. 34-42, 2013. Available: <https://www.sciencedirect.com/science/article/pii/S0040603113001196>. DOI: <https://doi.org/10.1016/j.tca.2013.02.029>.

- [11] A. Ibrahim, H. Peng, A. Riaz, M. Abdul Basit, U. Rashid and A. Basit, "Molten salts in the light of corrosion mitigation strategies and embedded with nanoparticles to enhance the thermophysical properties for CSP plants," *Solar Energy Mater. Solar Cells*, vol. 219, pp. 110768, 2021. Available: <https://www.sciencedirect.com.biblioteca5.uc3m.es/science/article/pii/S0927024820303676>. DOI: <https://doi.org.biblioteca5.uc3m.es/10.1016/j.solmat.2020.110768>.
- [12] M. Wittmann, M. Schmitz, H. G. Silva, P. Schmidt, G. Doppelbauer, R. Ernst, P. Santamaría, T. Miltkau, D. Golovca and L. Pacheco, "HPS2—demonstration of molten-salt in parabolic trough plants—Design of plant," in *AIP Conference Proceedings*, 2019, pp. 120024.
- [13] I. Hager, "Colour change in heated concrete," *Fire Technol.*, vol. 50, (4), pp. 945-958, 2014.
- [14] N. R. Short, J. A. Purkiss and S. E. Guise, "Assessment of fire damaged concrete using colour image analysis," *Constr. Build. Mater.*, vol. 15, (1), pp. 9-15, 2001. Available: <https://www.sciencedirect.com/science/article/pii/S0950061800000659>. DOI: [https://doi.org/10.1016/S0950-0618\(00\)00065-9](https://doi.org/10.1016/S0950-0618(00)00065-9).
- [15] M. C. Alonso and J. Puentes, "Self-Compacted Concrete with Self-Protection and Self-Sensing Functionality for Energy Infrastructures," *Materials*, vol. 13, (5), pp. 1106, 2020.
- [16] E. John, M. Hale and P. Selvam, "Concrete as a thermal energy storage medium for thermocline solar energy storage systems," *Solar Energy*, vol. 96, pp. 194-204, 2013.
- [17] M. C. Alonso, J. Vera-Agullo, L. Guerreiro, V. Flor-Laguna, M. Sanchez and M. Collares-Pereira, "Calcium aluminate based cement for concrete to be used as thermal energy storage in solar thermal electricity plants," *Cement and Concrete Research*, vol. 82, pp. 74-86, 2016. Available: <http://www.sciencedirect.com/science/article/pii/S0008884615003075>. DOI: <https://doi.org/10.1016/j.cemconres.2015.12.013>.
- [18] D. Laing, C. Bahl, T. Bauer, M. Fiss, N. Breidenbach and M. Hempel, "High-Temperature Solid-Media Thermal Energy Storage for Solar Thermal Power Plants," *Proc IEEE*, vol. 100, (2), pp. 516-524, 2012. . DOI: 10.1109/JPROC.2011.2154290.
- [19] J. López Sanz, F. Cabello Nuñez and F. Zaversky, "Benchmarking analysis of a novel thermocline hybrid thermal energy storage system using steelmaking slag pebbles as packed-bed filler material for central receiver applications," *Solar Energy*, vol. 188, pp. 644-654, 2019. . DOI: 10.1016/j.solener.2019.06.028.
- [20] C. Xu, Z. Wang, Y. He, X. Li and F. Bai, "Sensitivity analysis of the numerical study on the thermal performance of a packed-bed molten salt thermocline thermal storage system," *Appl. Energy*, vol. 92, pp. 65-75, 2012. Available: <http://www.sciencedirect.com.biblioteca5.uc3m.es/science/article/pii/S0306261911006970>. DOI: <https://doi.org.biblioteca5.uc3m.es/10.1016/j.apenergy.2011.11.002>.
- [21] G. Wang, S. Yu, S. Niu, Z. Chen and P. Hu, "A comprehensive parametric study on integrated thermal and mechanical performances of molten-salt-based thermocline tank," *Appl. Therm. Eng.*, vol. 170, pp. 115010, 2020. Available: <http://www.sciencedirect.com.biblioteca5.uc3m.es/science/article/pii/S1359431119367638>. DOI: <https://doi.org.biblioteca5.uc3m.es/10.1016/j.aplthermaleng.2020.115010>.

- [22] S. M. Flueckiger and S. V. Garimella, "Second-law analysis of molten-salt thermal energy storage in thermoclines," *Solar Energy*, vol. 86, (5), pp. 1621-1631, 2012. . DOI: 10.1016/j.solener.2012.02.028.
- [23] C. Odenthal, F. Klasing and T. Bauer, "Parametric study of the thermocline filler concept based on exergy," *Journal of Energy Storage*, vol. 17, pp. 56-62, 2018. . DOI: 10.1016/j.est.2018.01.009.
- [24] A. Gil, M. Medrano, I. Martorell, A. Lázaro, P. Dolado, B. Zalba and L. F. Cabeza, "State of the art on high temperature thermal energy storage for power generation. Part 1—Concepts, materials and modellization," *Renewable and Sustainable Energy Reviews*, vol. 14, (1), pp. 31-55, 2010. Available: <http://www.sciencedirect.com/science/article/pii/S1364032109001774>. DOI: <https://doi.org/10.1016/j.rser.2009.07.035>.
- [25] D. Brosseau, J. W. Kelton, D. Ray, M. Edgar, K. Chisman and B. Emms, "Testing of thermocline filler materials and molten-salt heat transfer fluids for thermal energy storage systems in parabolic trough power plants," *J.Sol.Energy Eng.*, vol. 127, (1), pp. 109-116, 2005.

Chapter 8

Heat transfer analysis

This chapter includes the heat transfer analysis of the mock-up section of a thermocline tank made of concrete, whose details for the construction, commissioning and operation phases were comprised in **Chapter 6** and **7**. The results of temperature obtained for the experimental performance of the mock-up needs for a deeper understanding of how the heat transfer was produced within the layers. The effect of convection in the air chamber needs better knowledge because the constructive requirement might lead to the loss of the thermal energy stored.

For that reason, *section 8.1* presents a thermal model of heat transfer of the mock-up in order to quantify the amount of energy that is lost to the surroundings in every layer of the prototype. Additionally, the convection heat transfer coefficient in the air gap was calculated from the experimental test so as to determine the type of convection in the air gap.

Secondly, *section 8.2* includes the simulations of temperature profiles across all the layers of the mock-up for different case studies that took place during the thermal cyclic operation.

Section 8.3 gives some lessons learned from the heat transfer analysis and presents limitations of the model.

Finally, *section 8.4* gives a brief overview of the main conclusions obtained through the heat transfer analysis.

8.1. Thermal model of the prototype

8.1.1. Definition of variables and thermal powers

Figure 8.1 shows all the layers of the prototype section of a thermocline tank as well as the thermal powers involved. The schema also reflects the names of the temperatures at the surface of the layers. Additionally, Figure 8.2 shows the circuit of equivalent thermal

resistances in the mock-up where the thermal powers, temperatures and thermal resistances are included.

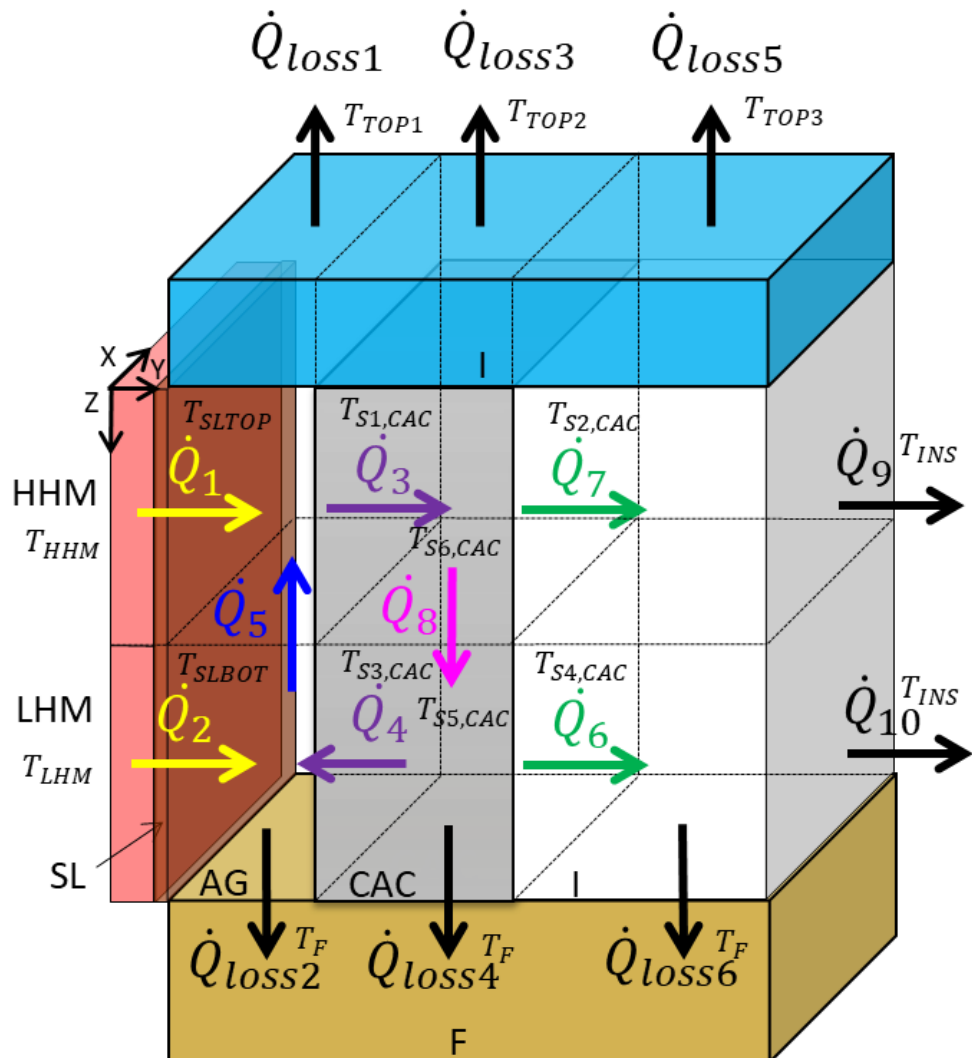


Figure 8.1: Schema of the thermal powers across the prototype

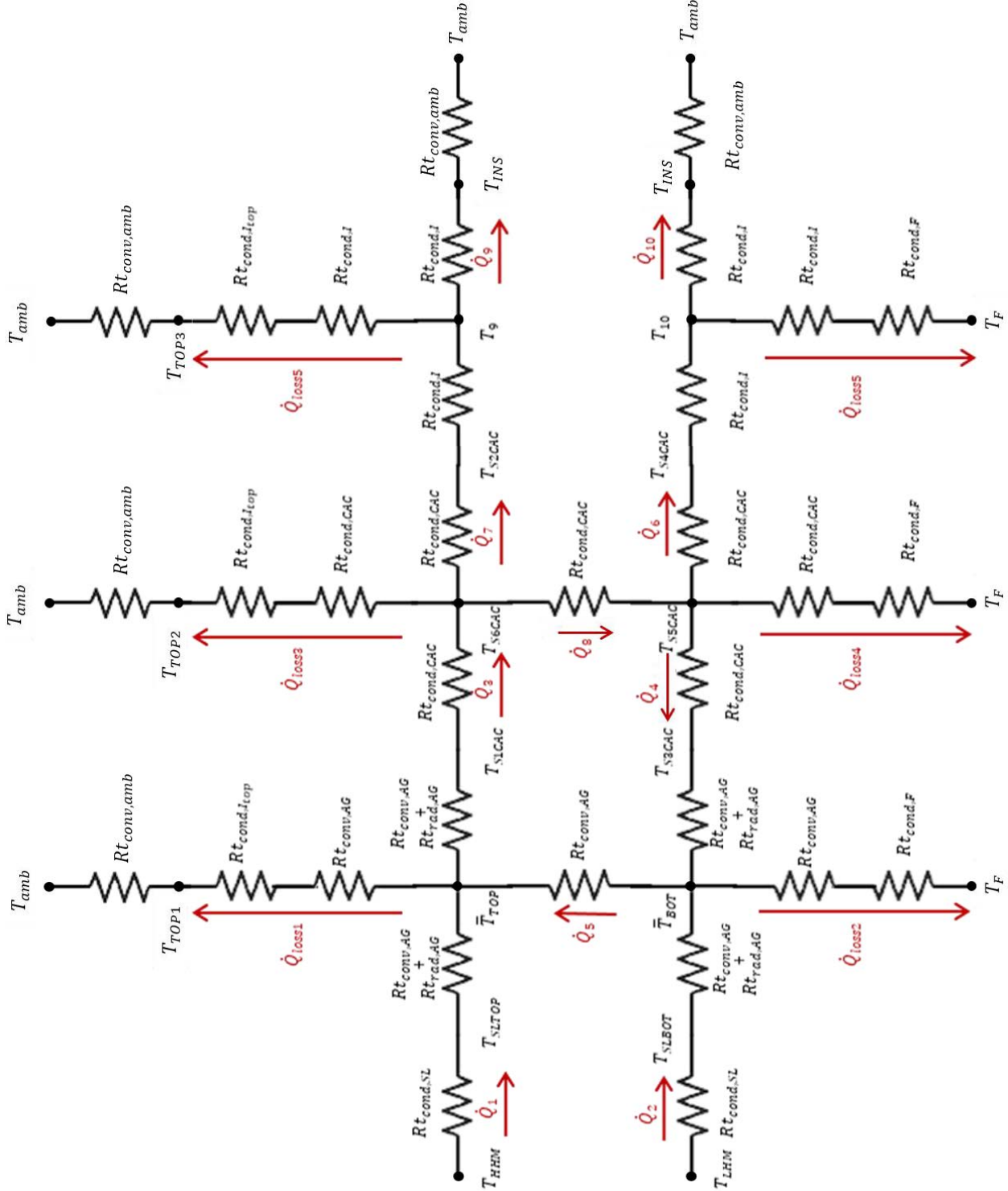


Figure 8.2: Circuit of equivalent thermal resistances of the prototype.

Before starting with the heat transfer analysis, it is important to note the variables that are known and the dimensions and properties of the different elements that constitute the prototype. Table 8.1 shows the values of the different geometric elements as well as some properties, which are involved in the thermal model explained in the previous section. Regarding the thermal properties of the layers involved in the mock-up, Table 8.2 includes the evolution of the thermal conductivity (k) for all of the layers and kinematic viscosity (ν)

and thermal diffusivity (α) for the air, whose dependence with the temperature was taken into consideration in the model as well. The values of the thermal properties were obtained from the literature [1-4], except the evolution of the thermal conductivity on CAC concrete, whose thermal conductivity was obtained in **Chapter 4** and published on [5].

| Layer | Material | Volume [mm ³] | Dimensions & properties |
|-----------------------|----------------|---------------------------|--|
| Steel liner | Steel AISI 316 | 1000×500×10 | $e_{SL} = 0.01 \text{ m}$ $\varepsilon_{SL} = 0.88$ |
| Air gap | - | 1000×500×15 | $A_{CONVAG} = 7.5 \cdot 10^{-3} \text{ m}^2$ $A_{Rad} = 0.25 \text{ m}^2$ |
| Concrete | CAC concrete | 1000×500×300 | $A_{CACL} = 0.15 \text{ m}^2$ $A_{CACT} = 0.25 \text{ m}^2$ $\Delta h_{CAC} = 0.5 \text{ m}$ $\varepsilon_{CAC} = 0.85 - 0.95$ |
| Insulating | Rockwool | 1000×500×600 | $e_{INS} = 0.6 \text{ m}$ $A_{INSL} = 0.3 \text{ m}^2$ $A_{INST} = 0.25 \text{ m}^2$ $\Delta h_{INS} = 0.25 \text{ m}$ $e_{INSTOP} = 0.35 \text{ m}$ |
| Foundations | Expanded clay | 2000×2000×200 | $e_F = 0.1 \text{ m}$ |
| Insulation top | Rockwool | 1000×5000×200 | $e_{INSTOP} = 0.2 \text{ m}$ |

Table 8.1: Dimensions and properties of layers of the prototype.

| Material | Thermal properties | | | | | | Source |
|-----------------------------|---|-------|-------|-------|-------|--|--------------|
| Steel AISI 316 ¹ | T [°C] | 27 | 127 | 327 | 527 | | [1, 2] |
| | k [W/(m·K)] | 13.4 | 15.2 | 18.3 | 21.3 | | |
| Air ² | T [°C] | 27 | 127 | 327 | 527 | | [1] |
| | k·10 ³ [W/(m·K)] | 26.3 | 33.8 | 46.9 | 57.3 | | |
| | v·10 ⁶ [m ² /s] | 15.89 | 26.41 | 52.69 | 84.93 | | |
| | α·10 ⁶ [m ² /s] | 22.5 | 38.3 | 76.9 | 120 | | |
| Rockwool | $k \left[\frac{W}{m \cdot K} \right] = 0.033$ | | | | | | [3] |
| Expanded clay | $k \left[\frac{W}{m \cdot K} \right] = 0.14$ | | | | | | [4] |
| CAC concrete ³ | $k \left[\frac{W}{m \cdot K} \right] = 1.3311 - 0.001 \cdot T_{CAC} + 7 \cdot 10^{-7} \cdot T_{CAC}^2$ | | | | | | Ch. 4 [5] |

¹ Thermal conductivity of steel depending on temperature.

² Thermal properties of air depending on temperature.

³ Thermal conductivity of CAC concrete depending on temperature.

Table 8.2: Thermal properties of layers of the prototype.

Additionally, Table 8.3 summarises all the variables that are part of the heat transfer model: surfaces, widths, thicknesses, thermal conductivities, heat transfer coefficients, thermal resistances, thermal powers, temperatures, temperature differences and adimensional numbers among others.

| Parameter | Description |
|--------------------------------------|---|
| Surfaces | |
| A_{CACL} | Surface of concrete in z-plane [m ²] |
| A_{CONVAG} | Surface of convection in z-plane [m ²] |
| A_{INSL} | Surface of Insulating in y-plane |
| A_{INST} | Surface of Insulating in z-plane [m ²] |
| A_{Rad} | Surface of radiation in y-plane [m ²] |
| Widths and thickness | |
| e_{AG} | Thickness of the Air Gap [m] |
| e_{INS} | Width of the Insulating layer [m] |
| e_{INSTOP} | Width of the Insulating located at the top of the prototype [m] |
| e_F | Width of the thermocouples located in the Foundations [m] |
| e_{SL} | Thickness of the Steel Liner [m] |
| Thermal conductivities | |
| k_{air} | Thermal conductivity of the air [W/(m·K)] |
| k_{CAC} | Thermal conductivity of the Concrete [W/(m·K)] |
| k_F | Thermal conductivity of expanded clay [W/(m·K)] |
| k_{INS} | Thermal conductivity of Rockwool® [W/(m·K)] |
| k_{SL} | Thermal conductivity of AISI 316 [W/(m·K)]. |
| Coefficients | |
| h_{CONVAG} | Convection heat transfer coefficient at the AG [W/(m ² ·K)] |
| h_{RadBOT} | Radiation heat transfer coefficient at the bottom of the AG [W/(m ² ·K)] |
| h_{RadTOP} | Radiation heat transfer coefficient at the top of the AG [W/(m ² ·K)] |
| Thermal resistances | |
| R_1 | Thermal resistance of half Insulating layer [K/W] |
| R_2 | Thermal resistance from the Insulating layer at the top [K/W] |
| R_3 | Thermal resistance from the Insulating layer to the room [K/W] |
| R_{eq} | Equivalent thermal resistance at the top of the Insulating layer [K/W] |
| Thermal power and heat losses | |
| \dot{Q}_{net} | Net power of the heating mat [W] |
| \dot{Q}_1 | Power of the HHM [W] |
| \dot{Q}_2 | Power of the LHM [W] |
| \dot{Q}_3 | Thermal power AG-Concrete at the top [W] |
| \dot{Q}_4 | Thermal power AG-Concrete at the bottom [W] |
| \dot{Q}_5 | Thermal power in the AG [W] |
| \dot{Q}_6 | Thermal power Concrete-Insulating at the bottom [W] |
| \dot{Q}_7 | Thermal power Concrete-Insulating at the top [W] |
| \dot{Q}_8 | Thermal power in the Concrete [W] |
| \dot{Q}_9 | Thermal power Insulating-Surroundings at the top [W] |
| \dot{Q}_{10} | Thermal power Insulating-Surroundings at the bottom [W] |
| \dot{Q}_{loss1} | Heat losses from the AG to the top [W] |
| \dot{Q}_{loss2} | Heat losses from the AG to the bottom [W] |

| | |
|-------------------------------|--|
| \dot{Q}_{loss3} | Heat losses from the CAC to the top [W] |
| \dot{Q}_{loss4} | Heat losses from the CAC to the bottom [W] |
| \dot{Q}_{loss5} | Heat losses from the Insulating to the top [W] |
| \dot{Q}_{loss6} | Heat losses from the Insulating to the bottom [W] |
| \dot{Q}_{RaTOP} | Radiation power SL-AG at the top [W] |
| \dot{Q}_{RaBOT} | Radiation power SL-AG at the bottom [W] |
| Temperatures | |
| T_{AGBOT} | Temperature of the AG at the bottom [°C] |
| T_{AGTOP} | Temperature of the AG at the top [°C] |
| T_{amb} | Temperature of the room [°C] |
| T_F | Temperature of the foundations [°C] |
| T_{HHM} | Temperature of the HHM [°C] |
| T_{INS} | Temperature at the end of the Insulating layer [°C] |
| T_{LHM} | Temperature of the LHM [°C] |
| T_{SLTOP} | Temperature of the SL at the top [°C] |
| T_{SLBOT} | Temperature of the SL at the bottom [°C] |
| $T_{S1,CAC}$ | Temperature AG-Concrete at the top [°C] |
| $T_{S2,CAC}$ | Temperature Concrete-Insulating at the top [°C] |
| $T_{S3,CAC}$ | Temperature AG-Concrete at the bottom [°C] |
| $T_{S4,CAC}$ | Temperature Concrete-Insulating at the bottom [°C] |
| $T_{S5,CAC}$ | Temperature at the middle of the Concrete at the bottom [°C] |
| $T_{S6,CAC}$ | Temperature at the middle of the Concrete at the top [°C] |
| T_{TOP1} | Temperature at the end of the top of Insulating layer, section 1 [°C] |
| T_{TOP2} | Temperature at the end of the top of Insulating layer, section 2 [°C] |
| T_{TOP3} | Temperature at the end of the top of Insulating layer, section 3 [°C] |
| T_9 | Temperature at the middle of the Insulating at the top [°C] |
| T_{10} | Temperature at the middle of the Insulating at the bottom [°C] |
| Temperature difference | |
| ΔT_{CAC} | Difference of temperature in the CAC concrete layer [°C] |
| ΔT_{INS} | Difference of temperature in the insulating material [°C] |
| Adimensional numbers | |
| Nu | Nusselt number [-] |
| Nu_{free} | Nusselt number for free convection [-] |
| Nu_{forced} | Nusselt number for forced convection [-] |
| Nu_T | Nusselt number for combined free and forced convection [-] |
| Pr | Prandtl number [-] |
| Ra | Rayleigh number [-] |
| Re | Reynolds number [-] |
| Greek symbols | |
| α | Thermal diffusivity [m^2/s] |
| Δh_{CAC} | Distance in direction z between T5 and T6 [m] |
| ϵ_{CAC} | Emissivity of Concrete [-] |
| ϵ_{SL} | Emissivity of AISI 316 [-] |
| σ | Constant of Stefan Boltzmann equal to $5.67 \cdot 10^{-8} \text{ W}/(m^2 \cdot K^4)$ |
| ν | Kinematic viscosity [m^2/s] |

Table 8.3: Parameters of the heat transfer analysis

The following assumptions were employed in order to simplify the heat transfer analysis:

- 1- The heating mats do not lose energy to the exterior because they are well insulated. For that reason, its external surface is considered adiabatic.
- 2- The prototype is well insulated for the planes $X=0$ mm and $X=500$ mm. Heat losses are neglected for those faces of the prototype, whose surfaces are considered adiabatic.
- 3- Both top and bottom of the heating mats and steel liner are considered adiabatic. Therefore, the heat losses from those surfaces to the surroundings are neglected.
- 4- The temperatures of the external surfaces of insulating material at the top are considered proportional to the decrease of temperature obtained in the insulating layer along with the longitudinal section of the mock-up. In the same way, the difference of temperature experienced in the concrete layer in the transversal direction is assumed to be equal to the temperature difference recorded in the concrete layer across the longitudinal section, showed in Figure 7.7 and Figure 7.8.
- 5- The temperature in the foundations (T_F) is constant at the same depth along with the distance of the prototype.
- 6- The temperatures are considered constant in the whole surface of heat exchange.
- 7- The thermal conductivity of different layers is constant except for the CAC concrete, whose dependency with temperature was obtained in **Chapter 4**.
- 8- The radiation effect in the air gap is taken into consideration. Properties of emissivity of both steel and concrete are considered constant with temperature.
- 9- Another essential aspect is that inside the air chamber, the content is only air and no vapour is produced during the thermal cyclic operation.
- 10- The pressure in the air gap is considered atmospheric pressure and the air is supposed incompressible.
- 11- The air gap layer is considered as a rectangular cavity enclosed.
- 12- The convection heat transfer coefficient is constant in the cavity, independently of the direction longitudinal or transversal.

Once all the assumptions are known, the following subsections detail the quantification of the heat transfer losses across all the layers of the prototype in order to determine the thermal powers and heat losses that take place in all the layers. The energy balances with the thermal powers and thermal resistances have been obtained by using the expressions that are included in [1]. Additionally, the convection heat transfer coefficient in the air gap or film coefficient is determined in order to determine the type of convection.

8.1.2. Energy balances

8.1.2.1. Energy balance in the STEEL LINER

The heat source had a net power of 4212W operating at 500°C of maximum temperature [6]. Therefore, the power of the heat source depending on the programmed temperature of the heating mats follows the expression below. Subindex 1 and 2 is referred to the thermal power of the higher and lower heating mats, respectively.

$$\dot{Q}_{\{2\}} = Q_{net} \cdot \frac{T_{HJM} - T_{amb}}{T_{max} - T_{amb}} [W] \quad (9)$$

where:

- \dot{Q}_{net} is the net power equal at 4212 [W].
- T_{HJM} is the temperature of the higher heating mat [$^{\circ}\text{C}$].
- T_{amb} is the temperature of the room [$^{\circ}\text{C}$].
- T_{max} is the maximum temperature of operation of the mats equal to 500 $^{\circ}\text{C}$.

Conduction is the heat transfer mechanism that takes place in the steel liner. The thermal conductivity of the steel AISI 316 varying with temperature is considered to obtain the thermal resistance in the steel liner [1]. Having a depth of 0.01 m and a surface of the heating mat of 0.25 m^2 , the thermal resistance in the air gap is obtained by the following expression:

$$R_{th,cond_SL} = \frac{e_{SL}}{k_{SL}} \left[\frac{K \cdot m^2}{W} \right] \quad (10)$$

where:

- e_{SL} is the width of the steel liner equal to 0.01 [m].
- k_{SL} is the thermal conductivity of AISI 316 [$\text{W}/(\text{m}^2 \cdot \text{K})$].

As the heat source only transfer energy to the surface in contact with the steel liner and the other surfaces are considered adiabatic as well as the steel liner, which has been assumed for not losing energy from top and bottom, the total energy provided by the heat source goes to the air gap. Therefore, the temperatures at the end of the width of the steel liner are obtained as follows for the top and bottom:

$$T_{SL\{TOP\}} = T_{\{HJM\}} - \frac{\dot{Q}_{\{2\}} \cdot R_{th,cond_{SL}}}{A_{SL}} [^{\circ}\text{C}] \quad (11)$$

Being $T_{SL\{TOP\}}$ the temperature at the end of the steel liner for both top and bottom surfaces in contact with the air chamber.

8.1.2.2. Energy balance in the AIR GAP

The thermal powers that come into the air chamber and out of the air gap layer through the CAC layer are known. Nevertheless, inside the air gap, there are air and the heat transfer mechanism in convection. During the experimental tests, the velocity of the air inside the chamber was not measured and, for that reason, it is not possible to determine whether the type of convection was natural or forced. Nonetheless, the coefficient of convection heat transfer can be obtained by knowing the thermal powers involved in the air gap layer.

In parallel with this, it is worth noting that the temperatures of the heat source arrive in some cases at 500 $^{\circ}\text{C}$. That is the reason why the radiation heat transfer mechanism should be considered as well because plays an important role in the air gap. Not taking into account

the radiation effect might lead to obtaining an erroneous value of the film coefficient of convection. Hence, the thermal radiation that takes place at the top and bottom of the air gap is calculated as follows, as well as the radiation coefficients. It is important to note that the temperatures in equations (12) to (15) are expressed in Kelvin by using the conversion ($K = ^\circ C + 273.15$).

$$\dot{Q}_{Rad}^{(TOP)}_{BOT} = \varepsilon_{SL} \cdot \sigma \cdot A_{Rad} \cdot \left(T_{SLTOP}^4 - T_{S3CAC}^4 \right) [W] \text{ when } T_{SLTOP} > T_{S3CAC} \quad (12)$$

$$\dot{Q}_{Rad}^{(TOP)}_{BOT} = \varepsilon_{CAC} \cdot \sigma \cdot A_{Rad} \cdot \left(T_{S1CAC}^4 - T_{SLTOP}^4 \right) [W] \text{ when } T_{SLTOP} < T_{S1CAC} \quad (13)$$

$$h_{Rad}^{(TOP)}_{BOT} = \varepsilon_{SL} \cdot \sigma \cdot \left(T_{SLTOP} + T_{S3CAC} \right) \cdot \left(T_{SLTOP}^2 + T_{S3CAC}^2 \right) [W/m^2K] \quad (14)$$

when $T_{SLTOP} > T_{S3CAC}$

$$h_{Rad}^{(TOP)}_{BOT} = \varepsilon_{SL} \cdot \sigma \cdot \left(T_{S1CAC} + T_{SLTOP} \right) \cdot \left(T_{S1CAC}^2 + T_{SLTOP}^2 \right) [W/m^2K] \quad (15)$$

when $T_{SLTOP} > T_{S1CAC}$

where:

$\dot{Q}_{Rad}^{(TOP)}_{BOT}$ is the radiation power in the air gap at the top or bottom [W].

ε_{SL} is the emissivity of steel AISI 316 equal to 0.88 [-]. Source [1].

ε_{CAC} is the emissivity of the concrete, supposed equal to 0.88-0.94 [-]. Source [1].

σ is the constant of Stefan Boltzmann, $5.67 \cdot 10^{-8} \text{ W}/(\text{m}^2 \cdot \text{K}^4)$.

A_{Rad} is the surface of radiation equal to 0.25 m^2 .

$h_{Rad}^{(TOP)}_{BOT}$ is the radiation heat transfer coefficient [$\text{W}/(\text{m}^2 \cdot \text{K})$].

On the other hand, as the thermal losses to the environment for the heating mats and steel liner are neglected, all the thermal power of the heat source comes into the air gap through both convection and radiation heat transfer mechanisms. In the same way, radiation and convection are acting through the surface of the concrete exposed to the air. Therefore, as both mechanisms act in parallel on both surfaces, the convection heat transfer mechanism can be obtained as follows:

$$h_{CONVAG} = \frac{\dot{Q}_2 \cdot A_{SL} + \dot{Q}_4}{(T_{SLBOT} - T_{S3CAC}) \cdot A_{SL}} - h_{RadBOT} \left[\frac{\text{W}}{\text{m}^2 \cdot \text{K}} \right] \quad (16)$$

Once the film coefficient was found, it is possible to determine the heat transfer losses to the foundation (\dot{Q}_{loss2}) and apply energy balances at the top and bottom and obtained all the thermal powers involved in the air gap.

$$T_{AGBOT} = \frac{\dot{Q}_4}{A_{SL} \cdot (h_{CONVAG} + h_{RadBOT})} + T_{S3CAC} \text{ [°C]} \quad (17)$$

$$\dot{Q}_{loss2} = \frac{T_{AGBOT} - T_F}{\frac{1}{h_{CONVAG} + h_{RadBOT}} + \frac{e_F}{k_F \cdot A_{CONVAG}}} \text{ [W]} \quad (18)$$

$$\dot{Q}_5 = \dot{Q}_2 - \dot{Q}_4 - \dot{Q}_{loss2} \text{ [W]} \quad (19)$$

$$\dot{Q}_{loss1} = \dot{Q}_1 + \dot{Q}_5 - \dot{Q}_3 \text{ [W]} \quad (20)$$

8.1.2.3. Energy balance in the CAC CONCRETE layer

The prototype recorded temperatures in both external surfaces of the concrete layer and some punctual locations embedded in the concrete. For that reason, the calculation of the thermal powers within the concrete layer is simplified, because the temperature is known in all of them. Further to this, a heat transfer power within the concrete material (\dot{Q}_8) was established between the top and bottom due to the thermal gradients experienced between those regions. Hence, the heat losses from the top (\dot{Q}_{loss3}) and bottom (\dot{Q}_{loss4}) and the thermal power of conduction in the concrete is obtained by using the following expressions:

$$\dot{Q}_8 = \frac{T_{S5CAC} - T_{S6CAC}}{\frac{\Delta h_{CAC}}{k_{CAC} \cdot A_{CACL}}} \text{ [W]} \quad (21)$$

$$\dot{Q}_{loss3} = \frac{T_{S6CAC} - T_{TOP2}}{\frac{\Delta h_{CAC}}{2 \cdot k_{CAC} \cdot A_{CACL}} + \frac{e_{INSTOP}}{k_{INS} \cdot A_{INSL}}} \text{ [W]} \quad (22)$$

$$T_{TOP2} = T_{S6CAC} - \Delta T_{CAC+INS} = T_{S6CAC} - \Delta T_{CAC} \cdot \frac{\Delta h_{CAC}}{0.3} - \Delta T_{INS} \cdot \frac{e_{INSTOP}}{0.6} \text{ [°C]} \quad (23)$$

$$\dot{Q}_{loss4} = \frac{T_{S5CAC} - T_F}{\frac{\Delta h_{CAC}}{2 \cdot k_{CAC} \cdot A_{CACL}} + \frac{e_F}{k_F \cdot A_{CACL}}} \text{ [W]} \quad (24)$$

The thermal resistances involved in the CAC concrete layer can be obtained by using the energy balances at the top and bottom:

$$\dot{Q}_3 + \dot{Q}_8 = \dot{Q}_7 + \dot{Q}_{loss3} \text{ [W]} \quad (25)$$

$$\dot{Q}_4 = \dot{Q}_6 + \dot{Q}_8 + \dot{Q}_{loss4} [W] \quad (26)$$

8.1.2.4. Energy balance in the INSULATING layer

The upper part of the insulating layer loose thermal power at the top (\dot{Q}_{loss5}) and at the end of the insulating layer (\dot{Q}_9). Both external surfaces are at the temperature of the insulating, top and the external surface of the transversal section of the mock-up, as is shown in equation (27). Having the circuit of equivalent thermal resistances (Figure 8.3), the first step is to calculate the equivalent thermal resistance and then the thermal powers involved in this layer, by using the expressions as follows.

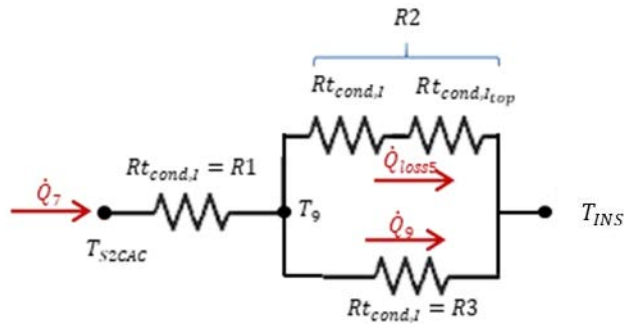


Figure 8.3: Thermal resistances in the upper part of the insulating layer.

$$T_{TOP3} = T_{S2CAC} - \Delta T_{INS} = T_{S2CAC} - (T_{S2CAC} - T_{INS}) = T_{INS} [\text{°C}] \quad (27)$$

$$R1 = \frac{e_{INS}}{2 \cdot k_{INS} \cdot A_{INST}} [K/W] \quad (28)$$

$$R2 = \frac{\Delta h_{INS}}{k_{INS} \cdot A_{INSL}} + \frac{e_{INSTOP}}{k_{INS} \cdot A_{INSL}} [K/W] \quad (29)$$

$$R3 = \frac{e_{INS}}{2 \cdot k_{INS} \cdot A_{INST}} [K/W] \quad (30)$$

$$R_{eq} = R1 + \frac{R2 \cdot R3}{R2 + R3} [K/W] \quad (31)$$

$$\dot{Q}_7 = \frac{T_{S2,CAC} - T_{INS}}{R_{eq}} [W] \quad (32)$$

$$\dot{Q}_9 = \frac{T_{S2,CAC} - \dot{Q}_7 \cdot \frac{e_{INS}}{2 \cdot k_{INS} \cdot A_{INST}} - T_{INS}}{\frac{e_{INS}}{2 \cdot k_{INS} \cdot A_{INST}}} [W] \quad (33)$$

With those thermal powers, the temperature at the middle of the insulating can be obtained:

$$T_9 = T_{S2,CAC} - \dot{Q}_7 \cdot \frac{e_{INS}}{2 \cdot k_{INS} \cdot A_{INST}} \text{ [°C]} \quad (34)$$

Applying the energy balance at the top, the heat transfer losses from the top, \dot{Q}_{loss5} is calculated:

$$\dot{Q}_{loss5} = \dot{Q}_7 - \dot{Q}_9 \text{ [W]} \quad (35)$$

Regarding the lower part of the insulating layer, the heat power is lost from the bottom to the foundation (\dot{Q}_{loss6}) and to the environment through the external surface at the end of the layer (\dot{Q}_{10}). As the temperatures of the foundation and the room are different, another assumption that both thermal losses take place between the mean temperature of the insulation and the end temperature whether it be room temperature, or the foundations temperature is made. Therefore, the heat losses are obtained as follows:

$$T_{10} = T_9 \text{ [°C]} \quad (36)$$

$$\dot{Q}_{10} = \frac{T_{10} - T_{INS}}{\frac{e_{INS}}{2 \cdot k_{INS} \cdot A_{INST}}} \text{ [W]} \quad (37)$$

$$\dot{Q}_{loss6} = \frac{\bar{T}_{10} - T_F}{\frac{\Delta h_{INS}}{k_{INS} \cdot A_{INSL}} + \frac{\Delta h_F}{k_F \cdot A_{INSL}}} \text{ [W]} \quad (38)$$

The heat power that goes into the lower part of the insulation can be obtained by applying the energy balance at the bottom:

$$\dot{Q}_6 = \dot{Q}_{10} + \dot{Q}_{loss6} \text{ [W]} \quad (39)$$

Once those thermal powers are known, it is possible to go upwards and calculate the thermal powers that are located at the CAC concrete layer.

8.1.2.5. Energy balance in the prototype

Once all the thermal powers are known it is possible to apply the global energy balance in the whole prototype system, as follows:

$$\dot{Q}_1 + \dot{Q}_2 = \dot{Q}_{loss1} + \dot{Q}_{loss2} + \dot{Q}_{loss3} + \dot{Q}_{loss4} + \dot{Q}_{loss5} + \dot{Q}_{loss6} + \dot{Q}_9 + \dot{Q}_{10} \text{ [W]} \quad (40)$$

The equations shown in this subsection are programmed in MATLAB® with a code able to obtain the evolution of all the parameters for the test carried out. As the recorded data of temperatures were documented every 5 minutes during the testing time, the output parameters will have the same period. The outputs are convection and radiation heat transfer

coefficients and all thermal powers from top and bottom and variables temperature-dependant.

8.1.3. Convection heat transfer in the Air Gap

The results of the experimental performance of the mock-up shown in **Chapters 6 and 7** highlighted the effect of the air chamber in the reduction of the temperature that arrived at the concrete and the difference of temperature experienced between the top and bottom of the mock-up.

To have a better knowledge of the mechanisms of heat transfer that took place in the air gap, some adimensional numbers were obtained, following the method described in [1]. Firstly, the Rayleigh number (Ra) were obtained in order to determine if there were convection in the air gap. The expression for obtaining the Ra number is showed as follows:

$$Ra = \frac{g \cdot \beta \cdot (T_1 - T_2) \cdot x^3}{\alpha \cdot \nu} \quad (41)$$

where:

- g is the constant of gravity equal to 9.8 m/s^2 .
- β is the thermal expansion coefficient [$1/\text{K}$].
- T_1 is the temperature of the surface 1 [$^\circ\text{C}$].
- T_2 is the temperature of the surface 2 [$^\circ\text{C}$].
- x is the distance between the surfaces 1 and 2 [m].
- α is the thermal diffusivity [m^2/s].
- ν is the kinematic viscosity [m^2/s].

Nevertheless, the type of convection is not restricted to laminar flow and the transition region between laminar and turbulent regime depends on the buoyancy and viscous forces of the fluid [1]. The Rayleigh number (Ra) gives the relation between those forces and the critical value is established in 1708 [1]. In the case of free convection, there are empirical correlations for enclosures such as in a rectangular cavity as the case of the air gap in the mock-up [1]. Particularly, for 2 opposing surfaces at different temperatures, whose other walls are insulated from the surroundings as in the present case, and are separated by an enclosed fluid, which in this study is air.

For values of Rayleigh below the limit ($Ra < 1708$), the heat transfer within the cavity occurs by conduction or both conduction and radiation. There is no advection in the cavity because the resistance given by viscous forces overcome the buoyancy forces. Values of $Ra > 1708$ indicate that the condition inside the cavity is thermally unstable and there is advection. When $Ra \gg 5 \cdot 10^4$ the fluid experiences different patterns before becoming turbulent on $Ra > 10^9$.

If there exist convection in the air gap ($Ra > 1708$), the next step is to determine the type of convection, free or forced. The typical values of the convection heat transfer

coefficient summarised at [1] depend on the process and the fluid and are shown in Table 8.4.

| Type of convection | Fluid | h_{conv} [W/(m ² ·K)] |
|-------------------------------------|-------------------------|------------------------------------|
| Free convection | Gases | 2-25 |
| | Liquids | 50-1000 |
| Forced convection | Gases | 25-250 |
| | Liquids | 100-20000 |
| Convection with phase change | Boiling or condensation | 2500-100000 |

Table 8.4: Type of convection and typical values. Source: [1].

The Nusselt number (Nu) indicates the relation between the convection and conduction heat transfer mechanisms. Numbers of $Nu = 1$ indicates that the heat transfer mechanism is carried out only by conduction [1]. Values of Nu between 1-10 indicates that there are laminar flow or transition. Higher values indicate a bigger effect of convection, which can have turbulent flow for Nu numbers ranging between 100-1000 [7].

The convection can be combined free and forced. The empirical correlations for the enclosures and, specifically for rectangular cavities allow the calculation of the Nusselt number (Nu) for free convection theoretically. Those correlations can be applied for specific conditions of the numbers of Prandtl (Pr), Rayleigh, the ratio height/length (H/L) of the cavity and the angle for inclined cavities [8-11]. However, the cavity in the mock-up presents a H/L=66.66 and the more precise correlations taking into account this ratio cannot be applied. For that reason, the Nu number can be obtained by using the first approximation of Globe and Dropkin [8] showed in expression (42) with the adimensional numbers of Rayleigh (41) and Prandt (43):

$$Nu_{free} = 0.069 \cdot Ra^{\frac{1}{3}} \cdot Pr^{0.074} \quad (42)$$

$$Pr = \frac{\nu}{\alpha} \quad (43)$$

In the case of obtaining the Nu for forced convection theoretically, the Reynolds number and the velocity of the fluid inside the cavity are needed. However, this parameter was not measured during the thermal performance of the mock-up section of a thermocline tank. For that reason, this parameter cannot be obtained theoretically.

Nevertheless, with the experimental obtention of the convection heat transfer coefficient, it is possible to calculate the Nu number total experimentally and validate the type of convection that took place in the air chamber of the mock-up, knowing that the convection includes the combination of free and forced, as is showed in equations (44) and (45).

$$Nu_T = h_{CONVAG} \cdot \frac{e_{AG}}{k_{air}} \quad (44)$$

$$Nu_T = Nu_{free} + Nu_{forced} \quad (45)$$

8.1.4. Case studies

Both the simulations of the temperature profiles and the outputs from the thermal model can be obtained for the entire testing time. However, as the temperature profiles change every 5 minutes, the pictures shown in this chapter attains at certain testing time. In order to have a representative simulation, some case studies were chosen by attaining different conditions of thermal cycling.

Table 8.5 shows the time and condition of the thermal cycle for the case studies to be analysed. To ensure steady-state conditions, the case studies analysed are referred to the last instants of the constant temperature of the heat source once the system has achieved equilibrium. Case study (CS) 1 represents the starting conditions before starting the cycling. CS 2 is related to the condition when both heating mats were at 500°C in the first thermal cycle. CS 3 shows the case when both heating mats were at 200°C. Regarding thermal cycling, CS 4 and 6 are associated with the operation at 500°C at the 2nd and 3rd cycle, respectively. In contrast, CS 5 and 7 correspond to the operation at 200°C at the 2nd and 3rd cycle, respectively.

| Case study | Temperature of the heat source | Time [h] |
|------------|--------------------------------|----------|
| 1 | 300°C | 8.66 |
| 2 | 500°C, 1 st cycle | 17.92 |
| 3 | 200°C, 1 st cycle | 30.00 |
| 4 | 500°C, 2 nd cycle | 38.00 |
| 5 | 200°C, 2 nd cycle | 50.00 |
| 6 | 500°C, 3 rd cycle | 61.58 |
| 7 | 200°C, 3 rd cycle | 71.33 |

Table 8.5: Case studies for the simulations and the thermal model.

8.1.5. Results of the theoretical thermal model

8.1.5.1. Thermal powers

The evolution of the thermal powers involved during the test in the air gap layer is shown in Figure 8.4. Having the heat supply \dot{Q}_1 and \dot{Q}_2 , the evolution of the heat in the air gap went to the upper part. This can be observed by analysing the curves \dot{Q}_5 and \dot{Q}_2 , whose evolution are overlapped. As the heat went up, the heat transfer losses to the foundations (\dot{Q}_{loss2}) were insignificant comparing among others. In contrast, heat transfer losses to the room by the upper part almost reached the sum of the heat source ($\dot{Q}_1 + \dot{Q}_2$).

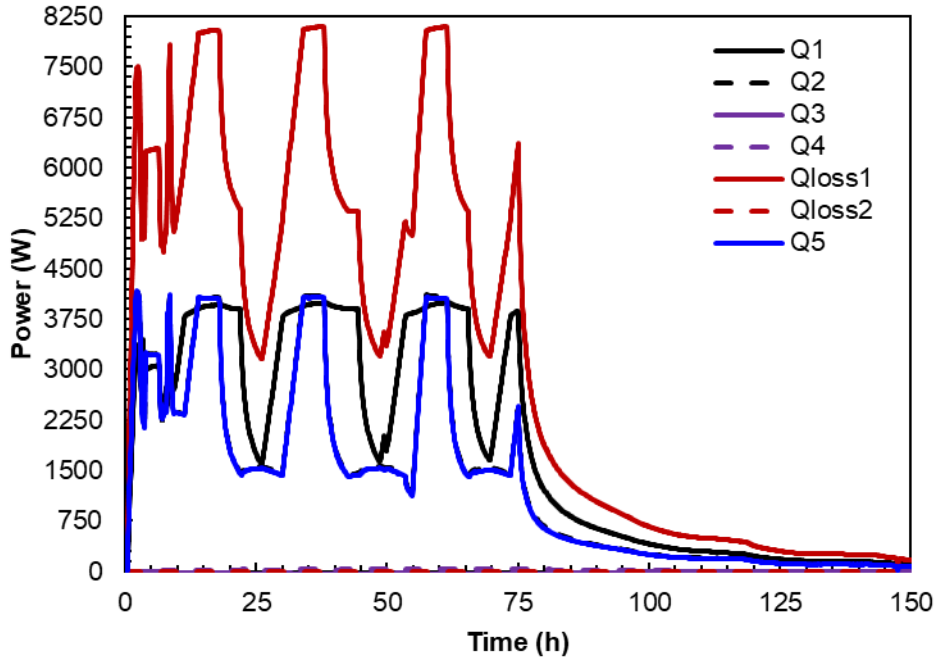


Figure 8.4: Thermal powers in the Air gap. Power supply (\dot{Q}_1, \dot{Q}_2), heat transfer powers to concrete (\dot{Q}_3, \dot{Q}_4), heat transfer losses ($\dot{Q}_{loss1}, \dot{Q}_{loss2}$) and heat power from bottom to top (\dot{Q}_5).

Regarding the heat transfer between the air gap and the concrete layer, \dot{Q}_3 and \dot{Q}_4 were very small compared to the heat supplied. It is following the fact that the vast majority of the heat supplied was lost to the environment (\dot{Q}_{loss1}).

Nevertheless, as the concrete also experienced an increase in the temperature during the test, the heat arrived at this layer. The heat transfer among the rest of the layers is represented in Figure 8.5. The thermal powers that took place in the concrete, insulating and the losses from both the top and the foundations differ 2 orders of magnitude to the heat supplied by the heat source.

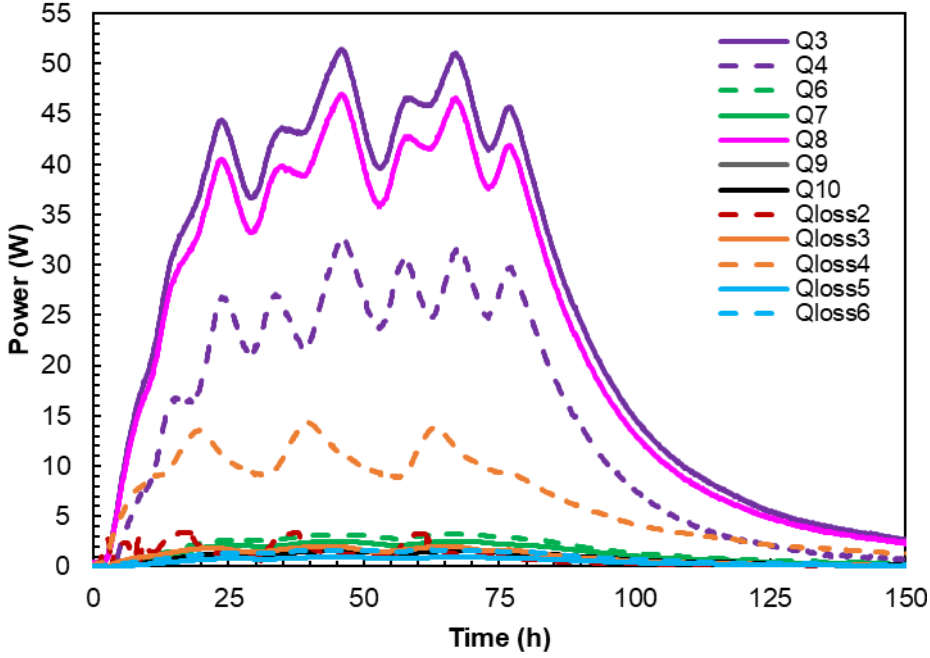


Figure 8.5: Thermal powers across all the layers and heat transfer losses.

The highest thermal powers were \dot{Q}_3 and \dot{Q}_8 , which took place at the top and the middle of the concrete layer between the upper and the lower part, respectively. The upper part of the concrete was heated at more temperature than the bottom and that is the reason why inside the material the heat went down. This fact also influenced the direction of the heat from the concrete to the air gap (\dot{Q}_4). The positive sense of this heat flux (\dot{Q}_4) was taken considering that the concrete was at a higher temperature than the AG at the bottom. Therefore, the concrete was being heated up to the top and cooled down from the bottom mainly to the air gap (\dot{Q}_4) and to the foundations (\dot{Q}_{loss4}).

The heat transfer fluxes from concrete to the insulating layer and then to the surroundings might be considered negligible, as they differ in 3 orders of magnitude compared to the heat supplied by the sources.

Having said that, as the biggest heat transfer fluxes took place in the air gap, the convection heat transfer mechanism had a special contribution.

8.1.5.2. Heat transfer in the Air Gap

As for the results presented in **Chapter 7** and in the previous section, the air gap had a notable contribution to the global heat transfer in the mock-up. Figure 8.6 shows the evolution of the Rayleigh number (Ra) during the testing time. It can be seen that the adimensional number always exceeded the limit of 1708 during the cyclic operation. Therefore, the air chamber experienced convection in the air gap layer, resulting in the cavity thermally unstable. On the other hand, as the Ra number ranges between 3500-7000 during the thermal cycling stage, those values indicate that the air in the rectangular cavity presented a laminar or slug flow according to [1].

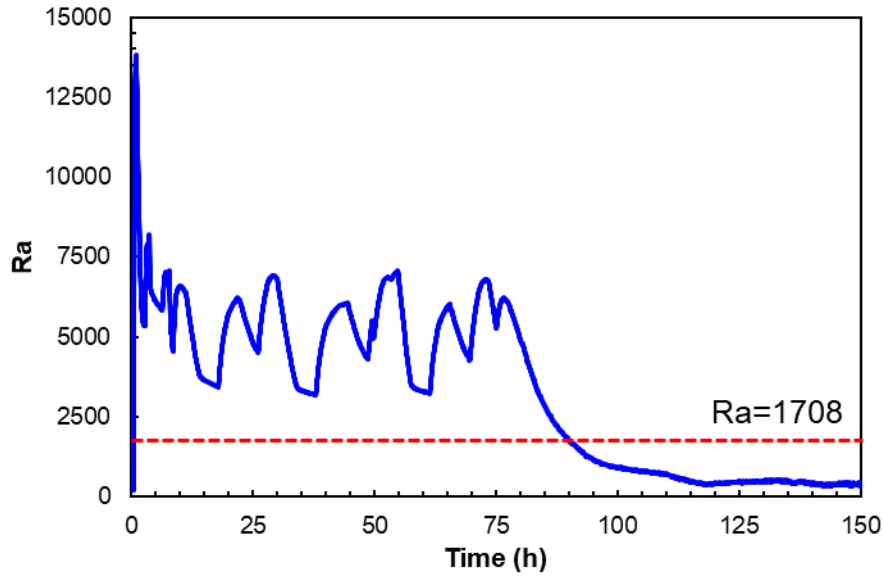


Figure 8.6: Evolution of the Rayleigh number during the testing time.

Once the convection heat transfer mechanism was demonstrated in the air gap, the following step was to determine the type of convection. Nonetheless, to evaluate this effect and indicate the type of convection, the convection heat transfer coefficient was obtained and represented in Figure 8.7 for the whole testing time. The chart also includes the limit between free and forced convection at $25 \text{ W}/(\text{m}^2 \cdot \text{K})$, as it was mentioned in Table 8.4 for gases and stated by the authors in [1].

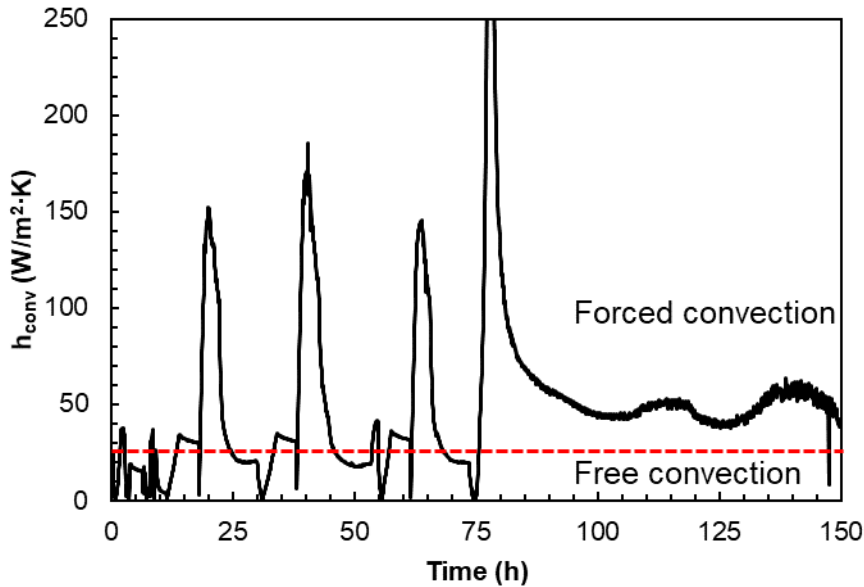


Figure 8.7: Evolution of the convection heat transfer coefficient in the air gap.

The air chamber experienced forced convection when both heat sources were operating at full power at 500°C . The three peaks reached at 146 , 185 and $145 \text{ W}/(\text{m}^2 \cdot \text{K})$ were obtained after 20 , 40 and 64 hours of starting the test, respectively. After that, when the heat source reduced their power to 200°C , the film coefficient decreased in all cases down

to 20, 18.9 and 16 W/(m²·K) after 30, 52 and 73 hours respectively. In those situations, the type of convection was free inside the air gap.

Regarding the peak reached after 75 hours, the coefficient increased very quickly, as for the previous peaks because of the increase of the heat source up to 500°C. However, once the heat sources were stopped, the difference of temperature between the concrete and the air gap was narrowing up to being at the same temperature at the peak. As the air gap was cooled down quicker than the concrete, the temperature decreased faster than the concrete. That is the reason why the peak is more significant than the others. Additionally, concrete was cooled down by the air gap and that is the reason why this region continues experiencing forced convection after the heat source was stopped.

Table 8.6 summarises the values of the film coefficient and the type of convection that took place for the 7 case studies mentioned in Table 8.5. Cases 2, 4 and 6 refers to the operation at net power and that is the reason why the type of convection is forced. Nonetheless, it is worth noting that those values are not the peaks because the temperature was stabilised at those testing times. Contrary to that, CS 3, 5 and 7 experienced a mechanism of free convection while the operation was at the minimum temperature of the cycling.

| Case study | h_{CONVAG} [W/(m ² ·K)] | Type of convection |
|------------|---|--------------------|
| 1 | 22.8 | Free |
| 2 | 29.6 | Forced |
| 3 | 20.2 | Free |
| 4 | 30.7 | Forced |
| 5 | 17.6 | Free |
| 6 | 31.4 | Forced |
| 7 | 19.5 | Free |

Table 8.6: Type of convection for the cases studied.

To validate the type of convection obtained by calculating the convection heat transfer coefficient, the evolution of the Nusselt number was theoretically obtained through the correlation of Globe and Dropkin [8] and is shown in Figure 8.8.

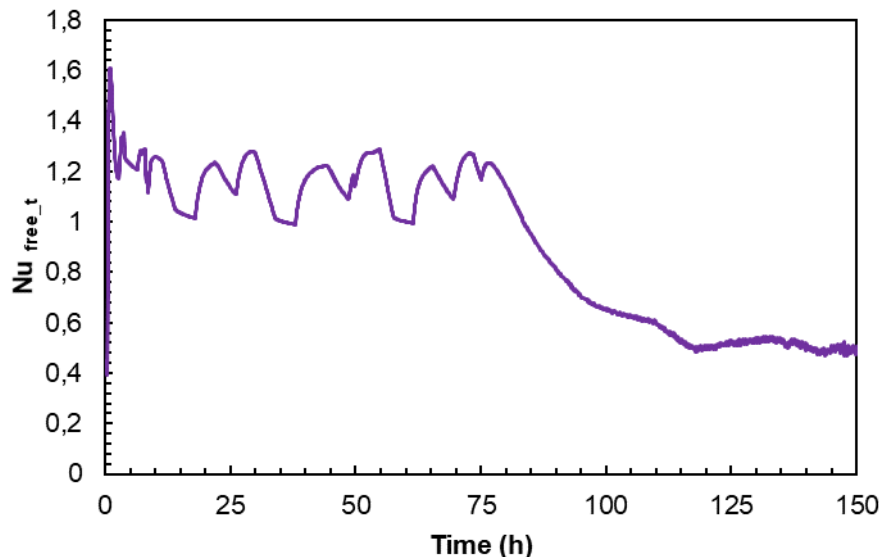


Figure 8.8: Evolution of the theoretical Nusselt number for free convection inside a rectangular cavity during the testing time.

On the other hand, the Nu number was experimentally obtained through the h_{CONVAG} (Figure 8.7) by the equation (44) and the evolution is shown in Figure 8.9. Comparing both graphs (Figure 8.8 and Figure 8.9), the experimental Nusselt number differs 1 order of magnitude during the operation, achieving values between 50-60 during the peaks of operation of the heat source at 500°C. Whereas the Nu calculated for free convection inside a cavity achieved values between 1-1.2 during the operation and below 1 when the test finished and the whole system experienced the cooling phase down to the room temperature.

Another interesting point here is that the experimental Nu (Figure 8.9) registered values below 10 when the heat source reduced their power to 200°C. This fact means that the flow was laminar or transitional but far for the turbulent, and it is in accordance with the results of the convection heat transfer coefficient, which indicate that in those periods the type of convection was free. On the contrary, when the heat source was operating at full power the Nu achieved higher values indicating that the convection increased the flow to transition regimes, and it is in accordance with the parameter h_{CONVAG} obtained.

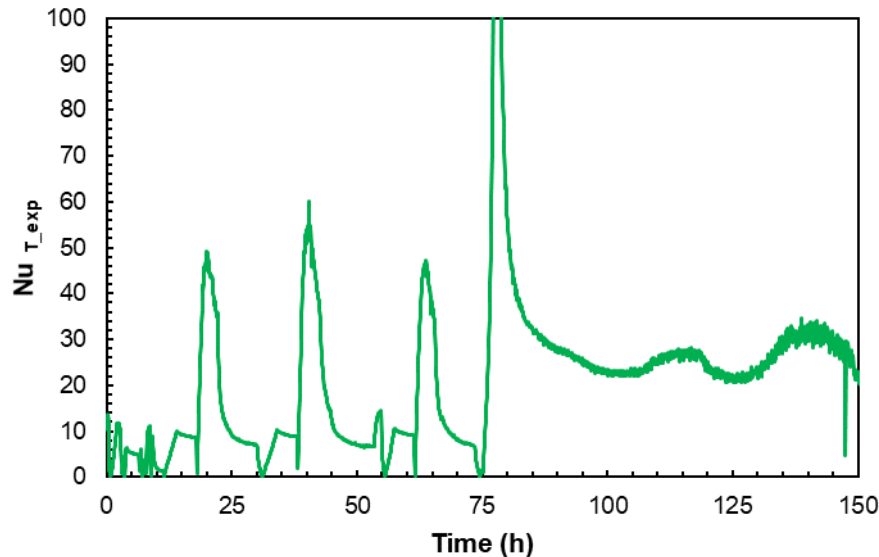


Figure 8.9: Evolution of the experimental Nusselt number during the testing time.

As the resulted convection is a combined free and forced convection and the contribution to the free convection (obtained through the theoretical Nu) was not significant when the mock-up was operating at full power, the explanation to this is that at those periods the type of convection was forced.

8.2. Simulations of the temperature of the prototype

8.2.1. Definition of the MATLAB code

Additionally, the evolution of the profiles of temperature in the prototype was obtained in order to see the depth of heat along with the prototype during the test. For such an aim, a MATLAB® routine was developed where the temperatures were known in some nodes corresponding to the locations of the thermocouples in the prototype. The MATLAB® code applies an interpolant function to determine the temperature in the whole prototype. The prototype has been simulated with a mesh of the same dimensions as the real prototype and the coordinates X, Y and Z and axes represented in the simulation follow the same coordinate system as the diagram shown in previous chapters.

The code was run for obtaining the 3D temperature colourmap across the prototype. As this only reflects 3 planes, more representations were done so as to reflect the temperature in slices at chosen locations. Firstly, the global 3D of the prototype with slices at positions $X=[0, -500]$ mm, $Y=[0, 925]$ mm and $Z=[0, -1000]$ mm. Secondly, slices in plane Y were chosen in order to obtain the evolution of temperatures with respect to the heat source. The selected slices in plane Y were: 0, 25, 85, 185, 270, 325, 925 mm, related to the surfaces of the air gap, the first concrete surface, thermocouples embedded into concrete (85-185-270 mm), interface layer between concrete and Rockwool (350 mm) and the end of the Rockwool (925 mm).

After that, the code was run for planes at different heights that were chosen according to the position of thermocouples in Z axes: 0, -250, -500, -750 and -1000 mm from the top. Finally, some X-planes were represented as well ($X=100, 120, 230, 270, 380$ and 500 mm) to evaluate the temperature profiles across the longitudinal section of the prototype.

On the other hand, the code was able to create a video with the complete simulation. Nonetheless, the results presented in this chapter are pictures taken at different times of the test.

The case studies summarized in Table 8.5 were chosen to obtain the temperature profiles of the X, Y and Z-planes mentioned above. Additionally, the convection heat transfer coefficient was obtained punctually in those testing times as those are representing conditions closer to reach steady-state regimes.

8.2.2. Results of the simulation of the temperature of the prototype

The evolution of the temperature colourmap in the prototype is shown in different images. All the pictures were obtained with an isometric perspective to have a good view of the three axes. Figure 8.10 shows the layers of the prototype with the isometric perspective used in the figure obtained through the MATLAB® code.

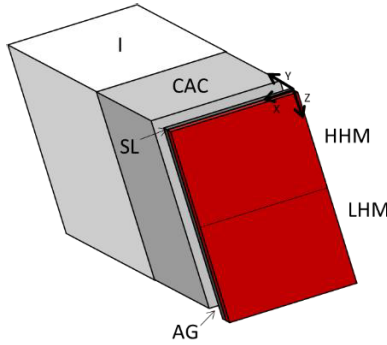
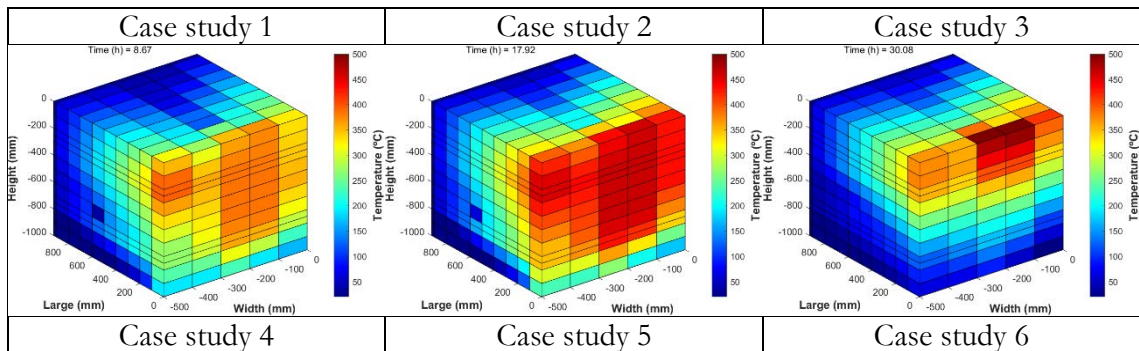


Figure 8.10: Layers of the prototype in isometric perspective.

All pictures are labelled as ‘Width’, ‘Large’ and ‘Height’ corresponding to the axes X, Y and Z, respectively. Table 8.7 includes the 3D temperature colourmap of the whole prototype, whose external surfaces were represented. The temperature is represented in the colour bar from **dark blue** at 20°C to **red** at 500°C.



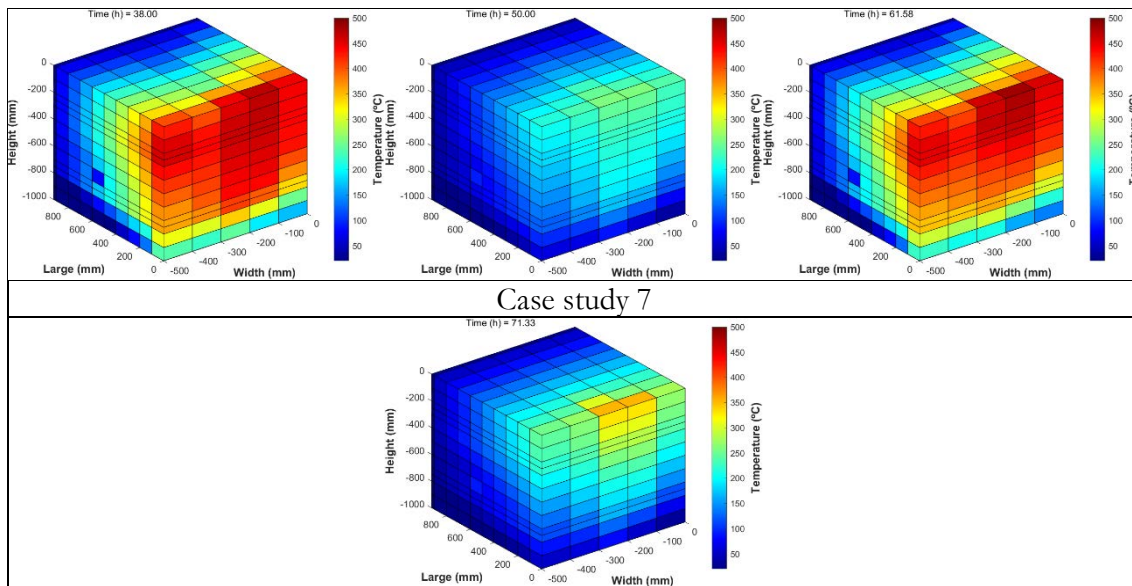


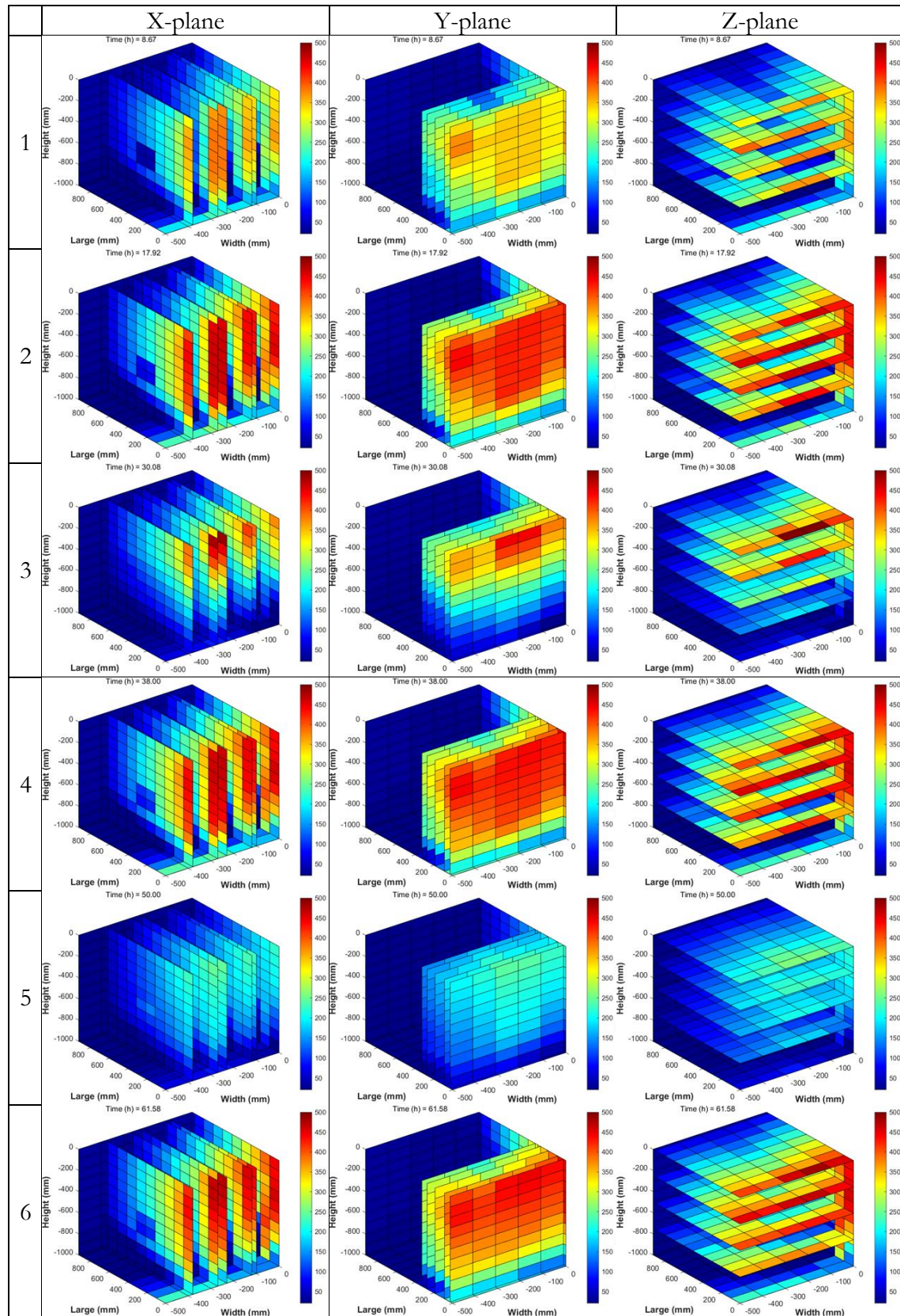
Table 8.7: Temperature profile of the prototype at different times of testing.

Analysing the profiles of case studies 2, 4 and 6 the evolution of temperatures in the external surfaces are almost similar because the heat source was operating at the maximum temperature (both heating mats at 500°C).

On the other hand, it is worth noting the effect of the thermocline that can be observed in case study 3, where the top was at a higher temperature than the bottom. This condition generated a ‘corner effect’ which is visible in the image taken after 30 hours of the start of the test. Nonetheless, this ‘corner effect’ will be evaluated across the internal layers below. Another interesting point is when the heat source was at the minimum temperature of cycling (200°C) as in cases 5 and 7, and the temperature is a little bit higher at the top. The explanation for this could be that the whole system was losing energy and, due to the air gap effect, the heat transfer losses were bigger at the top of the air gap. That is the reason why the temperature was higher at regions closer to the heat source and at the upper part.

On the other hand, in all cases, the temperature reached the maximum at the centre of the layer and the thermal parameter decreases when the location was closer to the corners. Although the heat transfer losses were lower, the loss of energy resulted in a decrease in the temperature in those regions.

To analyse how deep the heat went into the prototype, Table 8.8 summarises the evolution of temperature across different layers in X, Y and Z-planes for the 7 cases studied. Additionally, as the information of those layers is of interest, the evolution of every single layer at the three planes and for the 7 cases are collected in **Appendix C**.



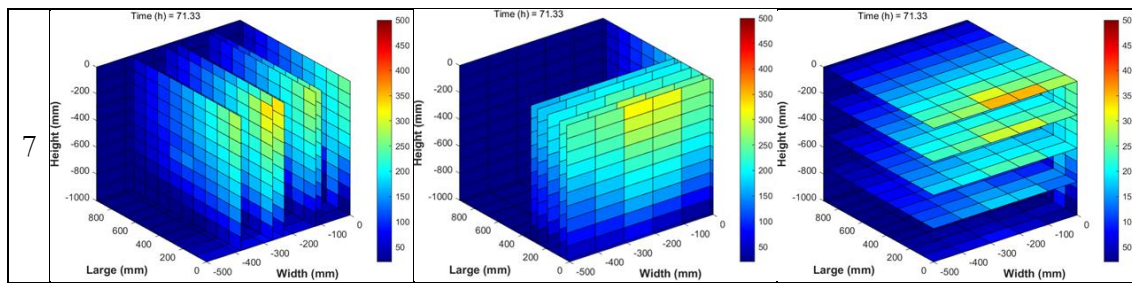


Table 8.8: Temperature across layers in X, Y and Z-planes for the case studies analysed.

Regarding the cases analysed at 500°C (CS 2, 4 and 6), the colour map patterns experienced similar results. Despite the prototype was being exposed to the maximum temperature, the heat did not arrive at the end of the concrete layer. Indeed, this layer was the one that underwent the highest difference of colour, meaning that the concrete layer acts as an insulating material.

On the other hand, the ‘corner effect’ when the prototype was operating with a thermocline region is more visual here (CS 3) than in Table 8.7. The difference of temperature was mainly undergone in depths between 0-380 mm from the heat source, being concrete the layer that experienced the most significant difference.

According to cases 5 and 7 when the whole system was being operated at 200°C, it is remarkable that the top part registered temperatures bigger than the bottom. The thermal inertia of the prototype and the heat transfer losses to the environment explain those temperature profiles during the cooling phase down to the minimum cyclic temperature.

8.3. Lessons learned and limitations of the model

The theoretical thermal model was able to demonstrate that the mock-up of a section of a thermocline experienced the biggest thermal losses for the upper part of the air gap layer. Moreover, the analysis of the thermal powers across the layers demonstrated that the concrete experienced thermal powers and temperature differences along both the longitudinal and transversal sections.

On the other hand, the heat transfer powers from concrete to the insulating layer and then to the surroundings might be considered negligible, as they differ in 3 orders of magnitude compared to the heat supplied by the sources. Again, the concrete layer has been demonstrated to be a suitable insulating material due to the withstanding of high temperature differences.

Combining results from both the theoretical model and the simulations lead to a remarkable effect on the air chamber. It is worth noting that this layer has only a depth of 0.015 m and the temperature difference experienced in the air had a big impact on the performance of the whole system. Indeed, it affects the closer layers, which experienced a heating process from the top and a cooling process at the bottom. The ‘corner effect’ produces differences in temperature in both longitudinal and transverse directions.

Regarding the type of convection, the air chamber only experienced the free mechanism when the heating source was operating at the minimum temperature of cycling. In the transitional conditions, the convection was forced as well as when the operation was

at full power. Despite the thermal cycle achieved equilibrium when it was being operated at 500°C, the convection was forced in those situations.

Nevertheless, there are limitations in the model. A more exhaustive analysis would have been done if the velocity of the air inside the cavity had been measured. With this value, the Reynolds and the Nusselt numbers would have been calculated in order to have the contribution to the forced convection heat transfer. With this information, a comparative analysis between the Nu experimental and theoretical would have been done to compare the experimental performance of the mock-up to the empirical solutions available in the literature for enclosure rectangular cavities.

According to the analysis of the enclosures, the lack of correlations for $H/L=66.66$ of this test made it not possible to calculate a more accurate Nusselt number. The expression used is more generic and it can be applied for $3 \cdot 10^5 \leq Ra < 7 \cdot 10^9$. The values for Ra obtained along the test was below the smallest limit and, for that reason, the correlation cannot be applied. However, the lack of correlations in the literature made it not possible to choose a more accurate expression and the results are a first approximation to the free convection mechanism. On the other hand, the walls of the cavity were different: concrete, steel and Rockwool and the roughness and thermal properties of those materials differ and have also an influence on the convection.

Regarding the hypotheses taken in the model, the assumption of having a constant and convection heat transfer coefficient in the air gap is not true for higher lengths of thermocline tanks that would increase the convection effect in the upper part of the tank. Nonetheless, the effect of the analysis of air gap layer commented in **Chapter 7** and along the present chapter are able for a geometry whose thermal expansions are not restricted. In a real prototype or tank filled with molten salts, the expansion of the tank due to the high temperatures would reduce the thickness of the air gap. This situation is completely different to the one presented here and needs a deeper analysis of the convection heat transfer mechanism and the loss of energy from the bottom to the top of the tank.

8.4. Conclusions

The analysis of heat transfer for the operation of the prototype has led to the following conclusions:

- The majority of the heat supplied was lost to the environment (\dot{Q}_{loss1}) by the air gap layer.
- The concrete was being heated up to the top and cooled down from the bottom mainly to the air gap (\dot{Q}_4) and to the foundations (\dot{Q}_{loss4}).
- The heat transfer among other layers can be neglected.
- The air chamber experienced forced convection when both heat sources were operating at full power at 500°C and free convection when they operated at 200°C.
- The convection in the air gap generated a ‘corner effect’ in the concrete, which experienced thermal gradients in both longitudinal and transverse directions. The highest temperatures at the top and in regions closer to the air gap.
- The concrete layer acts as an insulating material. (Chapter 9 on page 209)

8.5. References

- [1] F. P. Incropera, *Introduction to Heat Transfer*. (5th ed. ed.) Hoboken, NJ: Hoboken, NJ : John Wiley & Sons, 2006.
- [2] Y. S. Touloukian, R. K. Kirby, R. E. Taylor and T. Lee, "Thermophysical properties of matter," *New York*, pp. 89, 1970.
- [3] (Last visited on 20-12-20). *Thermal conductivity of Rockwool*. Available: <https://rti.rockwool.com/applications/marine-and-offshore/comfort/basic-theory/>.
- [4] (Last visited on 20-12-18). *Thermal conductivity of expanded clay*. Available: <https://frolleindanz.com/thermal-conductivity-of-expanded-clay-and-what-it-depends-on-photo/>.
- [5] T. Lucio-Martin, M. Roig-Flores, M. Izquierdo and M. C. Alonso, "Thermal conductivity of concrete at high temperatures for thermal energy storage applications: Experimental analysis," *Solar Energy*, vol. 214, pp. 430-442, 2021. . DOI: 10.1016/j.solener.2020.12.005.
- [6] (Last visited on 20-10-05). *Mantas calefactoras flexibles de alta temperatura para curado de composites*. Available: <http://santiescoin.com/resistencias-flexibles-2/mantas-calefactoras-flexibles-de-alta-temperatura-para-curado-de-composites/mantas-calefactoras-flexibles-de-alta-temperatura-para-curado-de-composites/>.
- [7] U. Roy and P. K. Roy, "Chapter 7 - advances in heat intensification techniques in shell and tube heat exchanger," in *Advanced Analytic and Control Techniques for Thermal Systems with Heat Exchangers*, L. Pekař, Ed. Academic Press, 2020, pp. 197-207 Available: <https://www.sciencedirect.com/science/article/pii/B9780128194225000074>. DOI: <https://doi.org/10.1016/B978-0-12-819422-5.00007-4>.
- [8] S. Globe and D. Dropkin, "Natural-convection heat transfer in liquids confined by two horizontal plates and heated from below," *Journal of Heat Transfer*, vol. 81, (1), pp. 24-28, 1959.
- [9] I. Catton, "Natural convection in enclosures," in *International Heat Transfer Conference Digital Library*, 1978.
- [10] R. K. MacGregor and A. F. Emery, "Free convection through vertical plane layers—moderate and high Prandtl number fluids," 1969.
- [11] K. Hollands, T. E. Unny, G. D. Raithby and L. Konicek, "Free convective heat transfer across inclined air layers," 1976.

This page has been intentionally left blank.

Chapter 9

Feasibility of industrialization and data protection of the monitoring of the drying process of concrete exposed to heat by a National Patent

The evolution of the electrical resistance when concrete is exposed to high temperature has been proved as a valuable method for following the drying process of concrete when it is exposed to heat. The procedure is able for following the drying in real time and for achieving accuracy in the drying above 90%, as it was explained in **Chapter 5** reaching a TRL 4 with the demonstration for laboratory testing of a prototype process and an integrated system. Additionally, the application of this methodology and device has been demonstrated and validated in **Chapter 7** in a prototype within a relevant environment, such as the mock-up of a section of a thermocline tank. Therefore, the Technology Readiness Level was improved, achieving a TRL 5.

The lack of knowledge in the monitoring in real time of the drying process made the researchers thinking about the chance of doing a patent of the technology developed. In this chapter, the initial feasibility study of a patent is described. Firstly, *section 9.1* includes the industrial applicability of the procedure to different fields. On the other hand, a study of patents related to the field is presented in *section 9.2*, as well as the evaluation of patentability following the requirements in *section 9.3*.

Finally, *section 9.4* details the application for a National Patent and *section 9.5* gives some conclusions related to the industrialization of part of the work developed in this thesis.

9.1. Background of the invention

There are various fields in which concrete is designed to withstand high temperatures. Examples of this are structures such as Geothermal and Nuclear Power Plants. In the former, the concrete infrastructure extracts heat from the interior of the earth and, thus, withstands

temperatures of around 300°C. In the case of Nuclear Power Plants, the reactors located inside the containment buildings are made of concrete. In the event of a failure in the core, the heat flow would be more aggressive on the concrete, increasing its thermal stress on the walls of the structure. On the other hand, it would be necessary to take into account possible cooling failures in the nuclear pools located inside the nuclear plant, which could increase the temperature up to 250°C, as shown in [1].

Mortars and concretes are used in other applications where they need to resist high temperatures. This is the case of Geothermal Oil and Gas wells whose infrastructure can operate at temperatures between 160 and 300°C, according to the authors in [2-4]. These structures operate under high-pressure conditions and the effect of temperature can generate decreases in the mechanical resistance of the material.

Other fields of application are tunnels and buildings, whose infrastructures are being improved for safety against fire risks. During a fire, the fast heating of the structure exposed to fire can lead to the spalling of concrete and end up with the collapse of the structure.

On the other hand, environmental conditions also influence the performance of concrete. The thermal response to drying from the manufacturing stage, the setting process and throughout its life in service influence the compressive strength, as the authors state in [5]. An example of this type is reflected in the fact that summer stages with high temperatures ($>30^{\circ}\text{C}$) and dry environments lead to the generation of cracks in the concrete that will affect its service life. To avoid this problem, it is necessary to evaluate in real time the evolution of both the thermal and electrical properties inside the structure and act accordingly.

However, technology advances in the field of construction and energy for sustainable development. Therefore, new applications of synergy between the two of them are appearing. In fact, one innovative application is the use of concrete as a solid medium for thermal energy storage. The thermal energy can be harvested from Waste Heat Recovery Systems (WHRS) in industry or even from Solar Thermal Power Plants (STPP), where the maximum operating temperature reaches 600°C.

Furthermore, refractory technology of industrial furnaces also performs a drying of the refractory bricks before the operation at high temperature. The authors in [6] include different drying curves depending on the type of installation and its maximum operating temperature. At the same time, they include reference values for operating at temperatures above 100°C, whose thermal gradients vary depending on the type of material whether it is conventional, light or dense refractory concrete with a medium-low content of cement.

As far as the material is concerned, when concrete is heated some physicochemical processes take place at different temperatures. However, the greatest risk takes place during the heating up to 100°C. During this process, the risk of spalling is not negligible due to the vaporization of the free water in the pores. The increase in temperature leads to an increase in pore pressure and this phenomenon is compounded by the replacement of air by the water that used to be in the pores. For this reason, infrastructures made of concrete need to accumulate low moisture in the pores before being exposed to high temperatures in order to avoid spalling risks and the collapse of the infrastructure.

The procedure for detecting the drying process of a concrete structure continuously and non-destructive could be applied to the industrial applications mentioned above. Therefore, with the aim of the industrialization of the procedure and the device carried out during the present Industrial PhD, this chapter comprises the evaluation of patentability of the invention.

9.2. Patent analysis

The first step to evaluate the possibility of applying for a patent is to look for a literature review on the field of application. The search was carried out by using different tools and software including national and international patents. The goal is to find patents related to: i) drying process of concrete or protocols for heating concrete structures and ii) devices for monitoring electrical and thermal parameters at high temperature in real time.

Nowadays, there are different software including national and international patents. The first analysis was carried out by searching in free and open software available such as Google Patents, INVENES, Espacenet and Patentscope. Firstly, Google Patents is a database from Google which includes national and international patents. Regarding the software INVENES, it is the database of the Spanish Patents and Trademarks Office, *Oficina Española de Patentes y Marcas* (OEPM). The documents contained in INVENES are national patents and utility models as well as European patents and PCT Spanish patents [7]. Espacenet belongs to the European Patent Office and more than 90 million European patents and international PCT, Patent Cooperation Treaty [8]. Finally, Patentscope is a search tool from the World Intellectual Property Organization which includes a PCT database of around 50 million documents of International applications and international patents [8].

The search was done including the same keywords in order to localize documents related to the field in previous databases: “Concrete”, “High Temperature”, “Electrical Resistance” and “Drying”. As a result of the investigation carried out, Table 9.1 shows a list of 20 documents found related to the scope. Those documents are closer to the prior art of the methodology and device for monitoring the drying process in real time of an infrastructure made of concrete.

Analysing documents from “Google Patents”, the inventions found (EP1478606A1, US20070125271, US2959489, and US4038093A) were related to cement and concrete compositions to be applied at high temperatures instead of heat treatments and monitoring devices. The same explanation can be applied to the patents found at Patentscope (201710375460.6) and Espacenet (CN107151118A).

According to the patents found at INVENES, ES0254526 describes an electrical device to determine the curing process of concrete, but it does not include a drying process at high temperatures. ES0213104 specifies types of concrete blocks as a component of drying ovens, but it does not mention the drying of the concrete block materials. ES0400379 describes a protocol for drying prestressed concrete beams by inducing an electrical current through the prestressed wires. However, the invention does not mention the temperature of the drying and the level of drying is not defined.

A high number of patents found uses the parameter of electrical resistance for analysing the setting (CN2237860Y), curing (US3649725A, WO1983001411A1,

US3982890A) and shrinkage (201310641654.8) processes. Nevertheless, the temperatures and conditions evaluated are ambient and the drying of concrete is not mentioned.

The document CA2948912A1 uses electrical tests for recording data of the curing, performance, and evolution of corrosion at different points, but it does not reference the drying process. The other documents present more technological distance with the object of study: CN101565970A, 201821094996.7, 201910432815.X, 20180260818.5, 1997042733.

| Keywords | Source | Number code | Title | Year |
|---------------------------|----------------|----------------|--|------|
| Conc. High T. | Google Patents | EP1478606A1 | Cement compositions for high temperature applications | 2004 |
| | Google Patents | US20070125271 | High temperature cements | 2007 |
| | Google Patents | US2959489 | High temperature portland cement mortars | 1960 |
| | Google Patents | US4038093A | Cement composition for high temperature wells and methods for producing the same | 1977 |
| | Google Patents | CN101565970A | Device for preventing high temperature caused by welding metal embedded part from burning out concrete base layer and method thereof | 2010 |
| | Patentscope | 2.0182E+11 | Concrete test block pore pressure testing arrangement under high temperature | 2019 |
| | Patentscope | 2.0171E+11 | High temperature resistant concrete | 2017 |
| | Patentscope | 201910432815.X | Method for improving high temperature resistance and freeze thawing resistance of high strength recycled concrete | 2019 |
| | ESPACENET | CN10715118A | High temperature resistant concrete | 2017 |
| Conc. Drying High T. | Google Patents | US3649725A | Methods for accelerating the curing of concrete | 1972 |
| | Google Patents | WO1983001411A1 | Method and device for controlling the curing rate of concrete | 1983 |
| | Google Patents | US3982890A | Method and apparatus for curing concrete products | 1976 |
| Conc. Elect. Res. High T. | Google Patents | CA2948912A1 | Electrical methods and systems for concrete testing | 2015 |
| Conc. Elect. Res. Drying | Google Patents | CN2237860Y | Sensor for measuring the initial setting time of concrete | 1995 |
| | Patentscope | 2.018E+10 | Concrete sample heat ageing and drying technology with minimum damage | 2018 |
| Conc. Drying | Patentscope | 2.0131E+11 | Method for measuring drying shrinkage constraint at concrete floor construction joint | 2014 |
| | INVENES | ES0400379 | Procedimiento de secado para vigas de hormigón pretensado | 1975 |
| | INVENES | ES0213104 | Bloque de hormigón para la construcción de hornos de secado | 1976 |
| Conc. Elect. Res. | Patentscope | 1997042733 | Crack sensor for concrete structure | 1998 |
| | INVENES | ES0254526 | Dispositivo eléctrico para el curado de hormigón | 1981 |

Table 9.1: Patents closer to the prior art of the methodology and device for monitoring the drying process from Google Patents, Patentscope, Espacenet and INVENES.

9.3. Evaluation of patentability

An invention can be considered patentable if it satisfies different requirements. The Spanish Law of Patents 24/2015 [9], indicates in article 4.1 that new inventions can be patentable whether they imply an inventive activity and they are susceptible to industrial application. The requirements for doing an invention patentable are as follows:

1) Novelty

According to article 6.1 of the Spanish Law of Patents 24/2015 [9], an invention is considered new when it has not been described previously in the closest prior art. It applies to national and international oral and written descriptions made before the application date. Additionally, the novelty requires that the description of all of the characteristics that component the patent has not been described before in the same document.

2) Inventive activity

Article 8.1 of the Spanish Law of Patents 24/2015 [9] considers that an invention presents inventive activity whether the invention is not evident for an expert in the field taking into consideration the closest prior art. Again, the prior art includes a description that is public through national or international oral or written communications before the application date. Indeed, the inventive activity evaluates if the invention can be deduced from previous documents published.

OEPM evaluates the inventive activity by using the method problem-solution [10] based on the points described as follows:

- Determine the closest prior art.
- Identification of the differences existing between the invention and the closest prior art.
- Analysis of the proposed solution and claims and evaluation of the previous pieces of evidence and whether the solution is evident or not for an expert in the field.

To evaluate the patentability of the monitoring of the drying process in real time of a concrete infrastructure, the search carried out was focus on the 20 patents found and showed in Table 9.1. Despite those patents are near to the prior art, they do not describe all of the technical characteristics and claims of the protocol and device developed during the present PhD thesis. Hence, the novelty requirement is satisfied.

On the other hand, regarding the inventive activity, with the documents found related to the prior art, it is not possible to deduce the solution proposed to follow the evolution of the level of drying of the concrete in real time.

Having fulfilled those requirements based on the studied prior art, the proposed invention could be patentable.

9.4. Application for a National Patent

After doing the initial analysis of the prior art, the researchers contacted the Intellectual Property Rights and Promotion of Technology-based Companies Unit from CSIC to evaluate the possibility of applying for a National Patent. The mentioned Unit did an internal evaluation and decided that the invention could be patentable. From that

moment, the legal procedure started, and this invention was presented on 28th October of 2020 at OEPM for the application for a patent of invention.

The title of the invention is “Procedimiento y equipo de medida para detectar, de forma continua y no destructiva, el secado de una estructura de hormigón”. The assigned application number is P202031076 and it was registered at OEPM Madrid Office on 28th October of 2020. The applicant and titular of the patent is Consejo Superior de Investigaciones Científicas and the inventors are María Cruz Alonso Alonso and Tamara Lucio Martín. More details of the application of the presentation to OEMP are included in **Appendix D**.

As the protocol and device developed during the present PhD are under revision for been patented, the document that describes the invention is not included in this PhD for intellectual property conflicts. Additionally, the evaluation of patentability has not been described in deep in this chapter for the same reason. Detailed differences between the invention and the closest prior art would highlight the technical characteristics and claims of the invention and would induce some conflicts of intellectual property.

9.5. Conclusions

After doing an initial search on the field and realize that there is a lack of knowledge in the monitoring of the drying process of a concrete infrastructure, the work developed during this investigation was thought to be protected. After the analysis, the following conclusions can be drawn:

- The procedure for detecting the drying process of a concrete structure continuously and non-destructive could be applied to industrial applications such as infrastructures of energy at high temperatures.
- The search of the closest prior art was done by open-access software of intellectual property such as Google Patents, INVENES, Patentscope and ESPACENET.
- A total of 20 patents were found and compared to the invention. The requirements for patentability (novelty and inventive activity) were analysed and the invention fulfilled those requirements compared to the prior art found.
- A National Patent was applied with the title “Procedimiento y equipo de medida para detectar, de forma continua y no destructiva, el secado de una estructura de hormigón”. The assigned application number is P202031076 and it was registered at OEPM Madrid Office. The applicant and titular of the patent is Consejo Superior de Investigaciones Científicas and the inventors are María Cruz Alonso Alonso and Tamara Lucio Martín.

(Chapter 10 on page 217)

9.6. References

- [1] A. Millard and P. Pimienta, *Modelling of Concrete Behaviour at High Temperature. State-of-the-Art Report of the RILEM Technical Committee 227-HPB*. Springer, 2019.
- [2] G. W. Hutterer, "The status of world geothermal power generation 1995–2000," *Geothermics*, vol. 30, (1), pp. 1-27, 2001. Available: <https://www.sciencedirect.com/science/article/pii/S037565050000420>. DOI: [https://doi.org/10.1016/S0375-6505\(00\)00042-0](https://doi.org/10.1016/S0375-6505(00)00042-0).
- [3] A. Stefánsson, R. Duerholt, J. Schroder, J. Macpherson, C. Hohl, T. Kruspe and T. Eriksen, "A 300 degree celsius directional drilling system," in *LADC/SPE Drilling Conference and Exhibition*, 2018, .
- [4] F. H. Z. Fridriksson, "An improved cement slurry formulation for oil and geothermal wells," *Master's Thesis, University of Stavanger, Norway*, 2017.
- [5] M. S. Gómez and S. Vidal, "Influencia en la Resistencia a Compresión de Hormigones por Efecto de la Temperatura Ambiente," *Revista De La Construcción*, vol. 5, (1), pp. 56-61, 2006.
- [6] German Association of Refractory and Chimney Engineering, *Refractory Engineering: Materials-Design-Construction*. Vulkan-Verlag GmbH, 2004.
- [7] B. Jürgens and V. Herrero-Solana, "Patents from Latin America and Spain with Latipat: Country coverage and ability to search for emerging topics like nanotechnology," *World Patent Information*, vol. 46, pp. 1-8, 2016. Available: <https://www.sciencedirect.com/science/article/pii/S0172219016300345>. DOI: <https://doi.org/10.1016/j.wpi.2016.05.003>.
- [8] B. Jürgens and V. Herrero-Solana, "Espacenet, Patentscope and Depatisnet: A comparison approach," *World Patent Information*, vol. 42, pp. 4-12, 2015. Available: <https://www.sciencedirect.com/science/article/pii/S0172219015000460>. DOI: <https://doi.org/10.1016/j.wpi.2015.05.004>.
- [9] Boletín Oficial del Estado, "Ley 24/2015, de 24 de julio, de Patentes," 2015.
- [10] Oficina Española de Patentes y Marcas, "Directrices de procedimiento de concesión, oposición, limitación e informe de búsquedas," 2017.

Chapter 10

Validation of objectives, working hypotheses and future work

The discoveries mentioned during the present thesis validate the initial working hypothesis suggested in **Chapter 1** as well as the partial objectives mentioned in section *1.5 Objectives*. The following subsections of this chapter summarise the validation of the partial objectives (*section 10.1*), working hypotheses (*section 10.2*), and the future works (*section 10.3*) of the research developed in this thesis.

10.1. Validation of Objectives

After developing the present thesis, the initial objective and all of the partial objectives were achieved.

- 1) *Analyses of the current knowledge on concrete exposed at high temperatures, including the evolution of thermal parameters at high temperatures and possible risks due to the operation at high temperatures. Identification of gaps. This study will also include the literature review of materials and configurations of thermal energy storage in CSP Plants.*

The literature review of the state of the art allowed understanding the mechanical, physical and chemical transformations that take place within the concrete in order to define the thermal exposure at high temperatures. Furthermore, mechanisms to avoid the spalling phenomenon of concrete, such as the addition of Polypropylene fibres were useful for designing the concrete mixes to achieve good adequacy to the high temperature regimes. On the other hand, the analysis of TES in CSP Plants and advances in new TES materials were essential to fix the limits of temperatures and regimes for the operation of the concrete in a TES infrastructure.

- 2) *Design of High Thermal Performance Concrete and experimental characterisation. Identify different concrete dosages and evaluation of the performance at high temperatures and to thermal cycles, following temperature regimes of molten salts (limits of stability between 290-550°C). This study will allow evaluating whether the concrete as thermal energy storage is a suitable*

material to withstand long-term high temperature regimes. The effect of the heat is evaluated through changes in mechanical and physicochemical properties as well as the risk of spalling.

According to the analysis of the risk of spalling:

- The design of the concrete composition should include PPF as a contingency for avoiding the risk of spalling in the first heating and thermally stable materials.
- Not only the design of the concrete mix influence the risk of spalling but also the geometry.
- The ageing also influences the spalling risk and up-scaled concrete specimens.
- Appropriate commissioning during the first heating is essential for homogenising the temperature within the concrete and reduce the thermal gradients.

According to the changes produced in the concrete after the thermal cycling:

- Regarding thermal exposure, the most significant degradation was produced after the first thermal cycle. On the contrary, the properties were only slightly degraded with each thermal cycle on successive heating and cooling cycles.
- After the thermal cycles, when using basalt, CAT, and São Domingos Slag aggregates, the compressive strength loss obtained was between 60-70% of the initial strength. When using siliceous aggregates, the compressive strength loss obtained was around 75%. In all cases, the mass loss produced after the thermal cycles ranges between 5.5 and 6.5% of the initial mass.
- The pore size distribution obtained after the thermal cycles showed a peak of porosity in the range of 24-27 µm, which is related to the presence of microcracks and the vaporization of the polypropylene fibres.
- The microcracking analysis showed that the area covered by cracks remains < 1% of the area analyzed, showing maximum crack widths below 80 µm after the thermal cycles performed.
- The concrete mixes analysed are recommended for thermal energy storage applications because of the stabilization of the mechanical and physicochemical properties in the long-term performance.

The results attained to this objective were presented in **Chapter 3** and they have improved the maturity in the technology at lab-scale from TRL 2 to TRL 3-4, where the evolution of those properties was experimentally validated.

- 3) *Characterisation of thermal properties of different concrete compositions exposed to high temperatures and thermal cycles. Evaluation of the effect of the heat in concrete at high temperatures.*

Regarding the thermal properties after the exposure at high temperatures:

- The thermal conductivity, volumetric heat capacity and thermal diffusivity experienced changes after cycles but measured at residual conditions.
- The volumetric heat capacity experienced a slower decrease in its value when the concrete was exposed to thermal cycles, achieving between $1.5\text{--}1.6 \cdot 10^6 \text{ J/(m}^3\text{·K)}$ after being exposed to 5 thermal cycles.
- The thermal diffusivity experienced significant changes in the binary composition containing basalt and CAT aggregates (B-C) and the one containing 100% CAT (C).

The thermal parameter experienced decreases of around 35-40% of its dried value after being exposed to thermal cycles. The ternary mix B-C-S15% experienced a more stable response, with a variation of around 20% after being exposed to thermal cycles. The values of diffusivity ranged between $0.4\text{--}0.5 \cdot 10^{-6} \text{ m}^2/\text{s}$.

- The thermal conductivity is similar in all the mixes with initial values around $1\text{--}1.20 \text{ W}/(\text{m}\cdot\text{K})$, and residual values after the thermal cycles around $0.80 \text{ W}/(\text{m}\cdot\text{K})$. The only mix with higher thermal conductivity is that with siliceous aggregates (S), which maintains a thermal conductivity of $1.25 \text{ W}/(\text{m}\cdot\text{K})$ after the thermal cycles. The thermal conductivity decreased between 30-35% after the first thermal cycle in the composition B-C-S15%. This decay reached a drop of 50% of its initial value in the siliceous composition.

Regarding the evolution of thermal conductivity at high temperatures:

- The thermal conductivity of concrete at high temperatures depends on the concrete mix and the aggregates. At room temperature, the values of thermal conductivity range for most of the concrete studied between $1.2\text{--}2 \text{ W}/(\text{m}\cdot\text{K})$, range obtained in concretes with calcareous, basalt, CAT and their combinations of aggregates. The use of siliceous aggregates improved thermal conductivity.
- In all the mixes, the biggest loss in the thermal conductivity takes place during the drying stage due to the loss of free water. When heating up to 600°C , the siliceous mix experienced the biggest drop ($\downarrow 50\%$) in the thermal conductivity compared to its initial value, while CAT and ternary mixes displayed more stable behaviour.
- In the first cooling down to 300°C , the thermal conductivity of most concrete mixes does not vary significantly, but siliceous and calcareous mixes recovered between 20-40% of the value at 600°C . In the second heating, the thermal conductivity achieves again the previous values at the equivalent temperatures. The last cooling produced a slight recovery in the thermal conductivity when samples were cooled at 200°C in mixes using siliceous, calcareous and basalt aggregates whereas the other mixes maintained the same value of the thermal parameter.
- The concrete mixes analyzed, excluding the siliceous mix, are recommended for thermal energy storage applications with temperatures between $290\text{--}550^\circ\text{C}$ (as expected in TES systems with Solar Salt as Heat Transfer Fluid), because of the stabilization of their thermophysical properties.
- The assumption of constant thermal conductivity in simulations of CTES is not appropriate for the first operating cycles and has to be decided depending on the concrete compounds.

The development has allowed the validation of the protocol for measuring the thermal conductivity at high temperatures at the laboratory, with an improvement in the Technology Readiness Level up to TRL 4. This research was developed in **Chapter 4**.

- 4) *Design and propose the commissioning of concrete infrastructures exposed to high temperatures through the evolution of the moisture content and dehydration of concrete by monitoring the evolution of the electrical resistance during the heating process. The demonstration of the viability of this challenging idea implies proposing methodologies for the commissioning, which will be*

validated in different concrete compositions, to evaluate the drying process by monitoring the structure in real time.

The methodology developed in **Chapter 5** and demonstrated at a higher scale in **Chapter 6** highlighted the following conclusions:

- The methodology developed regarding the measure of the electrical resistance for following the drying process continuously has been validated at lab-scale and up-scale and can be applied for preconditioning large-scale infrastructures of concrete before the operation at high temperatures.
- The procedure for detecting the drying process of a concrete structure continuously and non-destructive could be applied to industrial applications such as infrastructures of energy at high temperatures.
- While conventional concretes such as OPC-Core, OPC-Insulating and CAC-Ternary reached the equilibrium of drying at 72 hours, losing most of the water during the first 24 hours, OPC-UHPFRC needed 24 weeks for achieving the same equilibrium in samples of the same dimensions.
- The level of drying detectable with the measure of the electrical resistance was above 90% of the total mass lost and it was verified for all the concretes tested.
- The continuous measure of the electrical resistance permits following the drying process for a heating process and, hence, can avoid the spalling phenomenon.
- A total of 20 patents were found and compared to the invention. The requirements for patentability (novelty and inventive activity) were analysed and the invention fulfilled those requirements compared to the prior art found.
- A National Patent was applied with the title “Procedimiento y equipo de medida para detector, de forma continua y no destructiva, el secado de una estructura de hormigón”. The assigned application number is P202031076 and it was registered at OEPM Madrid Office.

The methodology described started from a concept (TRL 2) and ended with the validation of the protocol in a simulated relevant environment, improving the level of maturity up to TRL 5.

- 5) *Up-scaling and thermal operation of concrete specimens at high temperatures simulating the operating conditions of a CSP Plant. Commissioning of the test protocols at a higher scale and monitoring of thermal and electrical properties within the up-scaled concrete, simulating the operation of a thermocline tank. Lessons learned for the suitability of this application.*

A mock-up section of a thermocline tank made of concrete was built, commissioned (**Chapter 6**) and operated (**Chapter 7**). The following conclusions were drawn:

- A mock-up of a section of a thermocline tank was built. It includes a concrete layer made of the optimized concrete mix developed in **Chapter 3**, up-scaled up to 230 litres.
- A recommendation of pouring the concrete by phases in a real tank is given to reduce the peak of temperature reached during the setting period.

- A pre-heating process of the thermocline during the commissioning is needed to reduce risks such as high thermal gradients in the layers that could induce high internal stresses and affect the mechanical performance.
- The protocol developed in **Chapter 5** allows the monitoring of the drying process at different depths of a concrete infrastructure at large dimensions. Therefore, the industrial application of the protocol and device developed reaches a TRL 5 because the technology has been validated in a simulated relevant environment such as the mock-up section of a thermocline tank.
- The CAC concrete element has been able to withstand accurately the operation under regimes of high temperatures. For that reason, its use as an insulating element in thermal energy storage tanks is highly recommended for both the thermal response and the reduction of costs.
- The insulation with Rockwool after the CAC concrete and the expanded clay with sand compacted foundation experienced temperatures below 40°C, reducing heat transfer losses to the exterior.
- An initial heating process of the tank is needed before the entrance of the melted salts in the tank with a temperature higher than the melting point in order not to freeze the salts when they are incoming into the tank.
- The convection heat transfer mechanism in the air gap highly influences the evacuation of heat from the bottom to the top.
- The convection heat flow accelerates the heat transfer losses and for a thermocline tank concept, having an air gap is not the most efficient because the ratio cost vs energy is reduced. Nonetheless, the gap is needed from the mechanical point of view because the tank filled with molten salts will expand during the operation.
- A balance between the geometry, construction phase and the thermal operation of the infrastructure must be found.

The novel concept of using concrete as an insulating layer for tanks containing molten salts has been demonstrated for an up-scale achieving a TRL 5. The outcomes demonstrate that the configuration of TES analysed can be used in systems operating up to 500°C, and in the technology of Parabolic Trough collectors.

6) *Simulations of the up-scaled concrete exposed to high temperatures assuming the evolution of thermal conductivity with the temperature obtained experimentally.*

The heat transfer analysis was done from the experimental performance carried out in the mock-up section of the thermocline tank in **Chapter 8** and emphasised the following conclusions:

- The majority of the heat supplied was lost to the environment (\dot{Q}_{loss1}) by the air gap layer.
- The concrete was being heated up to the top and cooled down from the bottom mainly to the air gap (\dot{Q}_4) and to the foundations (\dot{Q}_{loss4}).
- The heat transfer among other layers can be neglected.
- The air chamber experienced forced convection when both heat sources were operating at full power at 500°C and free convection when they operated at 200°C.

- The convection in the air gap generated a ‘corner effect’ in the concrete, which experienced thermal gradients in both longitudinal and transverse directions. The highest temperatures at the top and in regions closer to the air gap.
- The concrete layer acts as a suitable insulating material because.

The simulations showed that the majority of the heat supplied was lost to the environment from the air gap layer and highlighted the importance of analyzing this layer during the thermal operation of a thermocline tank with thermal expansions during the operation.

The results reported along with the thesis and the main conclusions related to the partial objectives mentioned above have led to achieving the main objective of this thesis:

“To demonstrate the capacity of thermal energy storage of concrete at temperatures up to 550°C and to validate the performance in the commissioning and operating conditions of concrete infrastructures at high temperatures”.

Additionally, the research carried out for the validation of the objectives was published in two research articles in peer-reviewed journals. The information of the articles is mentioned below. Moreover, the accountability with the dissemination of the research developed in this thesis is included in **Appendix E**.

1) Article 1

Authors: M. Roig-Flores, T. Lucio-Martin, M.C. Alonso and L. Guerreiro

Title: Evolution of thermo-mechanical properties of concrete with calcium aluminate cement and special aggregates for energy storage

Journal: *Cement and Concrete Research*, vol. 141, 2021, 106323.

2) Article 2

Authors: T. Lucio-Martin, M. Roig-Flores, M. Izquierdo and M.C. Alonso.

Title: Thermal conductivity of concrete at high temperatures for thermal energy storage applications: Experimental analysis

Journal: *Solar Energy*, vol. 214, pp. 430-442, 2021.

On the other hand, the industrial application of the protocol developed for monitoring continuously the evolution of the drying for the heating process of a concrete infrastructure was validated in the mock-up section of a thermocline tank. For that reason, a National Patent and was registered at OEPM Madrid Office on 28th October 2020 with the assigned application number P202031076.

10.2. Validation of Working Hypotheses

The validation of the working hypotheses is detailed below point by point:

- *Some concrete structures are designed to withstand high temperatures in case of fire risk, but those concrete compositions might not be optimal for working under thermal fatigue cycles between 300-600°C.*

Despite the concrete needs to withstand high temperatures, the requirements are different owing to the boundary conditions. While a concrete exposed to fire needs to be designed for resisting under Ultimate Limit State (ULS), the application for energy storage should provide a long-term performance working between thermal cycles at high temperature. Therefore, in a TES infrastructure, the concrete needs to be designed to ensure a Serviceability Limit State (SLS).

Nevertheless, analysing the state of the art related to concrete exposed to fire, the introduction of polypropylene fibres into the design to avoid the spalling risk has been useful for the design of concretes for applications of energy storage. Therefore, the overview of the concrete in the field of the fire has allowed identifying the changes experienced for the concrete and design the thermal regime as well as the concrete compositions.

- *The concrete composition for an application of a solid medium of thermal energy storage is not optimized. The type of aggregates influences the thermal response and more thermal conductive aggregates might produce more cracking during the performance despite theoretically performing better the conduction of heat than the more thermal stable aggregates.*

In the analysis carried out in **Chapter 3**, this hypothesis was validated after testing more thermal stable compositions and a siliceous concrete mix characterised by having a high thermal conductive response. Although the percentage of cracking was similar among the mixes tested, the drop in the thermal conductivity parameter was more significant in the siliceous composition, as was demonstrated in **Chapter 4**.

- *The risk of spalling of concrete exposed to high temperature increases for temperatures above 100°C.*

From the survey of the state of the art of concrete exposed to heat, the present study found that the increases in the temperature induce high thermal gradients between the core and the surface and, at the same time, the pore pressures increases because of the water release and the evaporation of this component. Indeed, the two spalling experiences during the development of this thesis were carried out at temperatures above 100°C, as was explained in **Chapters 3 and 5**. It led to focus the investigation on how to do the commissioning and drying processes of concrete before its operation at high temperature and the discoveries in this field were presented for a National Patent, as was explained in **Chapter 9**.

- *Thermo-physical properties such as thermal conductivity present a temperature dependence and its evolution with temperature is not available in the literature.*

This hypothesis was validated in **Chapter 4** by experimental measurements carried out on concrete samples before and after thermal cycles on volumetric heat capacity, thermal diffusivity and thermal conductivity. The changes were also identified at high temperatures up to 600°C, improving the limit available in the literature review described in the state of the art. Additionally to this novelty, the thermal conductivity was measured during heating and cooling cycles, which was not reported before this study.

- *The effect of thermal fatigue cycles on thermal conductivity is unknown to the knowledge of the researchers.*

The search on the literature related to the field of concrete arose a lack of knowledge on this topic. It has been demonstrated in **Chapter 4** that repetitive heating and cooling did

not alter the value of thermal conductivity reached at the maximum temperature for different concrete compositions.

- *Numerical simulations of heat transfer usually employ constant values of thermal conductivity with temperature, which are far from optimal.*

When surveying the literature, the results found showed that the numerical heat transfer simulations of concrete as a thermal energy storage medium were carried out assuming a constant value of thermal conductivity. Furthermore, the assumed value was in most cases the one obtained at room temperature, which was far from the optimal for the operation. The effect of the type of aggregates has been demonstrated to have an influence on the thermal conductivity of concrete. Furthermore, the temperature and the physicochemical changes that take place in the concrete makes that thermal conductivity experiences a drop during heating that can decrease its initial value up to 50%. This fact highlighted the importance of taking into account the temperature dependence of thermal conductivity and, hence, its evolution in numerical simulations for having a more accurate model and prediction of thermal performance.

- *The commissioning of infrastructures based on concrete operating at high temperatures is not clear.*

As this use of concrete is relatively novel, there is a lack of knowledge on how to make a proper commissioning of the concrete infrastructures before its operation at high temperatures. For that reason, a procedure has been validated in this thesis for following the drying process for the commissioning of concrete before its operation. Additionally, the hypothesis was validated through surveying the closest prior art in patents and no similar results were found. For that reason, a patent on this matter was applied and registered to OEPM.

- *Although the suitability of concrete for applications at high temperatures has been demonstrated at lab-scale, the up-scaled infrastructures of concrete for TES at temperatures up to 500°C are not common in Industry.*

The novelty of this application influences the lack of infrastructures made of concrete for TES at 500°C. There are some pilots of modules of concrete for TES at temperatures up to 400-450°C to store thermal energy in the concrete element. However, the use of concrete can be extended to other applications such as the insulation of TES infrastructures, as was demonstrated in the thesis with the construction and operation of the mock-up section of a thermocline tank.

10.3. Future Work

Energy storage is a growing field of research where the development of new materials is increasing. New limits on the performance need to be achieved through the properties, structure and processes. The interdependencies among them are highly influenced by the materials' mechanical, electrical and chemical states as was probed in this thesis.

Regarding the specific work carried out in this thesis, the future research lines are mentioned as follows:

- Deeper knowledge in the long-term performance. Evaluation of the thermal cycling up to 9125 repetitive cycles, simulating a lifecycle of 25 years.

- Improve the repeatability of the experimental tests to have more accurate results of the thermal performance.
- Increase the temperature limit up to 800°C due to new advances in molten salts and measure the evolution of thermal conductivity at higher temperatures. Analyse the suitability of the material for the new limit.
- Improve the design of concrete materials depending on their function as an element for energy storage, insulating or structural.
- A deeper evaluation of the air gap and the convection effect in a thermocline tank during the operation.
- Applied the relationships related to the evolution of the thermo-physical properties with temperature in numerical heat transfer models.
- Further simulations of concrete infrastructures from both the thermo-mechanical and structural points of view including the degradation of the material to evaluate the long-term performance.
- A comparative study among different geometries of TES infrastructures made of concrete and thermo-economical analysis through an evaluation of ratio cost vs energy to reduce the Levelized Cost of Energy (LCOE).

There are several challenging types of research regarding the specific field of thermal energy storage at high temperatures that can be proposed for future work:

- New discoveries in TES mediums such as the molten salts have a direct influence on the infrastructure.

Therefore, higher levels of temperatures of the HTF will also be traduced in a higher temperature affecting the infrastructure, which also has to withstand those limits. Advanced performance usually means better efficiency, but also higher costs and the consumption of more resources, which are finite. For these reasons, the development of materials based on the circular economy, reusing resources and improving the performance will be key for the transition to renewable energy sources. Future advances in this field will be done and public funding goes also in the same direction.

- Commissioning and operation of the infrastructures according to the advanced limits of operation.

Similarly, as it was explained in this thesis, not only the design of the material is essential, but also the commissioning. Starting with the operation of infrastructure at high temperatures needs for defining a protocol so as not to produce damage in the material and further performance. As for the changes in the energy requirements and materials developed, the commissioning and operation of those infrastructures would need further research, as will depend on the specific characteristics of both the solar field and the TES infrastructure.

- Application of the lessons learned for the construction and operation of real thermocline TES facilities.

Indeed, the lesson learned from the construction and operation of the mock-up section of a thermocline tank described in this thesis will be applied in the prototype of thermocline that currently is being constructed at Évora Molten Salts Platform (EMSP)

under the NewSOL project. This large infrastructure will also improve the lessons learned for an up-scaled real thermocline tank made of concrete.

On the whole, this thesis includes a deeper contribution to the design, commissioning and operation of TES infrastructures made of concrete able to withstand cyclic temperatures up to 600°C. Nevertheless, there is still future work to be done in this field of research as soon as new materials and operation limits are advancing.

Conclusions

The research presented in this Industrial thesis aimed at improving the knowledge on the use of concrete for infrastructures of thermal energy storage in Solar Thermal Power Plants. The research was carried out at a lab scale and then it was validated at an up-scale, improving the Technology Readiness Level up to TRL 5 because the technology was simulated in a relevant environment.

The achievement of the main and partial objectives figure as follows:

Regarding the use of concrete for TES infrastructures (Objectives 1 and 2):

- The design and testing of concretes under regimes of temperatures of a CSP Plant were validated for being used in a TES infrastructure.
- It has been demonstrated that with a proper design and selection of and components, the concrete can withstand thermal cycles up to 550°C.
- The stabilization of the mechanical and physicochemical properties in long-term performance is a positive aspect for TES applications.

Regarding the evolution of the thermal parameters with the temperature (Objective 3):

- A protocol for measuring thermal conductivity at temperatures up to 600°C was developed, being the most complete work up to date in the evolution of thermal conductivity with temperatures up to 600°C and for repetitive heating and cooling cycles.
- The variations in the thermal conductivity of concretes exposed to the cycles experienced a significant variation in the first heating and, hence, the temperature-dependent expressions are valuable for models of heat transfer.
- The biggest loss in the thermal conductivity takes place during the drying stage at 105°C and then during the first heating up to 600°C. The thermal conductivity does not vary significantly with repetitive cooling and heating cycles.

Regarding the commissioning of concrete infrastructures at high temperatures (Objective 4):

- A protocol for monitoring continuously the evolution of the drying for the heating process in real time based on the measurement of the electrical resistance has been proposed and validated in a TRL 5.
- The level of drying detectable with the measure of the electrical resistance was above 90% of the total mass lost and it was verified for all the concretes tested.
- The industrial application of this protocol was proved in the mock-up section of a thermocline tank and a National Patent and was registered at OEPM Madrid Office on 28th October 2020 with the assigned application number P202031076.

Regarding the thermal operation and simulations of the up-scaled mock-up section of a thermocline tank made of concrete for TES (Objectives 5 and 6):

- The concrete element withstood accurately the operation under regimes of high temperatures. For that reason, its use as an insulating element in thermal energy storage tanks is highly recommended.
- The air chamber between the steel (container of the molten salts) and the concrete layer experienced convection heat transfer, which was forced when the heat source was operating at full power (500°C) and free when it was at the minimum cyclic temperature (200°C).
- The simulations showed that the majority of the heat supplied was lost to the environment from the air chamber of the configuration tested.

The results reported along with the thesis and the main conclusions related to the partial objectives have led to achieving the main objective of this thesis:

"To demonstrate the capacity of thermal energy storage of concrete at temperatures up to 550°C and to validate the performance in the commissioning and operating conditions of concrete infrastructures at high temperatures".

Appendix A

Evolution of thermal conductivity with temperature

The following expressions for the evolution of thermal conductivity with the temperature of concrete based on different types of aggregates can be used as input data for modelling the behaviour of concrete at temperatures up to 600°C. The proposed relationships can be of interests in applications of concrete for thermal energy storage or as a structural element exposed to fire.

1. First heating up to 600°C (1H):

- *CAT aggregate concrete – CAC cement (1-C):*
 $100 \leq T \leq 600^\circ\text{C}: 1.4587 - 0.0019T + 2 \cdot 10^{-6}T^2 \quad (\text{R}^2=0.4689)$
- *Basalt aggregate concrete – CAC cement (2-B):*
 $100 \leq T \leq 600^\circ\text{C}: 1.5173 - 0.0015T + 2 \cdot 10^{-6}T^2 \quad (\text{R}^2=0.1185)$
- *Basalt, CAT and Slag aggregate concrete – CAC cement (3-B-C-S):*
 $100 \leq T \leq 600^\circ\text{C}: 1.3311 - 0.001T + 7 \cdot 10^{-7}T^2 \quad (\text{R}^2=0.9477)$
- *Calcareous aggregate concrete – CAC cement (4-CAL):*
 $100 \leq T \leq 600^\circ\text{C}: 0.989 + 0.0017T - 3 \cdot 10^{-6}T^2 \quad (\text{R}^2=0.944)$
- *Siliceous aggregate concrete – CAC cement (5-S):*
 $100 \leq T \leq 600^\circ\text{C}: 2.1622 - 0.0004T - 2 \cdot 10^{-6}T^2 \quad (\text{R}^2=0.6628)$

2. First cooling down to 300°C (1C):

- *CAT aggregate concrete – CAC cement (1-C):*
 $300 \leq T \leq 600^\circ\text{C}: -0.1958 + 0.0068T - 8 \cdot 10^{-6}T^2 \quad (\text{R}^2=0.5933)$
- *Basalt aggregate concrete – CAC cement (2-B):*
 $300 \leq T \leq 600^\circ\text{C}: 2.887 - 0.0089T + 10^{-5}T^2 \quad (\text{R}^2=0.9657)$
- *Basalt, CAT and Slag aggregate concrete – CAC cement (3-B-C-S):*
 $300 \leq T \leq 600^\circ\text{C}: 0.7119 + 0.0015T - 2 \cdot 10^{-6}T^2 \quad (\text{R}^2=0.9317)$
- *Calcareous aggregate concrete – CAC cement (4-CAL):*

$$300 \leq T \leq 600^\circ\text{C}: \quad 0.768 + 0.0025T - 4 \cdot 10^{-6}T^2 \quad (\text{R}^2=0.7618)$$

- *Siliceous aggregate concrete – CAC cement (5-S):*

$$300 \leq T \leq 600^\circ\text{C}: \quad 2.528 - 0.0041T + 3 \cdot 10^{-6}T^2 \quad (\text{R}^2=0.9861)$$

3. Second heating up to 600°C (2C):

- *CAT aggregate concrete – CAC cement (1-C):*

$$300 \leq T \leq 600^\circ\text{C}: \quad -0.4386 + 0.0088T - 10^{-5}T^2 \quad (\text{R}^2=1)$$

- *Basalt aggregate concrete – CAC cement (2-B):*

$$300 \leq T \leq 600^\circ\text{C}: \quad 2.8374 - 0.0079T + 8 \cdot 10^{-6}T^2 \quad (\text{R}^2=0.6669)$$

- *Basalt, CAT and Slag aggregate concrete – CAC cement (3-B-C-S):*

$$300 \leq T \leq 600^\circ\text{C}: \quad 2.1378 - 0.0056T + 6 \cdot 10^{-6}T^2 \quad (\text{R}^2=0.8783)$$

- *Calcareous aggregate concrete – CAC cement (4-CAL):*

$$300 \leq T \leq 600^\circ\text{C}: \quad 2.3181 - 0.0053T + 5 \cdot 10^{-6}T^2 \quad (\text{R}^2=0.9861)$$

- *Siliceous aggregate concrete – CAC cement (5-SIL):*

$$300 \leq T \leq 600^\circ\text{C}: \quad 3.5903 - 0.0096T + 9 \cdot 10^{-6}T^2 \quad (\text{R}^2=0.9166)$$

4. Second cooling down to room temperature:

- *Basalt aggregate concrete – CAC cement (2-B):*

$$25 \leq T \leq 600^\circ\text{C}: \quad 0.7897 + 0.0024T - 4 \cdot 10^{-6}T^2 \quad (\text{R}^2=0.4072)$$

- *Basalt, CAT and Slag aggregate concrete – CAC cement (3-B-C-S):*

$$25 \leq T \leq 600^\circ\text{C}: \quad 0.9371 + 0.0006T - 9 \cdot 10^{-7}T^2 \quad (\text{R}^2=0.4238)$$

- *Calcareous aggregate concrete – CAC cement (4-CAL):*

$$25 \leq T \leq 600^\circ\text{C}: \quad 1.2557 + 0.0004T - 10^{-6}T^2 \quad (\text{R}^2=0.8382)$$

- *Siliceous aggregate concrete – CAC cement (5-SIL):*

$$25 \leq T \leq 600^\circ\text{C}: \quad 1.7776 + 0.0006T - 3 \cdot 10^{-6}T^2 \quad (\text{R}^2=0.7691)$$

Appendix B

Location of thermocouples in the core samples

| | Theoretical position | | | Measured value | | | | | |
|--------|----------------------|-----|---------|----------------|------|-------|---------------|------|-------|
| | Coordinates | | | Sensor input | | | Sensor output | | |
| | X | Y | Z | X_1 | Y_1 | Z_1 | X_2 | Y_2 | Z_2 |
| Core 2 | 250± 40 | | 250± 40 | | | | | | |
| T6 | 270 | 60 | 250 | 262.4 | 58.2 | 212 | 260.4 | 60.5 | 291.1 |
| T5 | 270 | 160 | 250 | 246.1 | 217 | 209.5 | 244.3 | 203 | 293.3 |
| T4 | 270 | 245 | 250 | 247.3 | 159 | 209.1 | 240.3 | 153 | 293.2 |

| | Theoretical position | | | Measured value | | | | | |
|--------|----------------------|-----|---------|----------------|------|-------|---------------|------|-------|
| | Coordinates | | | Sensor input | | | Sensor output | | |
| | X | Y | Z | X_1 | Y_1 | Z_1 | X_2 | Y_2 | Z_2 |
| Core 5 | 250± 40 | | 500± 40 | | | | | | |
| T6 | 270 | 60 | 500 | 250.9 | 36.6 | 207.5 | 268.5 | 25.2 | 534.8 |
| T5 | 270 | 160 | 500 | 237.5 | 142 | 458.7 | Not localized | | |
| T4 | 270 | 245 | 500 | Not localized | | | | | |

| | Theoretical position | | | Measured value | | | | | |
|--------|----------------------|-----|---------|----------------|-------|-------|---------------|-----|-------|
| | Coordinates | | | Sensor input | | | Sensor output | | |
| | X | Y | Z | X_1 | Y_1 | Z_1 | X_2 | Y_2 | Z_2 |
| Core 3 | 125± 40 | | 250± 40 | | | | | | |
| T3 | 100 | 60 | 250 | Not localized | | | | | |
| T2 | 100 | 160 | 250 | 86.9 | 153.3 | 234.7 | 84.1 | 154 | 260.2 |
| T1 | 100 | 245 | 250 | Not localized | | | | | |

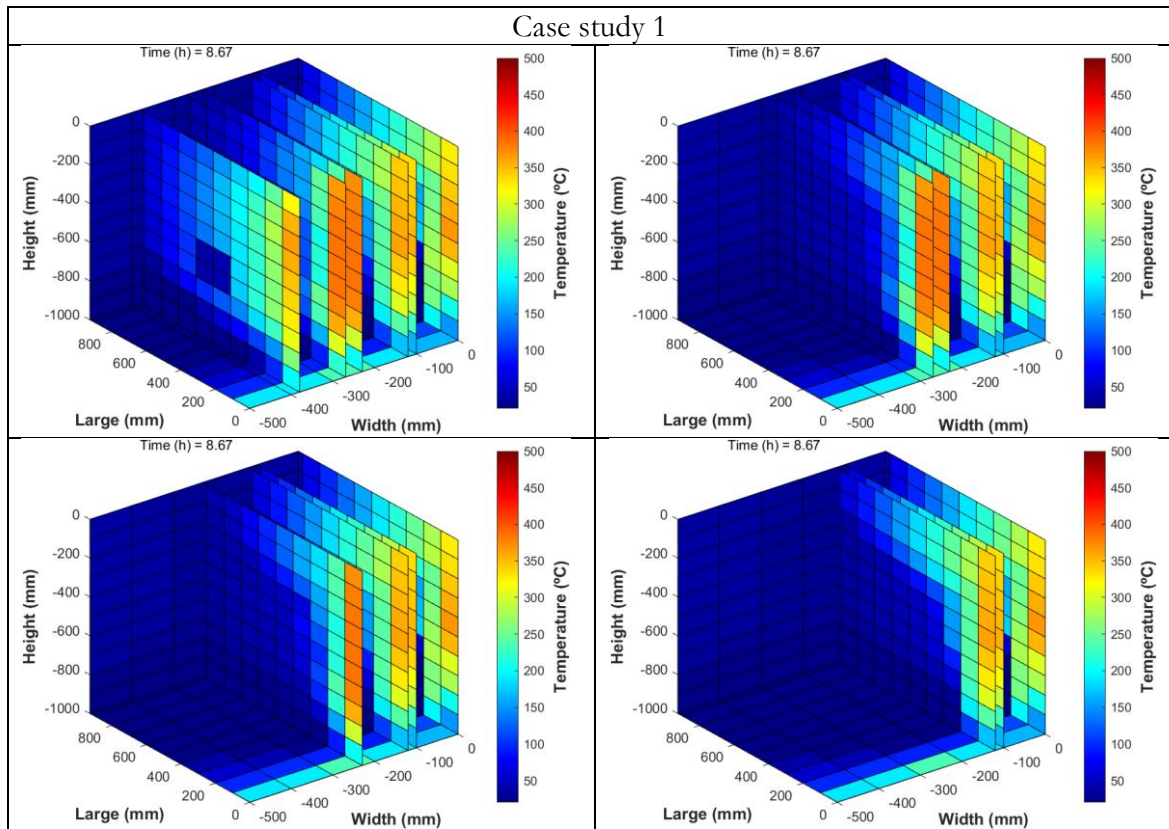
| | Theoretical position | | | Measured value | | | | | |
|--------|----------------------|-----|---------|----------------|-----|-----|---------------|-----|-----|
| | Coordinates | | | Sensor input | | | Sensor output | | |
| | X | Y | Z | X_1 | Y_1 | Z_1 | X_2 | Y_2 | Z_2 |
| Core 6 | 125± 40 | | 500± 40 | | | | | | |
| T3 | 100 | 60 | 500 | Not localized | | | | | |
| T2 | 100 | 160 | 500 | Not localized | | | | | |
| T1 | 100 | 245 | 500 | Not localized | | | | | |

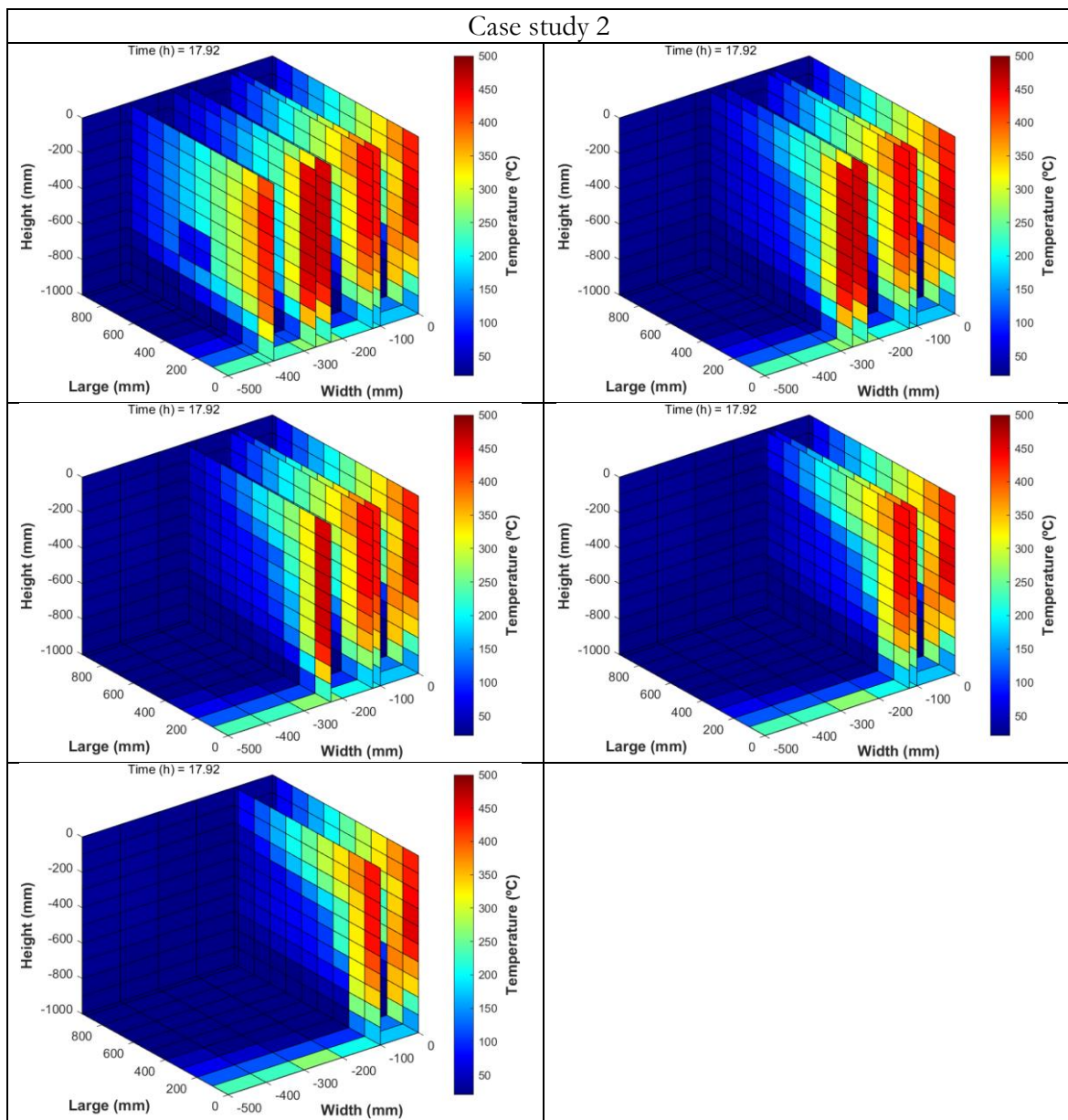
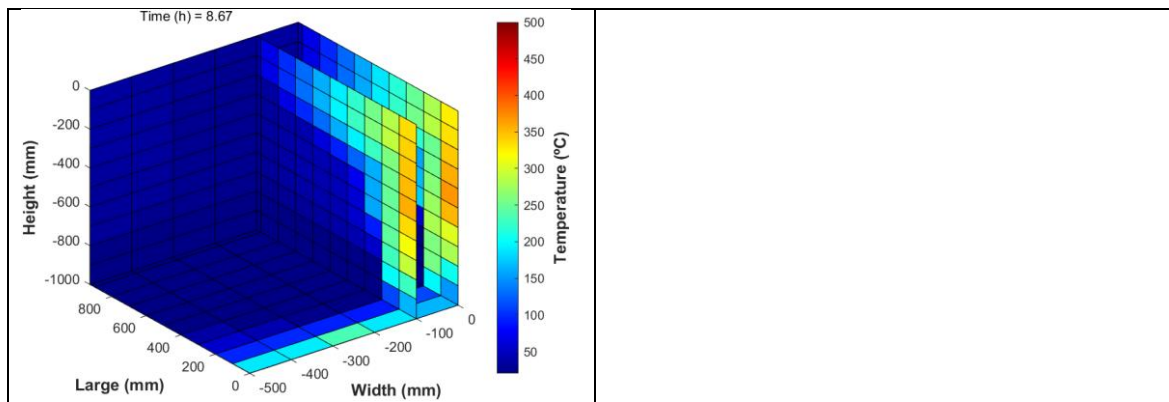
| | Theoretical position | | | Measured value | | | | | |
|--------|----------------------|-----|---------|----------------|-----|-----|---------------|-----|-----|
| | Coordinates | | | Sensor input | | | Sensor output | | |
| | X | Y | Z | X_1 | Y_1 | Z_1 | X_2 | Y_2 | Z_2 |
| Core 9 | 125± 40 | | 750± 40 | | | | | | |
| T3 | 100 | 60 | 750 | Not localized | | | | | |
| T2 | 100 | 160 | 750 | Not localized | | | | | |
| T1 | 100 | 245 | 750 | Not localized | | | | | |

Appendix C

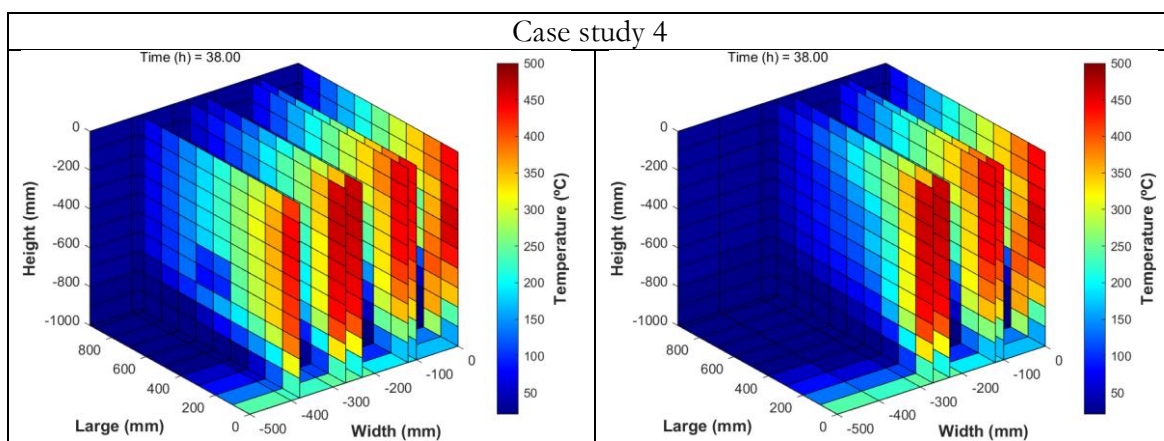
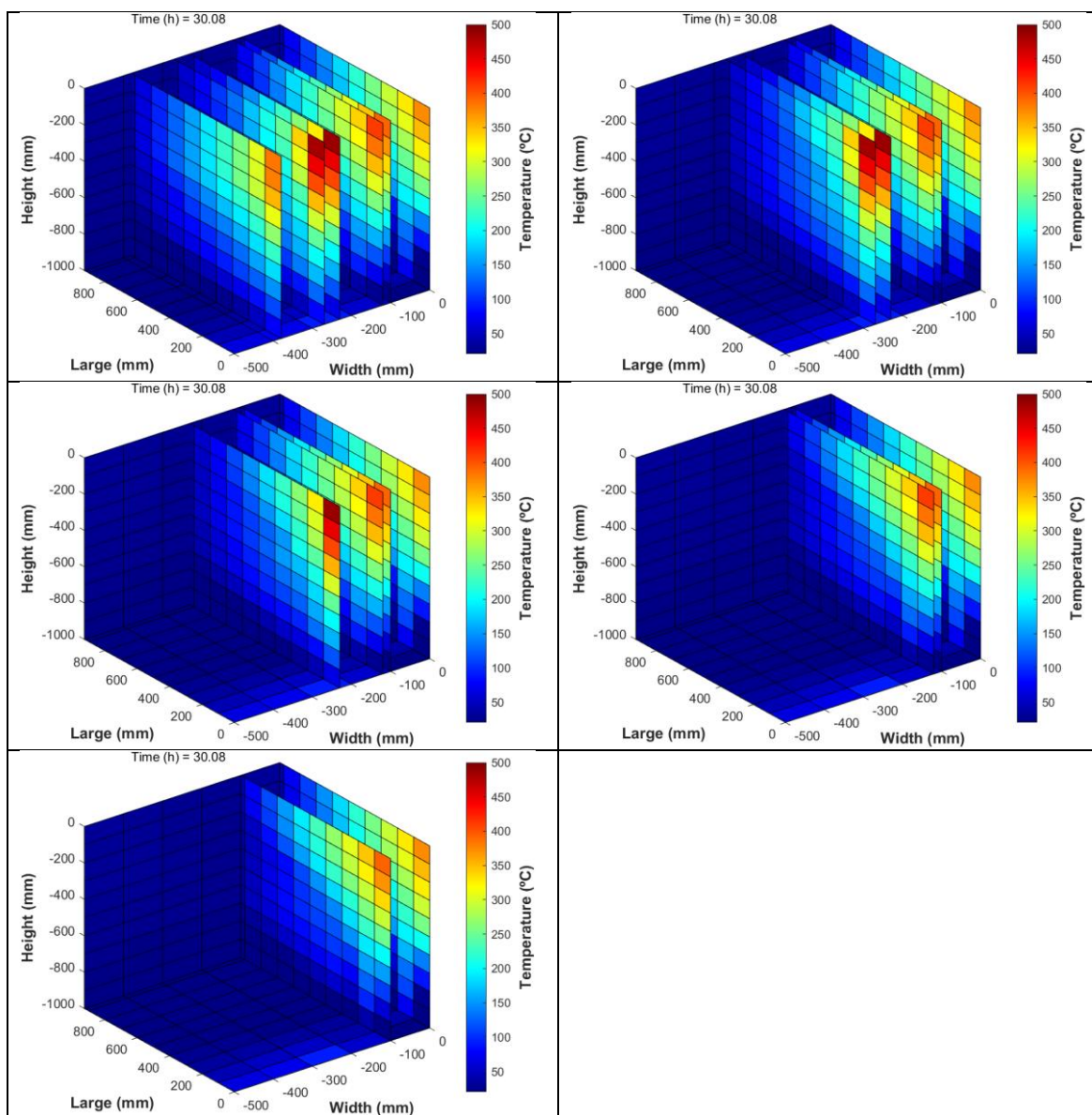
Simulations of the thermal operation of the mock-up section of a thermocline tank

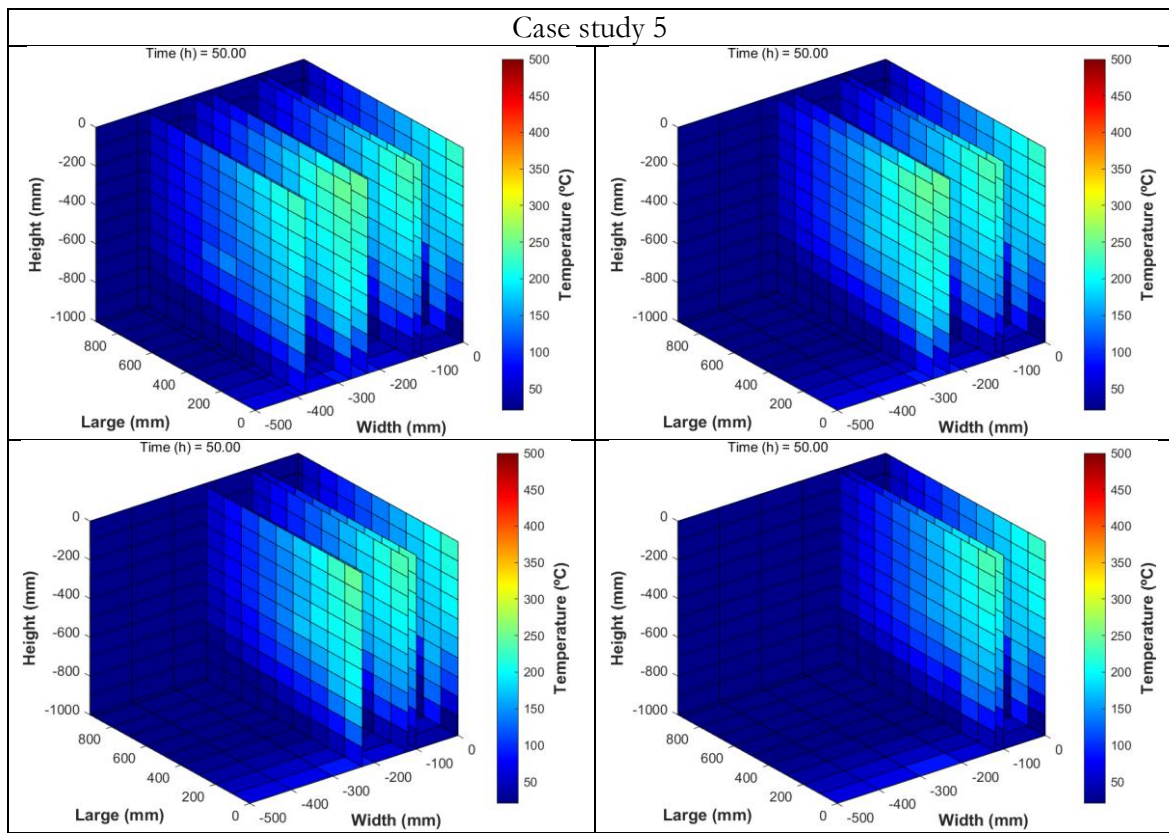
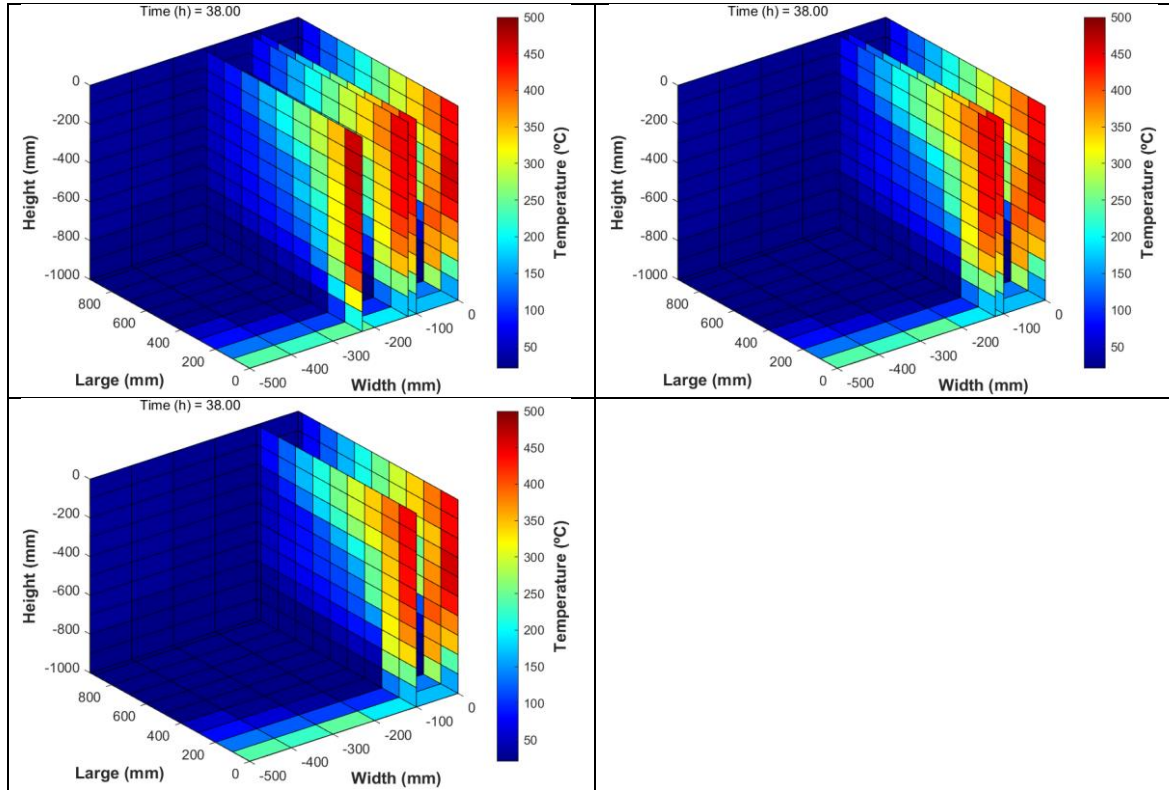
C.1) Temperature profiles at different depths (X-Planes)

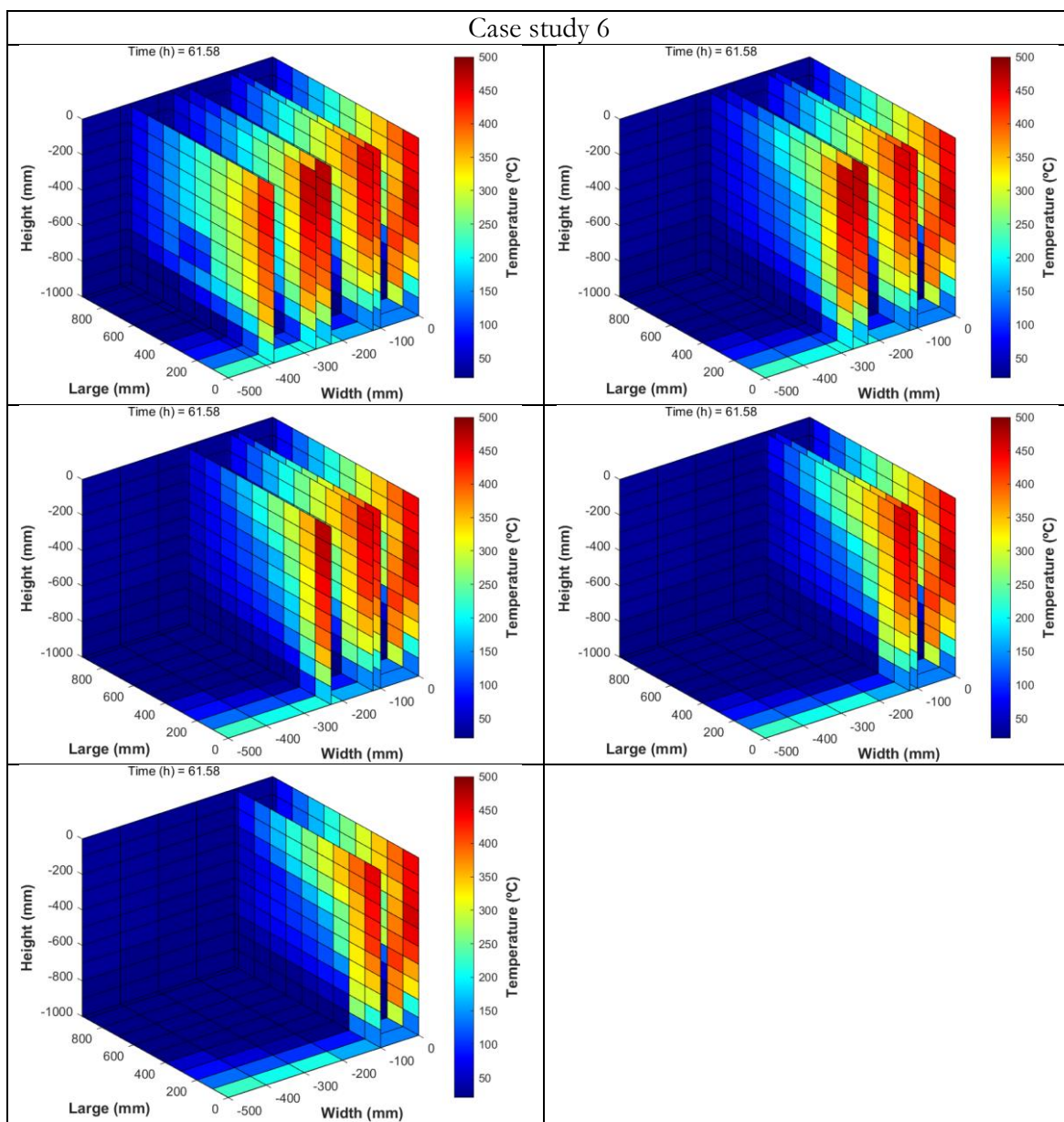
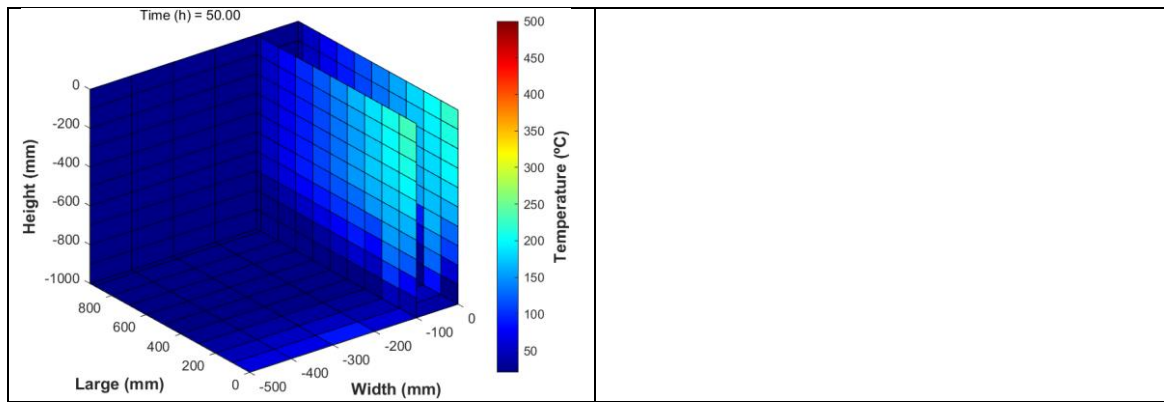




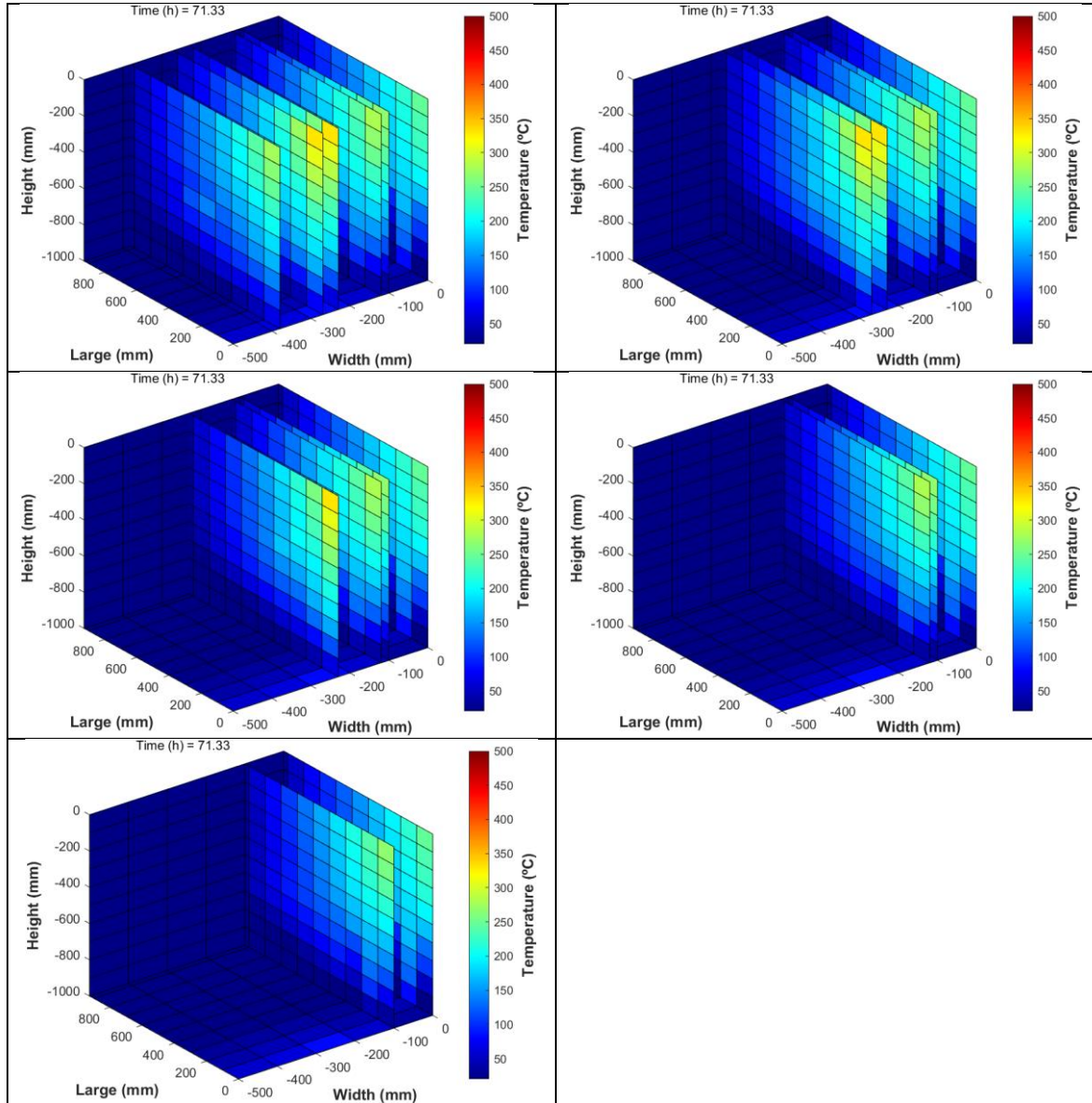
Case study 3



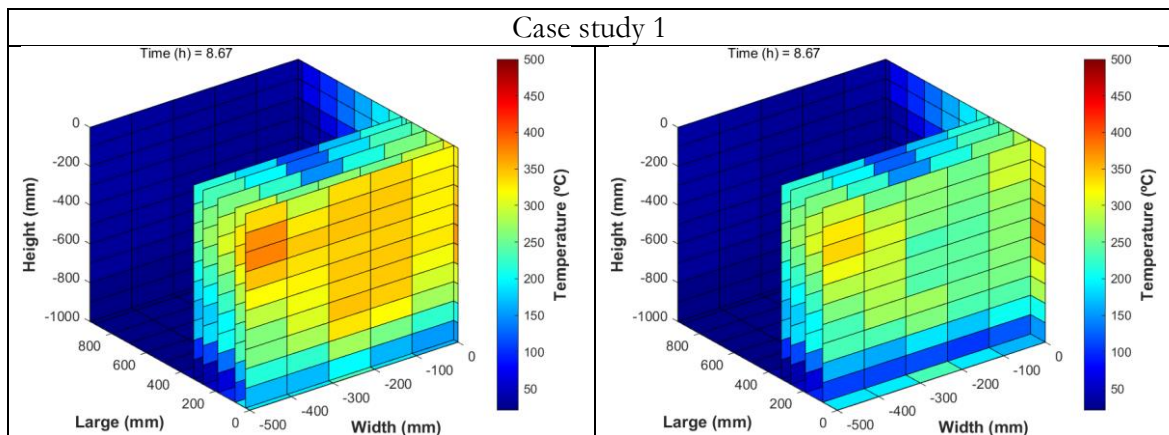


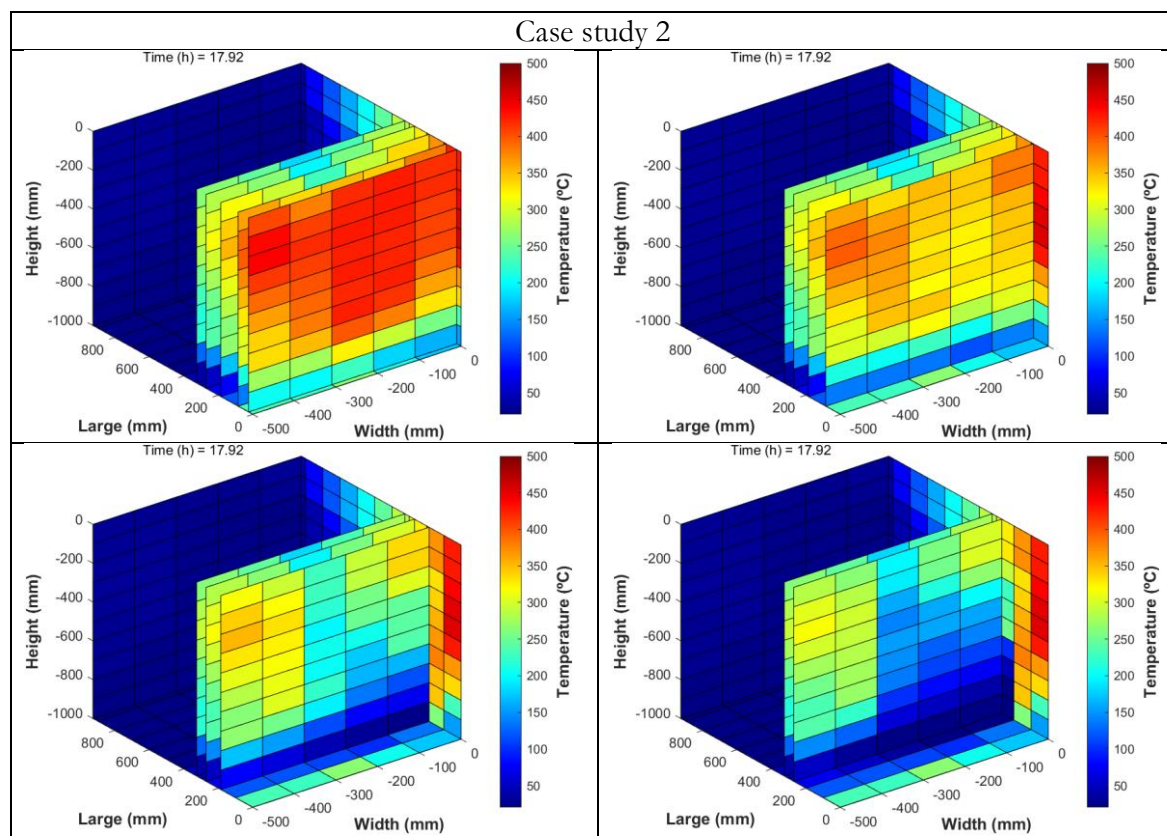
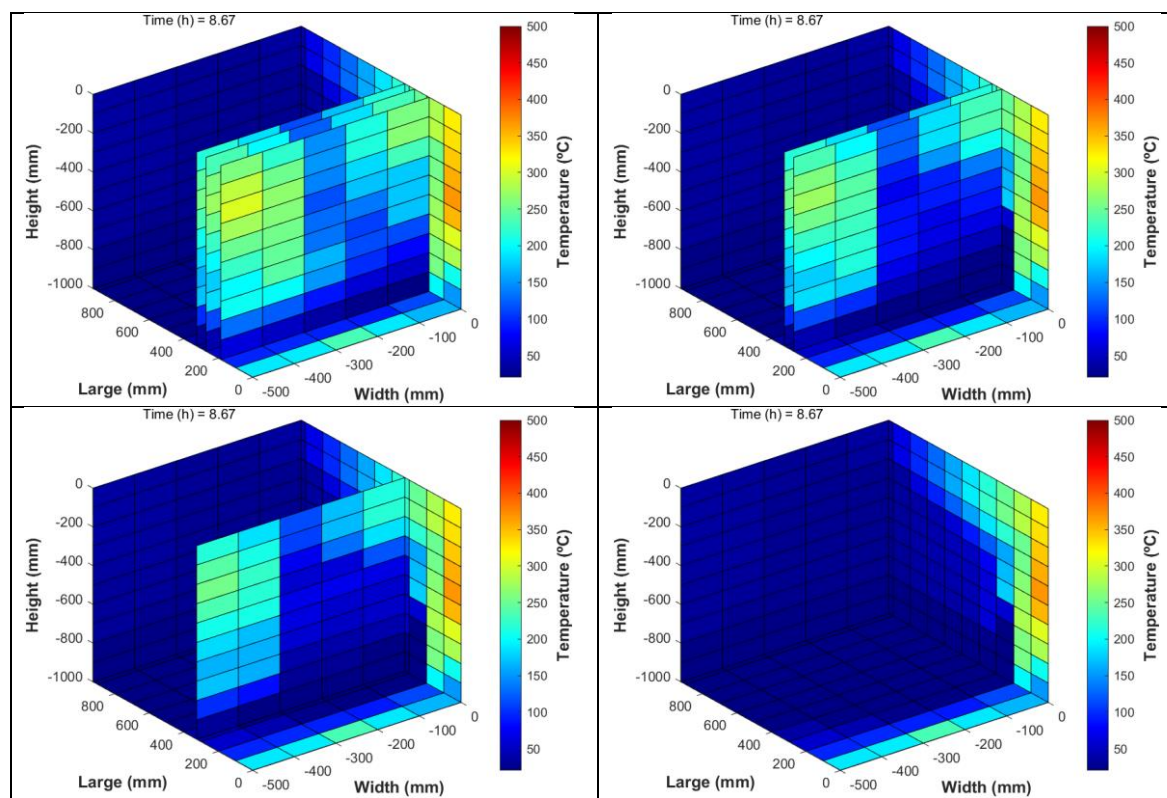


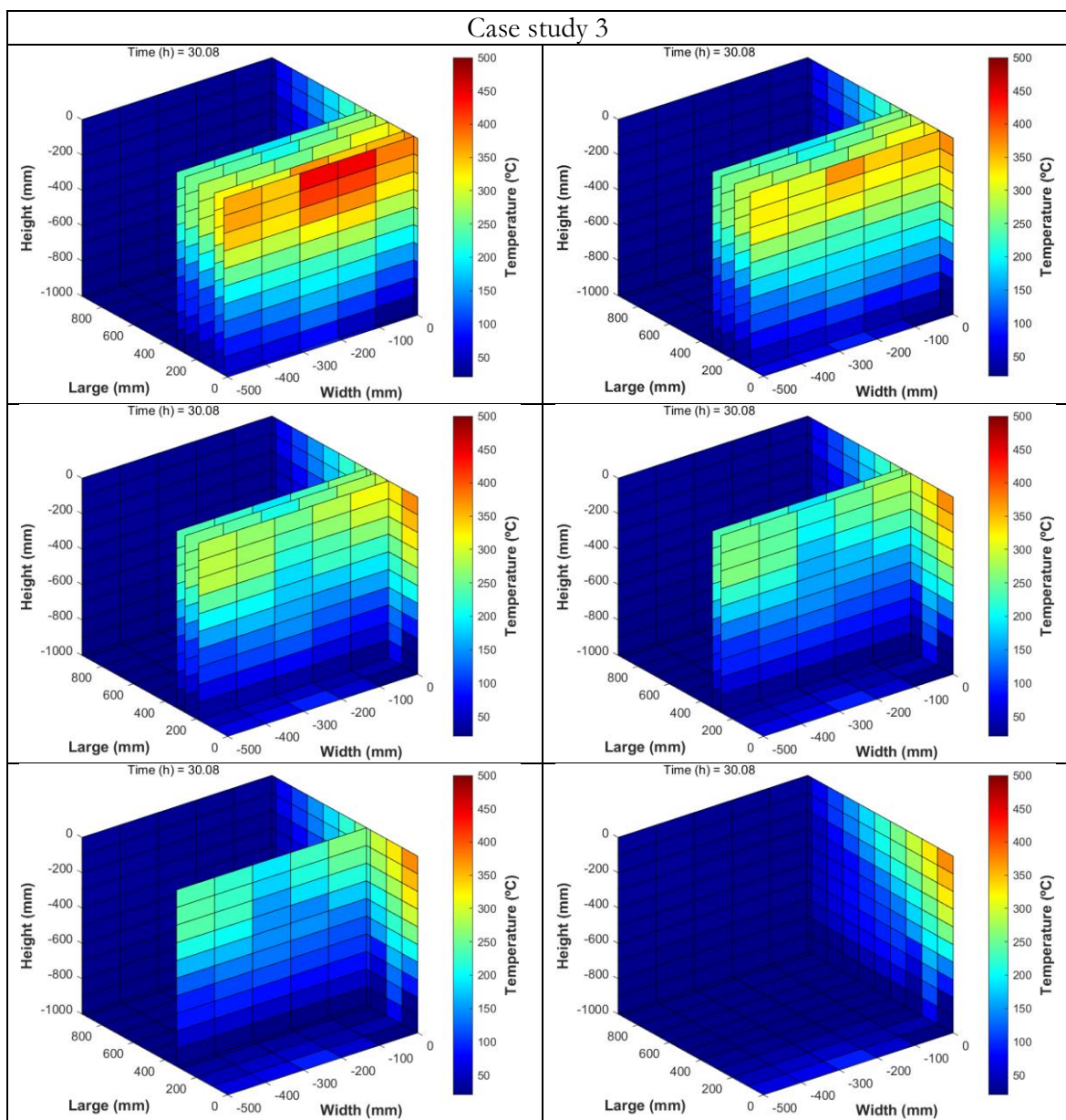
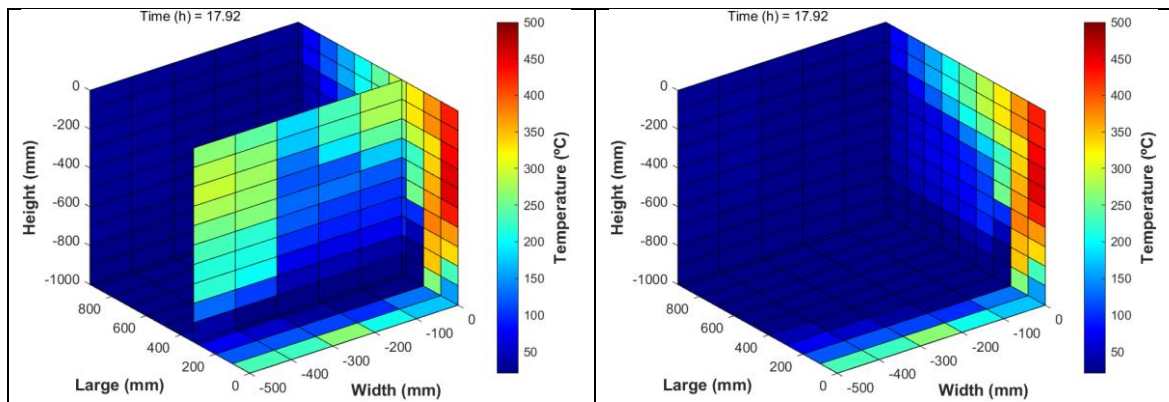
Case study 7



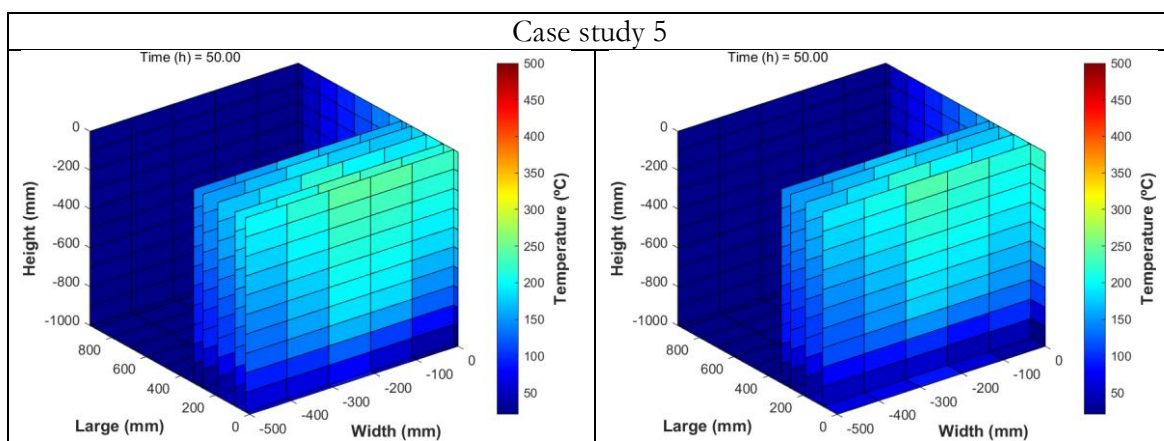
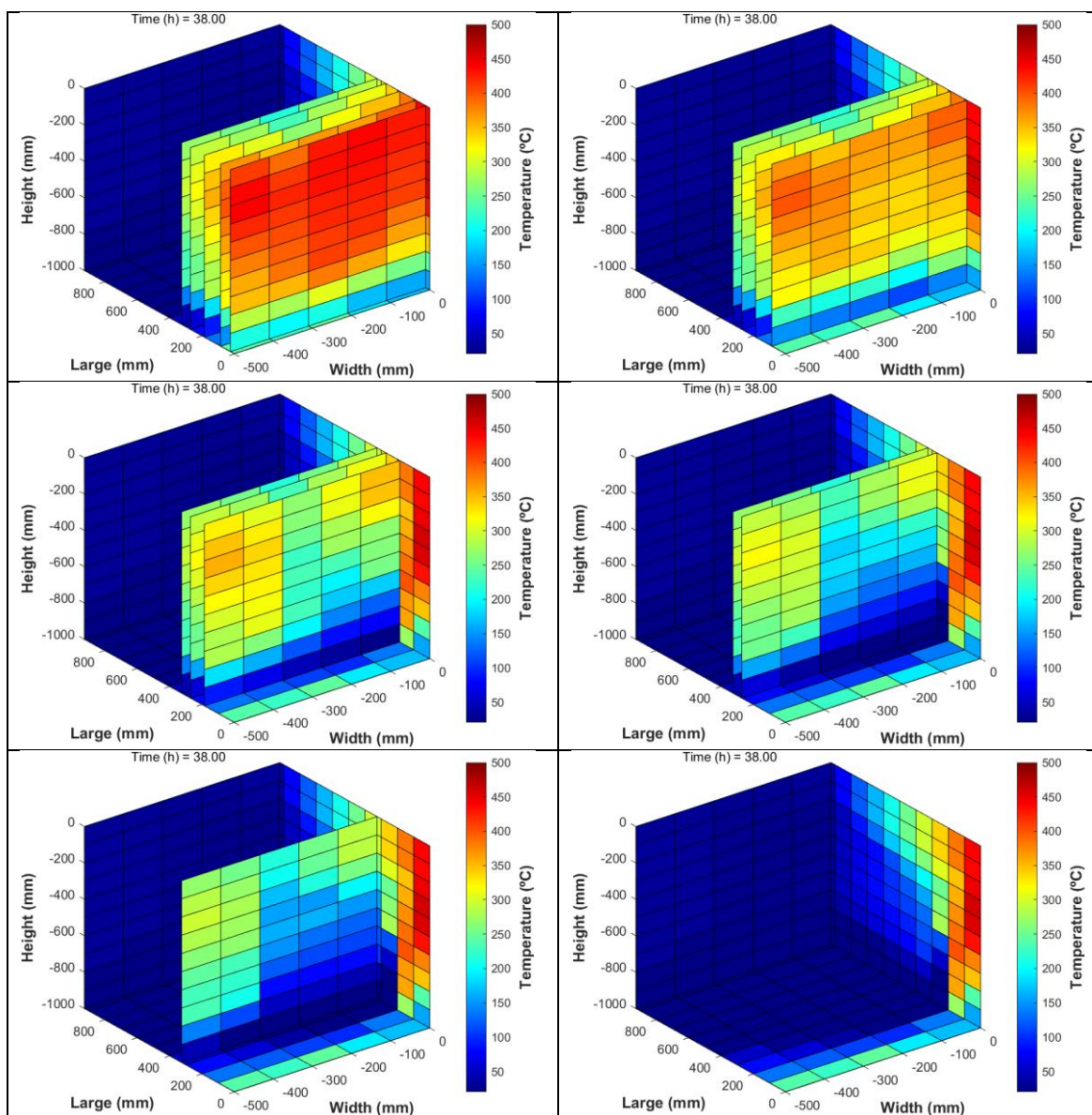
C.2) Temperature profiles at different depths from the heat source (Y-Planes)

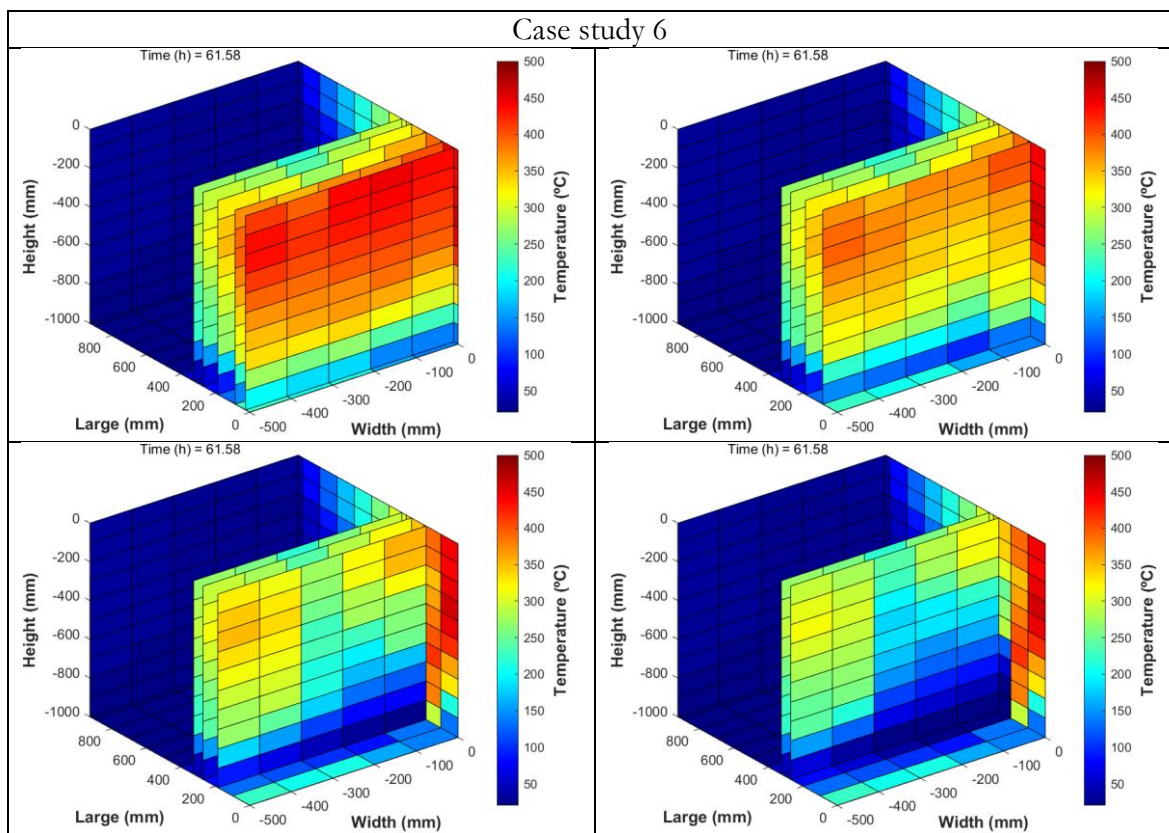
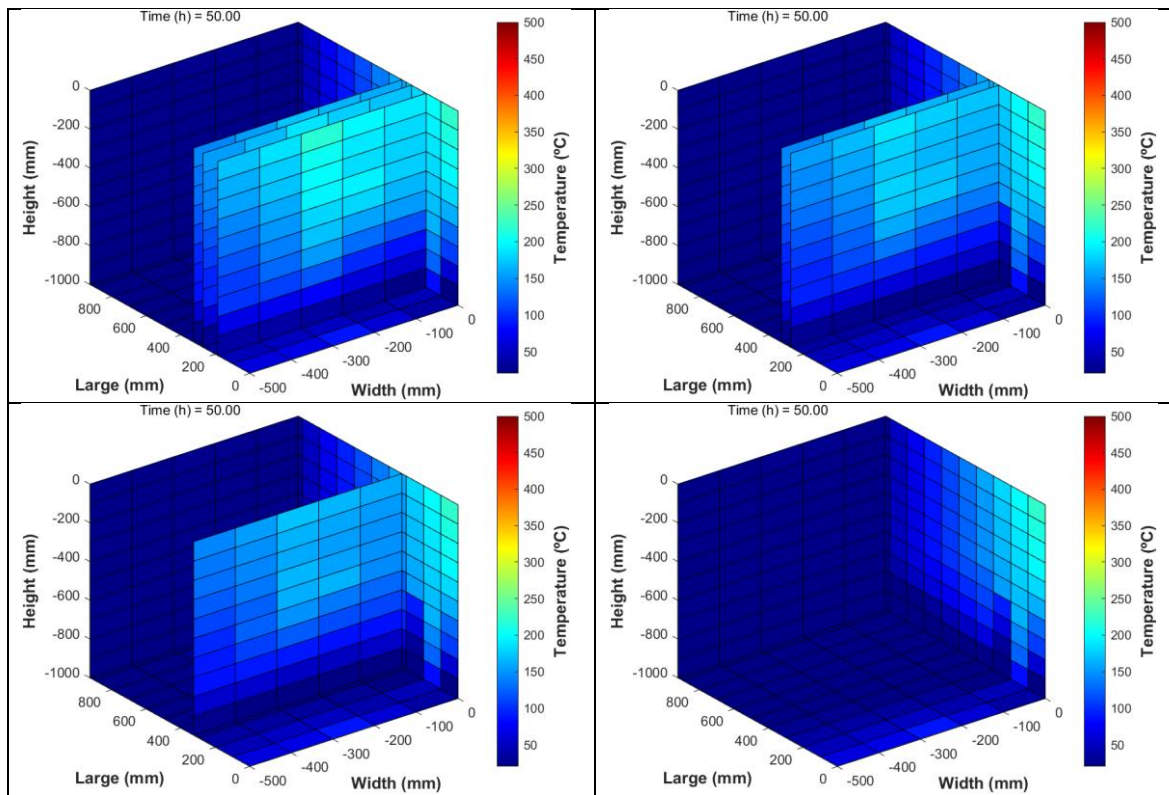


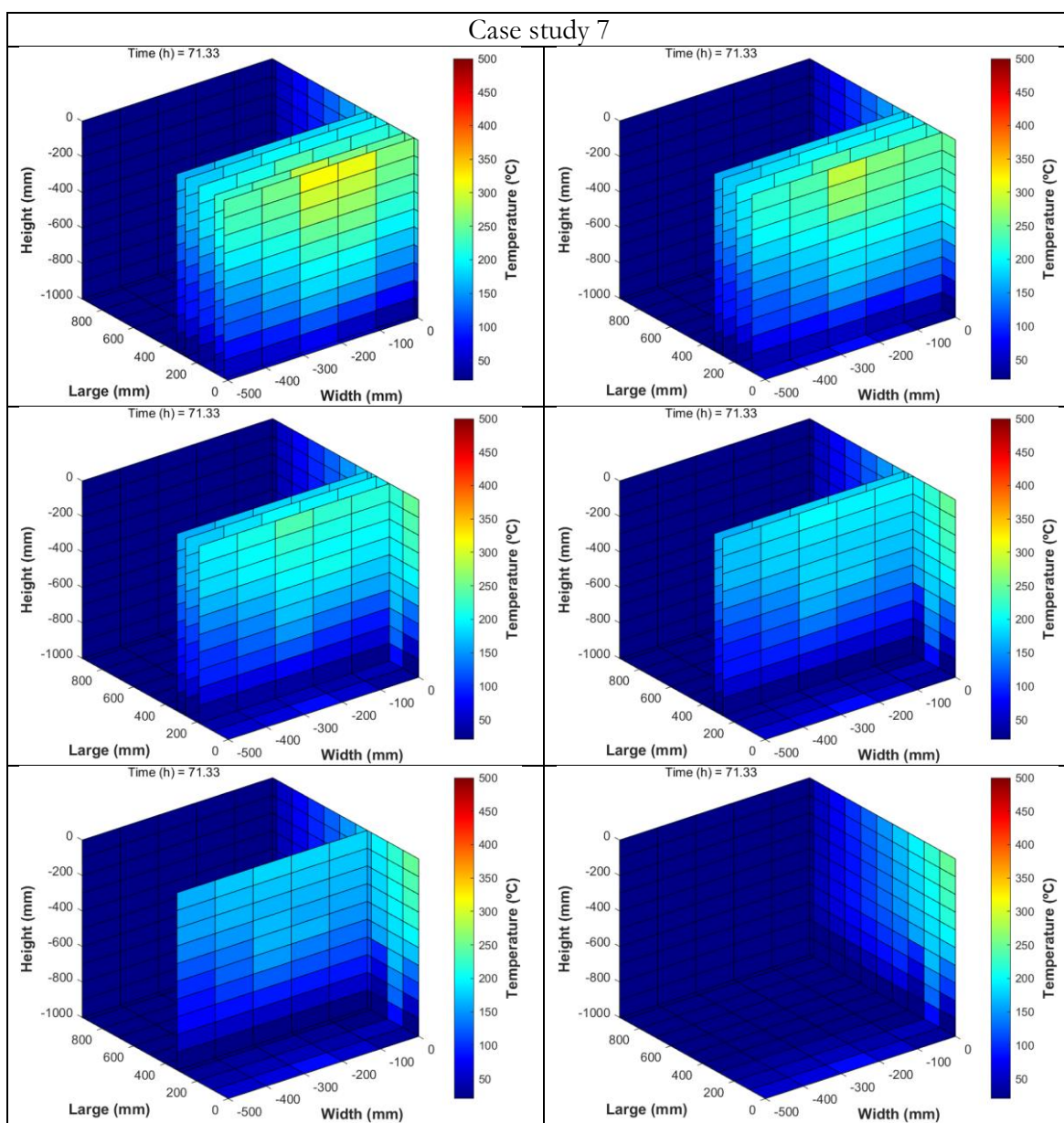
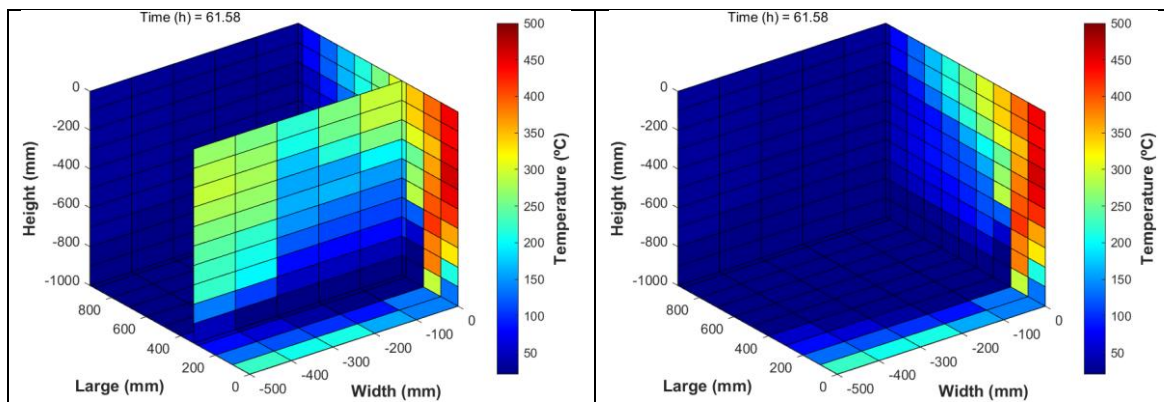




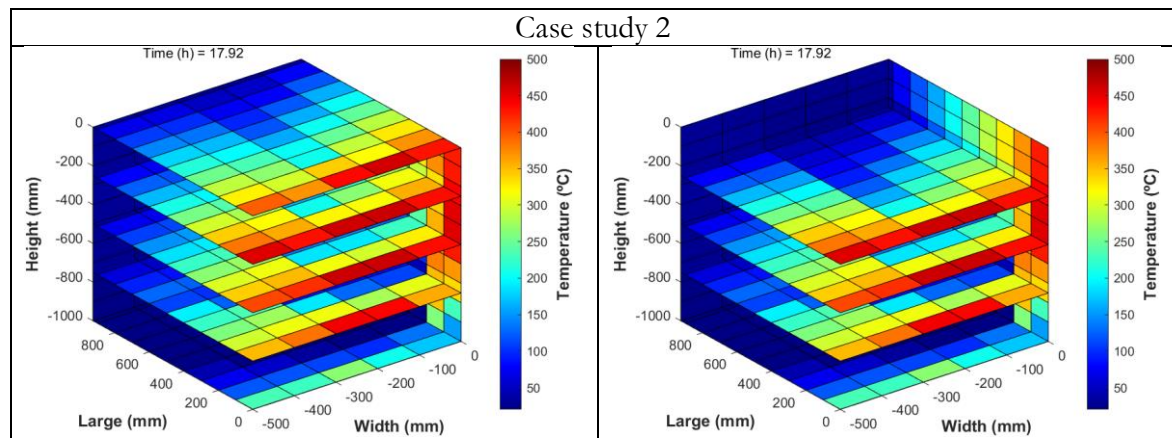
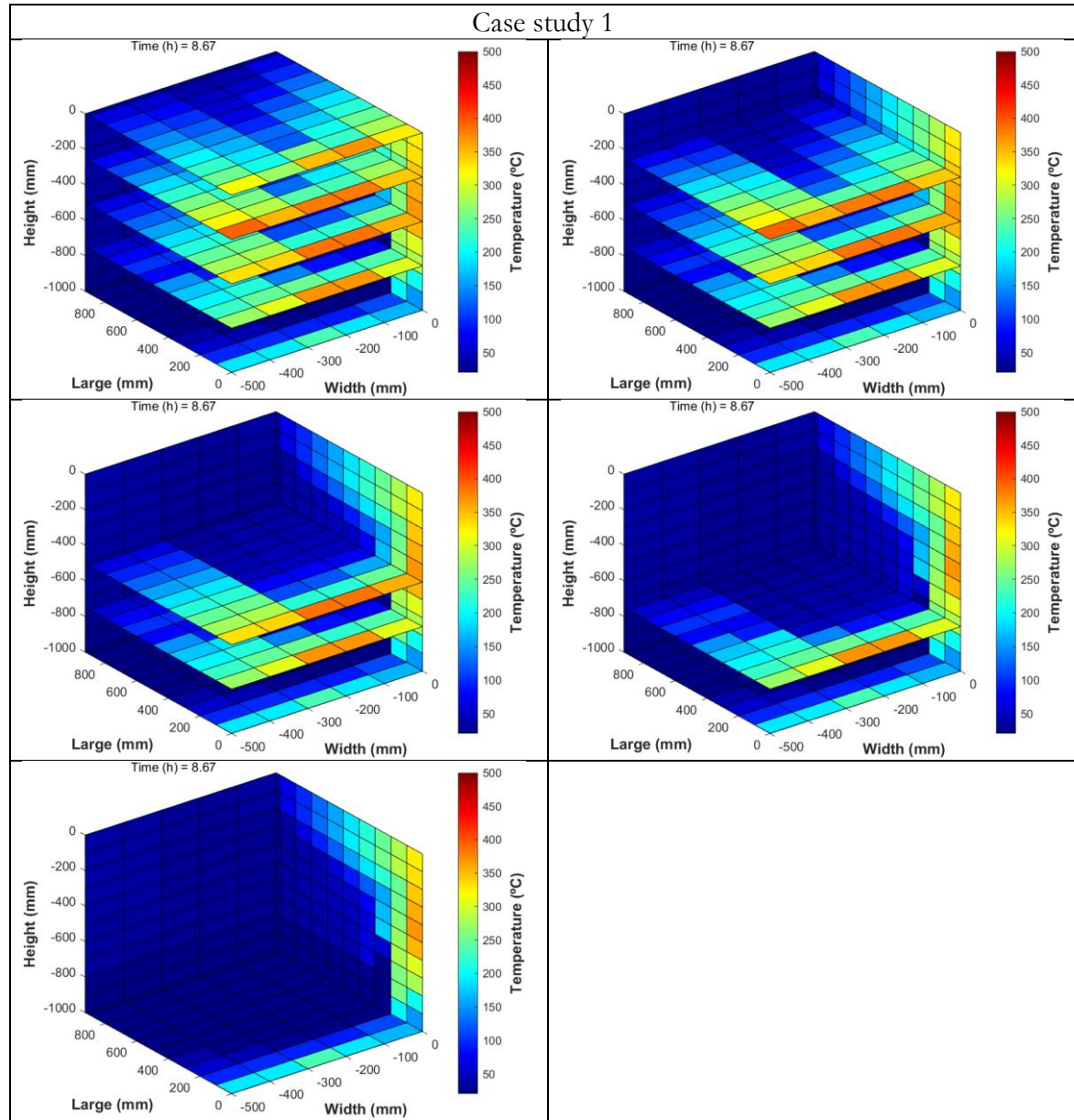
Case study 4

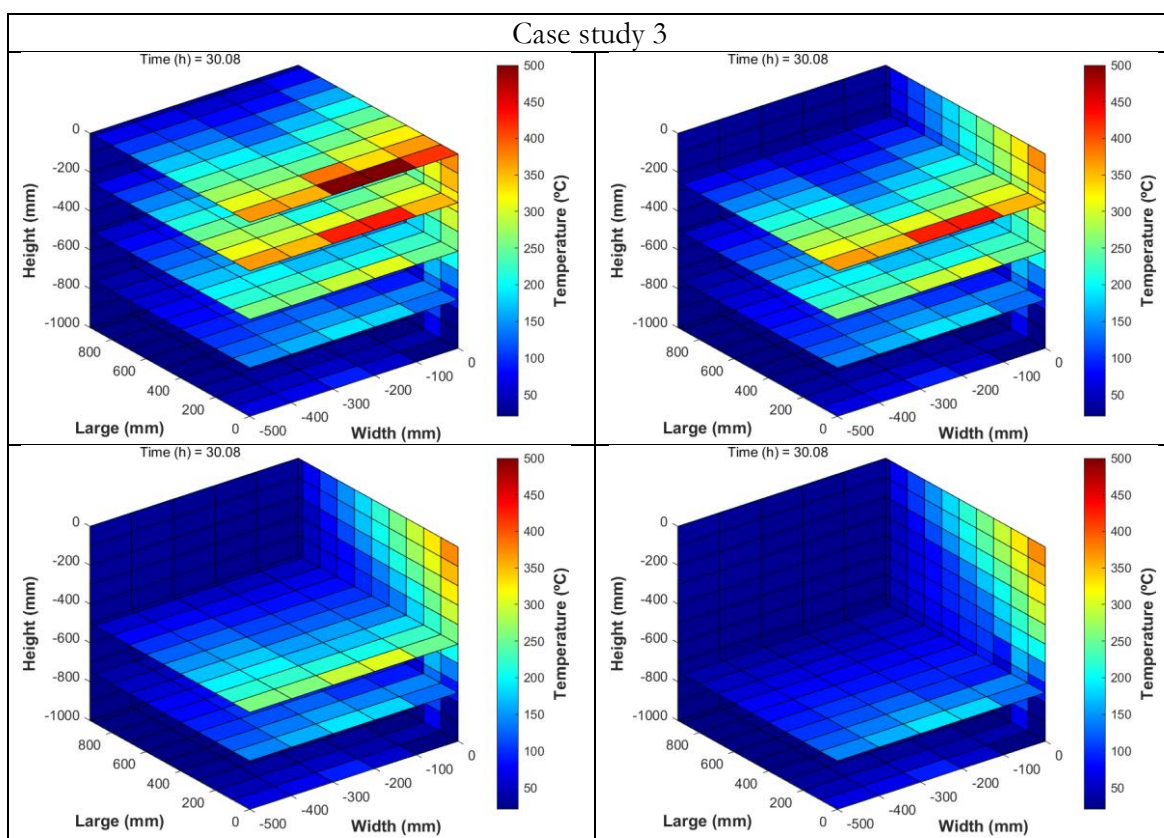
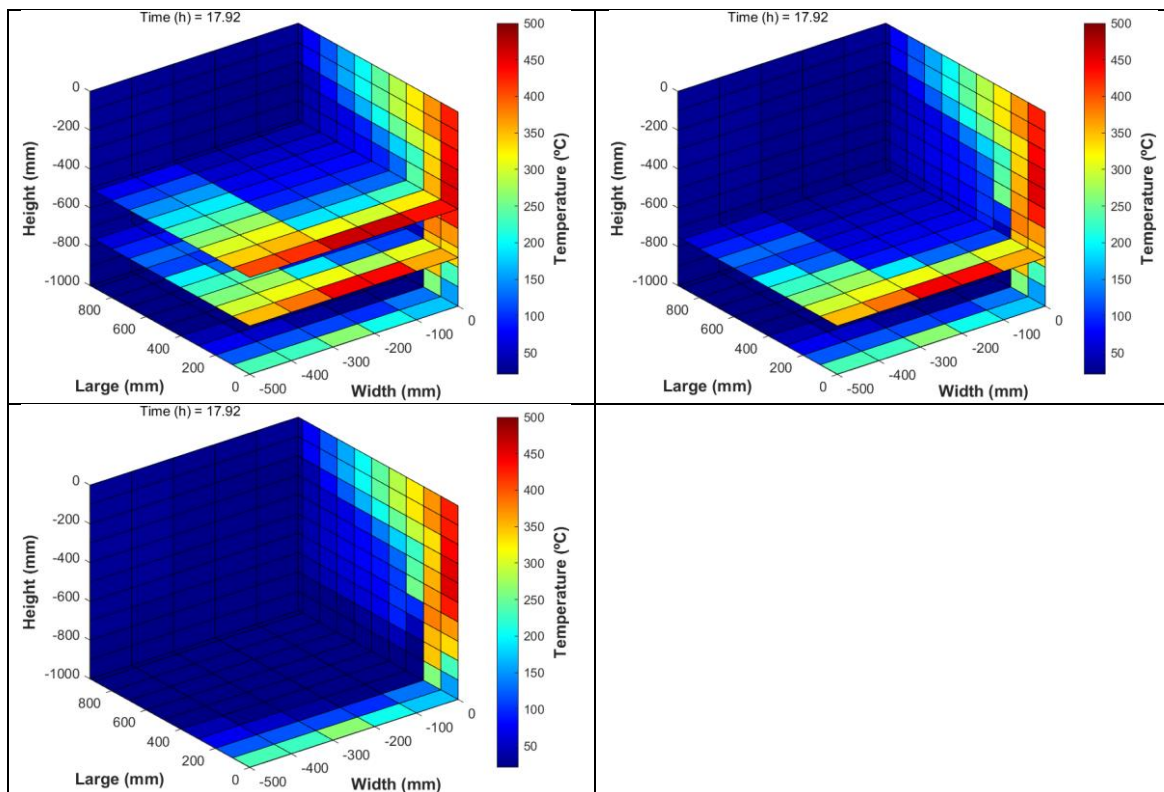


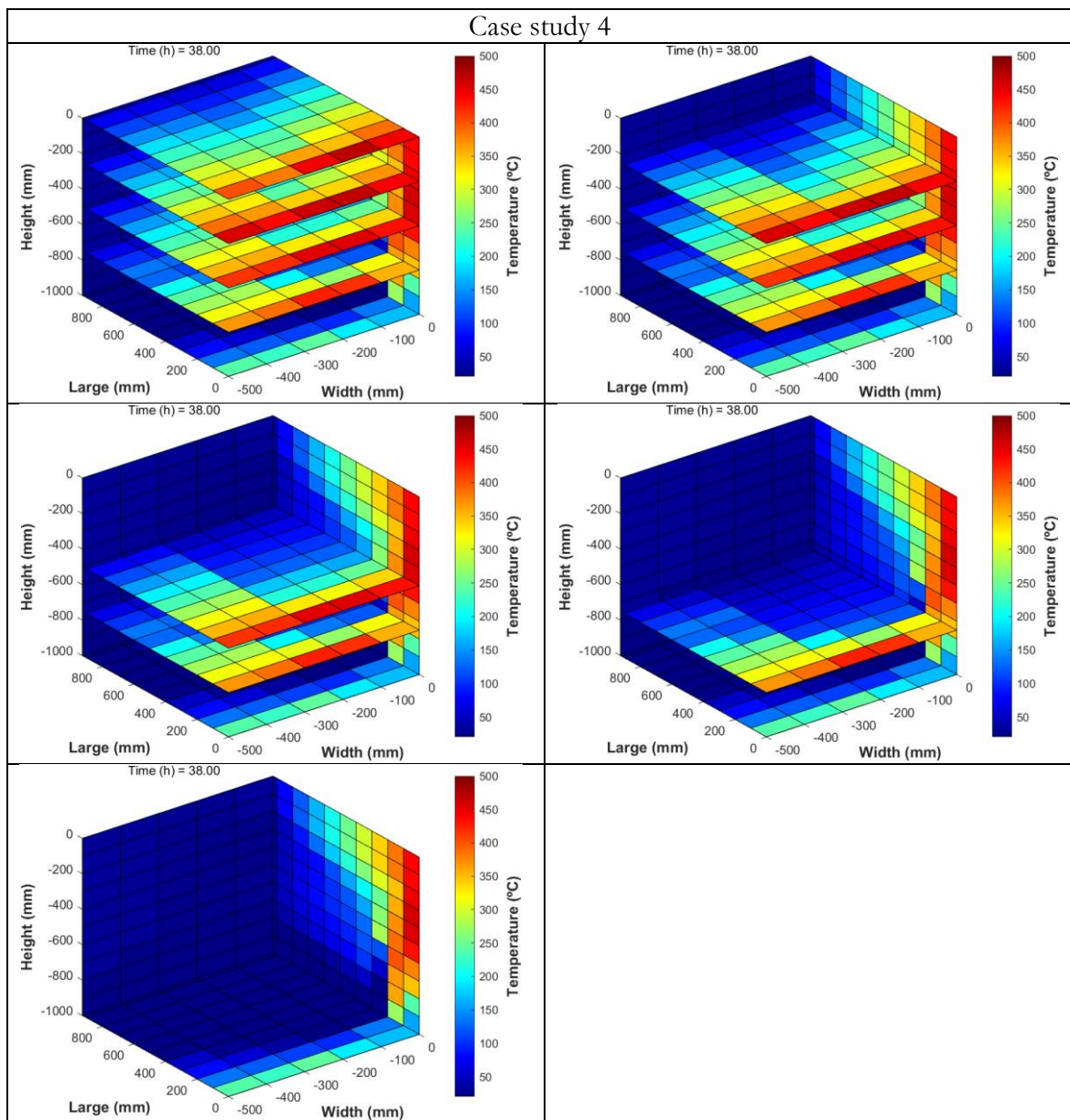
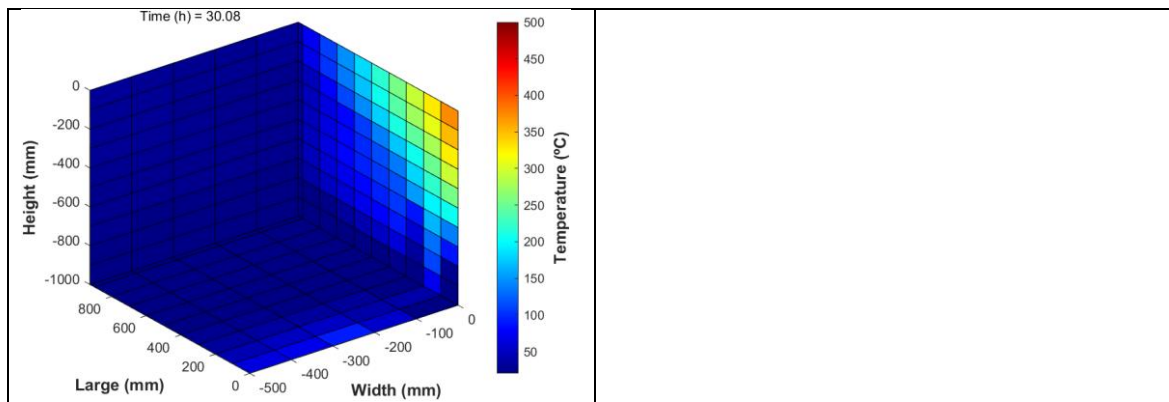




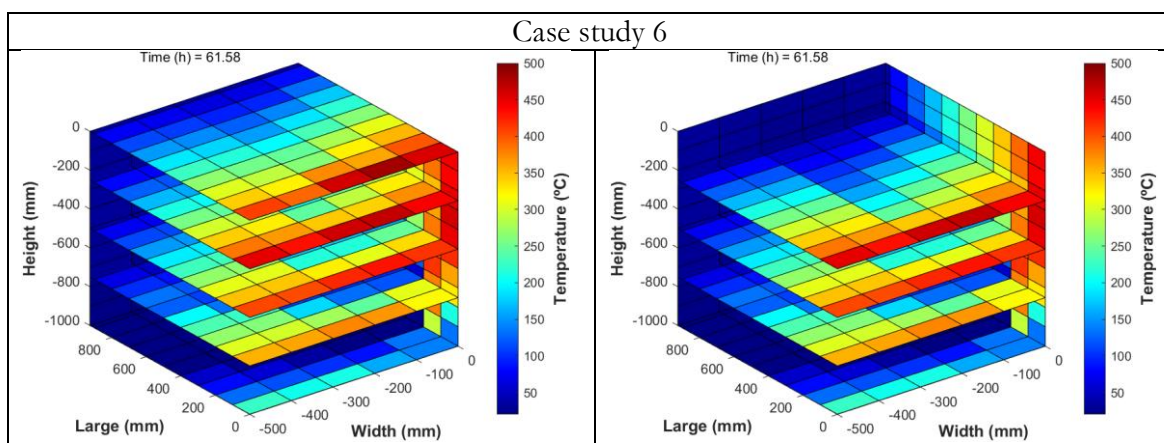
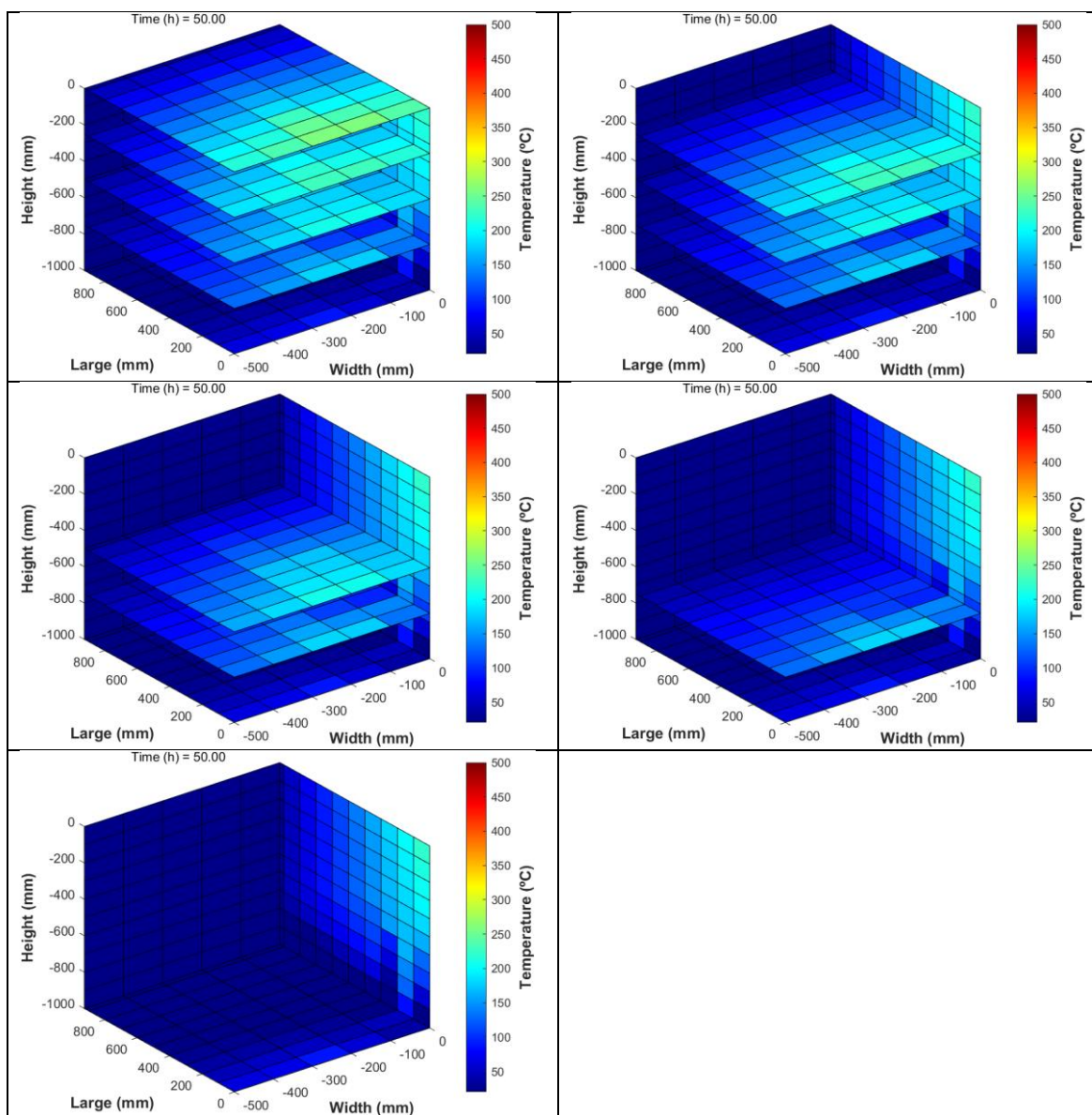
C.3) Temperature profiles at different heights (Z-Planes)

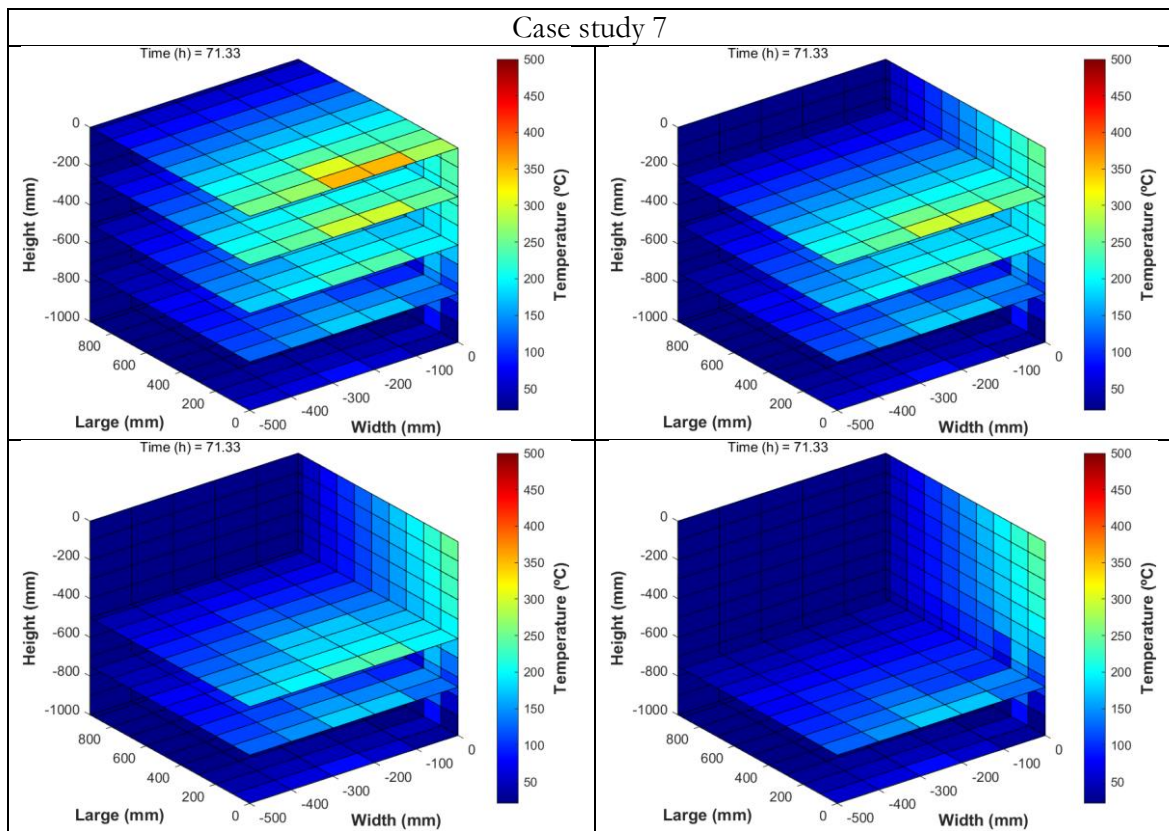
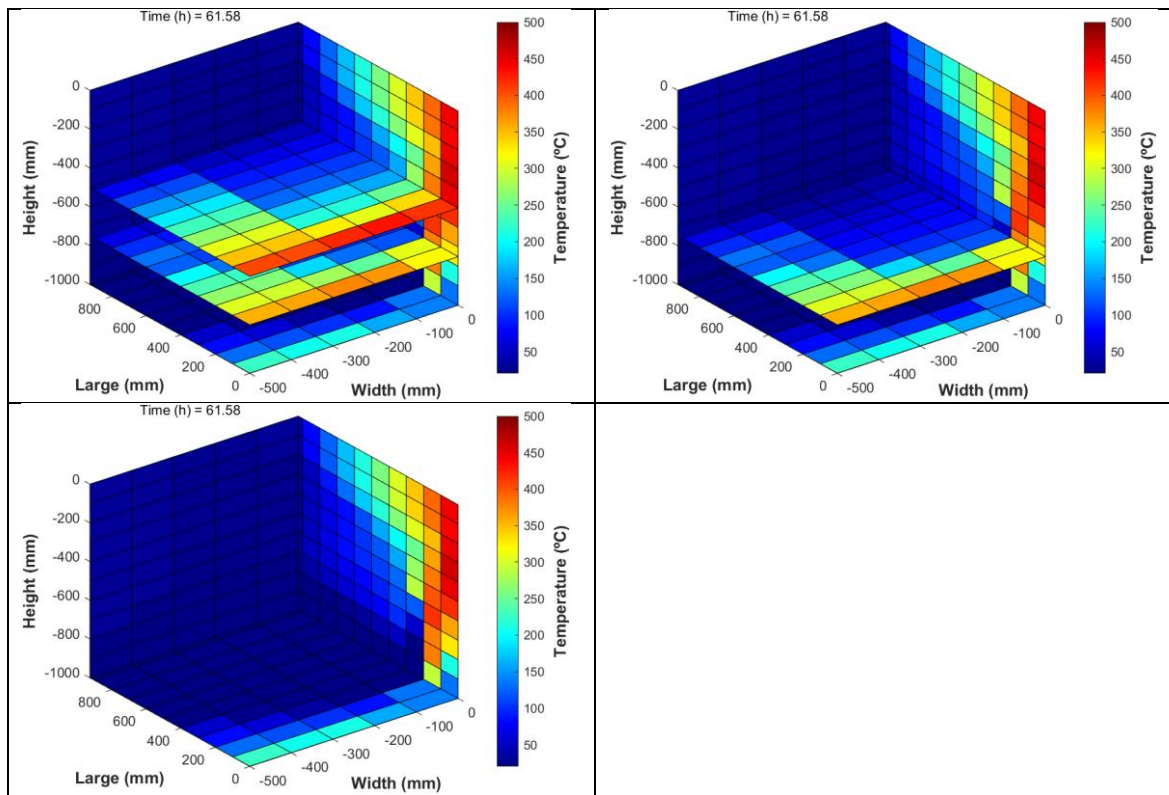


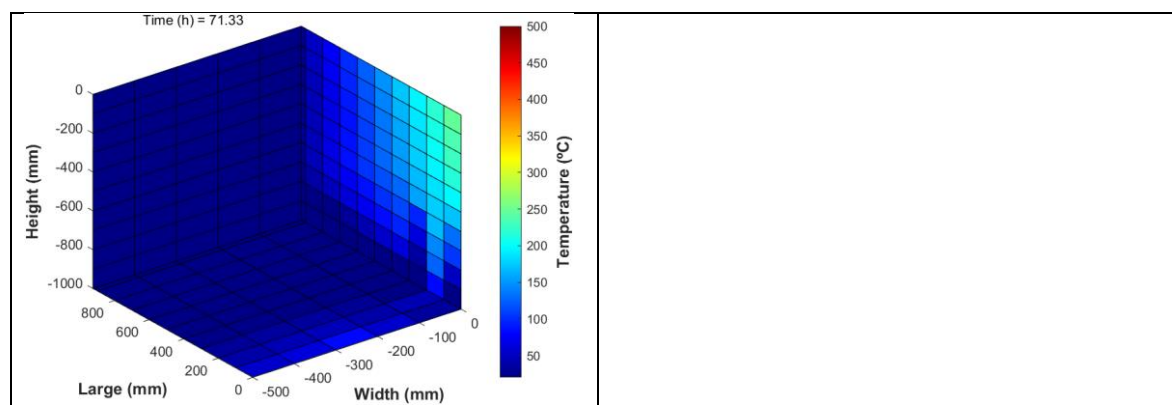




Case study 5







This page has been intentionally left blank.

Appendix D

Application for a National Patent



Justificante de presentación electrónica de solicitud de patente

Este documento es un justificante de que se ha recibido una solicitud española de patente por vía electrónica utilizando la conexión segura de la O.E.P.M. De acuerdo con lo dispuesto en el art. 16.1 del Reglamento de ejecución de la Ley 24/2015 de Patentes, se han asignado a su solicitud un número de expediente y una fecha de recepción de forma automática. La fecha de presentación de la solicitud a la que se refiere el art. 24 de la Ley le será comunicada posteriormente.

| | | |
|----------------------------|--|---|
| Número de solicitud: | P202031076 | |
| Fecha de recepción: | 28 octubre 2020, 10:19 (CET) | |
| Oficina receptorá: | OEPM Madrid | |
| Su referencia: | ES1641.1594 | |
| Solicitante: | Consejo Superior de Investigaciones Científicas (CSIC) | |
| Número de solicitantes: | 1 | |
| País: | ES | |
| Título: | PROCEDIMIENTO Y EQUIPO DE MEDIDA PARA DETECTAR, DE FORMA CONTINUA Y NO DESTRUCTIVA, EL SECADO DE UNA ESTRUCTURA DE HORMIGÓN | |
| Documentos enviados: | Descripción.pdf (11 p.) Reivindicaciones-1.pdf (3 p.) Dibujos-1.pdf (6 p.) Resumen-1.pdf (1 p.) OLF-ARCHIVE.zip FEERCPT-1.pdf (1 p.) FEERCPT-2.pdf (1 p.) | package-data.xml es-request.xml application-body.xml es-fee-sheet.xml feesheet.pdf request.pdf |
| Enviados por: | C=ES,O=PONS PATENTES Y MARCAS INTERNACIONAL SL,2.5.4.97=#0C0F56415445532D423834393231373039,CN=50534279 J ANGEL PONS (R: B84921709),SN=PONS ARIÑO,givenName=ANGEL,serialNumber=IDCES-50534279J,description=Reg:28065 /Hoja:M-421468 /Tomo:23494 /Folio:199 / Fecha:22/02/2012 /Inscripción:9 | |
| Fecha y hora de recepción: | 28 octubre 2020, 10:19 (CET) | |

Codificación del envío: E3:89:A7:F1:92:F8:16:3E:AD:75:37:A2:B8:59:57:2D:56:47:30:9C

AVISO IMPORTANTE

Las tasas pagaderas al solicitar y durante la tramitación de una patente o un modelo de utilidad son las que se recogen en el Apartado "Tasas y precios públicos" de la página web de la OEPM (http://www.oepm.es/es/propiedad_industrial/tasas/). Consecuentemente, si recibe una comunicación informándole de la necesidad de hacer un pago por la inscripción de su patente o su modelo de utilidad en un "registro central" o en un "registro de internet" posiblemente se trate de un fraude. La anotación en este tipo de autodenominados "registros" no despliega ningún tipo de eficacia jurídica ni tiene carácter oficial.

En estos casos le aconsejamos que se ponga en contacto con la Oficina Española de Patentes y Marcas en el correo electrónico informacion@oepm.es.

ADVERTENCIA: POR DISPOSICIÓN LEGAL LOS DATOS CONTENIDOS EN ESTA SOLICITUD PODRÁN SER PUBLICADOS EN EL BOLETÍN OFICIAL DE LA PROPIEDAD INDUSTRIAL E INSCRITOS EN EL REGISTRO DE PATENTES DE LA OEPM, SIENDO AMBAS BASES DE DATOS DE CARÁCTER PÚBLICO Y ACCESIBLES VÍA REDES MUNDIALES DE INFORMÁTICA.

Para cualquier aclaración puede contactar con la O.E.P.M.

/Madrid, Oficina Receptora/



| | | |
|--|---|---|
| (1) MODALIDAD: | PATENTE DE INVENCION MODOLO DE UTILIDAD | <input checked="" type="checkbox"/> [] |
| (2) FORMULARIO 5101. TIPO DE SOLICITUD: | PRIMERA PRESENTACION SOLICITUD DIVISIONAL CAMBIO DE MODALIDAD TRANSFORMACION SOLICITUD PATENTE EUROPEA PCT: ENTRADA FASE NACIONAL | <input checked="" type="checkbox"/> [] |
| (3) EXP. PRINCIPAL O DE ORIGEN: | MODALIDAD: N.º SOLICITUD: FECHA SOLICITUD: | |
| 4) LUGAR DE PRESENTACIÓN: | OEPM, Presentación Electrónica | |
| (5-1) SOLICITANTE 1: | | |
| DENOMINACIÓN SOCIAL: UNIVERSIDAD PÚBLICA | | |
| NACIONALIDAD: CÓDIGO PAÍS: NIF/NIE/PASAPORTE: CNAE: PYME | | |
| DOMICILIO: LOCALIDAD: PROVINCIA: CÓDIGO POSTAL: PAÍS RESIDENCIA: CÓDIGO PAÍS: TELÉFONO: FAX: CORREO ELECTRÓNICO: | | |
| EMPRENDEDOR: PERSONA DE CONTACTO: | | |
| MODO DE OBTENCIÓN DEL DERECHO: | | |
| INVENCION LABORAL: CONTRATO: SUCESIÓN: OTROS: | | |
| PORCENTAJE DE TITULARIDAD: 100,00 % | | |
| (6-1) INVENTOR 1: | | |
| APELLOS: NOMBRE: NACIONALIDAD: CÓDIGO PAÍS: | | |
| DOMICILIO: LOCALIDAD: | | |
| CÓDIGO POSTAL: PAÍS RESIDENCIA: CÓDIGO PAÍS: | | |

| | |
|--|--|
| <p>TELÉFONO: FAX: CORREO ELECTRÓNICO: EL INVENTOR RENUNCIA A SER MENCIONADO:</p> <p>(6-2) INVENTOR 2:</p> <p>APPELLIDOS: NOMBRE: NACIONALIDAD: CÓDIGO PAÍS: DOMICILIO: LOCALIDAD: CÓDIGO POSTAL: PAÍS RESIDENCIA: CÓDIGO PAÍS: TELÉFONO: FAX: CORREO ELECTRÓNICO: EL INVENTOR RENUNCIA A SER MENCIONADO:</p> | <p>[]</p> <p>Lucio Martín Tamara España ES</p> <p>[]</p> |
| <p>(7) TÍTULO DE LA INVENCION:</p> <p>PROCEDIMIENTO Y EQUIPO DE MEDIDA PARA DETECTAR, DE FORMA CONTINUA Y NO DESTRUCTIVA, EL SECADO DE UNA ESTRUCTURA DE HORMIGON</p> | |
| <p>(8) NÚMERO DE INFORME TECNOLÓGICO DE PATENTES (ITP):</p> | |
| <p>(9) SOLICITA LA INCLUSIÓN EN EL PROCEDIMIENTO ACELERADO DE CONCESIÓN</p> <p>SI [] NO [✓]</p> | |
| <p>(10) EFECTUADO DEPÓSITO DE MATERIA BIOLÓGICA:</p> <p>SI [✓] NO []</p> | |
| <p>(11) DEPÓSITO:</p> <p>REFERENCIA DE IDENTIFICACIÓN: INSTITUCIÓN DE DEPÓSITO: NÚMERO DE DEPÓSITO: ORÍGEN BIOLÓGICO:</p> | |
| <p>(12) RECURSO GENÉTICO</p> <p>NÚMERO DE REGISTRO: NÚMERO DE CERTIFICADO DE ACCESO AL RECURSO: UTILIZACIÓN DEL RECURSO GENÉTICO: CONOCIMIENTO TRADICIONAL ASOCIADO A UN RECURSO GENÉTICO:</p> | |
| <p>(13) DECLARACIONES RELATIVAS A LA LISTA DE SECUENCIAS:</p> <p>LA LISTA DE SECUENCIAS NO VA MÁS ALLÁ DEL CONTENIDO DE LA SOLICITUD LA LISTA DE SECUENCIAS EN FORMATO PDF Y ASCII SON IDENTICOS</p> <p>[] []</p> | |
| <p>(14) EXPOSICIONES OFICIALES:</p> <p>NOMBRE: LUGAR: FECHA:</p> | |
| <p>(15) DECLARACIONES DE PRIORIDAD:</p> <p>PAÍS DE ORIGEN: CÓDIGO PAÍS: NÚMERO: FECHA:</p> | |
| <p>(16) REMISIÓN A UNA SOLICITUD ANTERIOR:</p> <p>PAÍS DE ORIGEN: CÓDIGO PAÍS: NÚMERO: FECHA:</p> | |

| | | |
|---|--|---|
| (17) AGENTE DE PROPIEDAD INDUSTRIAL: | APELLIDOS: NOMBRE: CÓDIGO DE AGENTE: NÚMERO DE PODER: | PONS ARIÑO ÁNGEL 0499/5 20081765 |
| (18) DIRECCIÓN A EFECTOS DE COMUNICACIONES: DIRECCIÓN ASOCIADA AL PRIMER SOLICITANTE | DOMICILIO: LOCALIDAD: CÓDIGO POSTAL: PAÍS RESIDENCIA: CÓDIGO PAÍS: TELÉFONO: FAX: CORREO ELECTRÓNICO: MEDIO PREFERENTE DE COMUNICACIÓN | |
| (19) RELACION DE DOCUMENTOS QUE SE ACOMPAÑAN: | <p>DESCRIPCIÓN:</p> <p>REIVINDICACIONES <input checked="" type="checkbox"/> N.º de páginas: 11 <input checked="" type="checkbox"/> N.º revindicaciones: 8 <input checked="" type="checkbox"/> N.º de dibujos: 7 <input checked="" type="checkbox"/> N.º de páginas: 1 <input checked="" type="checkbox"/> N.º de figura(s): <input checked="" type="checkbox"/></p> <p>DIBUJOS: <input type="checkbox"/> N.º de páginas:</p> <p>RESUMEN: <input checked="" type="checkbox"/> N.º de páginas: 1 <input checked="" type="checkbox"/> N.º de figura(s): <input checked="" type="checkbox"/></p> <p>FIGURA(S) A PUBLICAR CON EL RESUMEN: <input type="checkbox"/> N.º de páginas:</p> <p>ARCHIVO DE PRECONVERSIÓN: <input type="checkbox"/> N.º de páginas:</p> <p>DOCUMENTO DE REPRESENTACIÓN: <input type="checkbox"/> N.º de páginas:</p> <p>JUSTIFICANTE DE PAGO (1): <input checked="" type="checkbox"/> N.º de páginas: 1 <input checked="" type="checkbox"/> N.º de páginas: 1 <input type="checkbox"/> N.º de páginas: <input type="checkbox"/></p> <p>JUSTIFICANTE DE PAGO (2): <input type="checkbox"/> N.º de páginas:</p> <p>LISTA DE SECUENCIAS PDF: <input type="checkbox"/> N.º de páginas:</p> <p>ARCHIVO PARA LA BUSQUEDA DE LS: <input type="checkbox"/> N.º de páginas:</p> <p>OTROS (Aparecerán detallados): <input type="checkbox"/> N.º de páginas:</p> | |
| (20) EL SOLICITANTE SE ACODE A LA REDUCCIÓN DE TASAS PARA EMPRENDEDORES PREVISTA EN EL ART. 186 DE LA LEY 24/2015 DE PATENTES Y, A TAL EFECTO, APORTA LA SIGUIENTE DOCUMENTACIÓN ADJUNTA: | [] | |
| (21) NOTAS: | | |
| (22) FIRMA: | <p>FIRMA DEL SOLICITANTE O REPRESENTANTE: <input type="text" value="50534279J ANGEL PONS (R: B84921709)"/></p> <p>LUGAR DE FIRMA: <input type="text" value="MADRID"/></p> <p>FECHA DE FIRMA: <input type="text" value="28 Octubre 2020"/></p> | |

Appendix E

Accountability

The advances of the work carried out during the present thesis were presented at Universidad Carlos III de Madrid every year for the evaluation of the requirements of the PhD Programme of Mechanical Engineering and Industrial Organization. With such aim, the initial research plan and modifications of the research plan were submitted at the end of the scholar year for the assessment. The documents were validated and approved by the Academic Commission.

On the other hand, this appendix comprises the accountability of the work carried out during this period, including the candidate's scientific production in journals and international and national conference papers.

E.1) Publications in Journals Indexed in the Journal Citation Report

T. Lucio-Martin, M. Roig-Flores, M. Izquierdo and M.C. Alonso.

Thermal conductivity of concrete at high temperatures for thermal energy storage applications: Experimental analysis

Journal: *Solar Energy*, vol. 214, pp. 430-442, 2021.

[Solar Energy 214 \(2021\) 430–442](#)



Thermal conductivity of concrete at high temperatures for thermal energy storage applications: Experimental analysis



T. Lucio-Martin ^{a,*}, M. Roig-Flores ^{a,b}, M. Izquierdo ^a, M.C. Alonso ^a

^a Consejo Superior de Investigaciones Científicas, Eduardo Torroja Institute for Construction Sciences (CSIC-IETcc), Spain

^b Universitat Politècnica de Valencia, Institute of Concrete Science and Technology (UPV-ICITECH), Spain

ARTICLE INFO

Keywords:
Thermal conductivity
Concrete
High temperature
Thermal energy storage

ABSTRACT

Thermal conductivity plays an important role in energy storage when the materials are charging and discharging. This paper presents an experimental investigation of the evolution of thermal conductivity up to 600 °C in different concretes. Moreover, the thermal conductivity was measured during thermal fatigue cycles when temperature ranged between 300 and 600 °C, simulating the operation conditions in a storage system of molten salts in a Concentrating Solar Power Plant (CSP). Five concrete compositions were analysed using diverse types of aggregates with different thermal response, covering a wide range of the initial thermal conductivity. The results confirm that the loss of thermal conductivity with temperature during the first heating is mainly due to the free water loss. Moreover, the type of aggregate influences the overall thermal performance of concrete due to its thermal conductivity and the volumetric differences with the cement paste. Siliceous aggregates underwent the highest decrease of thermal conductivity of concrete (+50%) with regard to room temperature. Regarding the cooling phase, thermal conductivity recovers between 20% and 40% depending on the type of aggregate. The outcomes of the present study demonstrate that the assumption of a constant thermal conductivity value in numerical simulations to predict its thermal capacity for energy storage is not appropriate.

T. Lucio-Martin, M. Roig-Flores, M. Izquierdo and M.C. Alonso

Corrigendum to “Thermal conductivity of concrete at high temperatures for thermal energy storage applications: Experimental analysis. [Sol. Energy 214 (2021) 430-442]”

Journal: *Solar Energy*, 2021.

ARTICLE IN PRESS

[Solar Energy xxx \(xxxx\) xxx](#)



Corrigendum

Corrigendum to “Thermal conductivity of concrete at high temperatures for thermal energy storage applications: Experimental analysis” [Sol. Energy 214 (2021) 430–442]

T. Lucio-Martin ^{a,*}, M. Roig-Flores ^{a,b}, M. Izquierdo ^a, M.C. Alonso ^a

^a Consejo Superior de Investigaciones Científicas, Eduardo Torroja Institute for Construction Sciences (CSIC-IETcc), Spain

^b Universitat Politècnica de Valencia, Institute of Concrete Science and Technology (UPV-ICITECH), Spain

M. Roig-Flores, T. Lucio-Martin, M.C. Alonso and L. Guerreiro

Evolution of thermo-mechanical properties of concrete with calcium aluminate cement and special aggregates for energy storage

Journal: *Cement and Concrete Research*, vol. 141, 2021, 106323.

[Cement and Concrete Research 141 \(2021\) 106323](#)



Contents lists available at [ScienceDirect](#)

Cement and Concrete Research

journal homepage: www.elsevier.com/locate/cemconres



Evolution of thermo-mechanical properties of concrete with calcium aluminate cement and special aggregates for energy storage



Marta Roig-Flores ^{a,*}, Tamara Lucio-Martin ^a, María Cruz Alonso ^a, Luis Guerreiro ^b

^a Consejo Superior de Investigaciones Científicas, Instituto Eduardo Torroja de Ciencias de la Construcción (CSIC-IETcc), c/ Serrano Galvache, 4, 28033 Madrid, Spain
^b University of Évora, Renewable Energies Chair, Casa Cordovil, Rua D. Augusto Eduardo Nunes, n.º, 7000-651 Évora, Portugal

ARTICLE INFO

Keywords:
Calcium aluminate cement
Concrete
Thermal cycles
Cracking
Thermal conductivity

ABSTRACT

With the ever-expanding presence of solar energy, the design of cost-efficient heat energy storage systems is becoming increasingly relevant. Concrete is a potential solid material for these systems but raises questions of its response at high temperatures in operating conditions. This work studies concrete designed with calcium aluminate cement and three types of aggregates that are stable at high temperatures. The designed concrete mixes were exposed to thermal cycles (290–550 °C), and their thermal fatigue response was evaluated with mechanical, cracking, thermal, and microstructural analyses at room temperature after heat cycles. The obtained results show that the main changes are mostly produced after the first thermal cycle and are stabilized during successive thermal cycles, with only a slight decrease in the thermo-mechanical properties. The results showed stabilization of cracking, crack widths between 10 and 80 µm, reduction of compressive strength, around 50–65%, and reduction of the thermal conductivity by 30%.

E.2) International Conference Papers

T. Lucio-Martin, M. Roig-Flores, M.C. Alonso and L. Guerreiro

Evolution of thermal conductivity on CAC concrete at high temperatures and during thermal fatigue tests

Proceedings of the 6th International Workshop on Concrete Spalling due to Fire Exposure, Sheffield (United Kingdom), September 2019.

Proceedings of the 6th International Workshop on Concrete Spalling due to Fire Exposure

Sheffield, United Kingdom
19-20 September 2019

Scientific Editors:
Dr Shan-Shan Huang
Prof Ian Burgess

The University Of Sheffield.

Department Of Civil & Structural Engineering.

Evolution of thermal conductivity on CAC concrete at high temperatures and during thermal fatigue tests

T. Lucio-Martin¹, M.C. Alonso^{1,*}, M. Roig-Flores² & L. Guerreiro³
¹Eduardo Torroja Institute for Construction Sciences (IETcc-CSIC), Madrid, Spain
²Universitat Politècnica de València, Valencia, Spain
³University of Evora, Evora, Portugal

* Corresponding author (lamarra.lucio@ietcc.csic.es, Serrano Galvache 4, CP: 28033, Madrid, Spain)

ABSTRACT

Heat transfer plays an important role when concrete works at high temperatures. For many applications, it is important to evaluate the effect of heat transfer on concrete to predict the thermo-mechanical response. Inside concrete, the dominant mechanism of heat transfer is conduction, and the main parameter involved in thermal conductivity. Heat transfer may play also a relevant role when spalling occurs.

In this paper, the evolution of thermal conductivity of concrete with temperature has been studied for different concrete types up to 600°C. The effect of cooling and thermal gradients are followed.

Results indicate that during the first heating, thermal conductivity decreases in several steps with temperature, first due to pore free water loss and second after dehydration up to 300°C. The water loss and the temperature gradients are also affected. Thermal gradients play a role in the risk of concrete spalling. When cooling, thermal conductivity recovered almost the same value at 300°C. Repetitive thermal cycles do not modify the thermal performance of concrete.

KEYWORDS: heat transfer, thermal conductivity, thermal gradients, thermal fatigue

INTRODUCTION

There are infrastructures of concrete which operate at high temperatures during its service life. Applications such as nuclear and geothermal power plants condition concrete structures to work at high temperatures. Nevertheless, concrete is being considered as a material for thermal energy storage systems for Concentrating Solar Power Plants (CSP). For such applications, concrete has to operate under high temperature for long periods and during cycles of charge and discharge. Several authors have already demonstrated at lab scale the potentiality of concrete up to 600°C [1-3].

Nevertheless, when concrete is exposed to high temperatures, the spalling risk increases owing to thermal gradients between the surface and the core and core pressures. The spalling caused by thermal gradients, which originates stresses, is one mechanism that has been widely accepted to explain the spalling phenomenon in concrete under fire [4-6].

T. Lucio-Martin, J. Puentes and M.C. Alonso

Effect of geometry in concrete spalling risk subjected to high temperatures for thermal inertia studies

Proceedings of the 6th International Workshop on Concrete Spalling due to Fire Exposure, Sheffield (United Kingdom), September 2019.

Proceedings of the 6th International Workshop on Concrete Spalling due to Fire Exposure

Sheffield, United Kingdom
19-20 September 2019

Scientific Editors:
Dr Shan-Shan Huang
Prof Ian Burgess

The University Of Sheffield.

Department Of Civil & Structural Engineering.

Effect of geometry in concrete spalling risk subjected to high temperatures for thermal inertia studies

T. Lucio Martin¹, J. Puentes¹ & M.C. Alonso^{1,*}
¹Eduardo Torroja Institute for Construction Sciences (IETcc-CSIC), Madrid, Spain

* Corresponding author (mcalonso@ietcc.csic.es, Serrano Galvache 4, CP: 28033, Madrid, Spain)

ABSTRACT

Several studies have demonstrated the feasibility of using concrete as a thermal energy storage material. An experimental procedure must be established during the concrete mix design to validate its performance when subjected to high temperature (up to 600°C) in order to extend the service life. The initial cement paste dehydration is considered to be the most critical part of the start-up of the concrete, due to the high probability of spalling. In addition, the material after this stage starts to be following heating and cooling cycles between 200 and 550°C.

The aim is to evaluate the thermal inertia of the concrete in order to minimize the risk of spalling in the dehydration stage of the concrete, as well as the damage evolution in the successive thermal fatigue cycles. A small-scale experimental study has been carried out using a Self-compacting concrete (SCC) thermally designed for energy storage in concrete. Specimens of different geometries were made to assess the behaviour against several factors: heating rate, thermal gradient, sample geometry and crack formation.

For this purpose, three different sizes and geometries of SCC samples have been manufactured. The behaviour has been studied during the heating and cooling cycles. Results indicate that the geometry defines the heating rate of the material and hence, the risk of spalling. Not only thermal gradients affected the spalling, but it also was influenced by the time of exposure. On the other hand, the long-term performance of the concrete mix was proved to be used as suitable for thermal storage because of its low degradation propagation after exposure of concrete to thermal fatigue cycles.

KEYWORDS: High temperature, thermal gradient, self-compacting concrete, spalling

INTRODUCTION

The behaviour of concrete exposed to high temperatures has been studied for a long time from the point of view of the material in the presence of fire. However, in recent years, new applications in energy infrastructures have consolidated their own line of research. The use of concrete as thermal energy storage in concentrated solar power plants (CSP) has been verified recently [1-3]. The highest concern in relation to the type of use of concrete is the thermal stability of the concrete when exposed to heat charge and discharge.

From the point of view of the development of high temperature concrete design, several alternatives have allowed a better performance. The use of polypropylene fibres (PPF) [2, 4], thermal stable and low expansion aggregates and its size distribution in the mix [2] has been proved useful to have a better performance. Concrete spalling risk is one of a major case of

E.3) National Conference Papers

T. Lucio-Martin, M. Roig-Flores, J. Carretero, M.C. Alonso and M. Izquierdo

Análisis de fisuración en hormigones de almacenamiento de energía sometidos a ciclos de fatiga térmica

II Jornadas de Jóvenes Científicos en Materiales de Construcción, Instituto de Ciencias de la Construcción Eduardo Torroja (IETcc-CSIC), May 2019.

II Jornadas de Jóvenes Científicos en Materiales de Construcción

28 de mayo 2019

Instituto de Ciencias de la Construcción Eduardo Torroja
Universidad Carlos III de Madrid
Instituto de Cerámica y Vidrio

PROGRAMA FINAL Y LIBRO DE ABSTRACTS

Graphical Abstract

Abstract

Los efectos irreversibles asociados al cambio climático han incrementado el interés por la búsqueda de nuevas fuentes de obtención de energía renovable. Para ello, el almacenamiento energético juega un papel fundamental ya que los picos de demanda y generación de energía son una procedente de centrales térmicas (CSP). Los regímenes de operación de CSP hacen que las estructuras experimenten cambios térmicos y cíclicos de fatiga térmica entre 200-550°C. El hormigón al ser sometido a altas temperaturas experimenta cambios micro y macroestructurales debidos principalmente a la deshidratación de la pasta y a la expansión de los óxidos. Este trabajo plantea un análisis de formación de huecos generados para almacenar energía que han sido sometidos a 10, 25 y 50°C y se realizan fotografías digitales en cuatro desfocalizaciones y se han obtenido los patrones de deformación mediante un software de edición fotográfica. A continuación se ha determinado el porcentaje de área cubierta por fisuras y se han medida las elevaciones de las mismas. Los resultados muestran que, la compatibilidad y expansión térmica es menor a 100°C y se observa una disminución de la resistencia a la tracción y a la compresión de fibras a largo plazo. Además, se ha verificado la durabilidad y la solubilidad de las desformaciones planificadas para aplicaciones de almacenamiento energético.

Los autores agradecen al proyecto NewSOL H2020-IA-NMBP-17-2016 (ID: 720985) la financiación recibida.

*Alonso, M.C.; Vera-Agudo, J.; Guererro, L.; Poir-Laguna, V.; Sanchez, M.; Collares-Pereira, M.; Cement and Concrete Research 2016, 82, 74-85.

T. Lucio-Martin, M.C. Alonso and M. Izquierdo

Evolución de las propiedades termofísicas de los componentes del hormigón a alta temperatura

I Jornada de Jóvenes Científicos en Materiales de Construcción, Escuela de Ingeniería de Caminos, Canales y Puertos, Universidad Politécnica de Madrid, June 2018.

I Jornadas de Jóvenes Científicos en Materiales de Construcción

18-19 de junio 2018

E. T. S. Ingenieros de Caminos, Canales y Puertos de la UPM
Instituto de Ciencias de la Construcción Eduardo Torroja
Instituto de Cerámica y Vidrio

PROGRAMA FINAL Y LIBRO DE ABSTRACTS

Graphical Abstract

Abstract

El hormigón sometido a alta temperatura experimenta cambios en su micro y macroestructura debidos tanto a la deshidratación de sus componentes cementantes como a las dilataciones térmicas que experimentan los distintos componentes: óxidos y pasta, que inducen, a su vez, tensiones sobre la estructura. Estos procesos alteran el comportamiento del hormigón debido a los cambios que se producen en el interior del material. Mientras que la pasta tiene un pequeño efecto térmico, los óxidos se expanden. Como los óxidos tienen una expansión térmica de varios veces de la de la pasta, se produce una tensión térmica que se incrementa con el fin de predecir con más precisión cómo será la respuesta global del hormigón. En el presente trabajo se hace un estudio de cómo evolucionan diferentes propiedades termofísicas: conductividad térmica y expansión térmica con la temperatura obtenidas a partir de la literatura. Se han analizado el SiO₂ y el CaO, presentes en los óxidos de tipo silicato y óxido de calcio respectivamente, ya que son los más utilizados en hormigón. Los óxidos presentan un descenso de la conductividad térmica a valores muy bajos, superiores al 50% cuando se alcanzan temperaturas de 700 K. En cambio, la expansión térmica aumenta, y es más sensible en óxidos de tipo níquelico de estructura cristalina. Logrado incluso a triplicar el valor inicial cuando se superan los 800 K. Estos efectos junto con la geometría y dimensiones del elemento contribuyen a que un hormigón pueda sufrir fenómenos de explosión cuando se expone a regímenes de calentamiento superiores a 373 K.

Los autores agradecen al proyecto NewSOL H2020-IA-NMBP-17-2016 (ID: 720985) la financiación recibida.